STRATEGIES FOR METALLIC NANOPARTICLES, METAL CHALCOGENIDE NANOCRYSTALS AND PEROVSKITE QUANTUM DOTS AND THEIR OPTICAL AND OPTOELECTRONIC PROPERTIES

A Dissertation
Presented to
The Academic Faculty

by

Young Jun Yoon

In Partial Fulfillment
of the Requirements for the Degree
Doctor of Philosophy in the
School of Materials Science & Engineering

Georgia Institute of Technology
December 2018

STRATEGIES FOR METALLIC NANOPARTICLES, METAL CHALCOGENIDE NANOCRYSTALS AND PEROVSKITE QUANTUM DOTS AND THEIR OPTICAL AND OPTOELECTRONIC PROPERTIES

Approved by:

Dr. Zhiqun Lin, Advisor
School of Materials Science & Engineering
Georgia Institute of Technology

Dr. Blair Brettmann
School of Materials Science & Engineering
Georgia Institute of Technology

Dr. Vladimir Tsukruk
School of Materials Science & Engineering
Georgia Institute of Technology

Dr. Yulin Deng
School of Chemical & Biomolecular Engineering
Georgia Institute of Technology

Dr. Dong Qin
School of Materials Science & Engineering
Georgia Institute of Technology

Date Approved: October 25, 2018

ACKNOWLEDGEMENTS

I would like to express my sincere appreciation to my academic advisor, Dr. Zhiqun Lin, for his continual support, insightful guidance, and thoughtful encouragement during my Ph.D. life. I would also like to thank my thesis committee, Dr. Vladimir Tsukruk, Dr. Dong Qin, Dr. Blair Brettmann, and Dr. Yulin Deng, whom guided me towards completing my dissertation, and Dr. Zhitao Kang for his knowledgeable guidance in optical nanocrystals.

I would also like to thank our group members for their support whenever I was in need of their expertise. In particular I would like to mention, Dr. Jaehan Jung for leading me through the field of quantum materials; Dr. James Iocozzia and Dr. Yihuang Chen for guiding me through polymer synthesis; Dr. Yajing Chang and Dr. Shuguang Zhang for helping me with their expertise in optical materials. I would also like to thank Dr. Xinchang Pang, Dr. Hefeng Zhang, Dr. Hui Xu, Dr. Yanjie He, Dr. Cheng-Hsin Lu, Dr. Shuang Pan, Dr. Shiqiang Zhao, Dr. Ming He, Dr. Chaowei Fang, Dr. Meng Zhang, Zewei Wang, Yeu-Wei Harn, Jiwoo Yu, Matt Rager, Gill Biesold-Mcgee, Shuang Liang, Aurelia Wang, Qianqian Fan, and Cynthia Gomez for their insightful discussions during different stages of my Ph.D. life.

I would also like to thank my research collaborators. Dr. Sidney Malak, Dr. Chunhao Lin, Marcus Smith, and Shengtao Yu have been very helpful in regards to optical characterization of quantum nanomaterials.

Lastly, I would like to thank my family for their whole-hearted support throughout my Ph.D. studies. I know that I would not have been able to complete my studies without them.

TABLE OF CONTENTS

LIST OF TABLES

LIST OF SCHEMES

LIST OF FIGURES

SUMMARY

Nanomaterials have strikingly different and novel properties compared to their bulk counterpart. For bulk materials, which may include all materials with sizes beyond the micron-scale, physical properties are independent of size. But for nanomaterials, even a nanometer difference in size or a small change in shape may lead to tremendous changes in properties. Especially for optical nanocrystals (NCs) that interact with light, controlling size is extremely important. For instance, 2.3 nm cadmium selenide (CdSe) emits a blue color, 2.6 nm CdSe emits a green color, and 3.0 nm CdSe emits a red color upon UV excitation due to the quantum confinement effect. NCs with precisely tuned dimensions, spatial composition, and surface chemistry offers unique properties that may not be realized otherwise. Synthesizing nanomaterials of precisely tuned dimensions, spatial composition, surface chemistry, minimal size distribution and more importantly making sure these characteristics are stable over time, however, is challenging. My research takes on this challenge and focuses on exploring new strategies for synthesizing optical NCs with precisely tuned dimensions and unprecedented stability.

The first approach to controlling the growth of optical NCs is through the use of unimolecular non-linear block copolymer nanoreactors (i.e. nanotemplates) to create nanostructured materials with precisely tuned dimensions and enhanced stability that cannot be achieved via conventional ligand assisted methods. There are largely two categories of polymer nanoreactors depending on the shape. Unimolecular star-like block copolymers that initiate off from cyclic structured β-cyclodextrin allows for the formation

of zero-dimensional NCs (e.g. solid nanospheres, hollow nanospheres, core/shell nanospheres). Unimolecular bottlebrush-like block copolymers that initiate off from linear cellulose allows for the formation of one-dimensional NCs (e.g. nanorods, nanotubes, core/shell nanorods). The underlying key strategy for the nanoreactor approach is that inorganic precursors can form selective coordination bonds with certain polymer blocks (e.g. poly(acrylic acid), poly(4-vinylpyridine)) but not with other polymer blocks (e.g. polystyrene, poly(ethylene oxide), poly(3-hexylthiophene).

In this dissertation, I have focused on the synthesis of PS-capped gold nanoparticles (PS-capped Au NPs), PS-capped silver nanoparticles (PS-capped Ag NPs) and PS-capped all-inorganic perovskite quantum dots (PS-capped $CsPbX_3$ QDs) with tailored dimensions that are intimately and permanently tethered with polymers by employing rationally designed star-like block copolymer poly(acrylic acid)-*block*-polystyrene (PAA-*b*-PS) as nanoreactors. Precursor ions coordinate and selectively position themselves in the inner PAA block compartment which is composed of carboxylate functional groups. The selectively positioned precursors are then spatially fixed via a reduction reaction for PS-capped Au NPs & PS-capped Ag NPs and via a coprecipitation reaction for PS-capped $CsPbX_3$ QDs. By synthesizing the PAA blocks (i.e. inner compartment size) with low polydispersity via atom transfer radical polymerization (ATRP), I accurately control the size of PS-capped Au NPs, PS-capped Ag NPs, and PS-capped $CsPbX_3$ QDs, thus achieving strict control over light harvesting (for Au NPs, Ag NPs and $CsPbX_3$ QDs) and emission (for $CsPbX_3$ QDs) at desired wavelengths in the visible region. It is important to note that each PS-capped perovskite QD, for the first time, carries a layer of protective hydrophobic PS chains that can be precisely tailored to any desired length/thickness during

the ATRP of styrene monomers, thus allowing strikingly improved water stability. PS-capped $CsPbBr_3$ QDs showed up to twenty times increase in water stability compared to conventional ligand-capped $CsPbBr_3$ QDs. Moreover, due to the permanently ligated surface polymers, PS-capped $CsPbBr_3$ QD's QY, PL peak position, and FWHM in solution (toluene) was maintained for more than two months without any change, displaying excellent colloidal stability. In addition to perovskite QDs, PS-capped Au NPs and PS-capped Ag NPs synthesized via the nanoreactor approach also demonstrated exceptional colloidal stability as well as UV stability due to the permanently ligated surface polymers.

The second approach to controlling growth of NCs utilizes cation-exchange of well-defined inorganic NCs as nanotemplates to yield new NCs that maintain the same anionic framework of the original inorganic nanotemplates. This approach allows us to utilize well-known chemical reactivities of a certain group of compounds and replicate the NC structure for different compounds as well. For instance, the synthesis of core/graded shell-shell $CdSe/Cd_{1-x}Zn_xSe_{1-y}S_y/ZnS$ NCs utilizes different chemical reactivities of Cd, Zn, Se, and S to create a well-defined gradient core/shell structure. Cation exchange of these NCs allowed us to reproducibly synthesize IR NCs such as $PbSe/PbSe_{1-y}S_y/PbS$ or $AgSe/AgSe_{1-y}S_y/AgS$ NCs with precisely targeted dimensions. The obtained $PbSe/PbSe_{1-y}S_y/PbS$ QDs had PL wavelengths that range between 1700 nm to 2300 nm (SWIR region) that was precisely tunable by controlling the thickness of the PbS shell ($PbSe/PbSe_{1-y}S_y/PbS$ NC is a type-II core/shell NC), which can be easily tailored by the cation-exchange time. Moreover, I showed that the initial $CdSe/Cd_{1-x}Zn_xSe_{1-y}S_y/ZnS$ QD dimensions can also be utilized to accurately control the optical properties of $PbSe/PbSe_{1-y}S_y/PbS$ QDs in the IR region. It is worth mentioning that in addition to accurate structure control, this

strategy allows PbSe, which easily oxidizes in air to be immediately protected by a shell layer resulting in improved stability. It should be emphasized that the PbSe/$PbSe_{1-y}S_y$/PbS QDs have excellent colloidal stability (> 6 months) as well as oxidative stability (> 50 days).

Future work will include the use of bottlebrush-like block copolymers with distinct polymer blocks as nanoreactors to create one-dimensional nanomaterials that cannot be realized via conventional methods. We aim to craft perovskite nanorods and perovskite nanotubes that have tailorable dimensions and permanently tethered polymers as ligand by utilizing bottlebrush-like block copolymer PAA-*b*-PS and PS-*b*-PAA-*b*-PS as nanoreactors.

CHAPTER 1. INTRODUCTION

Nanomaterials have strikingly different and novel properties compared to their bulk counterpart. For bulk materials, which may include all material sizes beyond the micron-scale, physical properties are independent of size. But for nanomaterials, even a nanometer difference in size or a small change in shape may cause a large difference in properties. Especially for optical nanocrystals that interact with light, controlling size is extremely important. For instance, 2.3 nm cadmium selenide (CdSe) emits a blue color, 2.6 nm CdSe emits a green color, and 3.0 nm CdSe emits a red color when excited by a UV light source.[1] Synthesizing nanomaterials of desired size, dimensions, and minimal size distribution, however, is challenging. This dissertation takes on this challenge and focuses on synthesizing optical nanocrystals with precisely tuned dimensions and shape.

The two main approaches in controlling the growth of optical nanocrystals in this dissertation is through the use of unimolecular nonlinear block copolymer nanoreactors and well-defined inorganic nanotemplates. The polymer nanoreactor approach relies on polymerization techniques such as Atom Transfer Radical Polymerization (ATRP) and click chemistry which produce very low polydispersity (PDI) polymers and the inorganic nanotemplates approach relies on the different reactivities between chemical elements. Among various optical nanocrystals, we will focus on metallic nanoparticles, metal chalcogenide nanocrystals, and perovskite quantum dots.

Background information regarding basic polymerization techniques, current state-of-the-art in polymer templating strategies for nanocrystal synthesis, and current state-of-

the-art in optical nanocrystals are addressed. Completed research results are also presented and elaborated in the following chapters.

1.1 Polymers

1.1.1 Polymerization Techniques

1.1.1.1 Atom Transfer Radical Polymerization

Atom Transfer Radical Polymerization (ATRP) is a type of Reversible Deactivation Radical Polymerization (RDRP) technique that was independently discovered by Krzysztof Matyjaszewski and Mitsuo Sawamoto in 1995.[2-3] ATRP technique achieves very low polydispersity (PDI<1.1) via controlling the equilibrium between propagating radicals and dormant species as represented in **Figure 1.1**.[4] P_n* radical is in its active state at which it can attack a monomer (M) and P_n-X is in its dormant state at which it cannot attack a monomer. At any instant, there are always an excess of dormant species compared to their active counterpart. This is because the reaction equilibrium lies far left to the reactant side ($k_{act}<<<k_{deact}$), and this deters radical-radical termination (k_t) and allows P_n* radicals to attack only monomers.

The most important factor to consider in ATRP, is choosing the right catalyst complex (Mt^m/L). The catalyst complex activates P_n-X via oxidation and accepts the halide, leaving a P_n* radical which can polymerize (k_p). Choosing the right catalyst complex determines the reaction equilibrium that greatly influences PDI as well as the rate of reaction as seen in **Equation 1**.

Transition Metal (Copper(I)) Catalyzed ATRP

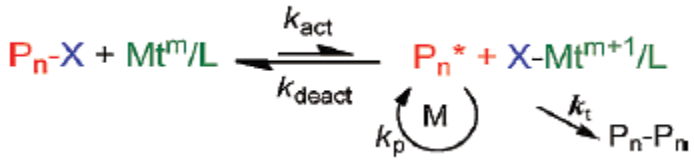

Figure 1.1 ATRP Equilibrium. *Mt^m – transition metal species in oxidation state m *L – ligand *P_n* - growing radicals *X- halide group * k_p – rate constant of polymerization *k_{act} – rate constant of activation *k_{deact} – rate constant of deactivation *k_t – rate constant of termination.[4] [Reprinted with permission from ref. 4, Copyright © 2012 American Chemical Society]

$$R_p = k_p[M][P_n^*] = k_p K_{ATRP}\left(\frac{[P_nX][Cu^I/L][M]}{[X-Cu^{II}]/L}\right)$$

Equation 1. Rate of ATRP.[4]

1.1.1.2 Click Chemistry

The first systematic study of 1,3-dipolar cycloaddition reaction was reported by Huisgen in the middle of the 20th century.[5] The Huisgen reaction was catalyst free but slow, required high temperatures, and produced a mixture of 1,4 and 1,5-disubstitution products (**Figure 1.2**).[6] In 2002, Fokin, Sharpless and Meldal reported the use of a copper iodide (CuI) catalyst that resulted in a lower temperature 1,3-dipolar cycloaddition reaction that was selective in producing only 1.4-disubstituted triazoles.[7-8]

Cu^{I}-catalyzed azide/alkyne cycloaddition (CuAAC)

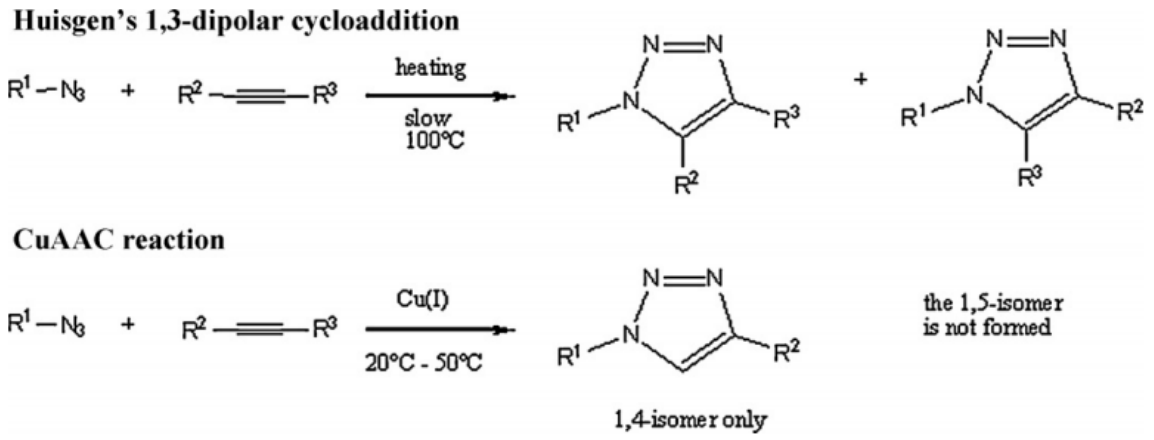

Figure 1.2. Comparison between Huisgen's 1,3-dipolar cycloaddition and CuAAC reaction.[6] [Reprinted with permission from ref. 6, Copyright © 2011 Elsevier Ltd]

CuAAC click reactions are easy to perform, produce high-yields, produce little to no by-products, unaffected by steric and electronic properties of other functional groups on the same molecule, and works well under many environments and conditions (i.e. 0-160^{o}C, pH 4-12, etc.).[9-10] The resulting triazole ring also has many advantages such as high chemical stability (i.e. inert to hydrolytic, oxidizing, and reducing environments), strong dipole moment, aromatic character, and hydrogen bond accepting ability.[2] The rate of a CuAAC click reaction is also much faster by a factor of 10^{7} relative to the non-catalytic thermal process.[10]

The CuAAC click reaction proceeds via a two-copper mechanism that was recently proven in 2013 by Fokin et al. (**Figure 1.3**) Briefly, copper forms a sigma bond with the alkyne group forming copper acetylide. Then a second copper atom forms a pi bond forming a catalytically active complex. Then the azide group forms a reversible

coordination with the active complex. Then annulation takes place creating the triazole ring structure.[11]

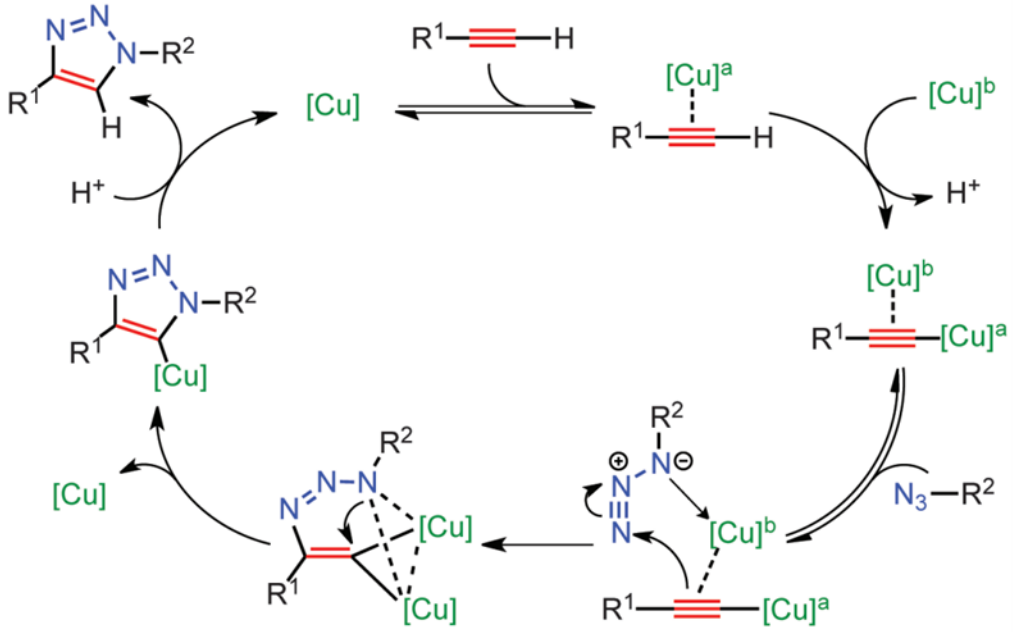

Figure 1.3 Proposed catalytic model for the CuAAC with two copper atoms.[11] [Reprinted with permission from ref. 11, Copyright © 2013 AAAS]

1.1.2 Polymers with Complex Architectures

In this dissertation, nanocrystals of precise dimension and shape is synthesized by taking on the shape of the pre-synthesized polymer nanoreactors. Specifically, we focus on the use of unimolecular polymer templates that are more robust compared to linear polymer micellar templating methods that are drastically affected by subtle changes in the

environment.[12-13] Thus it is important to investigate the plethora of structures that can be created via unimolecular polymers.

Figure 1.4 illustrates the representative unimolecular structures that can be synthesized via polymers. This dissertation focuses primarily on polymers with a star-like morphology that can be grown by ATRP or click reaction on macroinitiators (initiators with multiple activation sites) with a circular morphology.[14-15] Hyperbranched or network gels is also an interesting structure that can be synthesized by using inimers that contain both initiator as well as monomer in the same unit or use cross-linking agents to connect individual polymer strands.[16-17] However, due to the relatively uncontrolled nature of the system, will not be dealt further in this dissertation.

Types of Complex Macromolecular Architecture

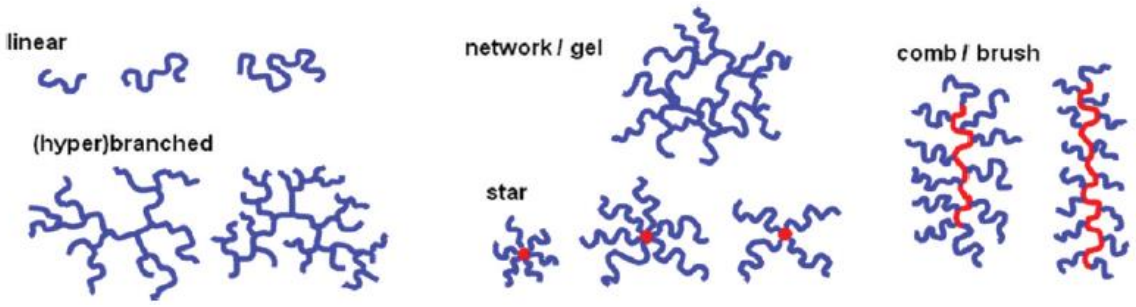

Figure 1.4 Examples of polymers with controlled topology prepared by ATRP.[4] [Reprinted with permission from ref. 4, Copyright © 2012 American Chemical Society]

1.1.2.1 Star-like Polymers

Star-like polymer synthesis can be divided largely into three different approaches (**Figure 1.5**). The first is the core first method in which the macroinitiator with multiple activation sites act as an anchor for multiple ATRP reactions. ATRP from the macroinitiator core allows the growth of very well-defined monodisperse star-like polymers. The second approach is the coupling onto approach in which complementary functional groups are located on the core and linear polymer chains. One of the most well-known reaction in this approach is the click reaction in which an azide and ethynyl functional group undergo a 1,3-dipolar cycloaddition reaction.[18] The third approach is the arm first approach in which one-end of a pre-synthesized linear polymer is cross-linked together to form a star-like polymer.[19-20] Among several approaches, the core-first approach and coupling-onto approach has proven to produce star-like block copolymers with the most precise dimensions and low PDI.

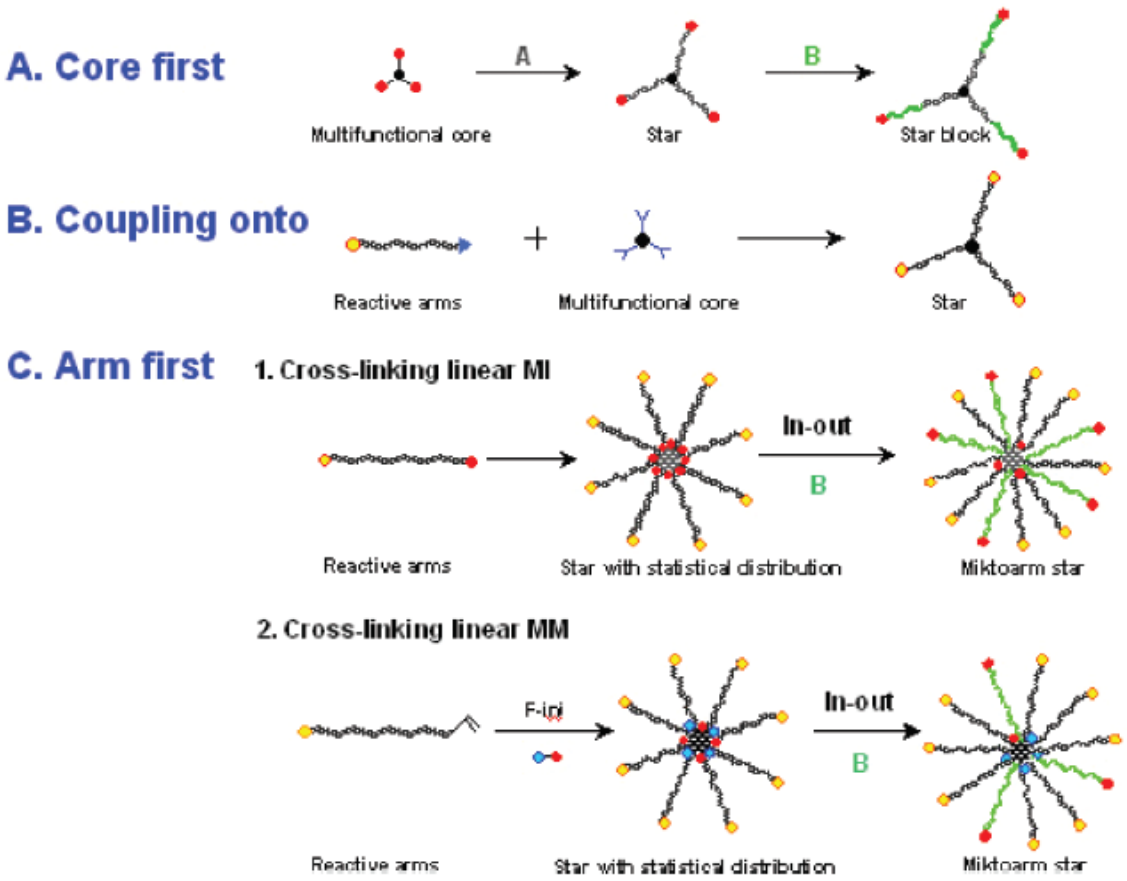

Figure 1.5 Three major approaches to synthesize star (co)polymers.[4] [Reprinted with permission from ref. 4, Copyright © 2012 American Chemical Society]

Current State-of-the-Art

Figure 1.6 illustrates how block copolymer synthesis via ATRP from a brominated β-cyclodextrin initiator (core first approach) allows formation of polymer nanoreactors that can create nanomaterials of three different architecture (solid sphere, core-shell, and hollow sphere).[14] **Figure 1.7** and **Figure 1.8** shows the successful synthesis of monodisperse nanomaterials utilizing the star-like unimolecular polymer nanoreactors. The polymer

nanoreactor basically relies on the electrostatic attraction or the coordination bonding between the nanomaterial precursors and the polyacrylic acid (PAA) block of the star-like polymer nanoreactor to situate precursors selectively in the PAA block followed by precursor reduction to fix the structure.

The most crucial factor to consider in synthesizing monodisperse nanoparticles via polymer nanoreactors is the solution medium. **Figure 1.7** depicts how the structure of PS tethered $PbTiO_3$ nanoparticle, synthesized via star-like PAA-*b*-PS block copolymers, is affected by the DMF:BA solvent mixture ratio during synthesis. In synthesizing monodisperse nanomaterials, using the right ratio of good and bad solvents for the polymer blocks is very important. Generally, it is ideal to choose a dominant solvent (DMF) that dissolves all polymer blocks and a minor solvent (BA) that is a good solvent for the inner blocks but a relatively bad solvent for the most outer block. In this way, the star-like template will form a fully extended inner block compartment that will attract precursors and a semi-collapsed outer block that will prevent precursors from escaping. When too much of the bad solvent is used, however, the outer PS block will completely collapse preventing precursors from fully reaching the inner compartment of the polymer template.

Figure 1.8b depicts the use of star-like PS-*b*-PAA-*b*-PS block copolymer nanoreactor to synthesize hollow Fe_3O_4 nanoparticles. The concept is very similar to the Star-like PAA-*b*-PS nanoreactor in that the PAA block attracts the precursors and the outer PS block forms a semi-collapsed cage. The inner PS block that is also partially collapsed forms an inner compartment that physically excludes precursors, thus forming a hollow Fe_3O_4 nanoparticle with permanently tethered PS on the surface.

Figure 1.8c depicts the use of star-like P4VP-*b*-PtBA-*b*-PS block copolymer nanoreactor to synthesize core/shell $Fe_3O_4/PbTiO_3$ nanoparticles. The process is complex compared to the sphere and hollow nanoparticle systems in that there are now three different types of block copolymers instead of just two. First, the P4VP block attracts the precursors into the most inner compartment where the precursors are reduced to Fe_3O_4. It should be noted that the hydrolysis of PtBA to PAA is performed after the synthesis of Fe_3O_4, because otherwise, Fe_3O_4 will also form in the middle compartment as well. When hydrolysis is complete, $PbTiO_3$ precursors are then introduced into the system forming a shell layer around the Fe_3O_4. It should be noted that the use of a polymer template allows the formation of core/shell structures with large lattice mismatch that normally cannot form via conventional methods.

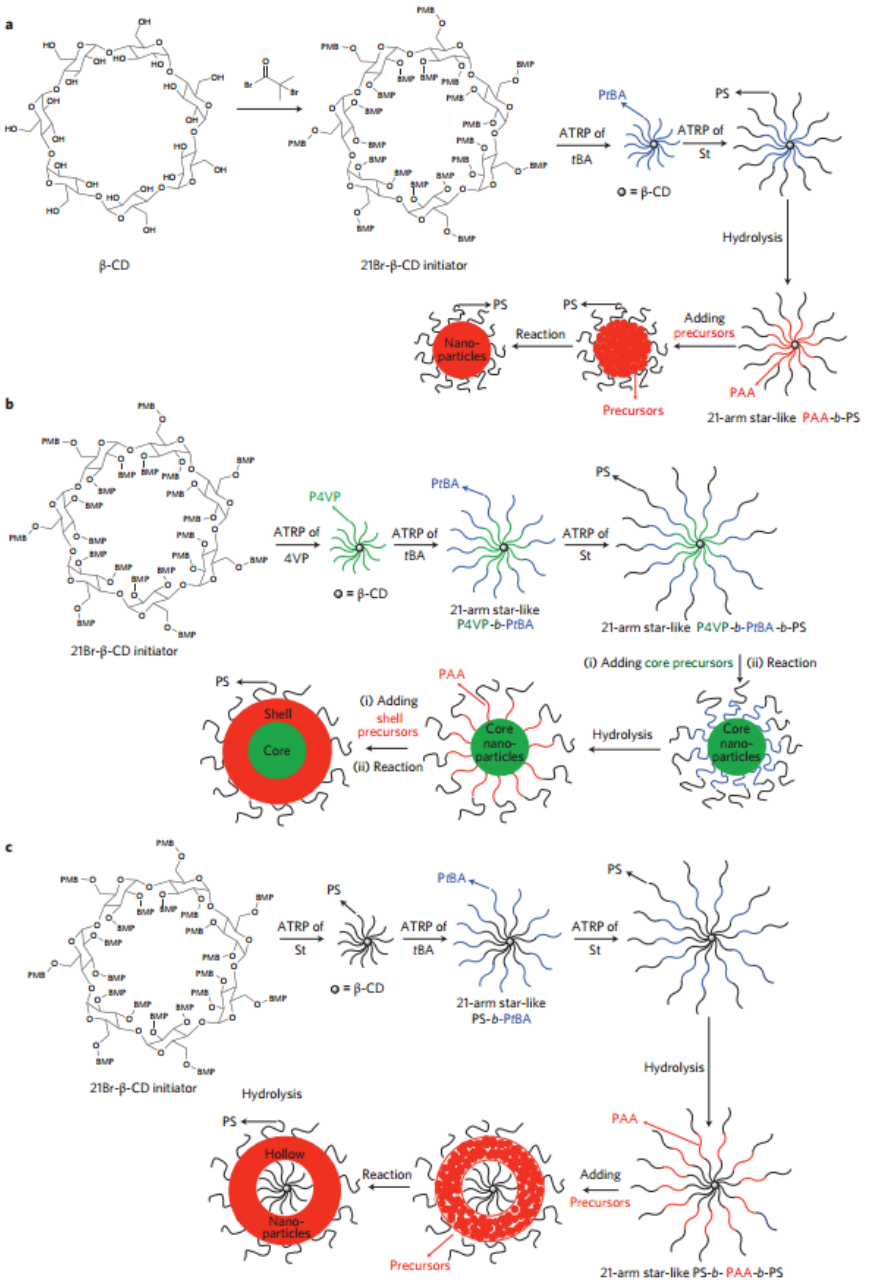

Figure 1.6 Schematic representation of synthetic strategies for nanoparticles with different architectures (plain, core-shell and hollow) using amphiphilic star-like block co-polymers as nanoreactors. Formation of (a) Plain nanoparticles (b) core-shell nanoparticles (c) and hollow nanoparticles. CD, cyclodextrin; BMP, 2-bromo-2-methylpropionate; St, styrene.[14] [Reprinted with permission from ref. 14, Copyright © 2013 Macmillan Publishers Limited]

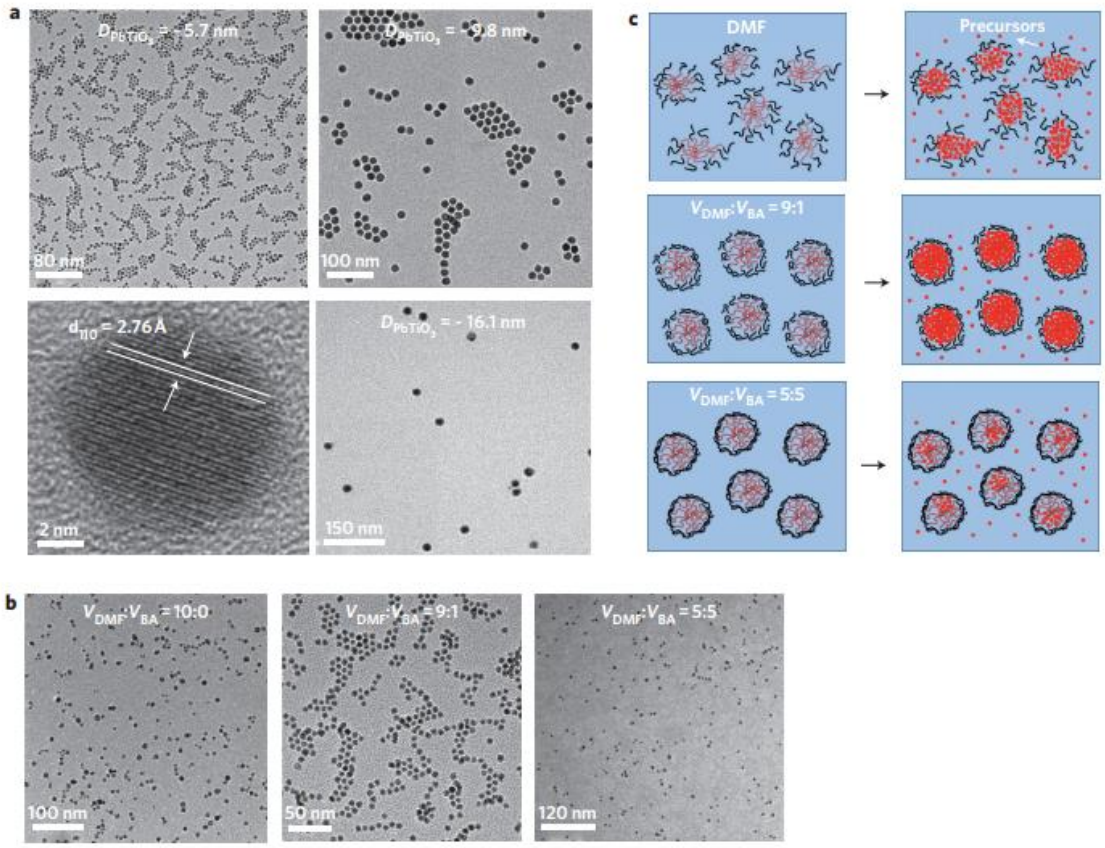

Figure 1.7 Formation of plain nanoparticles. (a) TEM images of three $PbTiO_3$ nanoparticles with different diameters prepared using three star-like PAA-*b*-PS templates with different molecular weights of PAA block as nanoreactors. (b) TEM images of $PbTiO_3$ nanoparticles formed in a mixture of DMF and benzyl alcohol (BA) at different volume ratios. (c) Proposed mechanism for the growth of uniform (V_{DMF}:V_{BA}=9:1) and non-uniform (V_{DMF}:V_{BA}=10:0 and V_{DMF}:V_{BA}=5:5) nanoparticles in DMF and BA.[14] [Reprinted with permission from ref. 14, Copyright © 2013 Macmillan Publishers Limited]

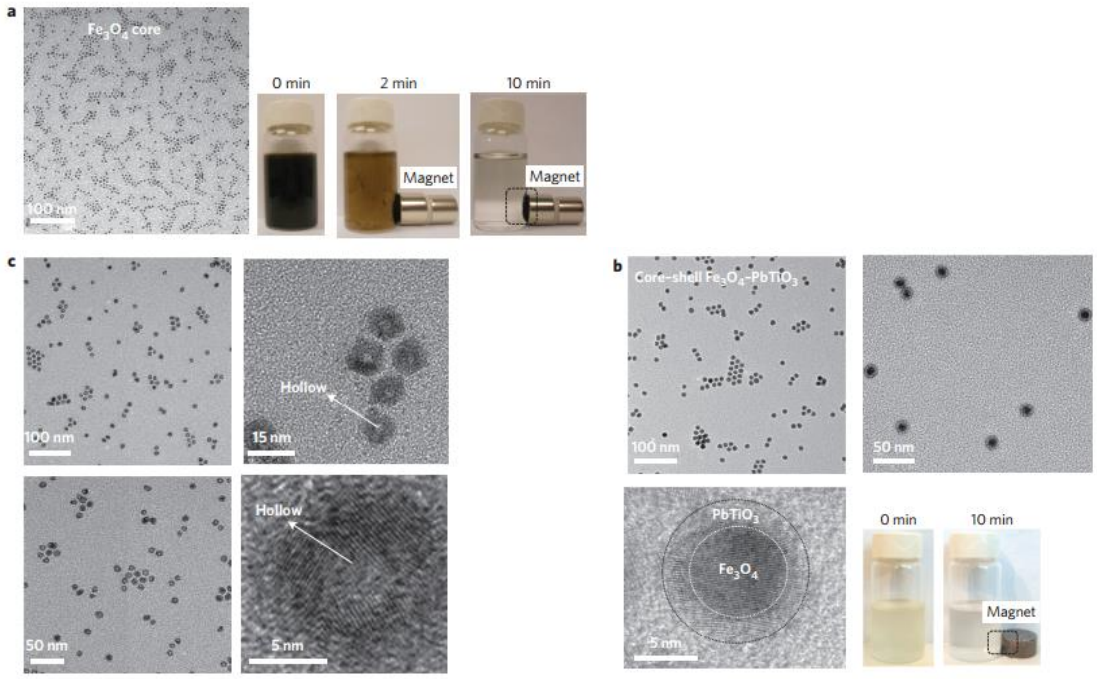

Figure 1.8 TEM and digital images of Fe_3O_4-$PbTiO_3$ core-shell nanoparticles and TEM images of hollow gold nanoparticles formed using star-like triblock co-polymers as nanoreactors. (a),(b) TEM images of Fe_3O_4 core (a, D_{Fe3O4}=6.1±0.3nm) and Fe_3O_4-$PbTiO_3$ core-shell nanoparticles at different magnifications (b, $PbTiO_3$ shell thickness=3.1±0.3nm). (c) TEM images of representative hollow gold nanoparticles with a uniform size distribution (thickness of gold, 3.2±0.3nm; diameter of hollow core, 5.6±0.4nm).[14] [Reprinted with permission from ref. 14, Copyright © 2013 Macmillan Publishers Limited]

1.1.2.2 Cellulose-based Rod-like Polymers

The mechanism for the rod-like polymer nanoreactor system is very similar or identical to that of the star-like polymer nanoreactor system in that there are block copolymers in the inner compartment that attract the nanomaterial precursors and outer block copolymers that form a semi-collapsed shell. The difference lies in that instead of β-cyclodextrin that is of only one size with 21 active sites for bromination, cellulose has a very high PDI and thus has varying numbers of active sites proportional to the number of repeat units. The fractionation of the cellulose macroinitiator by size is crucial to synthesizing monodisperse nanorods using the rod-like polymer nanoreactor. The fractionation of brominated cellulose (cellulose-Br), however, is a very daunting task which is time-consuming and yet result in very low yields. Improvements in lowering PDI of cellulose-Br and increasing yield has not been fully established and will be the target of future studies.

Current State-of-the-Art

Although difficult, the success of using cellulose-based rod-like nanoreactors for nanomaterial synthesis has recently been published. **Figure 1.9** depicts the strategies for synthesizing solid rod-like nanoreactors (cellulose-PAA-*b*-PS), solid core/shell rod-like nanoreactors (cellulose-P4VP-*b*-PtBA-*b*-PS), and hollow tube-like nanoreactors (cellulose-PS-*b*-PAA-*b*-PS). **Figure 1.10** demonstrates the use of rod-like cellulose-PAA-*b*-PS nanoreactors to synthesize upconversion $NaYF_4$:Yb/Er nanorods with permanently tethered PS. It should be noted that starting with longer cellulose-Br macroinitiators, nanorods with higher aspect ratios can be achieved when keeping the block copolymer length constant. **Figure 1.11** depicts the use of solid core/shell rod-like nanoreactors to

synthesize Au/Fe_3O_4 core/shell nanorods with permanently tethered PS and the use of hollow tube-like nanoreactors to synthesize Au hollow nanotubes with permanently tethered PS.

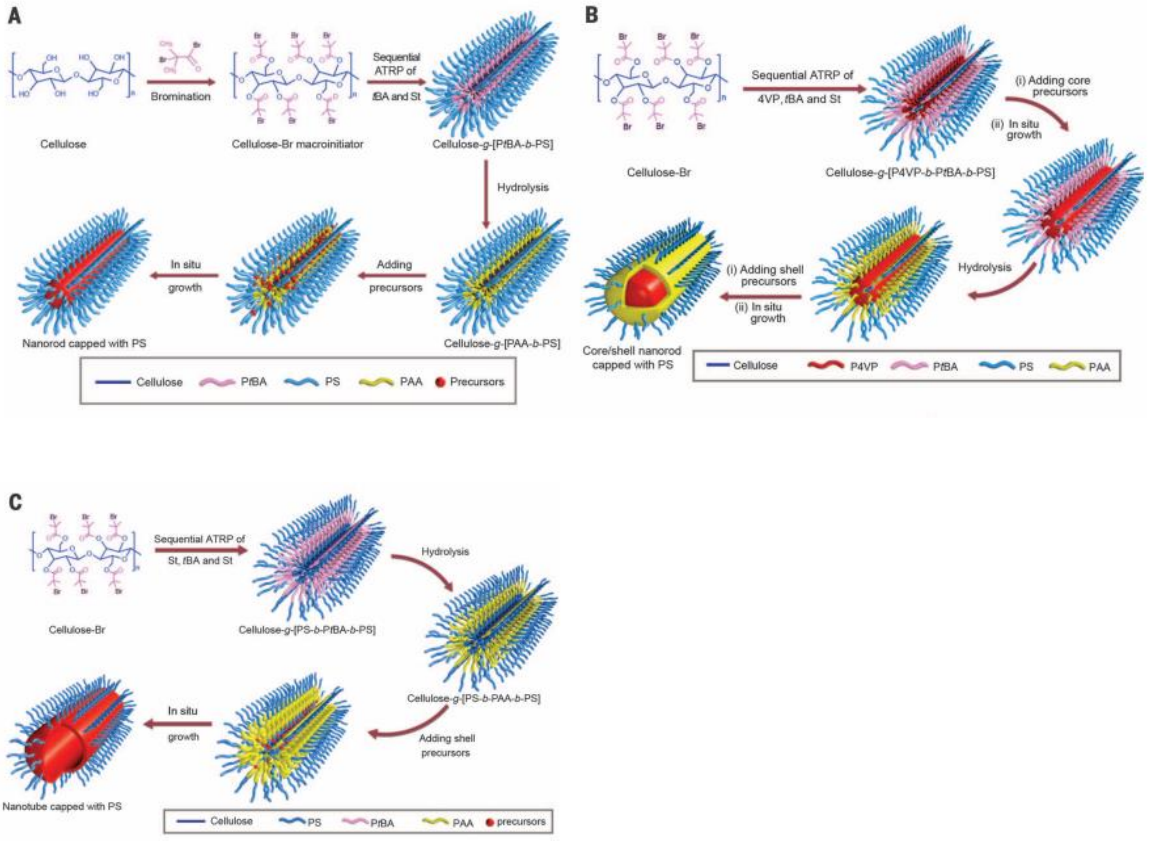

Figure 1.9 Synthetic strategies for 1D nanocrystals, using amphiphilic cylindrical BBCPs as nanoreactors. (A) Plain nanorods templated by cellulose-g-(PAA-*b*-PS). St, styrene; tBA, tert-butyl acrylate. (B) Core-shell nanorods templates by cellulose-g-(P4VP-*b*-PtBA-*b*-PS). (c) Nanotubes templated by cellulose-g-(PS-*b*-PAA-*b*-PS).[15] [Reprinted with permission from ref. 15, Copyright © 2016 AAAS]

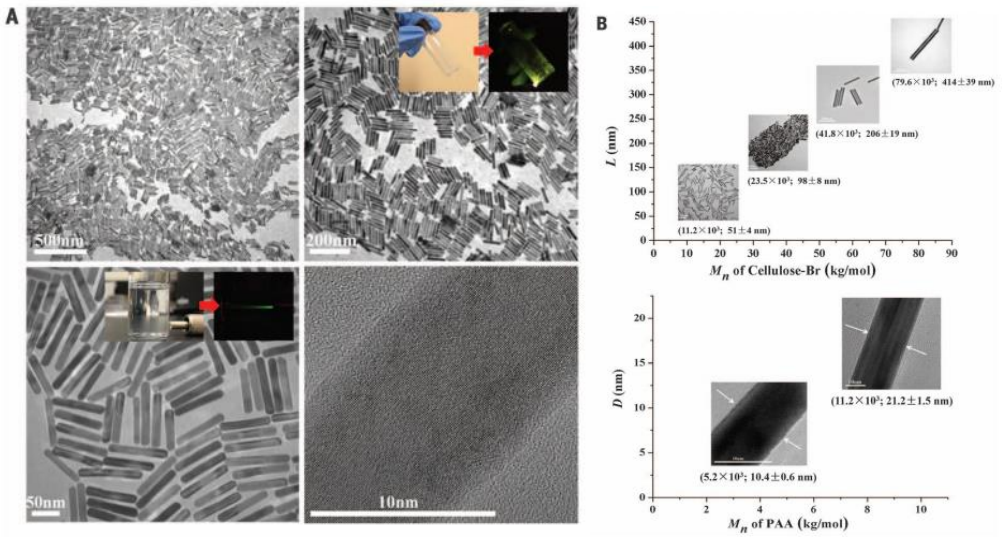

Figure 1.10 Formation of plain nanorods. (A) TEM images of upconversion $NaYF_4$:Yb/Er nanorods templated by cellulose-g-(PAA-*b*-PS). (B) The dimensional tunability of 1D Au nanorods is shown as an example.[15] [Reprinted with permission from ref. 15, Copyright © 2016 AAAS]

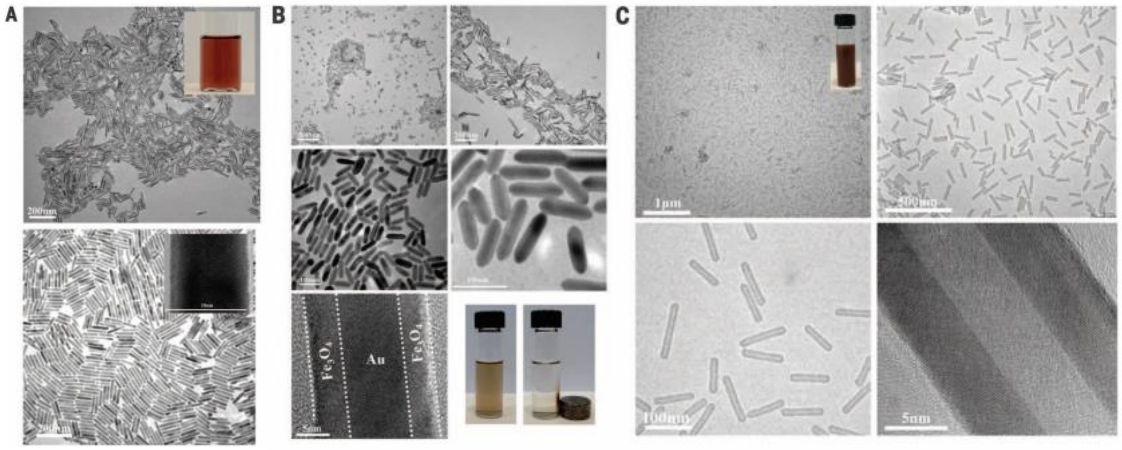

Figure 1.11 TEM and digital images of Au-Fe_3O_4 core-shell nanorods and Au nanotubes templated by cellulose-g-(P4VP-*b*-PtBA-*b*-PS) and cellulose-g-(PS-*b*-PAA-*b*-PS), respectively. (A) Au-core nanorods. (B) Au-Fe_3O_4 nanorods. (C) Au nanotubes.[15] [Reprinted with permission from ref. 15, Copyright © 2016 AAAS]

It should be noted that the polymer nanoreactor system is not limited to PAA, PS, and P4VP, but has already been demonstrated for different polymers by our research group. The scope of this dissertation, however, will not include other polymer systems and focus on the plethora of new nanomaterials that can be achieved with the above three polymers.

1.2 Optical Nanomaterials

1.2.1 Quantum Nanocrystals

Metal halide perovskite materials have garnered much attention over the past few years as an emerging material for optoelectronic applications (solar cells, LEDs, etc) due to their long carrier lifetime, low defect density, composition-dependent tunable bandgap, narrow FWHM, outstanding quantum yield (QY), and overall low production cost.[21-24] Especially solar cells utilizing organic-inorganic perovskite materials such as methylammonium (MA) lead halide and formamidinium (FA) lead halide perovskite in the active layer quickly reached PCEs over 20%.[25-27]

Importance of Perovskite Quantum Dots

Although perovskite material research has been intensive for the past decade, development of perovskite Quantum Dots (QD) have been rather neglected because initial focus of perovskite research was in increasing perovskite grain size in the active layer to achieve higher perovskite solar cell (PSC) performance.[28-30] There has been research showing that perovskite QDs ($MAPbBr_3$) with diameters of 2-3 nm deposited on

mesoporous TiO_2 perovskite solar cells exhibit a PCE of 11.14% which was promising but this was still far lower than the highest values reported for PSCs.[31]

A recent interesting development, however, proved that an interfacial perovskite QD layer between the perovskite active layer and hole transporting layer (HTL) in PSCs may actually be useful in improving the interfacial charge transfer by optimizing the energy band alignment.[26] For instance, Wang et al. introduced mixed halide perovskite QDs between the active layer and hole transporting material (HTM) layer. By adding a thin interfacial $MAPbBr_{0.9}I_{2.1}$ QD layer that has an intermediate valence band (VB) edge that lies above the active layer VB edge and below the highest occupied molecular orbital (HOMO) of the HTL, hole transfer was well-facilitated and resulted in a 29% increase in PCE.[32]

Since the pioneering work by Kovalenko et al.[33] perovskite QDs are not only limited to the field of solar cells, but are receiving growing attention in applications such as lasers[34-36], electroluminescence devices[35, 37], and sensors[38]. This is because of perovskite QD's characteristics such as broad wavelength tunability (400-800 nm) and narrow band emission .[32, 39-40] Especially, cesium based all inorganic perovskite QDs ($CsPbX_3$) have narrow emission line widths as low as 12 nm and excellent QY above 90% (**Figure 1.12** & **Figure 1.13**).[33] $CsPbX_3$ nanocrystals also have a bohr diameter up to 12 nm[33], thus resulting in a size-tunable bandgap in the visible region (410-700nm) as depicted in **Figure 1.14**. Moreover, post-synthetic treatment of these perovskite QDs with halide donators can easily tune the absorption and photoluminescence spectrum as well.[33, 41-42] With the development of perovskite QDs with excellent characteristics, the incorporation of these perovskite QDs into LEDs have now reached a remarkable electroluminescence yield of

5.7%.[35, 37] Stability, however, is still a major issue for perovskite materials regardless of its field of application. One example would be the PL shift that commonly occurs for mixed halide perovskite QDs possibly due to halide segregation.

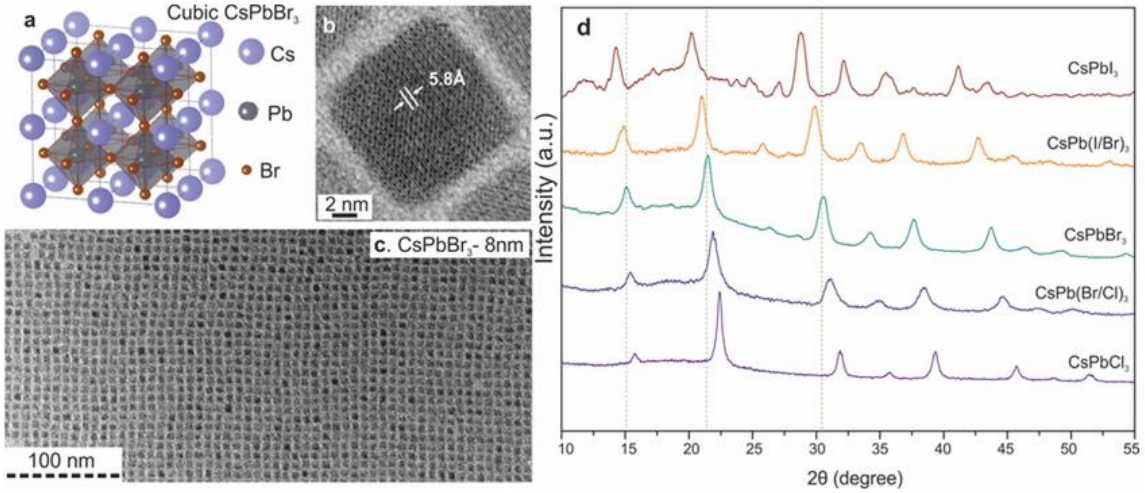

Figure 1.12 Monodisperse $CsPbX_3$ NCs and their structural characterization. (a) Schematic of the cubic perovskite lattice; (b,c) typical transmission electron microscopy (TEM) images of $CsPbBr_3$ NCs; (d) X-ray diffraction patterns for typical ternary and mixed halide NCs.[33] [Copyright © 2015 American Chemical Society]

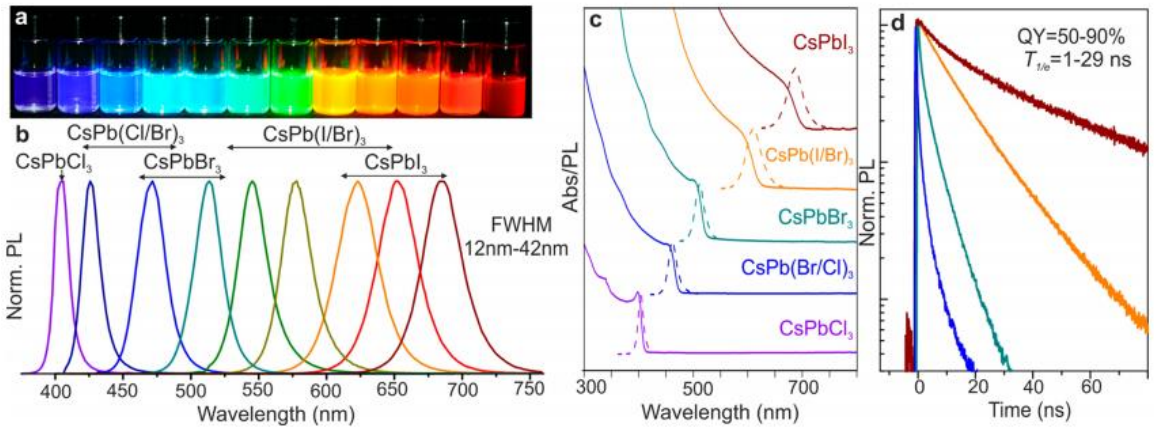

Figure 1.13 Colloidal perovskite $CsPbX_3$ NCs (X= Cl, Br, I) exhibit size- and composition-tunable bandgap energies covering the entire visible spectral region with narrow and bright emission; (a) colloidal solutions in toluene under UV lamp (λ=365nm); (b) representative PL spectra (λ_{exc} = 400nm for all but 350nm for $CsPbCl_3$ samples); (c) typical optical absorption and PL spectra; (d) time-resolved PL decays for all samples shown in (c) except $CsPbCl_3$.[33] [Copyright © 2015 American Chemical Society]

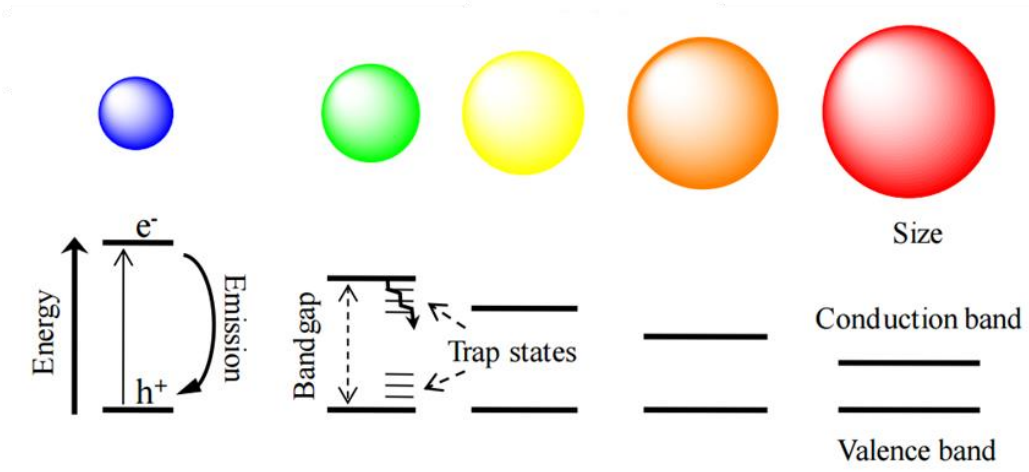

Figure 1.14 Illustration of size-tunable QDs and creation of the exciton (electron-hole pair) upon photoexcitation followed by radiative recombination (fluorescence emission) or relaxation through trap states.[43-44] [Copyright © 2009 MDPI]

Exciton Bohr Diameter: $MAPbBr_3$ (2.0nm)[31] $MAPbI_3$ (2.2nm)[31] $CsPbI_3$ (12nm)[33] $CsPbBr_3$ (7nm)[33]

Improving Stability

Although performance such as PCE and QY have shown clear advancements during the past decade, the major bottleneck for commercialization of perovskite materials has been stability.[45-46] Before stepping into this field of perovskite QD stability research, it is important to take into account the efforts by other groups in improving perovskite QD stability. Among the numerous instabilities that we must tackle, seven categories of issues are briefly introduced below.

Colloidal Stability

As any other colloidal system, perovskite QDs suffer from aggregation and degradation that results in changes to their optical properties. Kim et al. observed that each successive washing of $CsPbBr_3$ QDs results in a red-shift of the PL peak. The observed phenomenon was caused by dynamic ligand binding in which there is an equilibrium between the bound oleic acid/oleyl amine ligand used in the QD synthesis. With each successive washing, free ligands were washed away and overall there were fewer ligands in the system, which eventually caused incomplete surface coverage of ligands on the QDs. Incomplete surface coverage led to aggregation of the QDs and eventually a red-shift in optical properties.[47]

Yassitepe et al. observed that using oleyl amine, which is most commonly used as a surface binding ligand, may cause a blue-shift of the PL peak. The observed phenomenon

was allocated to the relatively strong binding strength of oleyl amine to the PbX_2 precursor, thus causing dissolution of the QD constituents.[48] Yassitepe et al. has thus developed an alternative amine-free approach in which only oleic acid was used as the ligand. The oleic acid only $CsPbBr_3$ QDs showed no peak shift upon washing and was also visually more transparent indicating less colloidal aggregation.[48]

Photo Stability

Wang et al. (**Figure 1.15**) observed that $CsPbBr_3$ QDs in hexane is unstable under continuous UV irradiation (365 nm, 6W). After 96 h, the PL intensity decreased by 60%. The deterioration was allocated to surface defects because perovskite QDs don't have a passivation layer.[46] To improve photo stability, Wang et al. deposited $CsPbBr_3$ QDs on mesoporous silica and after 96 h of UV irradiation the PL intensity decreased by just 20%. Wang et al. asserted that this improvement is due to the mesoporous silica that acts similar to a passivation layer and suppresses defect formation.[46]

Meyn et al. (**Figure 1.16**) also attempted to improve photostability by coating $CsPbBr_3$ with poly(maleic anhydride-alt-1-octadecene) (PMA). Meyn et al. asserted that the polymer coating reduces the interaction of the QD surface with the surrounding media and thus result in higher stability. When illuminated with a 365 nm pump under ambient conditions, $CsPbBr_3$-PMA showed 60% PL retention after 12 h, while $CsPbBr_3$ only showed that of 21%. XRD analysis of the QDs revealed that under long-term optical excitation, NCs grow and rearrange crystallographically, and this change was relatively suppressed in $CsPbBr_3$-PMA.[49]

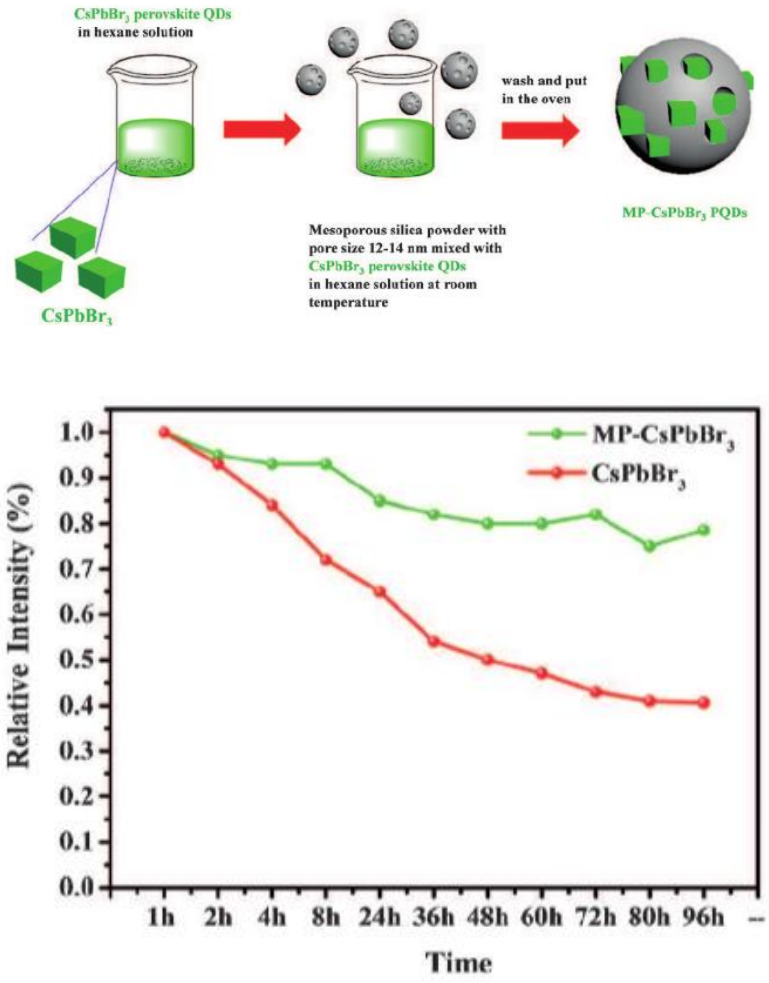

Figure 1.15 The synthesis of mesoporous silica green PQD nanocomposite (MP-PQDs) and its photostability.[46] [Reprinted with permission from ref. 46, Copyright © 2016 Wiley-VCH]

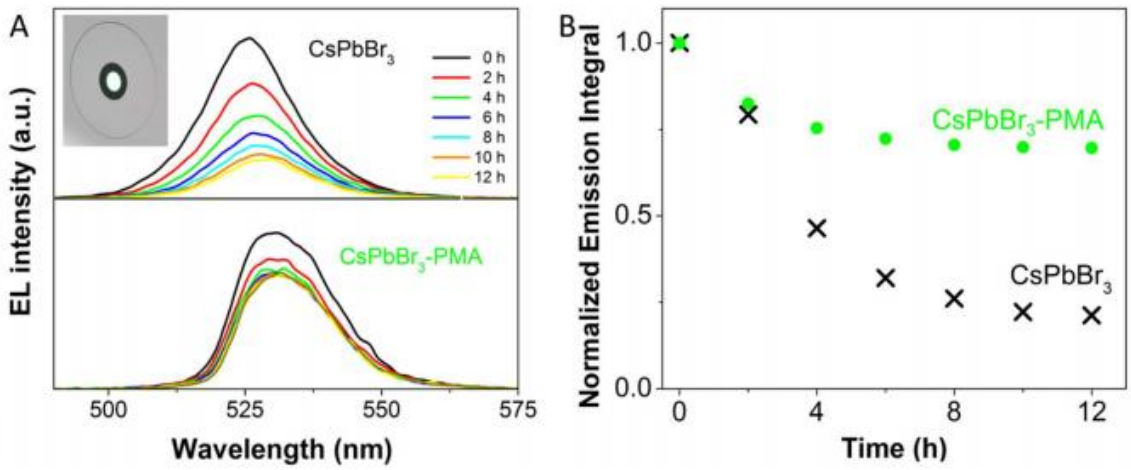

Figure 1.16 (A) Temporal evolution of the emission spectra with filters of $CsPbBr_3$ and purified $CsPbBr_3$-PMA on a UV-LED with 100 mW at 365 nm with 58.8 mA forward current. (B) Normalized integrals of the emission peaks between 460 and 600 nm showing a three times lower decrease of the emission signal with PMA within 12 hours of constant irradiation.[49] [Reprinted with permission from ref. 49, Copyright © 2016 American Chemical Society]

Compositional Stability

Wang et al. (**Figure 1.17**) showed that when green $CsPbBr_3$ QDs and $CsPb(Br_{0.4}I_{0.6})_3$ QDs were mixed in a silicone resin for LED application, the strong ion-exchange effect caused the PL of both green and red QDs to shift to an intermediate yellow.[46] Wang et al. showed that mixing MP-$CsPbBr_3$ QDs (QDs deposited on mesoporous silica) with $CsPb(Br_{0.4}I_{0.6})_3$ QDs in silicone resin did not result in any ion-exchange.[46] Huang et al. also showed that coating $CsPbX_3$ with polyhedral oligomeric silsesquioxane (POSS) (**Figure 1.18**) did not result in any ion-exchange in light emitting devices (**Figure 1.19**).[50]

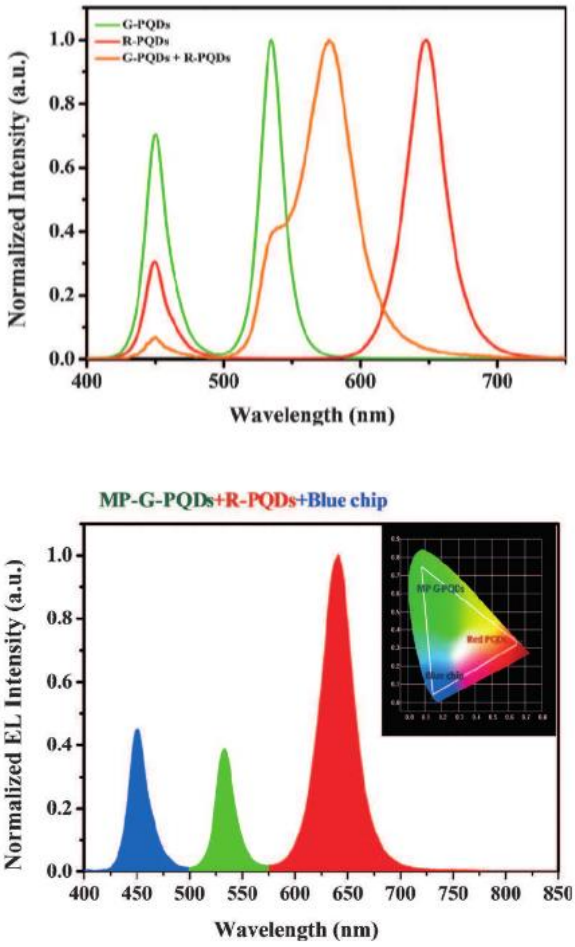

Figure 1.17 (a) Spectra of green, red, and mixed (green+red) PQDs under blue chip (450 nm) excitation. (b) Spectra of MP-$CsPbBr_3$ mixed with red PQDs under blue chip (450 nm) excitation.[46] [Reprinted with permission from ref. 46, Copyright © 2016 Wiley-VCH]

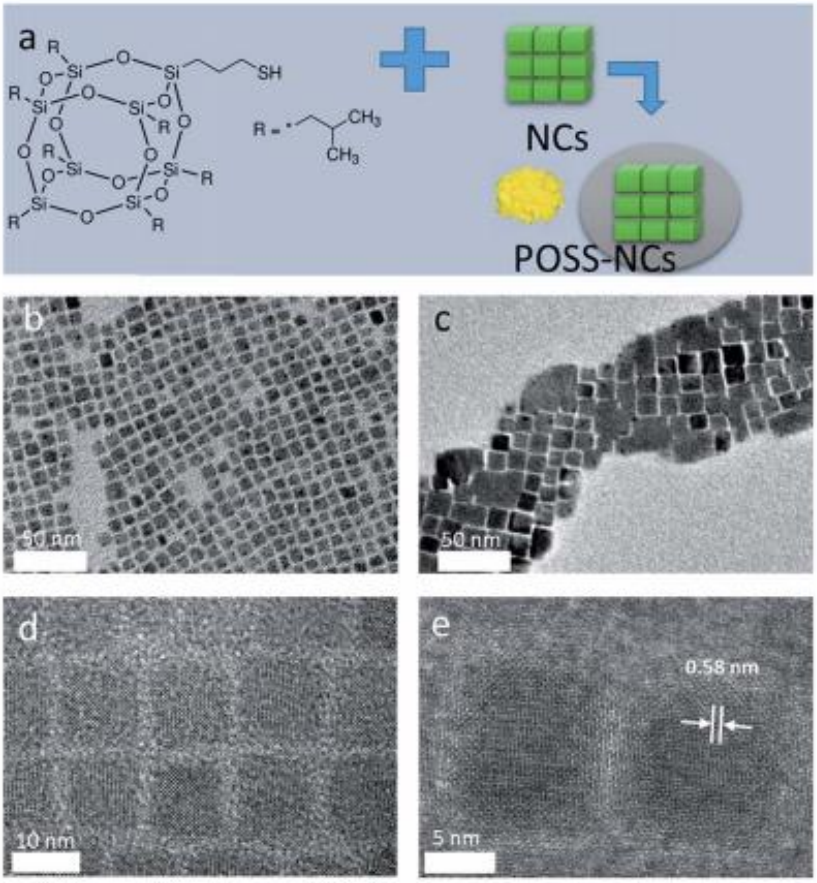

Figure 1.18 (a) Structure of a thiol-functionalized POSS, with a schematic diagram illustrating the POSS coating process for preparation of perovskite NC powders. (b and c) TEM images of $CsPbBr_3$ perovskite NCs before and after POSS coating. (d and e) HRTEM images of $CsPbBr_3$ perovskite NCs before and after POSS coating. A characteristic lattice plane distance of 0.58 nm for cubic phase $CsPbBr_3$ perovskite is indicated in (e).[50] [Copyright © 2016 The Royal Society of Chemistry]

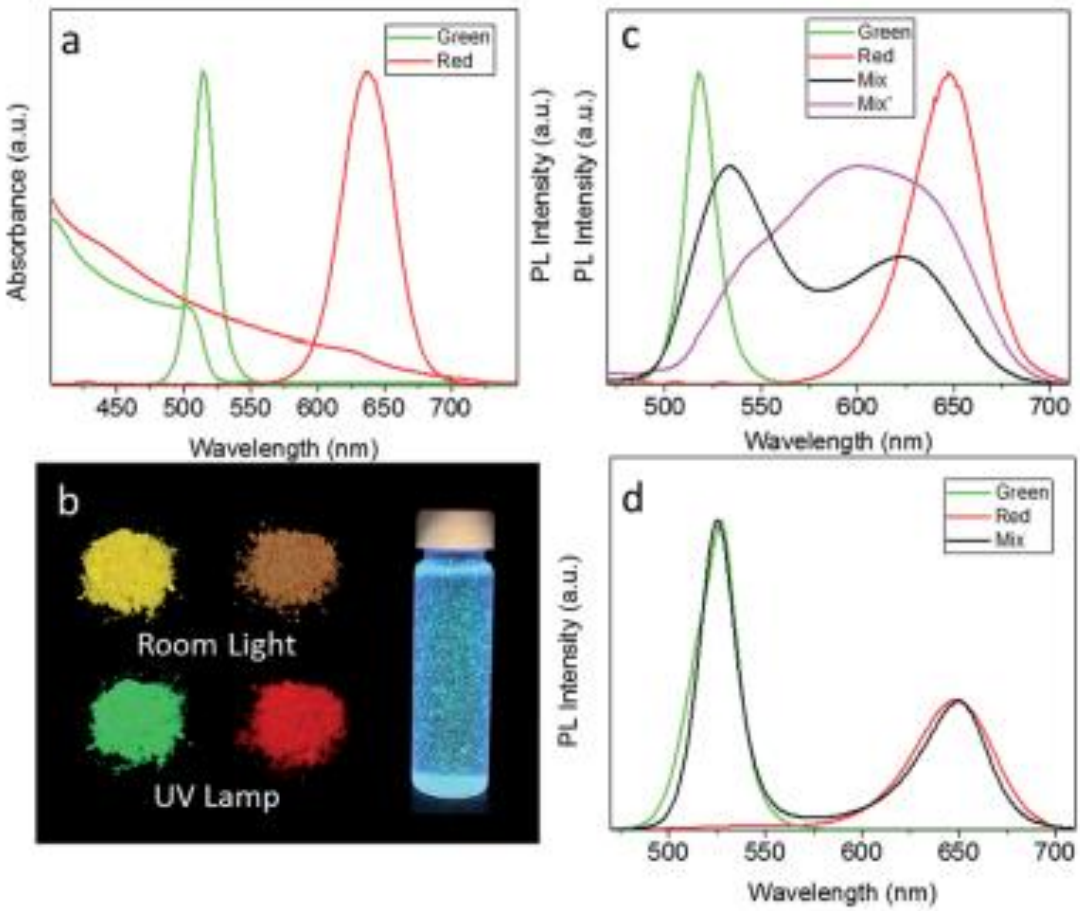

Figure 1.19 (a) UV-visible absorption and PL spectra of green-emitting $CsPbBr_3$ and red-emitting $CsPb(Br/I)_3$ POSS-coated NCs. (b) Photographs of $CsPbBr_3$ and $CsPb(Br/I)_3$ POSS coated NC powders under room light and UV light, and a vial with a $CsPbBr_3$ POSS-NC suspension in water after 10 weeks storage, under UV light. (c) Solid state PL spectra of non-capped $CsPbBr_3$ (sample Green) and $CsPb(Br/I)_3$ (sample Red) NC powders, and of their 1 : 1 molar% mixture taken immediately after mixing (sample Mix) and after 5 min of the solid state reaction (sample Mix0). (d) Solid state PL of POSS-capped $CsPbBr_3$ (sample Green) and $CsPb(Br/I)_3$ (sample Red) POSS-NC powder NCs, and of their 1 : 1 molar% mixture.[50] [Copyright © 2016 The Royal Society of Chemistry]

Stability in Polar Solvents

Kim et al. showed that $CsPbBr_3$ QDs are not stable in polar solvents. As seen from **Figure 1.20**, solvents with larger dipole moments generally lead to dissolution of the QD constituents.[47]

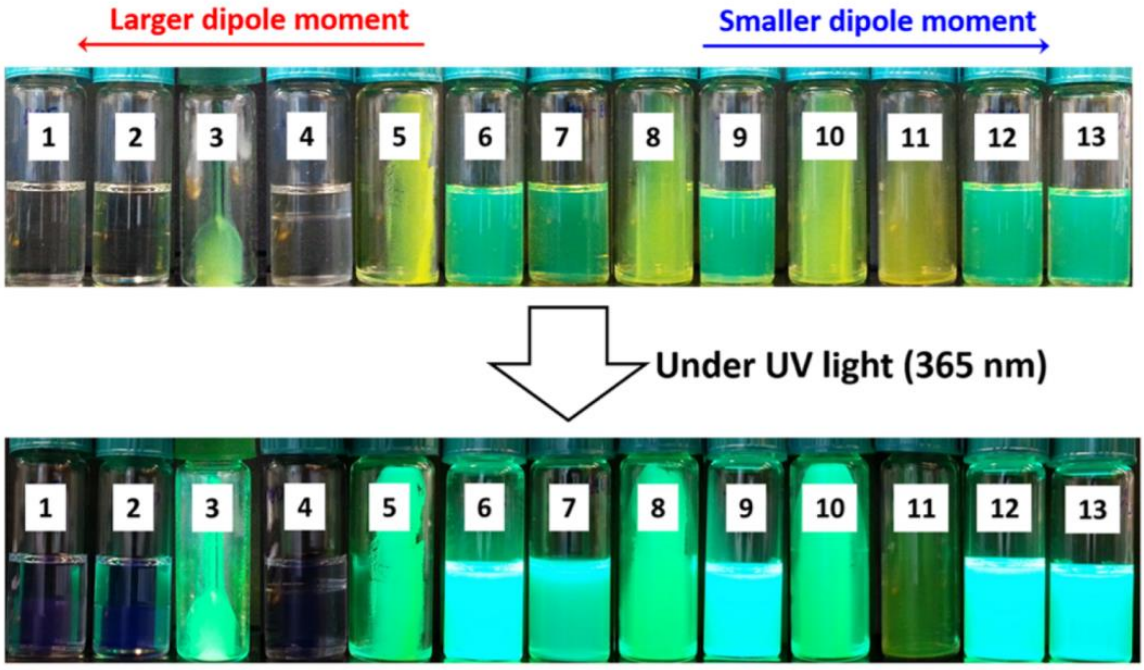

Figure 1.20 Effect of polar solvents on crude solutions of as-synthesized $CsPbBr_3$ nanocrystals. All mixtures of crude solution and polar solvents (with the volume ratio of one to one) in each vial were centrifuged at 8000 rpm for 30 min. The solvents are arranged in order of increasing dipole moment: (1) dimethyl sulfoxide, (2) dimethylformamide, (3) acetonitrile, (4) methanol, (5) acetone, (6) ethyl acetate, (7) tert-butanol, (8) 1- butanol, (9) tetrahydrofuran, (10) isopropyl alcohol, (11) ethanol, (12) chloroform, and (13)

dichloromethane, respectively.[47] [Reprinted with permission from ref. 47, Copyright © 2015 American Chemical Society]

Wang et al. (**Figure 1.21**) showed that adding polar solvents to $CsPbBr_{0.5}I_{2.5}$ and $FA_{0.33}Cs_{0.67}PbBr_{0.5}I_{2.5}$ both result in PL deterioration due to breakage of the perovskite constituents as well.[45]

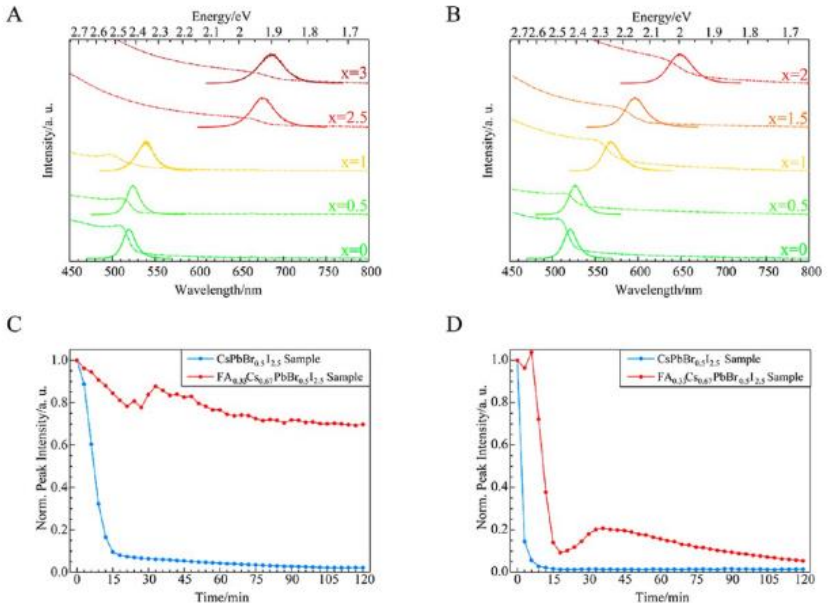

Figure 1.21 Optical characterizations of $FA_{0.33}Cs_{0.67}PbBr_{3-x}I_x$ nanocrystals. Optical absorption (dashed lines) and PL spectra (solid lines) for (A) $FA_{0.33}Cs_{0.67}PbBr_{3-x}I_x$ nanowires and (B) $FA_{0.33}Cs_{0.67}PbBr_{3-x}I_x$ nanosheets. Normalized PL intensity of $CsPbBr_{0.5}I_{2.5}$ and $FA_{0.33}Cs_{0.67}PbBr_{0.5}I_{2.5}$ nanowires in solvents made of (C) hexane−ethyl acetate and (D) hexane−acetone.[45] [Reprinted with permission from ref. 45, Copyright © 2017 American Chemical Society]

Stability in Water

Gomez et al. showed that encapsulation of $CsPbX_3$ in an amphiphilic polymer (poloxamer 188) via micelle formation in water can greatly extend its long term stability in water. As for $CsPb(Br_2I_8)_3$ QDs encapsulated in this amphiphilic polymer, PL intensity was maintained for up to 100 h. (**Figure 1.22**) However, due to the encapsulation process which involved micelle formation in water, initial perovskite QD exposure to water was unavoidable resulting in drastic QY loss. $CsPbBr_3$ QY went from 85% to 13% before and after polymer encapsulation. $CsPb(Br_2I_8)_3$ QY went from 33% to 9% before and after encapsulation. Also for both QDs, the PL peak blue shifted due to dissolution of the QDs during the short water exposure during polymer encapsulation (**Figure 1.23**).[51]

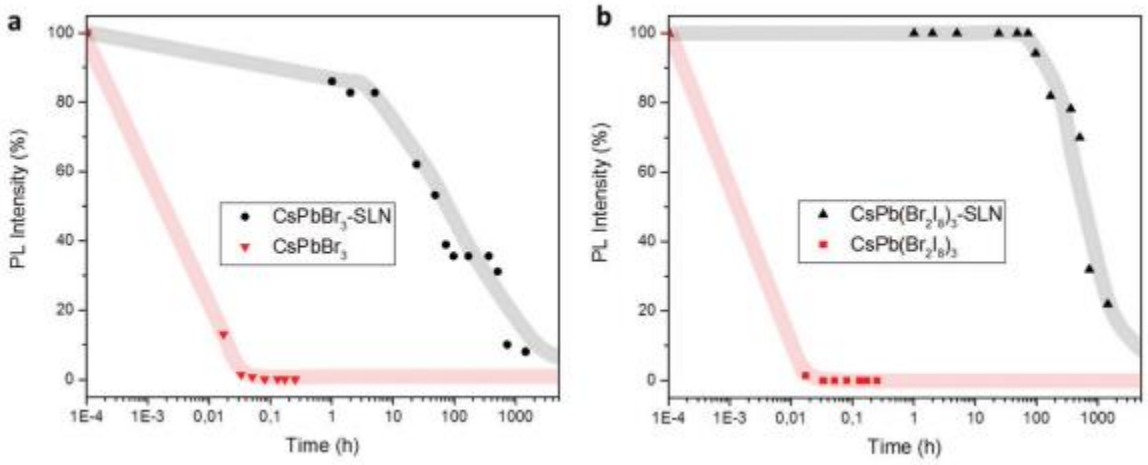

Figure 1.22 Photoluminescence intensity as a function of time for free-standing (red) and encapsulated (black) $CsPbBr_3$ (a) and $CsPb(Br_{0.2}I_{0.8})_3$ (b) nanocrystals dispersed in Milli-Q water. PL intensity is normalized (100%) to the value in toluene before contact with Milli-Q water (red), and with the emission of freshly prepared encapsulated perovskites

(black). The lines are a guide to the eye.[51] [Copyright © 2017 The Royal Society of Chemistry]

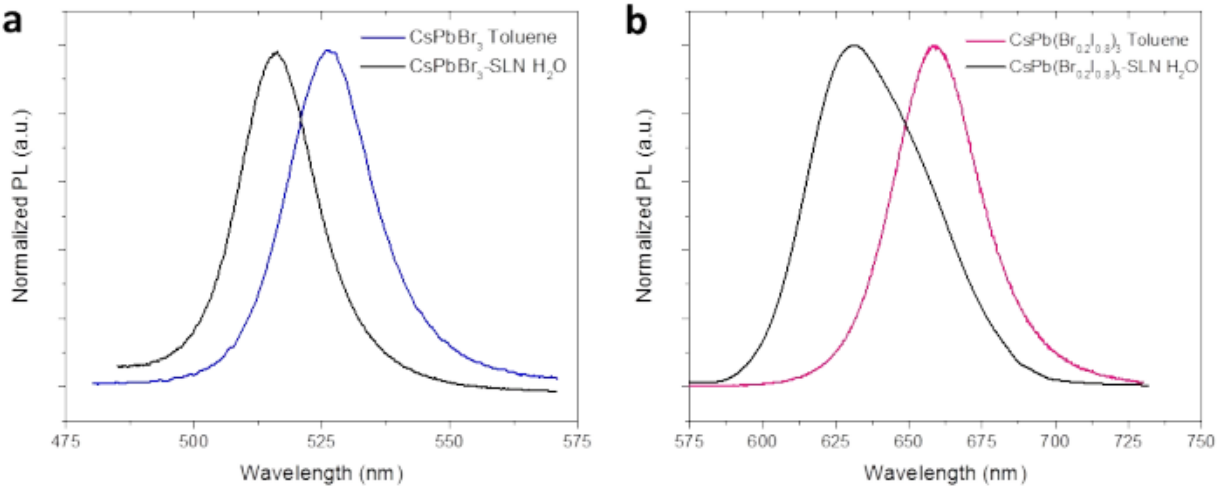

Figure 1.23 Photoluminescence ensemble spectra of perovskite NCs before and after encapsulation, in toluene and water, respectively. The emission peak blue-shifts when the NCs are encapsulated in comparison with the emission of free-standing NCs in toluene for (a) $CsPbBr_3$ and (b) $CsPb(Br_{0.2}I_{0.8})_3$.[51] [Copyright © 2017 The Royal Society of Chemistry]

Phase Stability

Phase stability is also a major hurdle against commercialization. When perovskite active layers with mixed halide composition is exposed to light, halide segregation results, creating regions of lower band gap.[52] Also when tuning the band gap for solar cells to 1.7~1.8 eV by mixing Br and I, an amorphous phase forms resulting in instability in the crystal structure.[25]

Gratzel et al. and Snaith et al. has recently shown that mixing FA cations with cesium cations can completely eliminate the problem of halide segregation as well as phase instability.[25, 53-55] Resolving the stability issue has opened up a new era for perovskite materials so that researchers can perform more in depth research into these fascinating but yet to be fully explored perovskite materials.

Thermal Stability

Wang et al. (**Figure 1.24**) observed that PL of $CsPbBr_3$ QDs deteriorate upon heating. $CsPbBr_3$ deposited on mesoporous silica, however, showed minimal PL loss upon thermal cycling.[46]

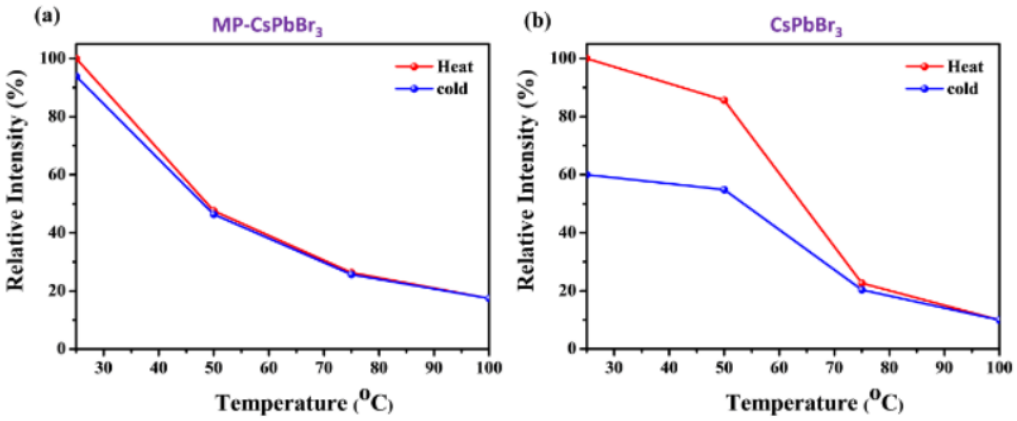

Figure 1.24 Thermal cycling of a) MP-$CsPbBr_3$ and b) $CsPbBr_3$.[46] [Reprinted with permission from ref. 46, Copyright © 2016 Wiley-VCH]

Our unique approach towards improving quantum nanocrystal stability via unimolecular star polymer nanoreactors as well as inorganic nanotemplates will be dealt with in Chapter 3 Research & Results.

1.2.2 Gold Nanocrystals

Gold nanocrystals are known for their low toxicity, excellent biocompatibility, and especially size-dependent and shape-dependent optoelectronic properties. These optoelectronic properties are based on the collective oscillation of conduction electrons which is commonly referred to as surface plasmon resonance (SPR). SPR of gold nanomaterials has found uses in bio-imaging, tumor treatment, and catalysis.[56]

Gold Nanospheres

Colloidal gold nanospheres are not yellow but actually red, violet, or purple when well dispersed in solution. This color comes about due to the absorption of gold nanospheres at around 520 nm which is caused by the collective oscillation of the electron cloud when bombarded with light photons. When gold nanospheres are smaller or similar in size to the incident light wavelength, there is strong interaction between the nanosphere and radiation wave. This interaction causes an oscillatory motion of the electron cloud, creating a dipole in the particle that may be used in solar cells to more efficiently separate excitons and hole. This phenomenon is termed the plasmonic effect (**Figure 1.25**).[57]

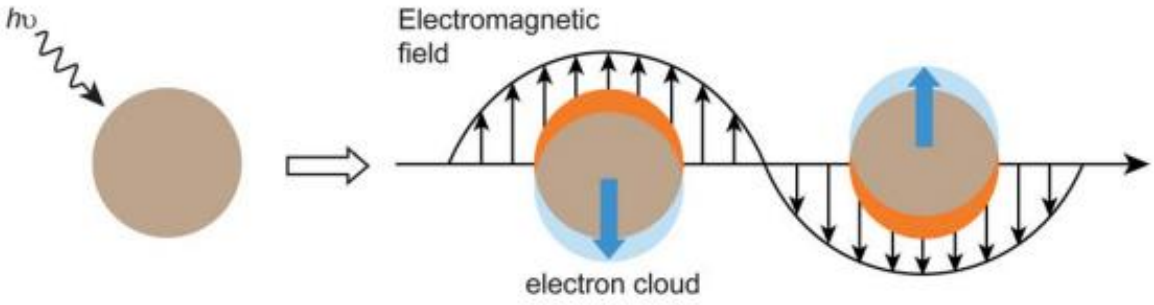

Figure 1.25 Schematic representation of the oscillation of conduction electrons across the nanoparticle in the electromagnetic field of the incident light.[58] [Reprinted with permission from ref. 58, Copyright © 2012 The Royal Society of Chemistry]

Gold Nanorods

Gold nanorod synthesis was pioneered by Murphy et al.[59] and El-Sayed et al.[60] Murphy et al. published one of the first seed-mediated wet-chemistry techniques to synthesize gold nanorods in 2001.[59] El-Sayed et al. improved the method developed by Murphy et al. and synthesized gold nanorods with higher yield and uniformity. The gold nanorods had an aspect ratio (AR) of 1.5-10 with surface plasmon absorption maxima ranging from 600 nm to 1300 nm via the silver assisted seed-mediated growth method[60]

In comparison to gold nanospheres, gold nanorods have a longitudinal plasmonic peak in the near-IR (**Figure 1.26**). This is due to electron oscillations along the longitudinal axis, in addition to commonly observed transverse plasmonic peak in the visible wavelength range as in gold nanospheres.[61-68]

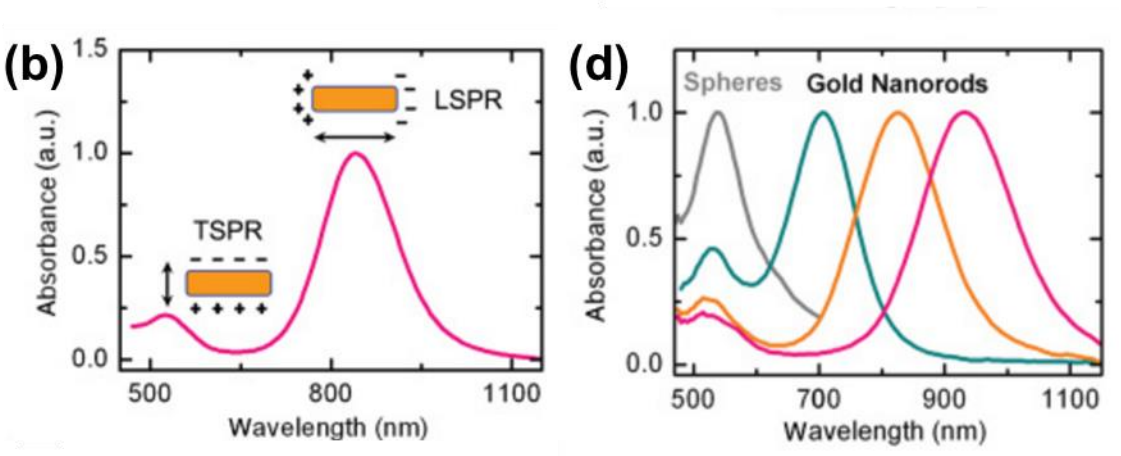

Figure 1.26 (b) Absorbance spectra of a gold nanorod solution. The insets show the schematic of the transverse and longitudinal SPR modes, which correspond to two absorption peaks, respectively. (d) Absorbance spectra of gold nanospheres and gold nanorods.[69] [Copyright © 2013 OSA Publishing]

Improving Stability

Gold nanoparticles as well as any other nanoparticles tend to aggregate due to their high specific surface area. Thus nanoparticles are covered by ligands to maintain colloidal stability. Ligands, however, are not covalently bound to the nanoparticle surface resulting in a dynamic equilibrium of bound and unbound ligands in the system. The equilibrium that maintains dynamic stability of the system may be altered when the environment (pH, temperature, etc.) changes.

Strategies to improve colloidal stability of nanoparticles include grafting-from, grafting-to, and unimolecular template approaches. These set of approaches allows the

formation of nanoparticles with permanently and covalently tethered polymers on the surface, so that colloidal stability can be less affected by changes in the environment.

Our unique approach towards improving gold nanoparticle stability via unimolecular star polymer nanoreactors will be dealt with in Chapter 3 Research & Results.

CHAPTER 2. MOTIVATION, OBJECTIVES & OVERVIEW

2.1 Motivation

Nanomaterials have strikingly different and novel properties compared to their bulk counterpart. Nanomaterials display a vast array of properties in relation to its dimensions (i.e. size and shape), spatial composition, and surface chemistry. Controlling these factors simultaneously, however, is a daunting task using conventional synthesis techniques that utilize non-covalently bound linear ligands. To that end, unimolecular non-linear polymer nanoreactors as well as inorganic nanotemplates have proven precision control over these factors. Nanoparticle synthesis through templating methods, however, have not been fully investigated for many material systems and still needs to be explored.

The first approach to nanomaterial synthesis is via unimolecular non-linear star-like polymer nanoreactors which is composed of 21 block copolymer arms grown off of cyclic structured β-cyclodextrin that has 21 activation sites. Its use in many novel materials, however, has not been fully explored. Especially, the recently emerging perovskite nanomaterials synthesized via star-like polymer nanoreactors are expected to bring about interesting characteristics that requires investigation. Through the interplay of ATRP and click chemistry we expect precise control over the size as well as surface functionality of perovskite nanomaterials which will offer many unique properties compared to perovskite nanomaterials grown via conventional ligand-assisted methods. In particular, the covalently bound surface polymers are expected to bring about drastic improvements in stability for the perovskite quantum dots whose major bottleneck for commercialization is poor stability due to two expectations. Firstly, compared to conventional ligands that are

in dynamic equilibrium between bound and free ligands from the nanomaterial surface, the permanent polymer capping will ensure consistent surface capping of the nanomaterials thus ensuring improved colloidal stability (e.g. no aggregation). Secondly, the permanent polymer capping will serve as a protective shell layer for each individual quantum dot that is difficult to achieve via conventional methods thus resulting in enhanced stability.

The second approach to controlling growth of nanocrystals is through the cation exchange of pre-synthesized and well-defined optical nanocrystals to create new nanocrystals with different cations while retaining its original anionic framework. In other words, well-defined traditional nanocrystals are used as nanotemplates to guide the growth of new nanocrystals via their sturdy anion framework which will not deform during cation exchange. This approach allows us to utilize well-known chemical reactivities of a certain group of compounds and replicate its nanocrystal structure for different compounds as well. For instance, the synthesis of core/graded shell-shell CdSe/$Cd_{1-x}Zn_xSe_{1-y}S_y$-ZnS nanocrystals utilizes different chemical reactivities of Cd, Zn, Se, and S to create a well-defined gradient core/shell structure. Cation exchange of these nanocrystals will allow us to reproducibly synthesize IR nanocrystals such as PbSe/$PbSe_{1-y}S_y$/PbS or AgSe/$AgSe_{1-y}S_y$/AgS nanocrystals with precisely targeted dimensions. The absorption and photoluminescence wavelength of CdSe/$Cd_{1-x}Zn_xSe_{1-y}S_y$-ZnS nanocrystals in the visible region are also expected to allow relatively facile characterization of the nanocrystals dimensions compared to IR range characterizations that are less accessible due to equipment cost. It should also be emphasized that in addition to accurate structure control, this strategy is expected to allow air-sensitive materials such as PbSe, which easily oxidizes in air to be immediately protected by a shell layer resulting in improved stability. Also for

core/shell nanocrystals which has a type II nanocrystal band gap structure (e.g. PbSe/$PbSe_{1-y}S_y$/PbS), the cation exchange method may be able to uniformly and precisely add additional outer shell layers enabling fine-tuning of band gap alignment between the core and shell materials. For IR range nanocrystals such as PbSe/$PbSe_{1-y}S_y$/PbS, the precise-tuning of band gap alignment may act as an effective means to push the PL wavelength to mid IR wavelengths.

2.2 Research Objectives

(1) Synthesis of well-defined unimolecular non-linear block copolymer nanoreactors based on β-cyclodextrin via combination of ATRP and click chemistry.

(2) Synthesis of polystyrene-capped (i.e. permanent covalent bonding) perovskite nanomaterials via the polymer nanoreactor approach.

(3) Application of polystyrene-capped (i.e. permanent covalent bonding) perovskite nanomaterials in optoelectronic devices.

(4) Synthesis of polystyrene-capped (i.e. permanent covalent bonding) metallic nanomaterials (e.g. Au & Ag) via the polymer nanoreactor approach

(5) Synthesis of well-defined inorganic nanocrystals with a gradient composition interfacial layer by utilizing reactivity differences between reactants for use as inorganic nanotemplates.

(6) Synthesis of novel nanomaterials with a gradient composition interfacial layer via cation exchange of inorganic nanotemplates with a gradient composition interfacial layer.

2.3 Map of Dissertation

This thesis reports on different strategies for synthesizing metallic nanoparticles, metal chalcogenide nanocrystals and perovskite quantum dots and their optical and optoelectronic properties. Chapter 1 is a general overview of the state-of-the-art synthetic approaches to crafting nanomaterials as well as a brief introduction to nanomaterials and the current challenges they face today. Chapter 2 presents the motivation of my work and organizes the specific research objectives that has been tackled throughout the dissertation. Chapter 3 presents the three main research results. Chapter 3.1 reports on the polymer-templated in-situ growth of all-inorganic perovskite quantum dots with well-controlled dimensions and characterizes their markedly enhanced stability as well as their precisely tunable optical properties. Chapter 3.2 reports on the polymer-templated in-situ growth of metallic nanoparticles (Au & Ag) with precisely controllable dimensions and distinctly improved stability under UV irradiation. Chapter 3.3 reports on the inorganic nanoparticle-templated growth of PbSe/$PbSe_{1-y}S_y$/PbS QDs with a gradient interfacial layer via the cation exchange mechanism. Characterization of their stability in air and their optical properties in the infrared region is presented as well. Chapter 4 summarizes the key findings from each chapter and introduces future work that will be undertaken in connection to the presented results. Chapter 5 lists the publications that have disseminated from the work.

CHAPTER 3. RESEARCH & RESULTS

3.1 Enabling Tailorable Optical Properties and Markedly Enhanced Stability of Perovskite Qunatum Dots by Permanently Ligating with Polymer Hairs via Amphiphilic Star-like Block Copolymer Nanoreactors

Y.J. Yoon, Y. Chang, S. Zhang, S. Pan, Y. He, C.H. Lin, S. Yu, Y. Chen, Z. Wang, J. Jung, N. Thadhani, V.V. Tsukruk, Z. Kang, Z. Lin*, "Enabling Tailorable Optical Properties and Markedly Enhanced Stability of Perovskite Quantum Dots by Permanently Ligating with Polymer Hairs", (Under Review).

Abstract

The past few years have witnessed rapid advances in synthesizing perovskite quantum dots (QDs), which has led to a rich variety of perovskite QDs of different dimensions, compositions, and optoelectronic properties. Nevertheless, despite these impressive developments, instability of perovskite QDs, particularly towards humidity, remains one of the major obstacles for their long-term use in optoelectronic materials and devices. Herein, we report a general amphiphilic star-like block copolymer nanoreactor strategy for *in-situ* crafting a set of hairy perovskite QDs with precisely tunable size and exceptionally high water and colloidal stabilities against decomposition and aggregation, respectively. Amphiphilic star-like diblock copolymers employed as nanoreactors are composed of inner hydrophilic blocks and outer hydrophobic blocks with well-defined respective molecular weights and low polydispersity. The selective partition of precursors within the compartment occupied by inner hydrophilic blocks of star-like diblock

copolymers imparts *in-situ* formation of hairy perovskite QDs permanently ligated by outer hydrophobic blocks via co-precipitation in nonpolar solvent. Notably, anion exchange of halide ions of perovskite enables the production of perovskite QDs with tunable emissions. Moreover, molecular weight (i.e., length) of each constituent block (i.e., inner hydrophilic and outer hydrophobic polymers) can be strictly regulated via atom transfer radical polymerization. Taken together, an array of uniform perovskite QDs of different sizes, emissions and lengths of outer hydrophobic polymers can thus be crafted, displaying tailorable optical properties. These size- and composition-tunable QDs reveal impressive water and colloidal stabilities as the surface of QDs is intimately and permanently ligated by a layer of outer hydrophobic polymer hairs. More intriguingly, the readily alterable length of outer hydrophobic polymers renders the remarkable control over the stability enhancement of hairy perovskite QDs. When assembled into a typical white light emitting diode (WLED) architecture, hairy perovskite QDs exhibit appealing performance, reflecting 116% and 163% color gamut of WLED over national television system committee (NTSC) and standard red green blue (sRGB) standards, respectively. By extension, the amphiphilic star-like block copolymer nanoreactor strategy can afford easy access to a wide range of stable perovskite QDs and other nanocrystals of interest with precise control over dimensions, compositions and surface chemistry for use in solar cells, LEDs, photodetectors, lasers, scintillators, sensors, nanotechnology and biotechnology.

3.1.1 Introduction

Perovskites represent an emerging class of materials by a generic chemical formula ABX_3 with A^+ = methylammonium ($CH_3NH_3^+$), formamidinium ($HC(NH_2)_2^+$), Cs, or their combination; B^{2+} = Pb^{2+} and/or Sn^{2+}; X^- = Cl^-, Br^- and/or I^-. Perovskite thin films have been the focus of perovskite research over the past decade for a variety of optoelectronic applications due largely to their long carrier lifetime, low defect density, composition-dependent tunable bandgaps, narrow full width at half maximum (FWHM), outstanding quantum yield, and low production cost.[21-24] For example, much effort has been centered on increasing the grain size in the perovskite photoactive layer for achieving high-performance perovskite solar cells (PSCs).[25-30] Recently, perovskite quantum dots (QDs)[33] has garnered tremendous attention owing to their broad visible-to-near infrared wavelength tunability (400-800 nm) and narrow band emission[32, 37, 40] for use in lasers,[34-36] electroluminescence devices,[35, 37] sensors,[38] and solar cells.[32] In the latter context, perovskite QDs have been employed as the interfacial layer between a thin film of perovskite photoactive layer and a hole transporting layer (HTL) in PSC to improve interfacial charge transfer by optimizing the energy band alignment among HTL, perovskite QDs and perovskite thin film, leading to increased power conversion efficiency.[32] Among perovskite QDs, all inorganic $CsPbX_3$ QDs possess narrow FWHM of emission (as small as 12 nm) and excellent quantum yield (50%~90%).[33, 70-71] They have a Bohr diameter up to 12 nm,[33] exhibiting a size-tunable bandgap in the visible region. It is also notable that the exchange of halide ions (Cl^-, Br^- and I^-) in as-synthesized perovskite QDs is highly effective, rendering easy and rapid access to a wide range of perovskite QDs with tunable absorption and photoluminescence (PL) spectra.[33, 41-42]

In spite of significant advances in perovskite research noted above, a key to the success of perovskite-based materials and devices is the stability of perovskites as they are susceptible to decomposition due to their ionic crystal nature.[45-46] Recently, several methods including coating with alumina by atomic layer deposition[72] or partial coating with SiO_2 via sol-gel process,[73] physical mixing with hydrophobic polymers,[51, 74-76] and encapsulation within mesoporous silica[46] or polymer beads[77] have proven to be effective in improving stability in polar and ambient environments. However, nearly all approaches described above for stability enhancement result in nanocomposites with multiple perovskite QDs encapsulated in microscopic protective matrices. These microscale nanocomposites may be disadvantageous for biomedical applications where cellular uptake is more feasible for smaller nanoscopic particles,[78] or LEDs where the processing of smaller luminescent particles often leads to their higher loading and packing density and thus film uniformity.[73] Clearly, the ability to deliberately and reliably improve the stability of perovskite QDs (e.g., against humidity and polar solvents) while retaining their individual nanometer size represents a critical step that underpins future advances in optoelectronic and biological applications.

Herein, we report a general and robust strategy by capitalizing on judiciously designed amphiphilic star-like diblock copolymers with well-controlled molecular weight and low polydispersity of each block as molecularly engineered nanoreactors to craft uniform perovskite QDs. Remarkably, these QDs simultaneously possess precisely tunable dimensions and considerably enhanced colloidal and water stabilities via an extremely facile and rapid co-precipitation reaction. The amphiphilic star-like diblock copolymer nanoreactors exploited are poly(acrylic acid)-*block*-polystyrene (denoted PAA-*b*-PS)

synthesized by atom transfer radical polymerization (ATRP), comprising hydrophilic inner PAA and hydrophobic outer PS block of different lengths. The selective partition of precursors within the compartment occupied by PAA blocks of star-like diblock copolymers due to strong coordination interaction between the carboxylic acid groups of PAA blocks in star-like PAA-*b*-PS nanoreactors and perovskite precursors (i.e., CsX and PbX_2) yields *in-situ* hairy all-inorganic perovskite $CsPbX_3$ QDs perpetually ligated by hydrophobic PS blocks via the co-precipitation of two precursors in the nonpolar solvent. It is noteworthy that as the molecular weight of PAA and PS blocks can be readily tuned by simply varying their respective ATRP reaction times. This in turn presents the twofold advantages, that is, simple yet reliable control over the diameter of $CsPbX_3$ QDs governed by the length of the inner PAA blocks, thereby leading to precisely size-tunable optical properties, and concurrently outstanding water and colloidal stabilities of $CsPbX_3$ QDs dictated by the length of the outer PS blocks. It is important to note that the outer PS blocks are originally covalently connected to the inner PAA blocks, so the surface capping of $CsPbX_3$ QDs with PS blocks is intimate and permanent (i.e., PS-capped $CsPbX_3$), ensuring excellent colloidal stability in nonpolar solvents and preventing QDs from aggregation. This contrasts sharply to conventional ligand-assisted methods, where ligands are non-covalently bonded to QDs, thus promoting agglomeration of QDs due to the dynamic association-dissociation of surface ligands over time. Moreover, the permanently attached outer PS block forms a protective hydrophobic shell around perovskite QD where the thickness of shell depends on the length of PS blocks, thereby assuring greatly enhanced stability against polar solvents (e.g., water). These PS-capped $CsPbX_3$ QDs are then utilized for white light emitting diode (WLED), displaying a 116% and a 163% color gamut

over that of national television system committee (NTSC) and standard red green blue (sRGB) standards, respectively. In addition to LED, this intriguing class of stable hairy perovskite QDs may find great potential for use in perovskite solar cells, scintillators, bioimaging, biosensors, etc.

3.1.2 Results and Discussion

Scheme 3.1 depicts the synthetic route to hairy all-inorganic perovskite QDs intimately and permanently ligated by PS chains via capitalizing on amphiphilic unimolecular star-like PAA-*b*-PS diblock copolymers as nanoreactors, where the formation of $CsPbBr_3$ QD is taken as an example. First, a series of star-like poly(*tert*-butyl acrylate)-*block*-polystyrene (denoted P*t*BA-*b*-PS; upper right panel in **Scheme 3.1**) diblock copolymers with precisely controlled molecular weight and low polydispersity of the inner P*t*BA and outer PS blocks were synthesized via sequential ATRP of *tert*-butyl acrylate (*t*BA) and styrene (St) monomers using 21-Br-β-CD as a macroinitiator (see *Experimental Section*).[12-15, 79-85] Subseqeuently, the inner P*t*BA blocks were hydrolyzed into PAA blocks, resulting in amphiphilic unimolecular star-like PAA-*b*-PS (lower right panel in **Scheme 3.1**). Notably, in contrast to conventional linear block copolymer micelles formed by much weaker forces of attraction,[86] there are 21 arms of PAA-*b*-PS diblock copolymer anchored covalently to a single macroinitiator. The molecular weights of star-like PAA-*b*-PS characterized by GPC and ^{1}H-NMR spectra are summarized in **Figure 3.1**, **Figure 3.2**, **Figure 3.3**, **Figure 3.4**, **Table 3.1**, and **Table 3.2**.

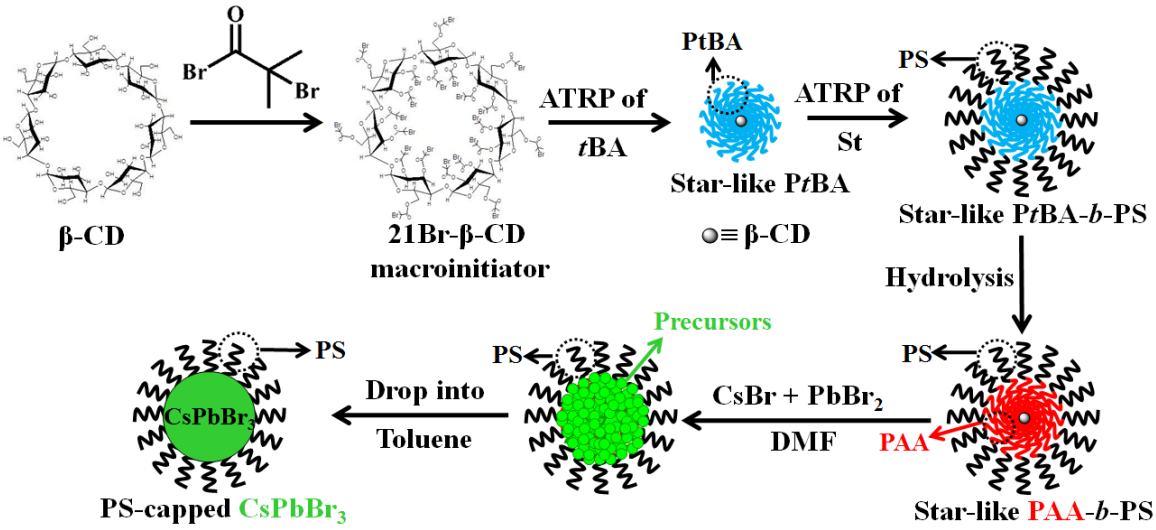

Scheme 3.1 Schematic stepwise representation of crafting hairy all-inorganic perovskite $CsPbBr_3$ QDs intimately and permanetnly capped by PS chains via capitalizing on amphiphilic star-like PAA-*b*-PS diblock copolymer as nanoreactor. Star-like all hydrophobic P*t*BA-*b*-PS diblock copolymer is syntheisezed via sequential atom transfer radical polymerization of tert-butylacrylate (*t*BA) and styrene (St) using 21Br-β-CD as macroinitiator. Hydrolysis of star-like P*t*BA-*b*-PS yields amphiphilic star-like PAA-*b*-PS. Perovskite precursors of CsBr and $PbBr_2$ are selectively partitioned in the compartment occupied by hydrophilic PAA blocks. Co-precipetation of CsBr and $PbBr_2$ in nonpolar solvent (e.g., toluene) leads to the formation of green-emitting PS-capped $CsPbBr_3$ QDs.

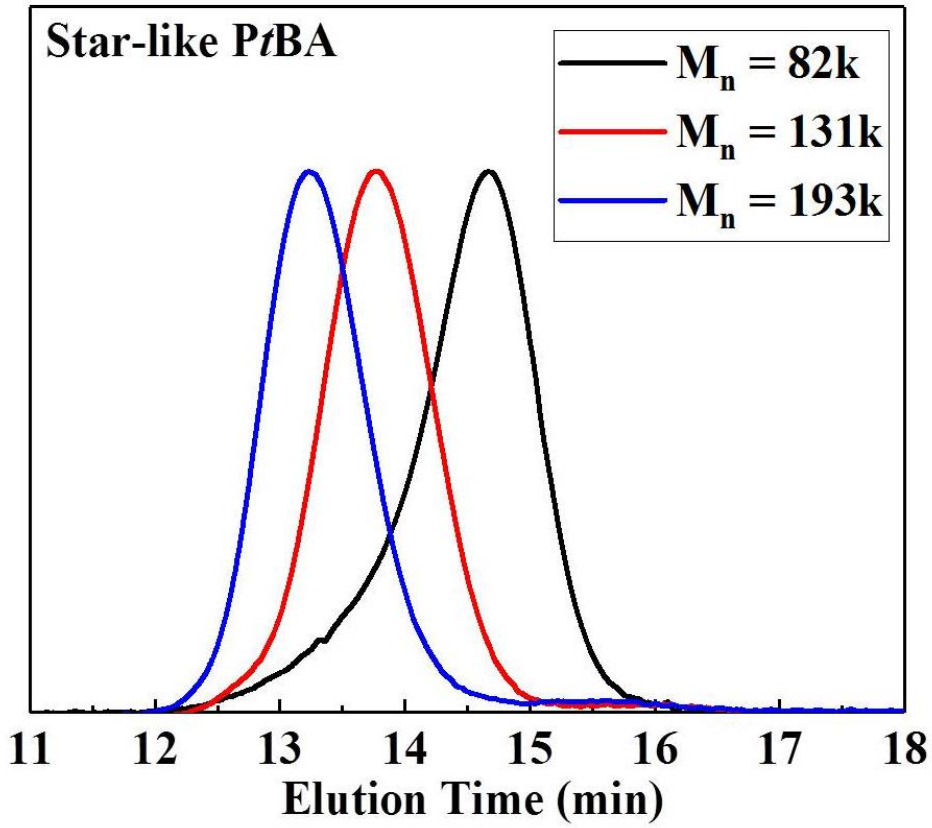

Figure 3.1 GPC curves of star-like P*t*BA of different molecular weights in THF.

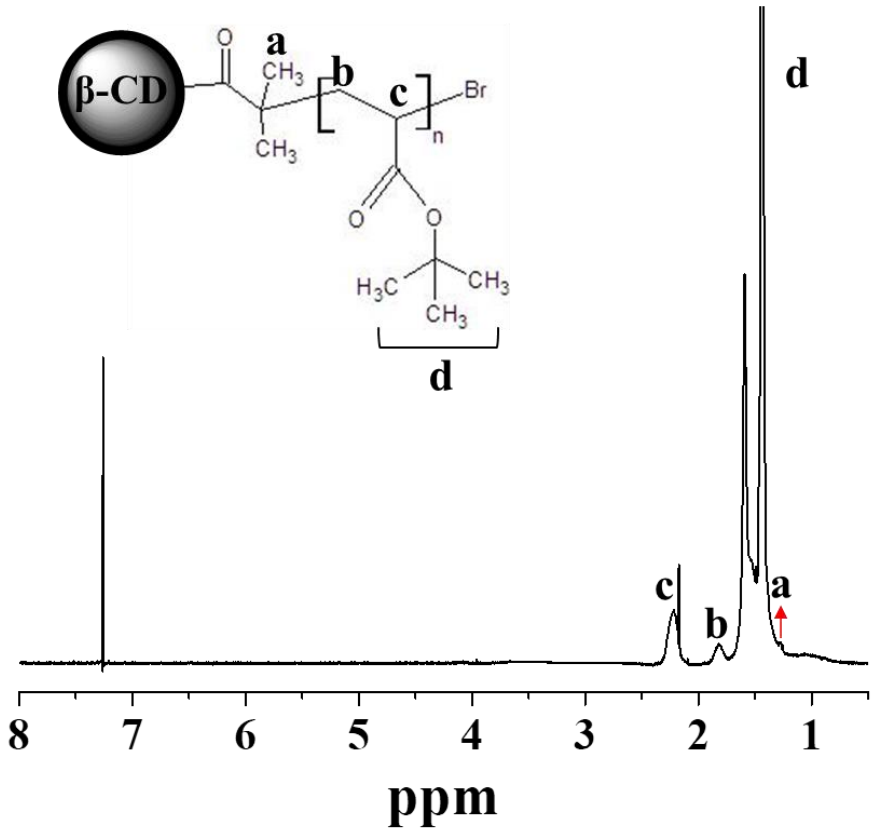

Figure 3.2 Representative ^{1}H-NMR spectrum of star-like P*t*BA in $CDCl_3$.

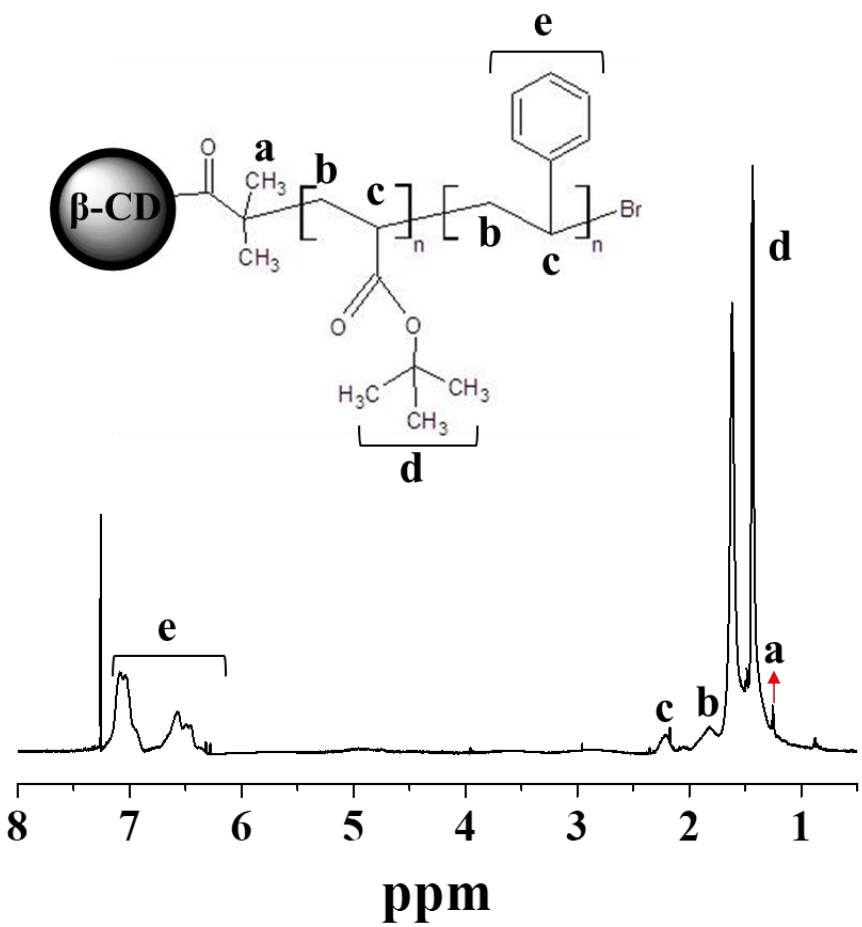

Figure 3.3 Representative ^{1}H-NMR spectrum of star-like P*t*BA-*b*-PS in $CDCl_3$.

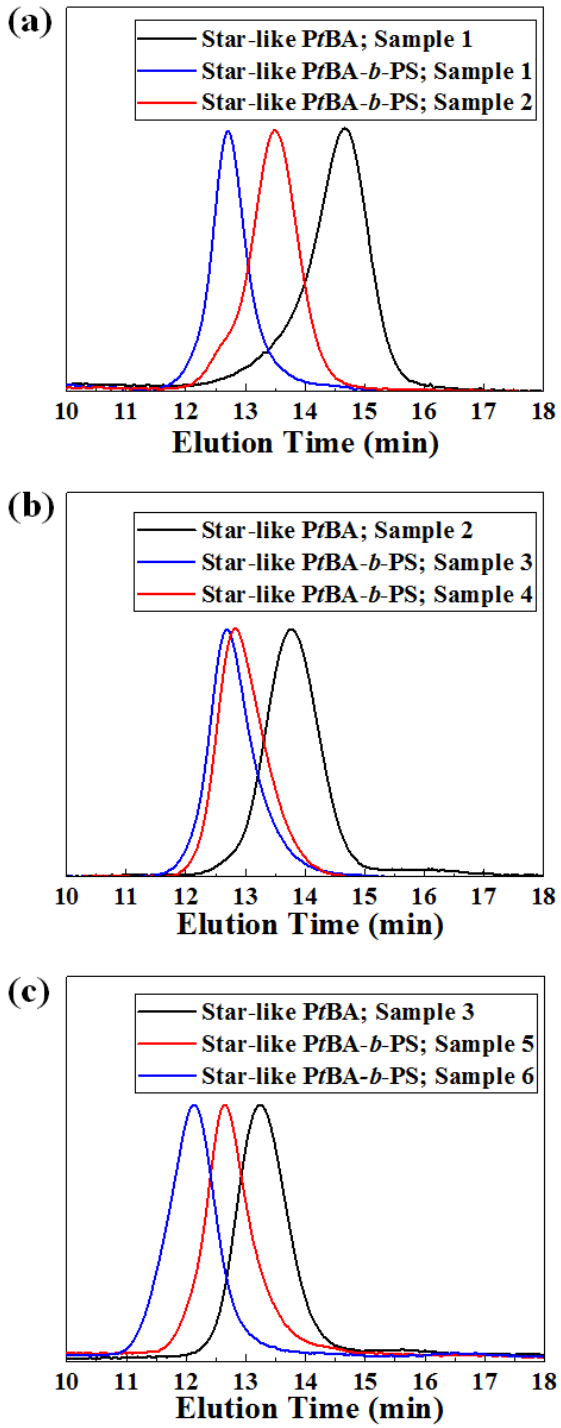

Figure 3.4 GPC curves of star-like P*t*BA-*b*-PS of different molecular weights (see **Table 3.1**) in THF.

Table 3.1 Molecular weights of amphiphilic star-like PtBA-*b*-PS diblock copolymers

Nanoreactor	M_n[a] (kg/mol)	PDI[b]	$M_{n,PtBA}$[c] (kg/mol)	$M_{n,PS}$[d] (kg/mol)
Star-like PtBA Sample 1	81	1.15	9.1	
Star-like PtBA-*b*-PS Sample 1	171	1.14	9.1	8.5
Star-like PtBA-*b*-PS Sample 2	318	1.13	9.1	16.9
Star-like PtBA Sample 2	133	1.12	13.9	
Star-like PtBA-*b*-PS Sample 3	250	1.17	13.9	9.6
Star-like PtBA-*b*-PS Sample 4	295	1.18	13.9	13.2
Star-like PtBA Sample 3	193	1.14	19.6	
Star-like PtBA-*b*-PS Sample 5	307	1.22	19.6	7.3
Star-like PtBA-*b*-PS Sample 6	611	1.28	19.6	16.4

Notes: [a]Number average molecular weight (M_n) of star-like polymer nanoreactor before hydrolysis (i.e., star-like P*t*BA and star-like P*t*BA-*b*-PS) determined by GPC in THF (**Figure 3.1** and **Figure 3.4**). [b]PDI of star-like polymer nanoreactor before hydrolysis (i.e., star-like P*t*BA and star-like P*t*BA-*b*-PS) determined by GPC in THF (**Figure 3.1** and **Figure 3.4**). [c]M_n of each PtBA block arm calculated from ^{1}H-NMR (**Figure 3.2**). [d]Mn of each PS block arm calculated from ^{1}H-NMR (**Figure 3.3**).

Table 3.2 Molecular weights of amphiphilic star-like PAA-*b*-PS diblock copolymers

Nanoreactor	$M_{n,PAA}$[a] (kg/mol)	$M_{n,PS}$[b] (kg/mol)
Star-like PAA-*b*-PS Sample 1	5.1	8.5
Star-like PAA-*b*-PS Sample 2	5.1	16.9
Star-like PAA-*b*-PS Sample 3	7.8	9.6
Star-like PAA-*b*-PS Sample 4	7.8	13.2
Star-like PAA-*b*-PS Sample 5	11.0	7.3
Star-like PAA-*b*-PS Sample 6	11.0	16.4

Notes: [a]M_n of each PAA block arm calculated from the molecular weight difference between the PtBA block (before hydrolysis) and PAA block (after hydrolysis). [b]Mn of each PS block arm calculated from ^{1}H-NMR (**Figure 3.3**).

Amphiphilic star-like PAA-*b*-PS diblock copolymers were then exploited as nanoreactors to template the synthesis of $CsPbBr_3$ QDs tethered by PS chains that were originally covalently bonded to PAA chains. First, the star-like nanoreactor, cesium bromide (CsBr), and lead bromide ($PbBr_2$) were fully dissolved in anhydrous N,N-dimethylformamide (DMF). The perovskite ions selectively occupied the inner PAA-containing compartment of nanoreactor by strongly coordinating with the carboxyl groups of the inner PAA blocks (i.e., forming the CsBr- and $PbBr_2$-loaded nanoreactor solution; lower central panel in **Scheme 3.1**).[14-15, 87-88] Subsequently, by dropping the solution into a poor solvent (i.e., toluene) for the perovskite precursors, $CsPbBr_3$ QDs were rapidly produced via co-precipitation[89] in toluene (lower left panel in **Scheme 3.1**), selectively confined within the inner PAA compartment. This is not surprising as perovskite QDs would otherwise be decomposed in DMF due to their ionic nature. It is worth noting that as PS dissolves well in toluene, the aggregation of PS-capped perovskite QDs in toluene was thus prevented.

Figure 3.5 compares the synthesis of $CsPbBr_3$ QDs by capitalizing on star-like PAA-*b*-PS nanoreactor (i.e., sample 5 in **Table 3.2**; where the molecular weight of a single PS chain is 7300 g/mol, thus the resulting QDs are referred to as PS(7k)-capped $CsPbBr_3$ QDs) and by utilizing oleic acid as the common linear ligand, respectively. For both systems, the precursor solution contains the same molar content of all reactants, and the reaction was conducted by adding nonpolar solvent toluene to co-precipitate two precursors (i.e., CsBr and $PbBr_2$) at room temperature. For the PS(7k)-capped $CsPbBr_3$ QDs, as the precursor solution was dropped into toluene, co-precipitation of CsBr and $PbBr_2$ occurred selectively within the inner PAA compartment of the star-like PAA-*b*-PS nanoreactor. Due

to hydrophobic PS capping, green-emitting QDs rapidly formed in the solution in less than 1 sec (**Figure 3.5a**), suggesting the homogeneous dispersion of QDs in toluene. In contrast, $CsPbBr_3$ capped with oleic acid (see *Experimental Section*; **Figure 3.5b**) and $CsPbBr_3$ with no ligand present (see *Experimental Section*; **Figure 3.6**) were initially bright when toluene was added into the precursor solution; however, the photoluminescence (PL) of $CsPbBr_3$ quickly disappeared (< 1 sec) due to aggregation of QDs as a result of weak binding of oleic acid to QD at room temperature. Notably, it has been reported that high-temperature hot-injection of precursors in the presence of oleic acid produces relatively stable $CsPbBr_3$ QDs,[48] due likely to the improved binding between oleic acid and QD. The observations noted above were verified by TEM measurements, where uniform PS(7k)-capped $CsPbBr_3$ QDs with an average size of 13.9±0.7 nm were seen (size distribution within 5% of average size, which can be regarded as monodisperse; **Figure 3.5**c**),** while aggregates of $CsPbBr_3$ was found for the oleic acid and no ligand samples **(Figure 3.5d** and **Figure 3.6**, respectively). The HRTEM studies (inset in **Figure 3.5c** and **Figure 3.7**) reveal that PS(7k)-capped $CsPbBr_3$ QD is crystalline. Clearly, the ability to craft uniform PS(7k)-capped $CsPbBr_3$ QDs demonstrates the effectiveness of star-like nanoreactor in synthesizing high-quality hairy $CsPbBr_3$ QDs.

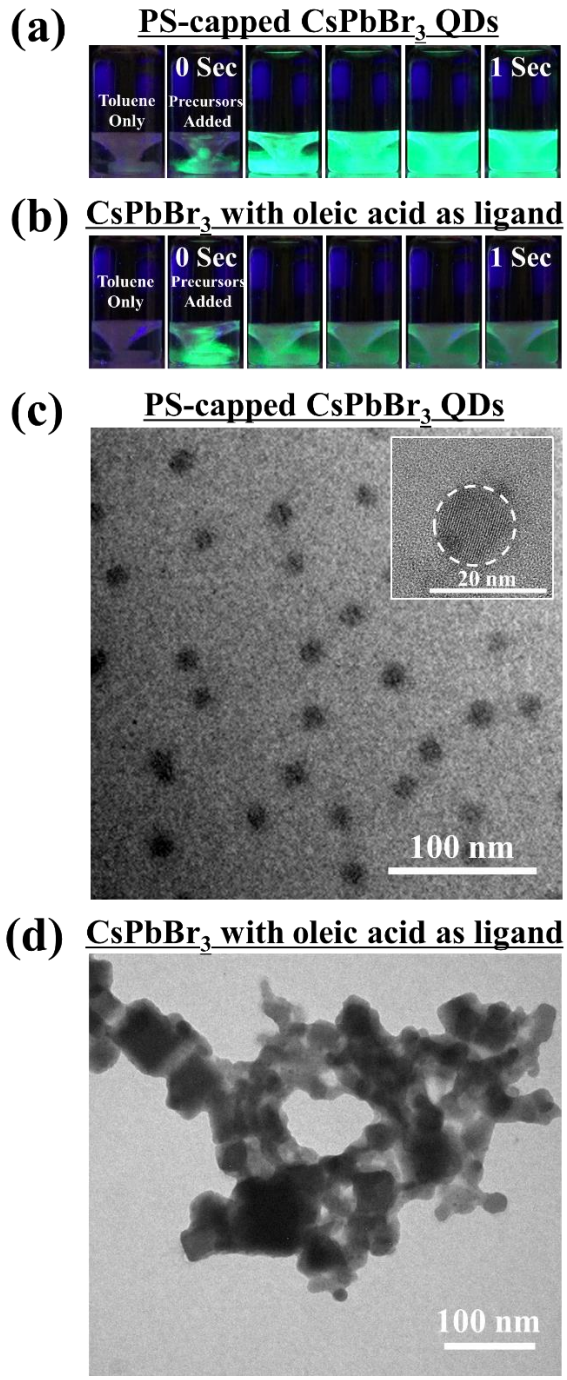

Figure 3.5 Synthesis of $CsPbBr_3$ with and without the use of star-like PAA-*b*-PS diblock copolymers as nanoreactors. Digital images displaying the rapid formation process of (a) PS-capped $CsPbBr_3$ QDs (capitalizing on star-like PAA-*b*-PS nanoreactors; sample 5 in **Table 3.2**), and (b) $CsPbBr_3$ (using oleic acid as ligand only; in the absence of star-like PAA-*b*-PS), by adding the precursors-containing (i.e., CsBr and $PbBr_2$) DMF solution into

toluene (i.e. a co-precipitation approach) over 1 sec at room temperature. TEM images of (c) PS-capped $CsPbBr_3$ QDs corresponding to the sample synthesized in (a) (average diameter, D = 13.9±0.7 nm), and (d) aggregated $CsPbBr_3$ nanocrystals corresponding to the sample produced in (b).

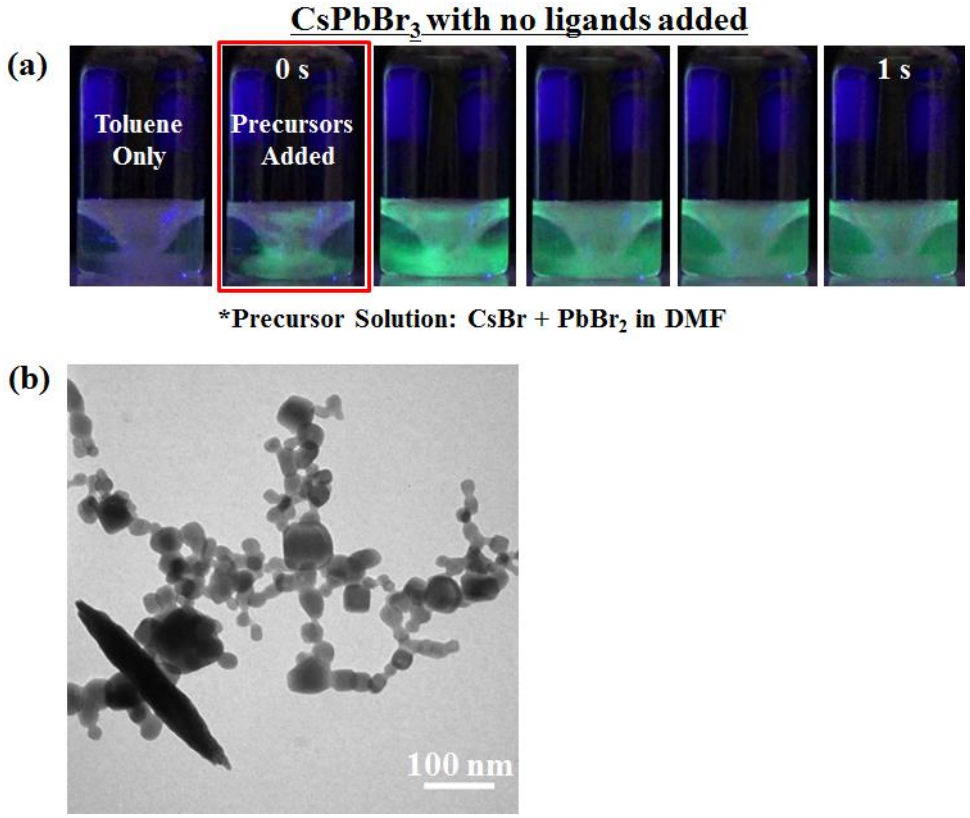

Figure 3.6 Control experiment (i.e., with no ligand added). (a) Digital image displaying the formation process of perovskite materials over 1 second. (b) The corresponding TEM image of perovskite materials synthesized.

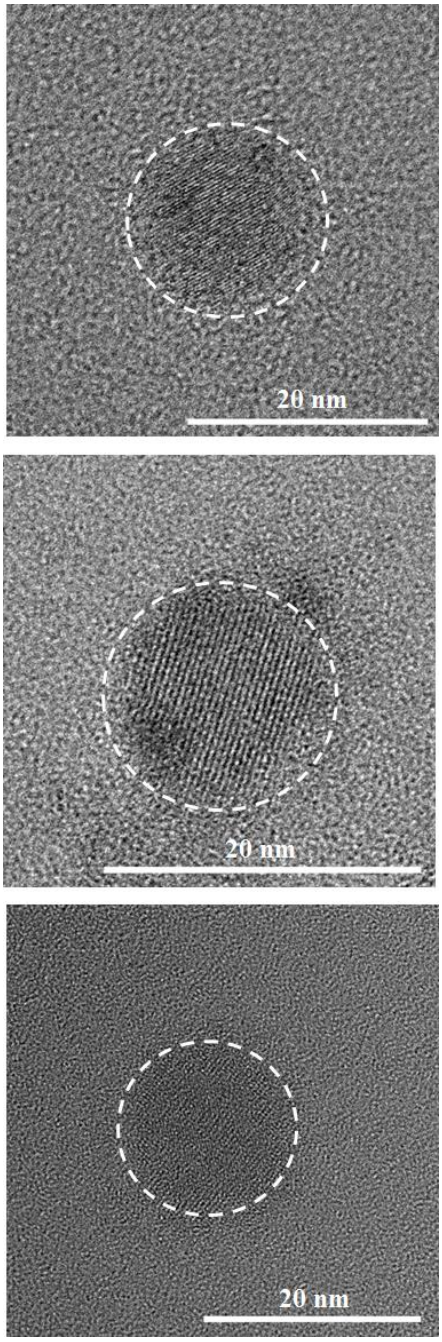

Figure 3.7 HRTEM image of three individual PS-capped perovskite $CsPbBr_3$ QD (D = 13.9 nm), revealing crystal lattices. $CsPbBr_3$ QDs were crafted using star-like PAA-*b*-PS diblock copolymers (i.e., sample 5 in **Table 3.2**) as nanoreactors.

Successful synthesis of green-emitting $CsPbBr_3$ QDs was further substantiated by absorption, PL and XRD measurements (**Figure 3.8**). PS(7k)-capped $CsPbBr_3$ QDs display the first exciton absorption peak at 503 nm and PL peak at 516 nm, which agrees well with conventional $CsPbBr_3$ QDs prepared by other methods (e.g., hot-injection).[33] It is interesting to note that the FWHM, an indirect measure of the monodispersity of QDs, is as low as 17.7 nm for PS(7k)-capped $CsPbBr_3$ QDs, which is comparable to the lowest value for $CsPbBr_3$ QDs reported.[90] The XRD diffraction peaks also coincide well with the monoclinic phase $CsPbBr_3$ (PDF#18-0364) observed for $CsPbBr_3$ QDs synthesized via co-precipitation method in literature.[89]

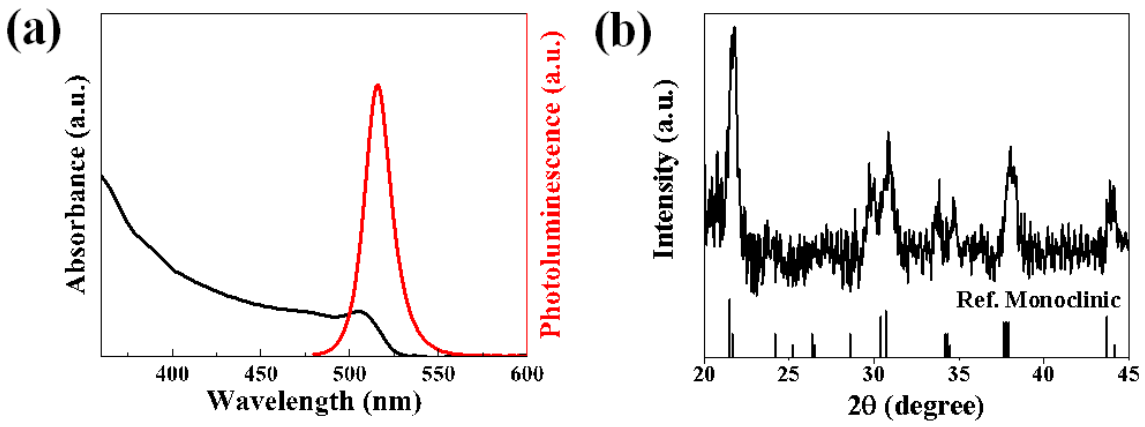

Figure 3.8 (a) Absorption and photoluminescence (PL) spectra of PS(7k)-capped $CsPbBr_3$ QDs, where the absorption and PL maxima are 503 nm and 516 nm, respectively. (b) XRD pattern of PS(7k)-capped $CsPbBr_3$ QDs crafted by employing star-like PAA-*b*-PS diblock copolymers (i.e., sample 5 in **Table 3.2**) as nanoreactors.

Anion exchange of the Br^- group in PS-capped $CsPbBr_3$ QDs using $ZnCl_2$ and ZnI_2[91] was then performed to yield blue-emitting $CsPbCl_3$ and red-emitting $CsPbI_3$ QDs (**Figure 3.9a**) with their PL peak positions blue-shifted to 427 nm and red-shifted to 700 nm, respectively (**Figure 3.9b**). The anion exchange process was proceeded by first dissolving zinc halide (ZnX_2) in methanol, followed by dropping the solution into as-synthesized PS-capped $CsPbBr_3$ QD solution (**Figure 3.9c**). Notably, as polar solvents such as methanol is known to be detrimental to perovskites, a control experiment was conducted in which the same amount of ZnI_2 in two different volumes of methanol was added. The results showed that small amounts of methanol (≤ 60 μl) did not have any effect in changing the PL peak position, signifying the reliability of anion exchange in fine-tuning the composition of PS-capped perovskite QDs (**Figure 3.10**). Subsequently, the overall iodide amount dropped into the QD solution was controlled to modulate the PL peak position while the methanol amount was kept constant. As more iodide was added into the QD solution, a steady red-shift in the PL peak position was observed (**Figure 3.11**). To verify the reproducibility of the anion exchange process, each anion exchange experiment was repeated once, and the results showed that for three different compositions, the PL spectra overlapped well between each trial (**Figure 3.12**).

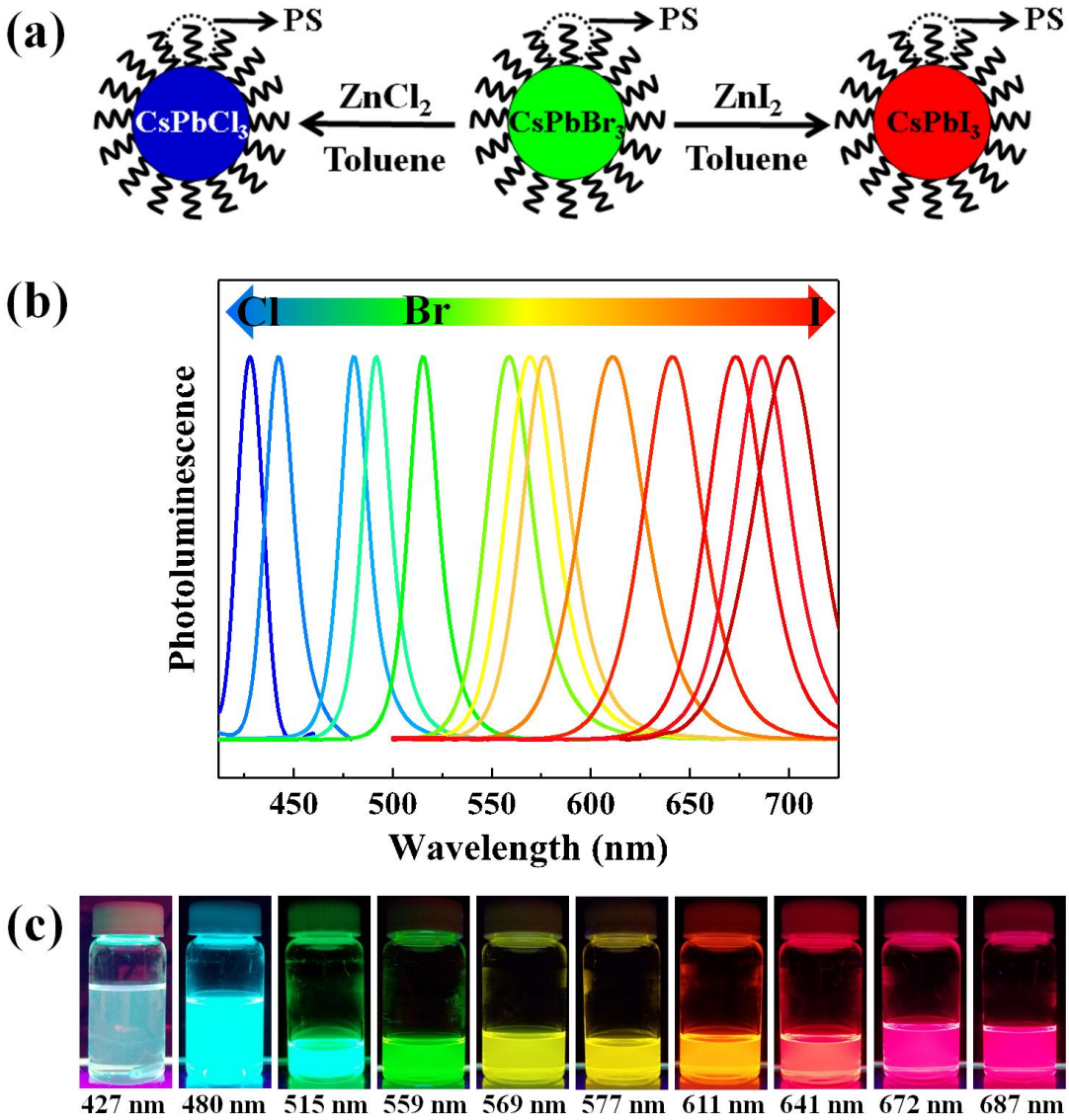

Figure 3.9 Control over optical properties of PS-capped perovskite $CsPbBr_3$ QDs crafted using star-like PAA-*b*-PS diblock copolymers (i.e., sample 5 in **Table 3.2**) as nanoreactors via anion exchange with zinc halide (i.e., $ZnCl_2$ and ZnI_2). (a) Schematic displaying synthetic route to PS-capped $CsPbCl_3$ QDs and PS-capped $CsPbI_3$ QDs via anion exchange with $ZnCl_2$ and ZnI_2, respectively. (b) Photoluminescence (PL) spectra and (c) digital images of a series of representative PS-capped perovskite QDs under UV excitation, where the contents of Cl and I in QDs are progressively varied, exhibiting systematic color change from green ($CsPbBr_3$) to blue ($CsPbCl_3$) as well as to red ($CsPbI_3$).

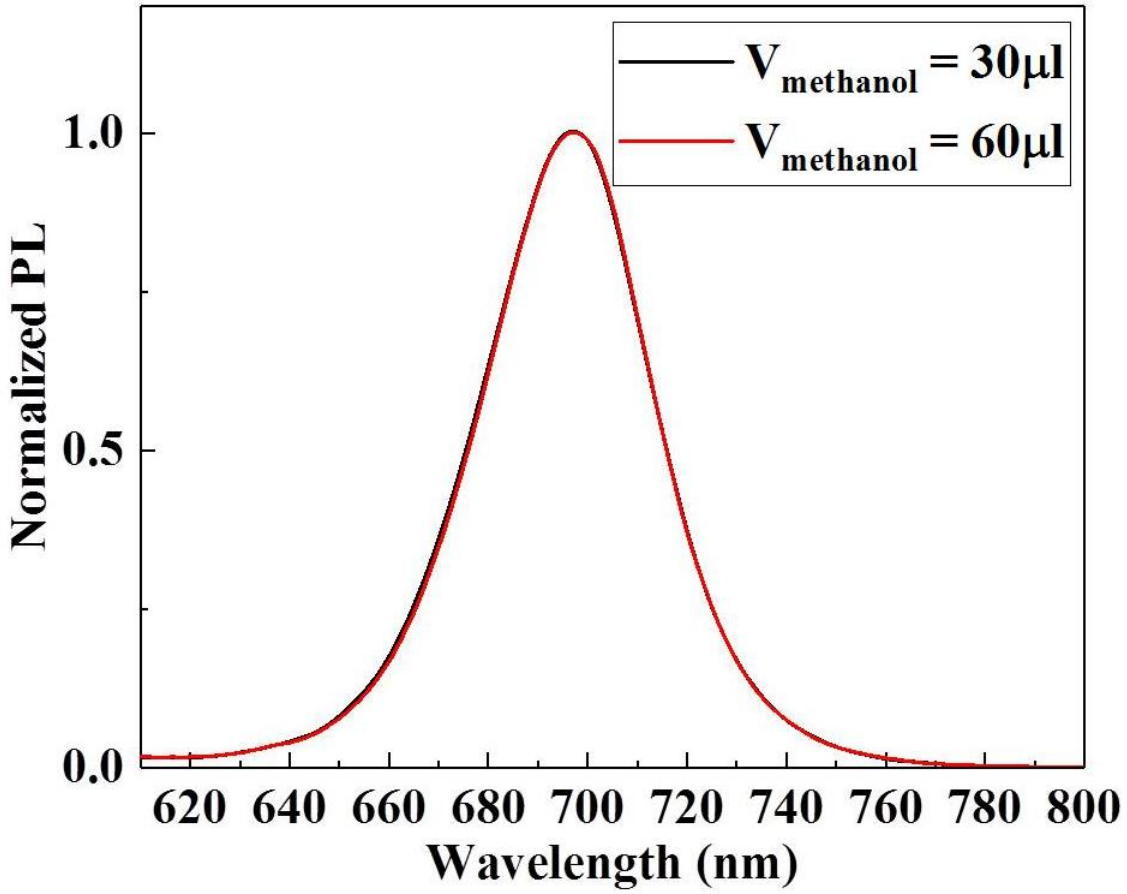

Figure 3.10 Effect of methanol during anion exchange of PS-capped perovskite $CsPb(Br_{0.10}I_{0.90})_3$ QDs on photoluminescence (PL).

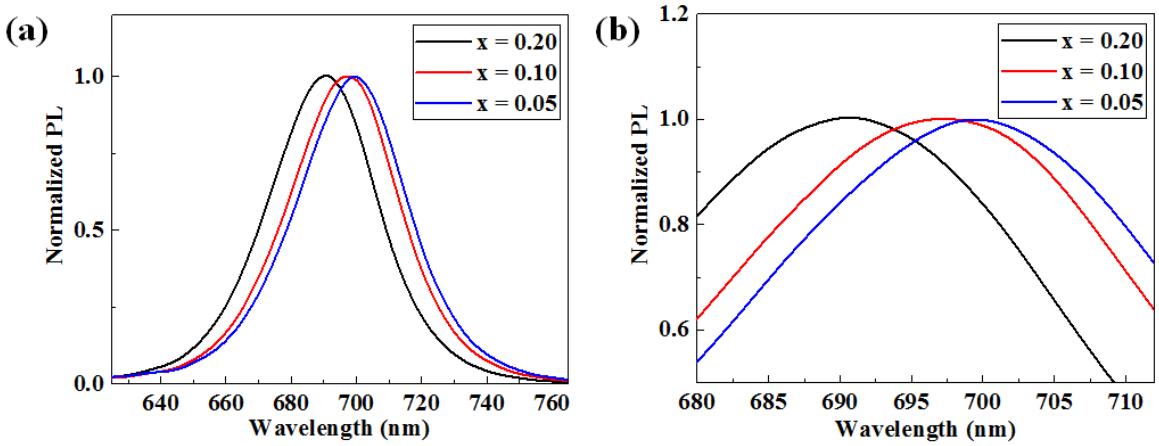

Figure 3.11 Anion exchange of PS-capped perovskite $CsPb(Br_xI_{1-x})_3$ QDs. Photoluminescence (PL) of $CsPb(Br_{0.20}I_{0.80})_3$, ($CsPb(Br_{0.10}I_{0.90})_3$, and $CsPb(Br_{0.05}I_{0.95})_3$ with the peak positions at 691.0 nm, 698.0 nm, and 700.0 nm, respectively. The average diameter of all these QDs is 13.9 nm.

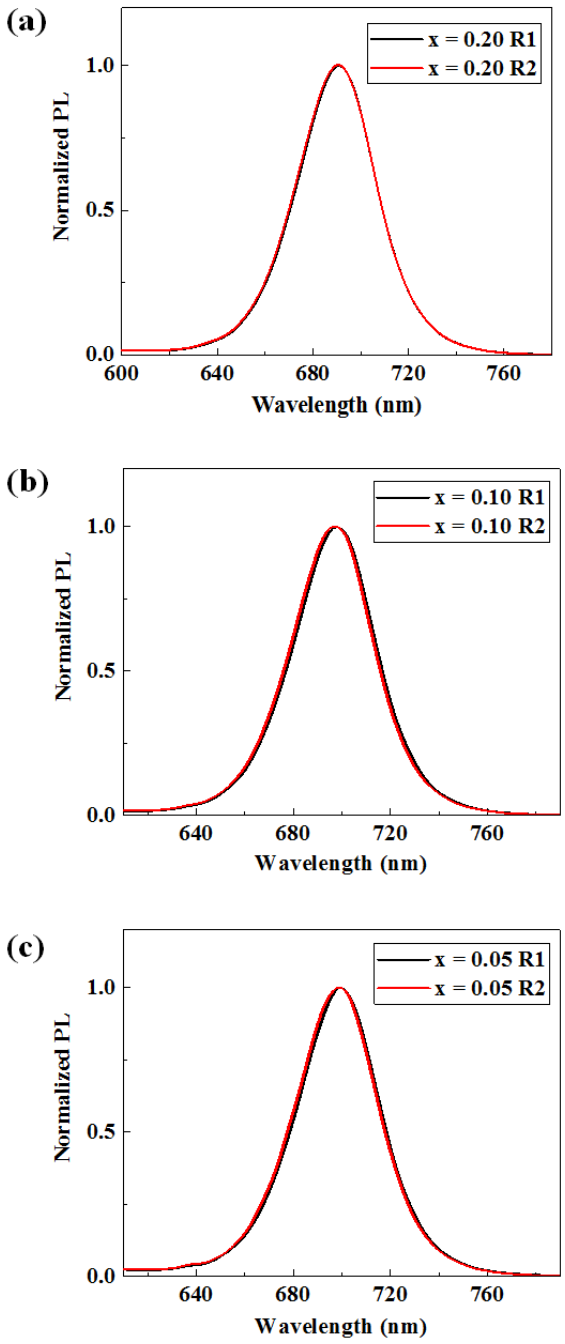

Figure 3.12 Reproducibility of anion exchange of PS-capped perovskite $CsPb(Br_xI_{1-x})_3$ QDs crafted by utilizing star-like PAA-*b*-PS diblock copolymers (i.e., sample 5 in **Table 3.2**) as nanoreactors. Abbreviation R stands for run. There are 2 runs total.

As ZnX_2 does not dissolve well in non-polar solvents such as toluene, there was a possibility that ZnX_2 in methanol can aggregate (i.e., precipitate) the PS-capped perovskite QDs during its addition to the QD toluene solution. However, TEM imaging on anion-exchanged PS-capped perovskite QDs shows that there was neither aggregation nor shape change of QDs caused by the anion exchange process (**Figure 3.13**), signifying that anion exchange via ZnX_2 is a viable approach for tailoring the PL emission wavelength for PS-capped perovskite QDs. The stability of anion-exchanged QDs was also confirmed by the retention of PL emission under UV excitation after storing the QD solution under ambient condition for 3 weeks, where no noticeable decrease in PL was found (**Figure 3.14**).

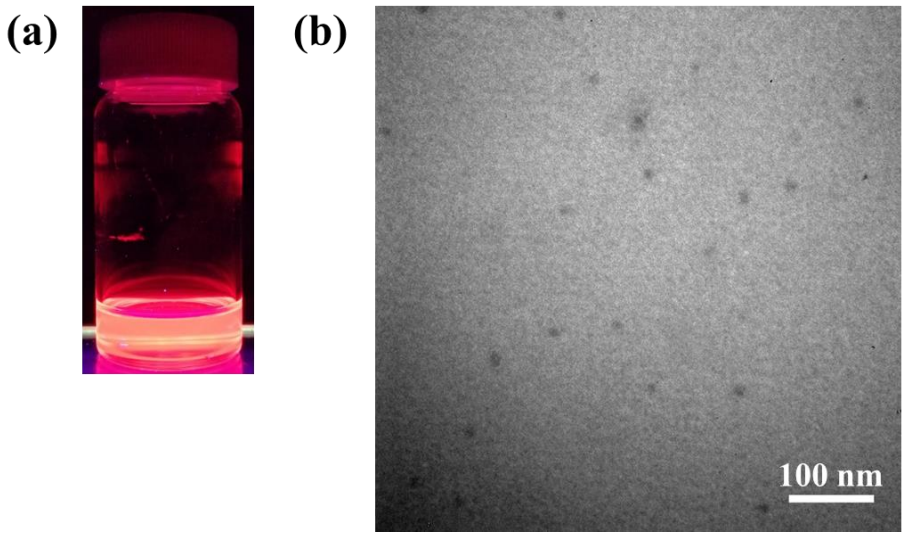

Figure 3.13 Anion-exchanged PS-capped perovskite QDs (i.e., $CsPb(Br_{0.40}I_{0.60})_3$). (a) Digital image of PS-capped perovskite QD solution under UV excitation. (b) TEM image of PS-capped perovskite QDs. The average diameter of QDs is $D = 14.2 \pm 0.8$ nm.

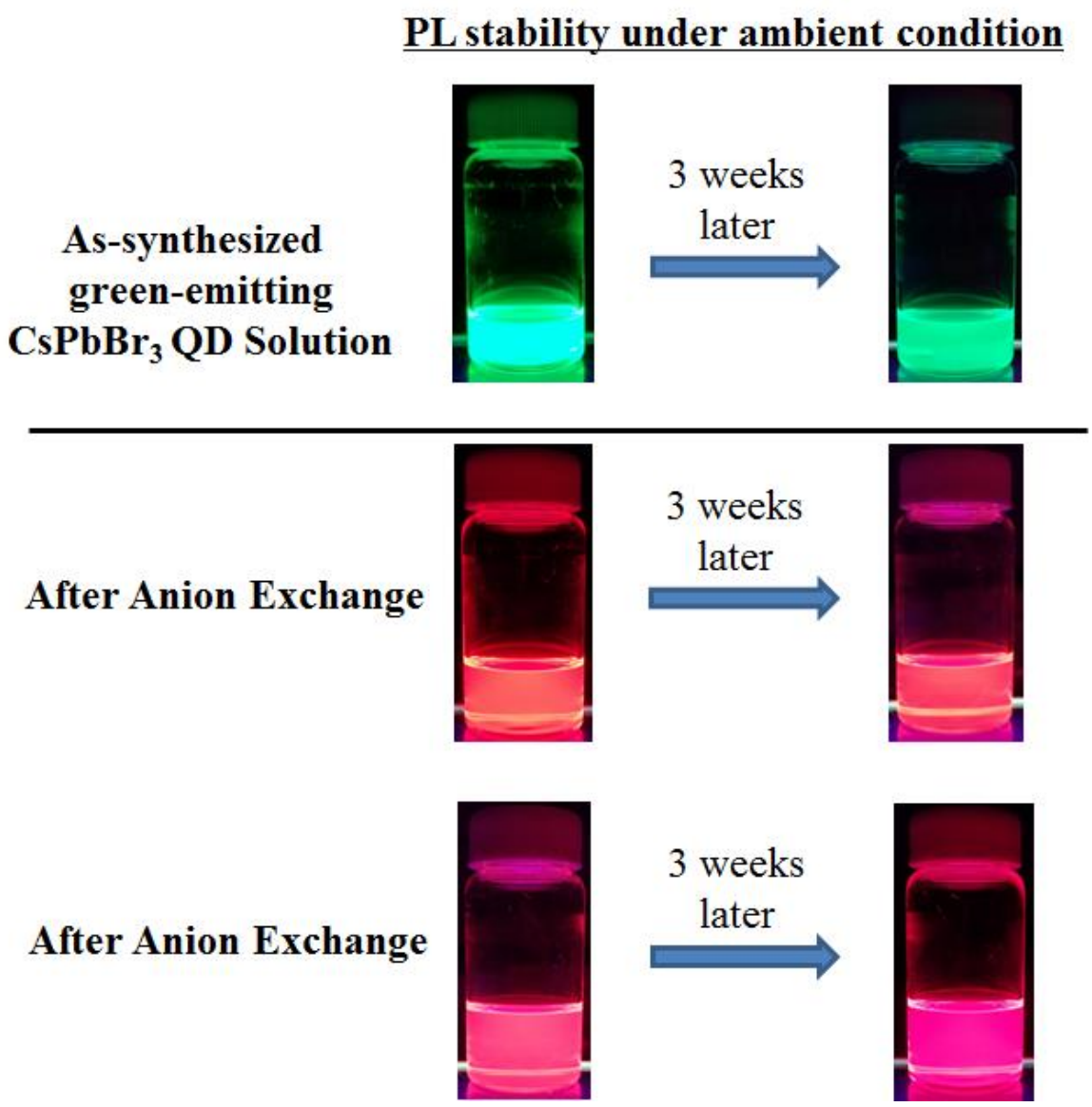

Figure 3.14 Digital images of anion-exchanged PS-capped red-emitting $CsPb(Br_{0.40}I_{0.60})_3$ QDs (central two panels) and red-emitting $CsPb(Br_{0.30}I_{0.70})_3$ (lower two panels) stored under ambient conditions (exposed to air but not light; stored at room temperature without stirring) for 3 weeks, demonstrating the outstanding stabilities of these PS-capped hairy QDs. The original green-emitting $CsPbBr_3$ QDs are shown on the upper two panels. The emission peaks for $CsPbBr_3$, $CsPb(Br_{0.40}I_{0.60})_3$, and $CsPb(Br_{0.30}I_{0.70})_3$ QDs are at 516 nm, 641 nm, and 673 nm, respectively.

In addition to the composition-dependent tuning of optical properties as noted above, remarkably, the star-like block copolymer nanoreactor strategy can also effectively alter the size of QDs to manipulate their optical properties. By synthesizing the star-like diblock copolymer with precisely controlled length (i.e., molecular weight) of each block and low polydispersity via ATRP, the size of perovskite QDs can be accurately regulated (**Figure 3.15**a, **Figure 3.16**, and **Table 3.3**), thereby rendering strict control over light harvesting and emission of QDs at desired wavelengths in the visible region (**Figure 3.15b-d**). The molecular weights and polydispersity index (PDI) of a series of star-like PAA-*b*-PS nanoreactors are summarized in **Table 3.1 and Table 3.2**. The size of the three PS-capped $CsPbBr_3$ QDs crafted are 8.6±0.3 nm, 10.1±0.6 nm, 13.9±0.7 nm, and their corresponding PL peaks are at 514 nm, 515 nm, and 516 nm, respectively (**Figure 3.15**). It is notable that as the sizes of these crafted QDs are above the Bohr diameter of $CsPbBr_3$ QD of 7 nm,[33] the PL peak position change is minimal. In contrast, for PS-capped $CsPb(Br_{0.1}I_{0.9})_3$ synthesized by partial anion exchange of $CsPbBr_3$ with ZnI_2 as descried above, which has a Bohr diameter of nearly 12 nm,[33] the PL peak positions are more distinctly apart at 685 nm, 695 nm, and 698 nm, respectively (**Figure 3.15c**), clearly displaying the quantum confinement effect (**Figure 3.15d**). All these PS-capped $CsPbBr_3$ QDs (D = 13.9 nm (**Figure 3.7**), 10.1 nm (**Figure 3.17**), and 8.6 nm (**Figure 3.18**)) are crystalline as revealed by HRTEM (lower panels in **Figure 3.15a**). The green-emitting PS-capped $CsPbBr_3$ QDs (D = 13.9 nm) exhibited a high PL quantum yield (QY) of 69% (**Figure 3.19**) and a FWHM as low as 17.7 nm. As the size of the PS-capped $CsPbBr_3$ QDs decreased, the QY decreased to 67% (D =10.1 nm) and 38% (D = 8.6 nm), which may be due to the higher weight fraction of PAA groups in smaller PS-capped $CsPbBr_3$ QDs

(**Figure 3.20**) and large surface-to-volume ratio of smaller-sized QDs that may possess higher density of surface defects.[92-93] It should be noted that despite the existence of PAA chains within $CsPbBr_3$ QDs and the lack of inorganic shell as in the core/shell QDs to reduce surface detects, the high QY observed in $CsPbBr_3$ QDs is due largely to the high defect-tolerance characteristic of perovskite material as a result of unique band structure and optical properties.[94] The valence band maximum (VBM) of perovskite is antibonding in nature and the conduction band minimum (CBM) is stabilized by strong spin−orbit coupling, as opposed to common II−VI and III−V QDs wherein VBM is constituted by bonding orbitals.[94]

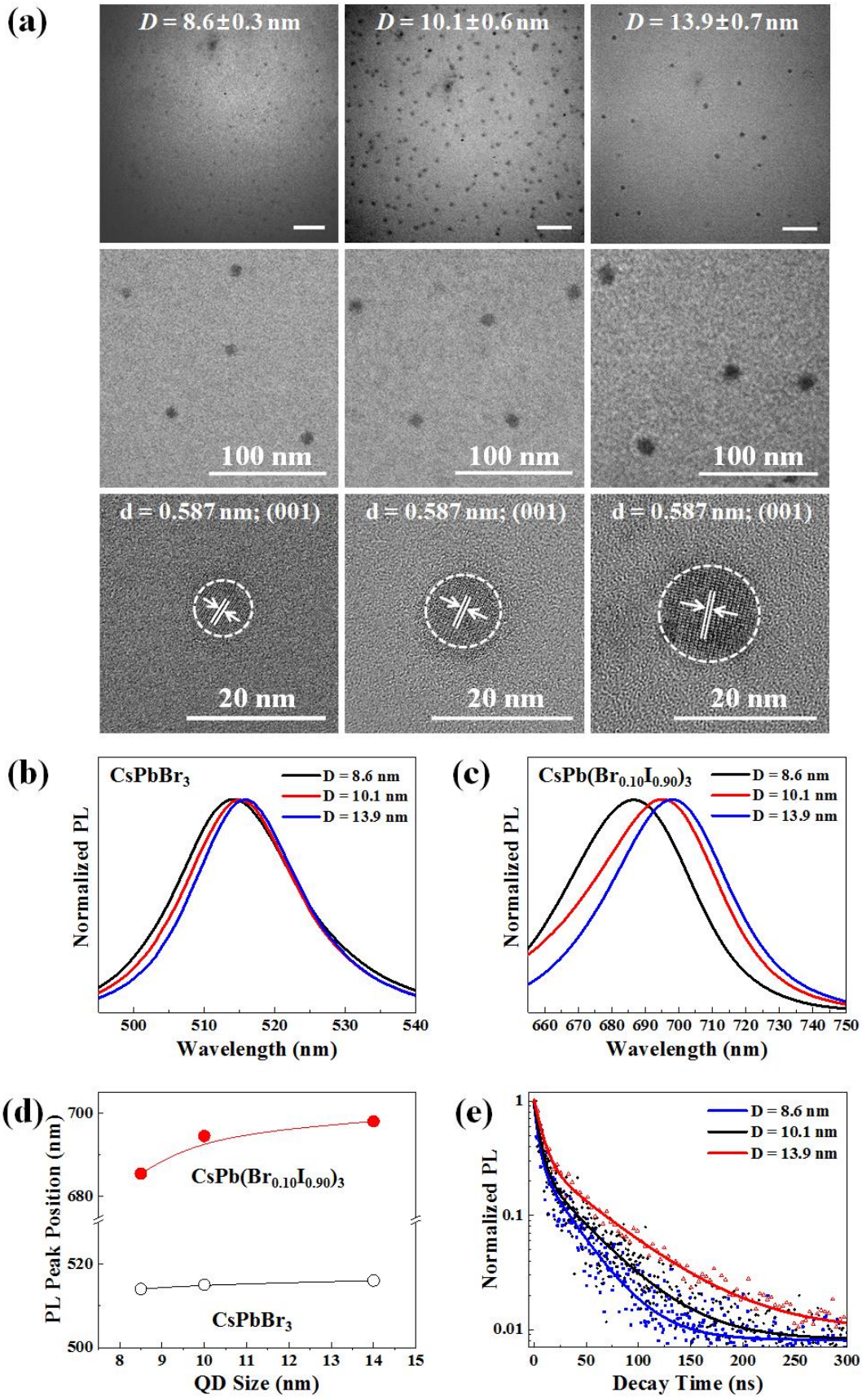
(a)
D = 8.6±0.3 nm
D = 10.1±0.6 nm
D = 13.9±0.7 nm
100 nm
100 nm
100 nm
d = 0.587 nm; (001)
d = 0.587 nm; (001)
d = 0.587 nm; (001)
20 nm
20 nm
20 nm
(b)
CsPbBr3
D = 8.6 nm
D = 10.1 nm
D = 13.9 nm
Normalized PL
500 510 520 530 540
Wavelength (nm)
(c)
CsPb(Br0.10I0.90)3
D = 8.6 nm
D = 10.1 nm
D = 13.9 nm
Normalized PL
660 670 680 690 700 710 720 730 740 750
Wavelength (nm)
(d)
PL Peak Position (nm)
700
680
520
500
CsPb(Br0.10I0.90)3
CsPbBr3
8 9 10 11 12 13 14 15
QD Size (nm)
(e)
D = 8.6 nm
D = 10.1 nm
D = 13.9 nm
Normalized PL
1
0.1
0.01
0 50 100 150 200 250 300
Decay Time (ns)

Figure 3.15 Size-dependent optical properties of PS-capped $CsPbX_3$ QDs. (a) TEM images of PS-capped $CsPbBr_3$ QDs of three different sizes. Column 1: D = 8.6±0.3 nm; crafted using sample 1 in **Table 3.2**). Column 2: D = 10.1±0.6 nm, crafted using sample 3 in **Table 3.2**. Column 3: D = 13.9±0.7 nm; crafted using sample 5 in **Table 3.2**. The corresponding HRTEM images are shown in the last row, where the (001) plane has a lattice spacing d of 0.587 nm. (b) PL spectra of green-emitting PS-capped $CsPbBr_3$ QDs of three different sizes. (c) PL spectra of red-emitting PS-capped $CsPb(Br_{0.1}I_{0.9})_3$ QDs of three different sizes. (d) Effect of QD size on the PL peak position. Open circle: PS-capped $CsPbBr_3$ QDs. Solid circle: PS-capped $CsPb(Br_{0.1}I_{0.9})_3$ QDs. (e) Time-resolved photoluminescence (TRPL) spectroscopy of PS-capped $CsPbBr_3$ QDs of three different sizes.

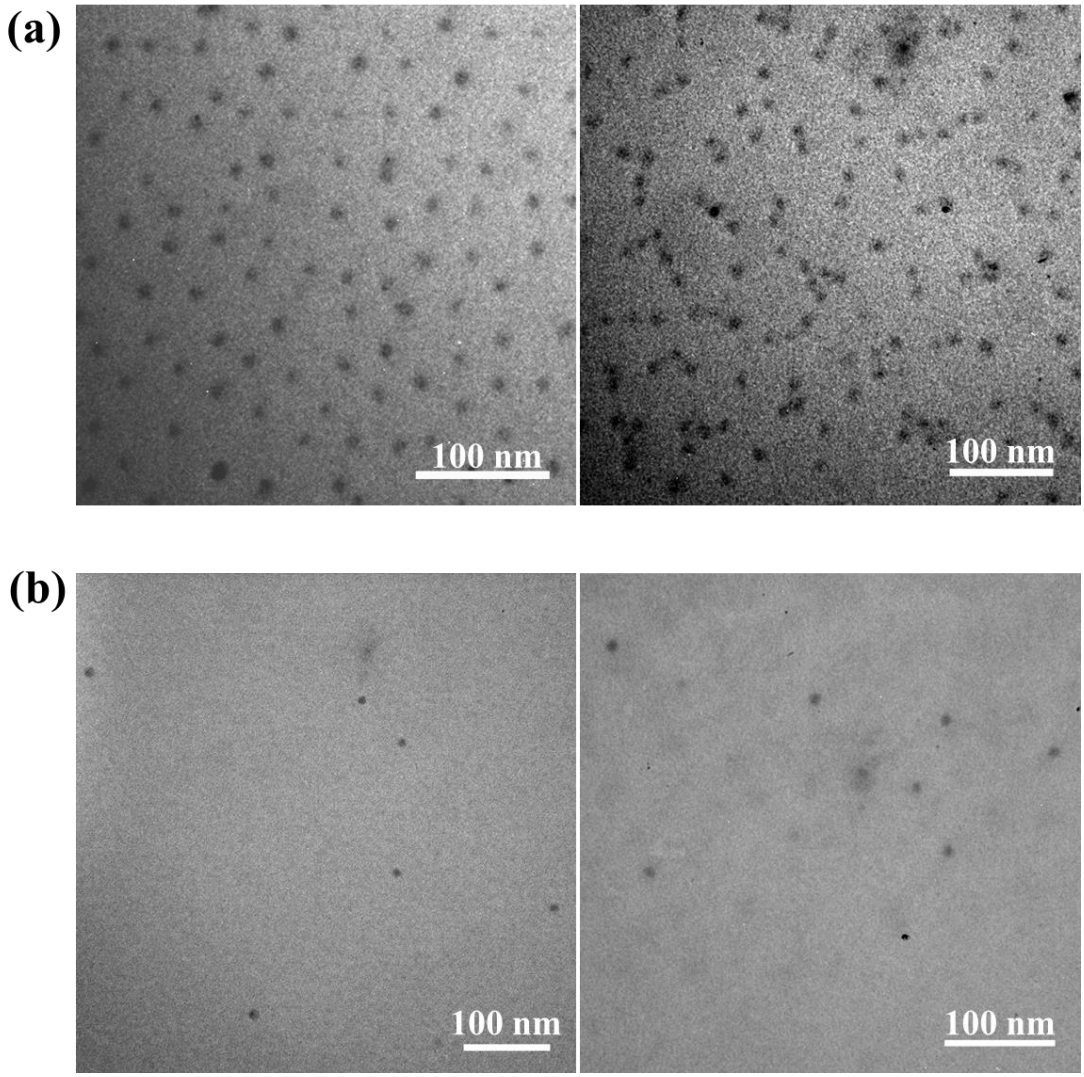

Figure 3.16 PS-capped perovskite $CsPbBr_3$ QDs of different sizes under different magnifications. (a) D = 10.1 nm and (b) D = 8.6 nm crafted by capitalizing on star-like PAA-*b*-PS diblock copolymers (i.e., sample 3 for (a) and sample 1 for (b) in **Table 3.2**) as nanoreactors.

Table 3.3 Calculated radius of gyration of star-like PAA homopolymers.

Nanoreactor[a]	M_n of each PAA arm[b]	R_g of Star-like PAA[c]	Diameter of PS-capped $CsPbBr_3$ QDs[d]
Star-like PAA; sample 1	5.1 kg/mol	4.04 nm	8.6 nm
Star-like PAA; sample 2	7.8 kg/mol	5.00 nm	10.1 nm
Star-like PAA; sample 3	11.0 kg/mol	5.93 nm	13.9 nm

Notes:

[a] Refer to **Table 3.1** & **Table 3.2** for details

[b] M_n of each PAA block (arm) calculated from ^{1}H-NMR.

[c] Radius of gyration, R_g of star-like PAA calculated based on the following equation:[95]

$$< R_g^2 >= \frac{Nb^2}{6}\left(\frac{3-2/f}{f}\right)$$

where N is the degree of polymerization of star-like PAA homopolymer calculated from M_n in **Table 3.2**, f is the number of arms, and b is the Kuhn length (~0.69 nm for PAA).[96]

[d] PS-capped QDs were synthesized using the corresponding star-like PAA-*b*-PS nanoreactors (D = 8.6 nm – star-like PAA-*b*-PS, **sample 1**; D =10.1 nm – star-like PAA-*b*-PS, **sample 3**; 13.9 nm – star-like PAA-*b*-PS, **sample 5**)

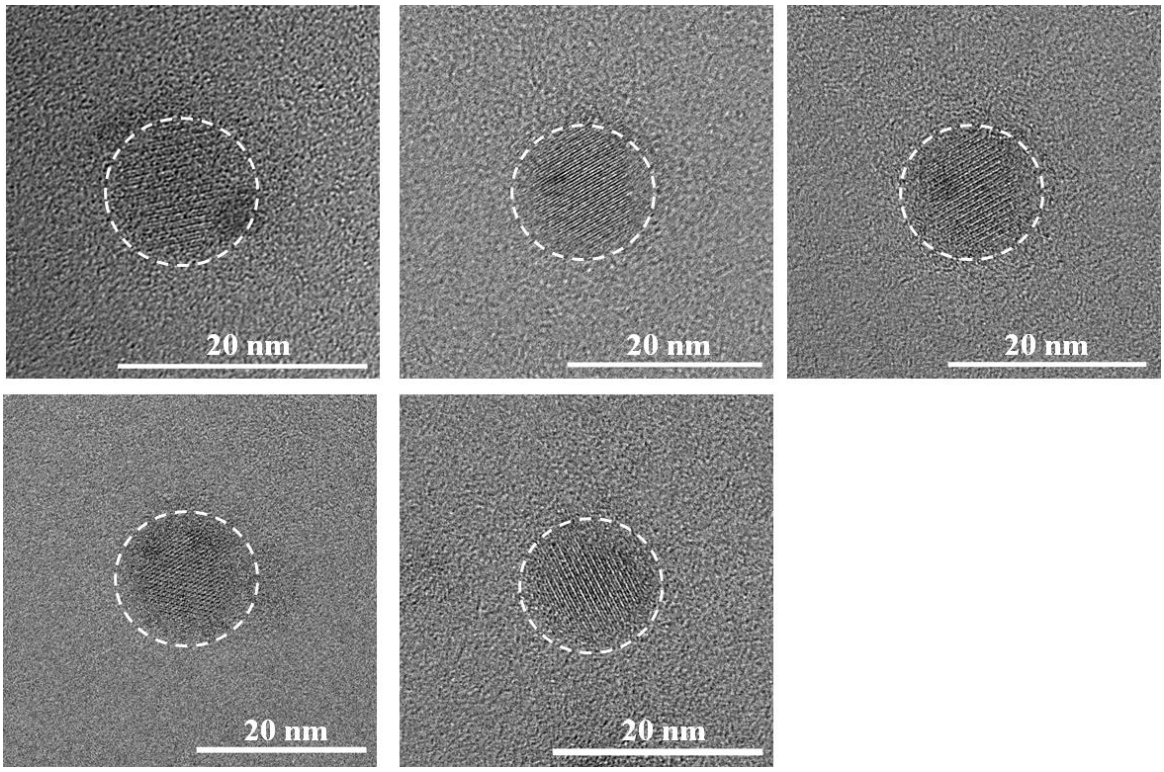

Figure 3.17 HRTEM image of five individual PS-capped perovskite $CsPbBr_3$ QD (D = 10.1 nm), revealing crystal lattices. The QDs were crafted by employing star-like PAA-*b*-PS diblock copolymers (i.e., sample 3 in **Table 3.2**) as nanoreactors.

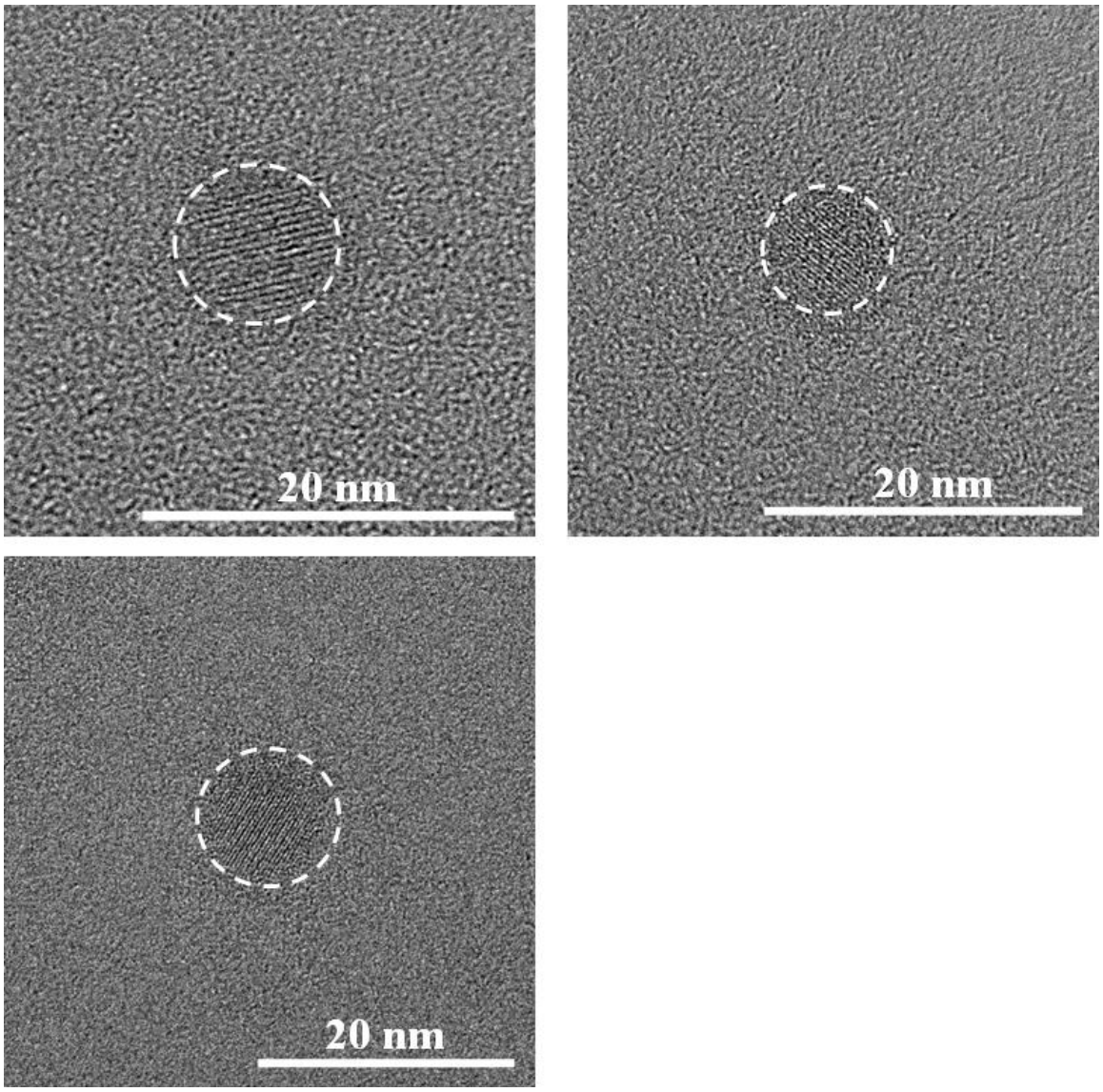

Figure 3.18 HRTEM image of three individual PS-capped perovskite $CsPbBr_3$ QD (D = 8.6 nm), revealing crystal lattices. The QDs were crafted utilizing star-like PAA-*b*-PS diblock copolymers (i.e., sample 1 in **Table 3.2**) as nanoreactors.

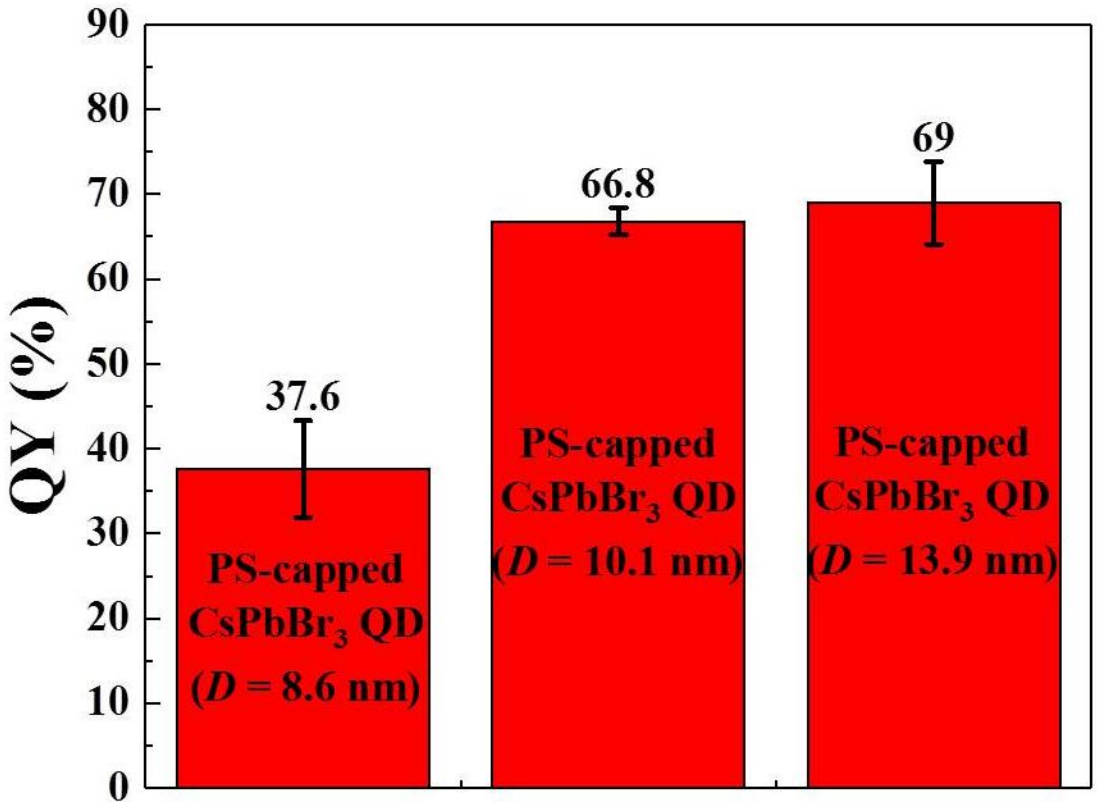

Figure 3.19 Quantum yields (QY) of $CsPbBr_3$ QDs of different sizes intimately and permanently capped by different length of PS chains.

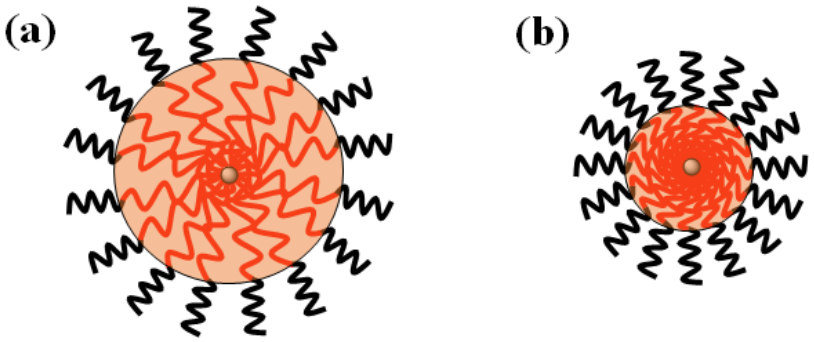

Diameter of PS-capped $CsPbBr_3$ QD	Weight Ratio of PAA in $CsPbBr_3$ QD
8.6 nm	9.9 wt%
10.1 nm	9.2 wt%
13.9 nm	5.2 wt%

Figure 3.20 Weight ratios of PAA blocks within PS-capped $CsPbBr_3$ QD of different sizes. The length of PS chains is identical in (a) and (b).

To further corroborate the effectiveness of star-like nanoreactors in fine-tuning QD size through the precise tailoring of the inner PAA block length, the characteristic time-resolved PL (TRPL) decay lifetime as a function of QD size was also measured (see *Experimental Section*; **Figure 3.15e** and **Table 3.4**). The TRPL decay curves were best-fit using a biexponential decay function:

$$A(t) = A_1 exp\left(-\frac{t}{\tau_1}\right) + A_2 exp\left(-\frac{t}{\tau_2}\right)$$

where A, A_1, and A_2 are constants; t is time; τ_1 and τ_2 are PL decay lifetimes.[97-98] For better comparison between each sample, the average PL decay lifetime was calculated using the following equation:

$$\tau_{avg} = \frac{A_1\tau_1^2 + A_2\tau_2^2}{A_1\tau_1 + A_2\tau_2}$$

The PS-capped $CsPbBr_3$ QDs of different sizes exhibited the average TRPL decay lifetimes of 21.5 ns (D = 8.6 nm), 28.7 ns (D = 10.1 nm), and 44.5 ns (D = 13.9 nm), which agrees well with the reported results in which the increase of QD size leads to the longer lifetimes (i.e., reduced recombination) due to the decreased overlap between the electron and hole wave functions.[98]

Table 3.4 Summary of time-resolved PL (TRPL) decay measurements, where the lifetimes of PS-capped $CsPbBr_3$ QDs in toluene solution can be derived.

Diameter of PS-capped $CsPbBr_3$ QDs	τ_1 **(ns)**	τ_2 **(ns)**	τ_{avg} **(ns)**
8.6 nm	4.2±0.3	30.6±1.9	21.5
10.1 nm	5.6±0.4	42.5±4.3	28.7
13.9 nm	7.6±0.5	57.6±4.6	44.5

Figure 3.21a-b clearly displays the robustness of the PS shell in protecting the $CsPbBr_3$ QDs from degradation by water. Intriguingly, by increasing the molecular weight (i.e., chain length) of PS blocks, the water stability of PS-capped QDs increased by 33% from 36.3±5.7 min for PS(7k)-capped $CsPbBr_3$ QDs (D = 13.9 nm) to 48.3±0.6 min for PS(16k)-capped $CsPbBr_3$ QD (D = 13.9 nm) (**Figure 3.21b**; see *Experimental Section*). More interestingly, by decreasing the QD size from 13.9 nm to 8.6 nm while keeping the PS length constant (i.e., $M_{n,\,PS}$ = 16 kg/mol), the water stability increased by 28%, that is, from 48.3±0.6 min for PS(16k)-capped $CsPbBr_3$ QDs (D = 13.9 nm) to 61.7±3.2 min for

PS(16k)-capped $CsPbBr_3$ QD (D = 8.6 nm) (**Figure 3.21b**). Remarkably, in stark contrast to $CsPbBr_3$ QDs synthesized via conventional ligand-assisted co-precipitation methods either capped by oleic acid (2.8±0.3 min) or co-capped by oleic acid and oleyl amine (5.0±0.5 min) (**Figure 3.21b**), the water stability of PS-capped $CsPbBr_3$ QDs was up to 20 times longer. We note that for the oleic acid- & oleyl amine-co-capped $CsPbBr_3$ QDs, an additional image was taken after removing the stir bar as the QDs formed a thin layer of film on the stir bar which maintained PL for a longer duration than the QDs in toluene.

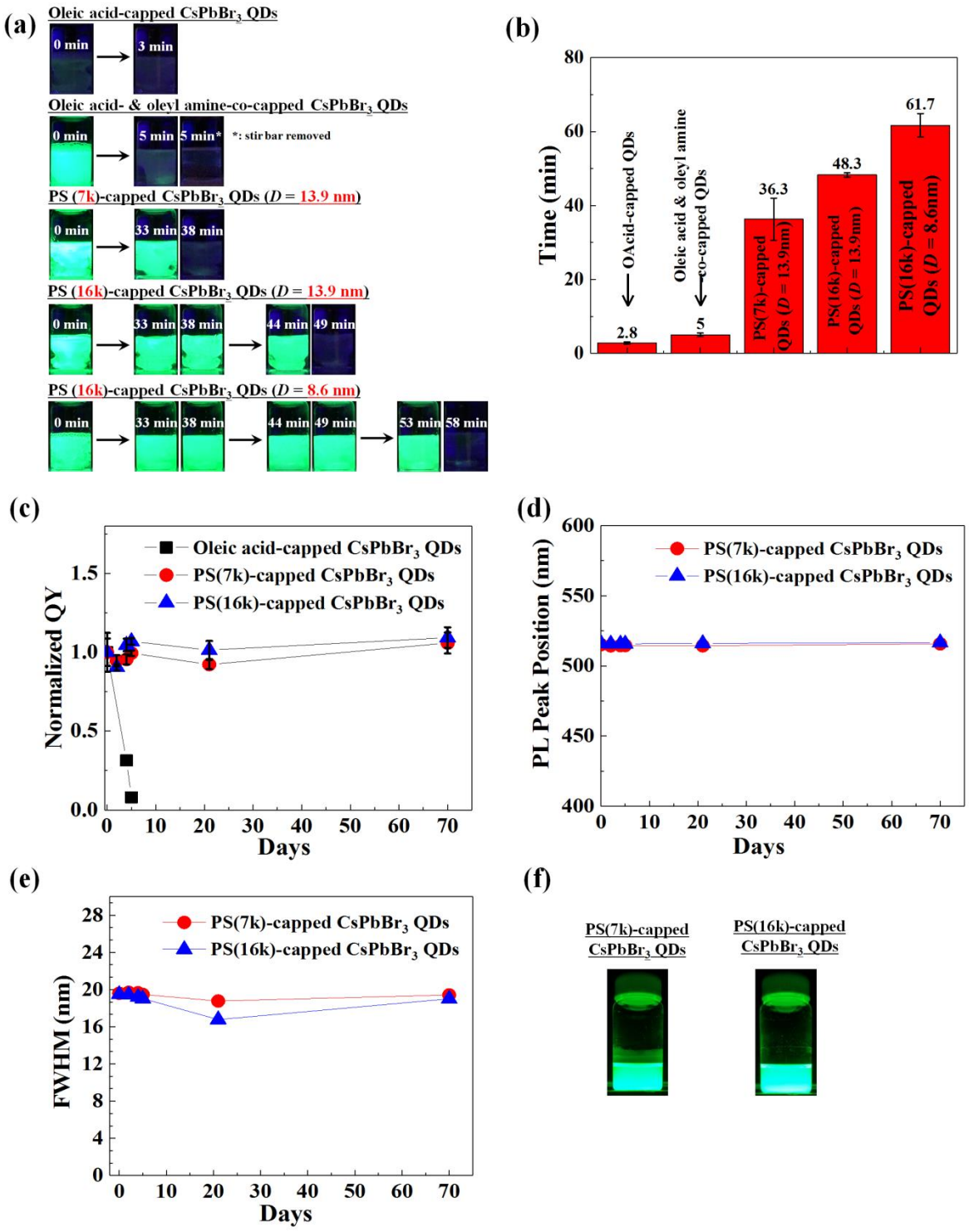

Figure 3.21 (a-b) Water stability of PS-capped $CsPbBr_3$ QDs. (a) Representative digital images, depicting water stability of $CsPbBr_3$ QDs. The QDs are under UV excitation. The far-right column of each row is the image taken immediately after the sharp and complete

disappearance of PL emission. PS(7k)-capped $CsPbBr_3$ QDs (D = 13.9 nm), PS(16k)-capped $CsPbBr_3$ QDs (D = 13.9 nm), and PS(16k)-capped $CsPbBr_3$ QDs (D = 8.6 nm) are crafted using sample 5, sample 6, and sample 2, respectively, in **Table 3.2** as nanoreactors. (b) Bar graph depicting an average duration of PL emission under constant UV excitation after QDs are exposed to water. The average time was calculated after running each experiment for 5 times. The time for each run is recorded immediately after the complete diminishing of PL emission. (c-f) Colloidal stability of PS-capped PS(7k)-capped and PS(16k)-capped $CsPbBr_3$ QDs crafted using sample 5 and 6, respectively, in **Table 3.2** as nanoreactors. (c) Quantum yield (QY) of PS-capped $CsPbBr_3$ QDs over 70 days. Oleic acid-capped $CsPbBr_3$ QDs synthesized via hot injection (see *Experimental Section*) was used as control. (d) PL peak position of PS-capped $CsPbBr_3$ QDs over 70 days. (e) FWHM of PS-capped $CsPbBr_3$ QDs over 70 days. (e) PS-capped $CsPbBr_3$ QD toluene solution under UV excitation after 12-month storage under ambient condition (i.e., exposed to air and light at room temperature without stirring).

It is not surprising that PS-capped $CsPbBr_3$ QDs also exhibited superior colloidal stability when stored in toluene (**Figure 3.21c**). The permanently ligated PS chains on the perovskite QD surface are well dissolved in good solvent, toluene, leading to excellent dispersion of PS-capped $CsPbBr_3$ QDs without aggregation. The QY of PS-capped $CsPbBr_3$ QD in toluene solution was maintained for more than 2 months without any decrease (see *Experimental Section*; **Figure 3.21c**). It is also notable that there was no significant shift in the PL peak position as well as the FWHM (**Figure 3.21d-e**), signifying minimal or no change in the size distribution of QDs over the 2-month period. In sharp contrast, oleic acid-capped $CsPbBr_3$ QDs (see *Experimental Section*; oleic acid-capped $CsPbBr_3$ QDs prepared via a hot-injection method) displayed a PL peak shoulder and a 22% increase in FWHM of PL spectrum only after 24 h storage under ambient conditions

(i.e., exposed to air and light at room temperature without stirring) (**Figure 3.22**). **Figure 3.21f** shows two representative highly luminescent PS-capped $CsPbBr_3$ QDs in toluene even after 12 months of storage under the same ambient condition as noted above.

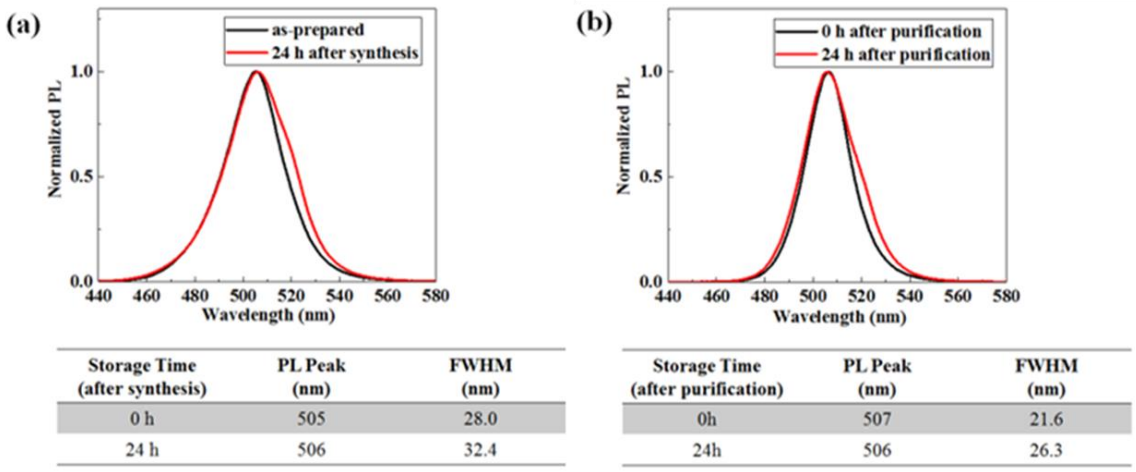

Storage Time (after synthesis)	PL Peak (nm)	FWHM (nm)
0 h	505	28.0
24 h	506	32.4

Storage Time (after purification)	PL Peak (nm)	FWHM (nm)
0h	507	21.6
24h	506	26.3

Figure 3.22 Instability of conventional oleic acid-capped $CsPbBr_3$ QDs synthesized via hot injection method. (a) PL of oleic acid-capped $CsPbBr_3$ QDs without any purification. (b) PL of oleic acid-capped $CsPbBr_3$ QDs with purification using acetone as precipitant. All QD solutions stored under ambient conditions (exposed to air and light; stored at room temperature without stirring).

The markedly improved colloidal and water stabilities of PS-capped QDs can be rationalized as follows. As toluene is a good solvent for PS, the intimately and permanently tethered PS chains on the perovskite QD surface are fully extended as a result of favorable interaction between toluene and PS, yielding excellent colloidal stability. However, when water is introduced, the hydrophobic PS chains collapse onto the perovskite QD due to the poor solubility of PS in water. The collapsed PS chain forms a PS shell surrounding the perovskite QD surface, thereby preventing water from reaching and degrading the

perovskite QD due to its ionic nature (**Figure 3.23b-d**). It is worth noting that the longer PS chains (16k PS (**Figure 3.23c)** compared to 7k PS (**Figure 3.23b)**) impart the denser hydrophobic PS shell situated on the perovskite QD surface and thus further effectively blocks the water penetration through the shell, leading to enhanced stability against water (**Figure 3.21a-b**). As the size of QDs capped with the same length of PS chains decreases (13.9-nm compared to 8.6-nm $CsPbBr_3$ QDs capped by 16k PS chains), the surface of QD is further adequately covered by PS, resulting in progressively improved water stability (**Figure 3.23d** and **Figure 3.21a-b**). Clearly, each PS-capped $CsPbBr_3$ QD, for the first time, possesses a separate protective shell that can be precisely tailored to any desired length (or thickness when in contact with water). In contrast to PS-capped $CsPbBr_3$ QDs, due to the weak coordination bonding between small-molecule ligands (e.g., oleic acid & oleyl amine) and QDs, these ligands collapsed on the $CsPbBr_3$ QD surface upon the addition of water would dissociate from the QD surface. Consequently, water contacts the exposed surface of QDs, causing their decomposition into precursors and the diminishing of fluorescence (**Figure 3.23a**).

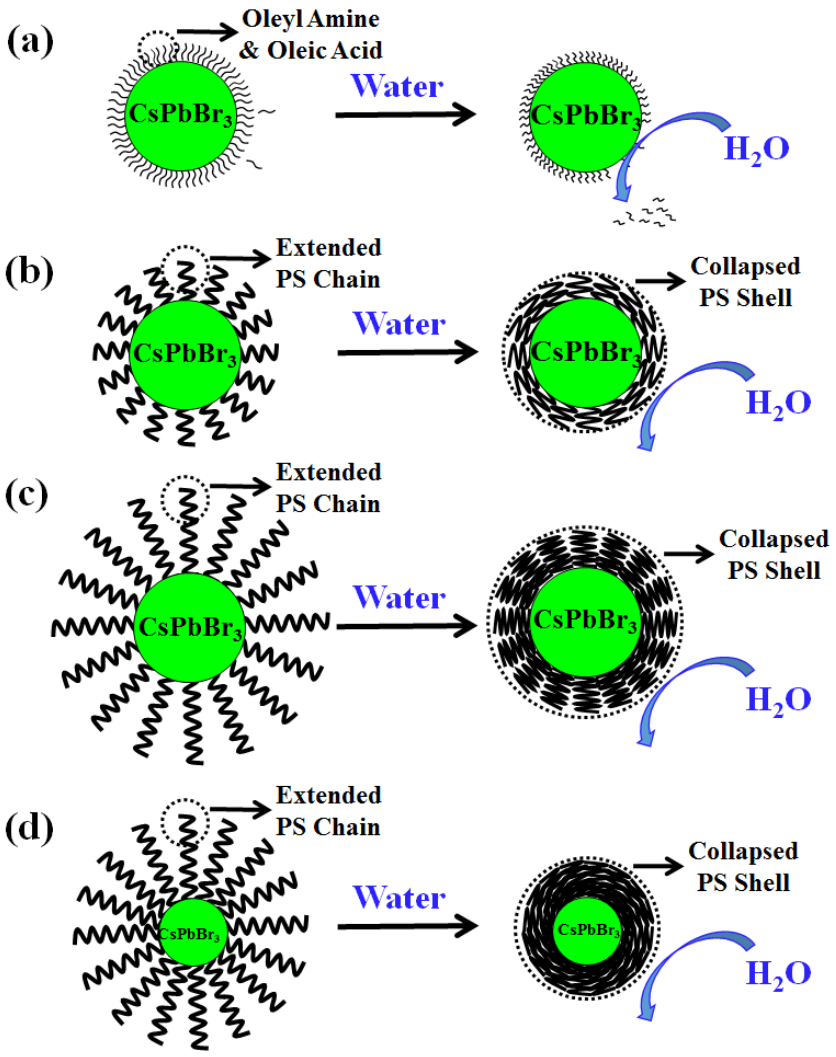

Figure 3.23 Schematic illustration of PS-capped QDs with varied QD sizes and length of PS chains for markedly improved colloidal and water stabilities. (a) Linear ligand (oleyl amine & oleic acid) loss from the perovskite QD surface upon water exposure in oleyl amine- & oleic acid-co-capped $CsPbBr_3$ QDs. (b-d) Polystyrene chains collapse onto the perovskite QD surface upon water exposure. (b) Permanently-grafted PS(7k) forms a layer of PS shell around $CsPbBr_3$ QD (D = 13.9 nm; PS(7k)-capped $CsPbBr_3$ QDs are synthesized using sample 5 in **Table 3.2**). (c) Permanently-tethered PS(16k) forms a layer of denser PS shell on the surface of $CsPbBr_3$ QD (D =13.9 nm; PS(16k)-capped $CsPbBr_3$ QDs are crafted using sample 6 in **Table 3.2**). (d) Permanently-capped PS(16k) forms a

layer of even denser PS shell situated on smaller-sized $CsPbBr_3$ QDs (D = 8.6 nm; PS(16k)-capped $CsPbBr_3$ QDs are yielded using sample 2 in **Table 3.2**)

Due to their high QY, narrow FWHM, size- and composition-dependent emission tunability, and solution processability,[99] perovskite QDs represent next-generation materials for use in display and solid-state lighting. In this context, as as-synthesized PS-capped perovskite QDs show good optical properties, their potential application in white light emitting diode (WLED) was demonstrated (**Figure 3.24**). A WLED prototype was fabricated by placing a composite of green-emitting PS-capped $CsPbBr_3$ QDs, red-emitting $CdSe/Cd_{1-x}Zn_xSe_{1-y}S_y/ZnS$ QDs synthesized according to our previous work,[100] and poly(methyl methacrylate) (PMMA) onto a blue-emitting GaN chip. **Figure 3.24a** presents the PL spectra of the WLED device with three distinct peaks from the GaN blue-chip (blue), PS-capped $CsPbBr_3$ QDs (green), and $CdSe/Cd_{1-x}Zn_xSe_{1-y}S_y/ZnS$ QDs (red),[100] respectively. A digital image of an actual WLED device emitting white light is shown as an inset. **Figure 3.24b** displays the Commission Internationale de L'Eclairage (CIE) diagram. The WLED prototype containing the PS-capped $CsPbBr_3$ QDs has a color coordinate of (0.31, 0.32), which is very close to the white color coordinate of (0.33, 0.33). The color gamut of PS-capped $CsPbBr_3$ QD-based WLED is 116% over that of national television system committee (NTSC) and 163% over that of standard red green blue (sRGB) standards (**Figure 3.25**).

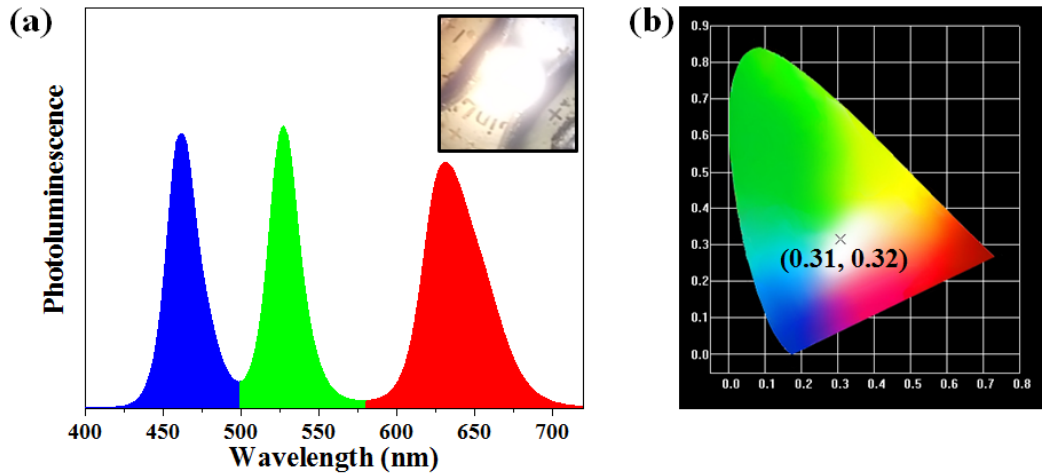

Figure 3.24 PS-capped $CsPbBr_3$ QD-based white light emitting diode (WLED). (a) PL spectra of PS-capped $CsPbBr_3$ QD-based WLED device operated at a current of 30 mA. Inset shows a digital image of the WLED device. (b) CIE color diagram of the WLED device. The "x" label indicates the color coordinate for the WLED device operated at 30 mA.

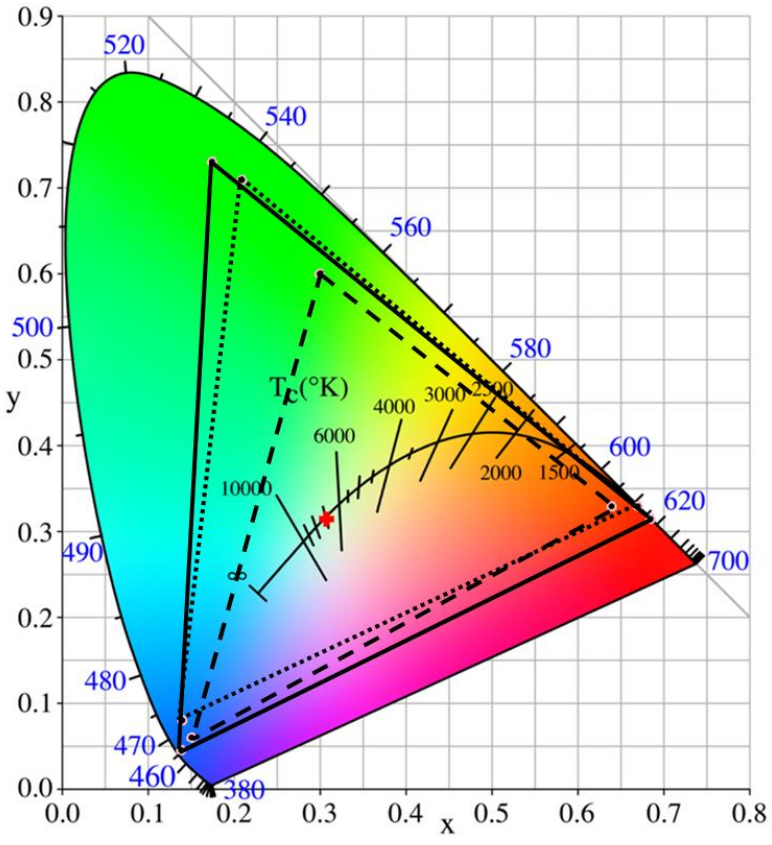

Coordinates for Color Triangle in This Study	X	Y
Red	0.685	0.315
Green	0.175	0.731
Blue	0.139	0.045

Figure 3.25 LED color gamut. Solid line: PS-capped perovskite QD-based LED; dotted line: NTSC standard; and dashed line: sRGB standard. We note that the comparison between our color triangle and standard color triangles (i.e., NTSC and sRGB) is performed by comparing the area of the color triangles. The color coordinates for the color triangle in our study is obtained from the PL spectrum, depending on the wavelength position and FWHM of PL.

3.1.3 Conclusion

In summary, we demonstrated the precision synthesis of perovskite QDs with varied sizes and compositions permanently anchored by hydrophobic polymer chains via capitalizing on judiciously designed amphiphilic star-like diblock copolymers as nanoreactors. The polymer nanoreactors are synthesized via sequential ATRP of *t*BA and St from a macroinitiator with multiple activation sites, yielding star-like P*t*BA-*b*-PS, followed by hydrolysis of the inner P*t*BA blocks. Due to living free radical polymerization characteristic, ATRP entails the synthesis of star-like diblock copolymer with well-controlled molecular weight and low PDI of each block. Consequently, the size of PS-capped perovskite $CsPbX_3$ QDs, formed via strong coordination interaction of perovskite precursors with the inner hydrophilic PAA blocks of star-like PAA-*b*-PS, can be precisely tailored, thereby offering delicate control over absorption and emission of $CsPbX_3$ QDs . Green-emitting PS-capped $CsPbBr_3$ QDs crafted exhibit high PL QY of 69% and low FWHM of 17.7 nm. Notably, subsequent anion exchange of the halide group renders a series of effective tuning of emission of PS-capped QDs from 427 nm (blue) to 700 nm (red). It is important to note that each PS-capped $CsPbX_3$ QD, for the first time, carries a layer of protective hydrophobic PS chains that can be readily regulated to any desired length during the ATRP of St monomers. Such permanently ligated length-tunable PS shell on the $CsPbX_3$ surface affords strikingly improved water and colloidal stabilities in harsh environment (e.g., deliberately added water) that is often not experienced under regular operating condition. When directly exposed to water, the PS chains collapse onto the perovskite QD due to its poor solubility in water, forming a dense PS cushion on the perovskite QD surface and thus greatly preventing water from reaching and dissolving the

perovskite QD. In striking contrast to $CsPbBr_3$ QDs synthesized via conventional ligand-assisted approaches, PS-capped $CsPbBr_3$ QDs impart a twentyfold improvement in water stability. In addition, PS-capped $CsPbBr_3$ QDs also manifest superior colloidal stability when stocked in toluene while exposing to air under constant ambient light at room temperature without stirring. This can be attributed to the fact that the perovskite QDs are intimately and stably ligated by PS chains that are fully extended in good solvent toluene. As a result, PS-capped $CsPbBr_3$ QDs demonstrate excellent colloidal stability for more than 2 months with no change in QY, PL peak position, and FWHM. WLED constructed using hairy perovskite QDs demonstrates 116% and 163% color gamut over NTSC and sRGB standards, respectively.

The PS-tethered perovskite QDs may facilitate uniform dispersion in PS or PS-containing polymer matrix, thus reducing or virtually eliminating enthalpic interactions of hairy perovskite QDs with host matrix for uniform perovskite QDs/polymer nanocomposites. Furthermore, by properly controlling the PS chain to an optimal length, homogenous films of PS-capped perovskite QDs (i.e., stand-alone hairy QD films) may be achieved, dispensing with the need for host polymer matrix. The PS-capped perovskite QDs nanocomposite films with easily tunable perovskite QDs to polymer ratio noted above may exhibit amplified stimulated emission in lasing applications where the QD loading is of key importance, in addition to stability. Moreover, large-sized PS-capped perovskite QD-containing nanocomposites can also be exploited in creating nanocomposite scintillators for spectroscopic gamma-ray detection and/or X-ray imaging where high QD loading is favorable.[97] To further improve the scintillator performance, organic scintillator molecules can be mixed into the PS matrix to shift the emission to longer wavelength and

thus reduce self-absorption and increase light yield. To further improve performance for lighting applications, the outer PS blocks of star-like diblock copolymer nanoreactor can be replaced by polymers with superior optical stability such as polydimethylsiloxane (PDMS) to improve optical and thermal stability. Finally, as star-like nanoreactor strategy is amenable for the synthesis of a large array of hairy polymer-capped nanocrystals, uniform perovskite QDs with controlled dimensions, desired functionality (e.g., environmentally benign, lead-free $CsSbBr_3$ QDs using star-like PAA-*b*-PE as nanoreactor; organic-inorganic hybrid perovskite QDs such as $CH_3NH_3PbI_3$; etc.), design complexity (e.g., hairy core/shell perovskite QDs using star-like triblock copolymer nanoreactors), and high stability can be conveniently crafted.

3.1.4 Experimental Section

Materials: N,N,N′,N′′,N′′-pentamethyldiethylene triamine (PMDETA, 99%), oleylamine (technical grade, 70%), were purchased from Sigma-Aldrich. Anhydrous 1-methyl-2-pyrrolidinone (NMP, 99.5%), anhydrous N,N-dimethylformamide (DMF, 99.8%), trifluoroacetic acid (TFA, 99.9%), 2-bromoisobutyryl bromide (98%), cesium acetate (99.9%), lead acetate trihydrate (99.995%), 1-octadecene (ODE) (tech. grade, 90%), oleic acid (OA) (tech. grade, 90%), and tetra-n-octylammonium bromide (TOABr) (98+%) were purchased from Alfa Aesar. Lead bromide was purchased from TCI. Cesium bromide was purchased from STREM Chemicals. Hexane (ACS reagent grade), acetone (ACS reagent grade), and toluene (ACS reagent grade) were obtained from BDH Chemicals. All chemical described above were used as received. β-cyclodextrin (β-CD, SigmaAldrich) was dried at 50 °C under vacuum overnight prior to use. CuBr (98%, Sigma-Aldrich) was

stirred in acetic acid for 15 h, washed subsequently with ethanol and diethyl ether, and then dried under vacuum prior to use. Tert-butyl acrylate (tBA, Alfa Aesar, 98%), styrene (St, Sigma-Aldrich, ≥99%), anisole (TCI America, 99.0%), and methyl ethyl ketone (MEK, Fisher Scientific, 99.9%) were dried with calcium hydride and distilled under reduced pressure prior to use.

Synthesis of 21-arm star-like poly(tert-butyl acrylate) (star-like P*t*BA): Heptakis[2,3,6-tri-O-(2-bromo-2-methylpropionyl)]-β-cyclodextrin (21Br-β-CD) was prepared according to previous reported procedure.[12-13] Star-like P*t*BA was synthesized by atom transfer radical polymerization (ATRP) of tert-butyl acrylate (*t*BA) monomers using 21Br-β-CD macroinitiator. Briefly, CuBr (35.0 mg), PMDETA (85.0 mg), 21Br-β-CD (50 mg), *t*BA (21 mL), and MEK (21 mL) were mixed in an argon bubbled ampoule. The ampoule was then sealed and placed in an oil bath at 60°C. The reaction was later quenched by cooling the ampoule in liquid nitrogen. The solution was then diluted with acetone and passed through an activated neutral alumina column to remove the catalyst, and subsequently underwent fractional precipitation with methanol/water (v/v = 1/1, precipitator) to remove monomers and linear polymers. The product was then dried at 40°C under vacuum for 24 h prior to use.

Synthesis of 21-arm star-like poly(tert-butyl acrylate)-*b*-polystyrene (star-like P*t*BA-*b*-PS): Star-like P*t*BA-*b*-PS was synthesized by ATRP of styrene (St) monomers from star-P*t*BA initiator. Briefly, Star-like P*t*BA-Br (i.e., Br in P*t*BA macroinitiator) : CuBr : PMDETA : St = 1 : 1 : 2 : 800 (molar ratio) in anisole (1ml solvent per 1g St) was placed

in an argon bubbled ampoule. The ampoule was then sealed and placed in an oil bath at 90°C. The reaction was later quenched by placing the ampoule in liquid nitrogen. The product solution was diluted with THF and passed through an activated neutral alumina column to remove the catalyst, and subsequently purified by fractional precipitation with methanol/water (v/v = 1/1) as the precipitator to remove unreacted monomers. The product was then dried at 40°C under vacuum for 24 h prior to use.

Synthesis 21-arm star-like poly(acrylic acid)-*b*-polystyrene (star-like PAA-*b*-PS): Star-like PAA-*b*-PS was synthesized by hydrolysis of tert-butyl ester groups of P*t*BA blocks of star-like P*t*BA-*b*-PS to acrylic acid groups. Briefly, star-like P*t*BA-*b*-PS (1 g) was fully dissolved in dichloromethane (200 mL), followed by the addition of trifluoroacetic acid (TFA) (10 mL). The reaction proceeded at room temperature for 24 h. After hydrolysis, the solvent was evaporated under reduced pressure. The final product was washed with dichloromethane and methanol, and thoroughly dried under vacuum at 40 °C for 24 h.

Synthesis of PS-capped $CsPbBr_3$ QDs: Star-PAA-*b*-PS was used as nanoreactor for the synthesis of PS-capped $CsPbBr_3$ QDs. The strong coordination interaction between the metal moieties of $CsPbBr_3$ precursors (i.e., CsBr and $PbBr_2$) and carboxyl groups (-COOH) of the inner hydrophilic PAA blocks of star-like PAA-*b*-PS facilitated the nucleation and growth of $CsPbBr_3$ QDs selectively within the inner compartment occupied by PAA blocks of the nanoreactor. In a typical procedure, star-like PAA-*b*-PS was dissolved in DMF at room temperature, followed by the addition of CsBr and $PbBr_2$. To allow ample time for

the precursors to diffuse into the inner PAA compartment of the nanoreactor, the solution was stirred for 12 h. The precursor solution was then dropped into toluene, upon which PS-capped $CsPbBr_3$ QDs immediately formed in solution. Although toluene is a poor solvent for perovskite QDs, the PS-capped $CsPbBr_3$ QDs were colloidally stable due to the permanently tethered PS chain situated on the QD surface.

Synthesis of oleic acid- & oleyl amine-co-capped $CsPbBr_3$ QDs via the co-precipitation method at room temperature: oleic acid- & oleyl amine-co-capped $CsPbBr_3$ QDs were synthesized via the method reported in the literature with minor modifications.[89] In a typical experiment, 0.10 mmol oleic acid, 0.10 mmol oleyl amine, 0.02 mmol CsBr, and 0.04 mmol $PbBr_2$ were added to 10 ml anhydrous DMF. The solution was stirred for 1 h or until all precursors dissolved in the solution. The precursor solution was then added to toluene dropwise. Similarly, Perovskite QDs formed instantaneously after being added into toluene.

Synthesis of oleic acid-capped $CsPbBr_3$ QDs via the hot-injection method: oleic acid-capped $CsPbBr_3$ QDs were synthesized via the hot injection method reported in the literature with minor modifications.[48] Briefly, 5 ml ODE, 2 ml oleic acid, 1 mmol cesium acetate, and 2 mmol lead acetate trihydrate were added into a reaction flask and vacuumed at 100^{o}C. At 70^{o}C, 2 mmol TOABr in toluene was swiftly added into the reaction flask. After 5 s, the reaction was quenched by placing the reaction solution in an ice bath.

Synthesis of $CsPbBr_3$ with oleic acid via the co-precipitation method at room temperature: 0.12 mmol oleic acid, 0.02 mmol CsBr, and 0.04 mmol $PbBr_2$ were dissolved in 10 ml anhydrous DMF. The solution was stirred for 1 h or until all precursors dissolved in the solution. The precursor solution was then added to toluene dropwise. Perovskite materials formed immediately after being added into toluene.

Synthesis of $CsPbBr_3$ with no ligand via the co-precipitation method at room temperature: $CsPbBr_3$ QDs were synthesized via the method developed by Li et al. with minor modifications.[89] In a typical experiment, 0.02 mmol CsBr, and 0.04 mmol $PbBr_2$ was added to 10 ml anhydrous DMF. The solution was stirred for 1 h or until all precursors dissolved in the solution. Then the precursor solution was added to toluene dropwise.

Anion exchange of PS-capped $CsPbBr_3$ QDs: Anion exchange was performed according to the procedure reported in the literature with minor modifications.[91] Briefly, an appropriate amount of zinc halide was dissolved in methanol. The zinc halide solution was added in drops into a vial containing PS-capped $CsPbBr_3$ QDs while stirring vigorously.

Fabrication of WLED devices: Poly(methyl methacrylate) (PMMA), $CdSe/Cd_{1-x}Zn_xSe_{1-y}S_y/ZnS$ QDs, and PS-capped $CsPbBr_3$ QDs were thoroughly mixed using toluene as solvent. The mixed QD/PMMA solution was then cast on a GaN blue chip.

Characterization: Number average molecular weight (M_n) and polydispersity index (PDI) of start-like polymers were measured by gel permeation chromatography (GPC) equipped

with an LC-20AD HPLC pump and a refractive index detector (RID-10A, 120V) at 35 °C. A series of monodisperse polystyrene in THF were used as standard to calibrate the GPC at a flow rate of 1.0 mL/min. ^{1}HNMR spectra of star-like P*t*BA and star-like P*t*BA-*b*-PS used $CDCl_3$ as solvent and were recorded using a Varian VXR-300 spectroscope. The size of PS-capped $CsPbX_3$ QDs were examined by TEM (JEOL 100; operated at 100 kV) and high-resolution TEM (HRTEM, TECNAIG2 F30; operated at 300 kV). Absorbance, photoluminescence and quantum yield were measured by spectrofluorophotometer (Shimadzu UV-vis-2450 spectrometer and Shimadzu fluorescent RF-5310PC spectrofluorophotometer). Lifetime measurements (Time-resolved photoluminescence) were collected using a Photon Technology International Laserstrobe Spectrofluorometer (PTI GL-3300 nanosecond nitrogen laser λ = 337 nm; photomultiplier tube; time-correlated single photon counting). WLED measurements were performed using a spectral irradiance meter (SIM-2 Plus). UV lamp at 365 nm (4W, UVGL-25) was used to excite perovskite QDs. The crystalline structures of QDs were evaluated by XRD (X'pert PRO, Netherlands). Colloidal stability was studied by measuring the QY after storing the PS-capped $CsPbBr_3$ QDs in toluene solution for different times. The PS-capped $CsPbBr_3$ QD solution was stored under ambient condition (i.e., exposed to air and light at room temperature without stirring). Water stability was studied by measuring the time duration at which the photoluminescence of the PS-capped $CsPbBr_3$ QDs in 5 ml toluene completely diminished under UV excitation after adding 5 ml water. The solution was stirred vigorously at 1500 rpm throughout the experiment to ensure the mixing between the QD solution and water.

3.2 Precisely Size-Tunable Monodisperse Hairy Plasmonic Nanoparticles via Amphiphilic Star-like Block Copolymers

Y. Chen†, Y.J. Yoon†, X. Pang, Y. He, J. Jung, C. Feng, G. Zhang*, Z. Lin*, "Precisely size-tunable monodisperse hairy plasmonic nanoparticles via amphiphilic star-like block copolymers", *Small* 12 (2016) 6714-6723. **†Co-First Author (Cover)** [Reproduced with permission from ref. 56, Copyright © 2016 WILEY-VCH]

Abstract

In situ precision synthesis of monodisperse hairy plasmonic nanoparticles with tailored dimensions and compositions by capitalizing on amphiphilic star-like diblock copolymers as nanoreactors are reported. Such hairy plasmonic nanoparticles comprise uniform noble metal nanoparticles intimately and perpetually capped by hydrophobic polymer chains (i.e., "hairs") with even length. Interestingly, amphiphilic star-like diblock copolymer nanoreactors retain the spherical shape under reaction conditions, and the diameter of the resulting plasmonic nanoparticles and the thickness of polymer chains situated on the surface of the nanoparticle can be readily and precisely tailored. These hairy nanoparticles can be regarded as hard/soft core/shell nanoparticles. Notably, the polymer "hairs" are directly and permanently tethered to the noble metal nanoparticle surface, thereby preventing the aggregation of nanoparticles and rendering their dissolution in nonpolar solvents and the homogeneous distribution in polymer matrices with long-term stability. This amphiphilic star-like block copolymer nanoreactor-based strategy is viable and robust and conceptually enables the design and synthesis of a rich variety of hairy functional nanoparticles with new horizons for fundamental research on self-assembly and

technological applications in plasmonics, catalysis, energy conversion and storage, bioimaging, and biosensors.

3.2.1 Introduction

Noble metal nanoparticles often exhibit strong characteristic surface plasmon resonance (SPR) owing to the collective oscillation of conduction electrons when exposing to the external electromagnetic field. They represent an important class of nanomaterials and have attracted much attention for use in biomedical diagnosis and therapy,[101] catalysis,[102] surface-enhanced Raman spectroscopy,[103] etc. In sharp contrast to fluorescent organic dyes which experience photobleaching and degradation during bioimaging, plasmonic nanoparticles (e.g., Au and Ag) possess at least five orders of magnitude larger optical cross-section owing to the surface plasmon enhancement and thus superior photostability.[101] They have also found applications as photothermal therapeutic agents for tumor treatment. Recent research has witnessed rapid advances in rational design and synthesis of plasmonic nano-particles with controllable and uniform size. They are often achieved by comparatively simple solution-based colloidal synthesis.[104] As nanoparticles tend to aggregate due to their high specific surface area, surface passivation of nanoparticle with ligands (e.g., small molecular surfactants and linear polymers) is of key importance in preventing them from agglomeration. However, the ligands capped on the plasmonic nanoparticle surface are often dynamically stable due to weak non-covalent binding between ligand and nanoparticle. Thus, the ligand dissociation may occur as experimental conditions (e.g., pH, temperature, UV irradiation, etc.) are changed.[105] Moreover, it

remains challenging to utilize small molecular ligand-capped plasmonic nanoparticles for certain applications, for example, surface-enhanced Raman scattering (SERS)-based sensing. The weak interaction between functional groups (e.g., acids and alcohols) in analytes and plasmonic nanoparticles often yield feeble SERS signals due largely to the dynamic adsorption and desorption of attached analytes.[106] Clearly, by employing polymeric ligands, the analytes will likely be encapsulated within the layer of polymeric ligands, thereby leading to the improved SERS.

In this context, several strategies including grafting-from and grafting-to[107] and amphiphilic linear block copolymer micelles[108] have emerged to passivate the surface of nanoparticles with polymer chains as ligands, forming polymer capped nanoparticles. We note that the grafting-from approach allows for a higher grafting density of polymer chains, and grafting-to approach may suffer from steric hindrance that limits the grafting density. Both approaches may still often encounter the unavoidable association and dissociation of grafted polymers from the nanoparticle surface over a certain period of time, resulting in incomplete and uncontrollable surface coverage or uniformity of polymers on the nanoparticle surface.[109] On the other hand, the size and shape of amphiphilic linear block copolymer micelles formed by self-assembly in the selective solvent depend sensitively on concentration, solvent properties, temperature, pH, etc. Thus, it is difficult to create and maintain strictly structurally stable spherical micelles containing amphiphilic linear block copolymers that can be employed as templates for the growth of nanoparticles.[110-112] A slight variation of experimental conditions noted above could result in nanoparticles with non-uniform size and shape. Clearly, it's highly desirable to develop a versatile synthetic

route to strictly size-controlled, homogeneously dispersed and stable nanoparticles with uniform polymer chains perpetually tethered on their surface.

Herein, we report a viable and robust strategy to craft monodisperse plasmonic nanoparticles with precisely tailorable dimensions and compositions intimately and permanently capped with a layer of polymer chains of uniform length (i.e., hairy plasmonic nanoparticles). The key to our strategy is to exploit a set of amphiphilic star-like poly(acrylic acid)-block-polystyrene (PAA-*b*-PS) diblock copolymers with well-defined molecular weights as nanoreactors (i.e., templates) that are rationally designed and synthesized via a sequential atom transfer radical polymerization (ATRP) of *tert*-butyl acrylate (*t*BA) and styrene (St) from a β-cyclodextrin-based macroinitiator, followed by the hydrolysis of inner poly(*tert*-butyl acrylate) (P*t*BA) blocks. The precursors are selectively partitioned in the space occupied by the inner hydrophilic PAA blocks of star-like PAA-*b*-PS diblock copolymers. The strong coordination interaction between the carboxylic acid groups of PAA blocks and the metal moieties of Au and Ag precursors lead to the nucleation and growth of PS-capped Au and PS-capped Ag nanoparticles, respectively. Unlike the dendrimer-encapsulated nanoclusters,[113] the diameters of plasmonic Au and Ag nanoparticles and the thickness of outer hydrophobic PS blocks on the nanoparticle surface can be conveniently tailored by varying the molecular weights of inner PAA blocks and outer PS blocks during the ATRP of *t*BA and St, respectively. It is worth noting that our nanoreactor strategy for creating polymer-capped nanoparticles differs significantly from the approaches noted above. First, in stark contrast to copious past works on nanoparticles synthesized from the conventional linear block copolymer micelles, our strategy enables the effective synthesis of monodisperse nanoparticles due to

the unimolecular micellar structure of amphiphilic star-like block copolymers. The integrity (i.e., size and shape) of amphiphilic star-like block copolymer templates remain during the reaction owing to their star-shaped nature (i.e., each PAA-*b*-PS diblock "hair" connected to a β-cyclodextrin core).[12-13] Second, the polymer "hairs" are permanently anchored on the nanoparticle surface, thus eliminating the aggregation of nanoparticles and imparting their superior solubility and long-term stability in nonpolar solvents and homogeneous distribution in polymer matrices. Conceptually, this amphiphilic star-like block copolymer nanoreactor-based strategy opens the possibility for synthesis of a large variety of hairy functional nanoparticles with accurate control over the size of nanoparticles, length of polymeric ligands, surface chemistry of nanoparticles, and solubility and long-term stability of nanoparticles.

3.2.2 Results/Discussion

Scheme 3.2 depicts the synthetic route to hairy noble metal nanoparticles (i.e., PS-capped plasmonic nanoparticles) by capitalizing on amphiphilic unimolecular star-like PAA-*b*-PS diblock copolymers as nanoreactors. First, 21 hydroxyl groups of β-cyclodextrin (β-CD) were converted to bromine groups via esterification, yielding 21-Br-β-CD macroinitiator[12-14, 48, 79-82, 84] (upper central panel in **Scheme 3.2**). A series of unimolecular star-like poly(tert-butyl acrylate)-block-polystyrene (PtBA-*b*-PS) diblock copolymers with well-defined molecular weight and narrow molecular weight distribution (i.e., low polydispersity index (PDI)) of each block were then synthesized by sequential ATRP of tBA and St monomers using 21-Br-β-CD macroinitiator (upper right and lower

right panels for star-like PtBA and PtBA-*b*-PS, respectively, in **Scheme 3.2**). The proton NMR (^{1}H NMR) spectra of representative star-like PtBA and PtBA-*b*-PS are shown in **Figure 3.26** and **Figure 3.27**. Subsequently, the inner hydrophobic PtBA blocks were transformed into hydrophilic PAA blocks by thoroughly hydrolyzing the tert-butyl groups of PtBA, resulting in amphiphilic star-like PAA-*b*-PS (lower central panel in **Scheme 3.2**; **Figure 3.28**). As noted above, in contrast to the conventional micelles formed from self-assembly of linear amphiphilic block copolymers, each amphiphilic PAA-*b*-PS arm in star-like PAA-*b*-PS diblock copolymer is connected to the β-CD-based macroinitiator core. Thus, stable spherical unimolecular micelle was obtained.[12-13]

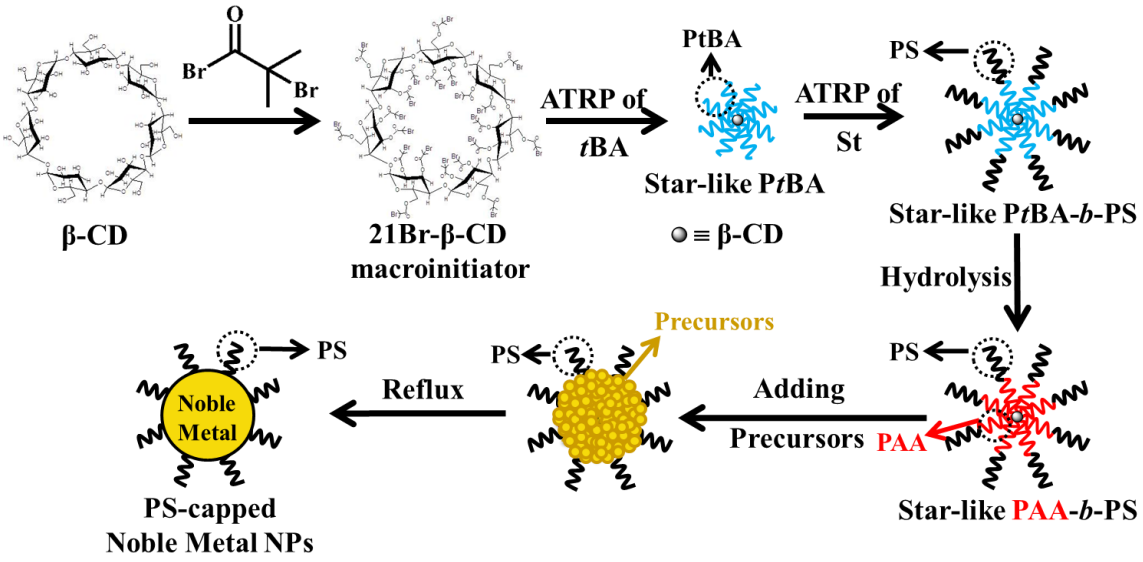

Scheme 3.2 Stepwise representative of synthesis of hairy plasmonic nanoparticles (e.g., PS-capped Au and Ag nanoparticles) using amphiphilic star-like PAA-b-PS diblock copolymers as nanoreactors (lower central panel).

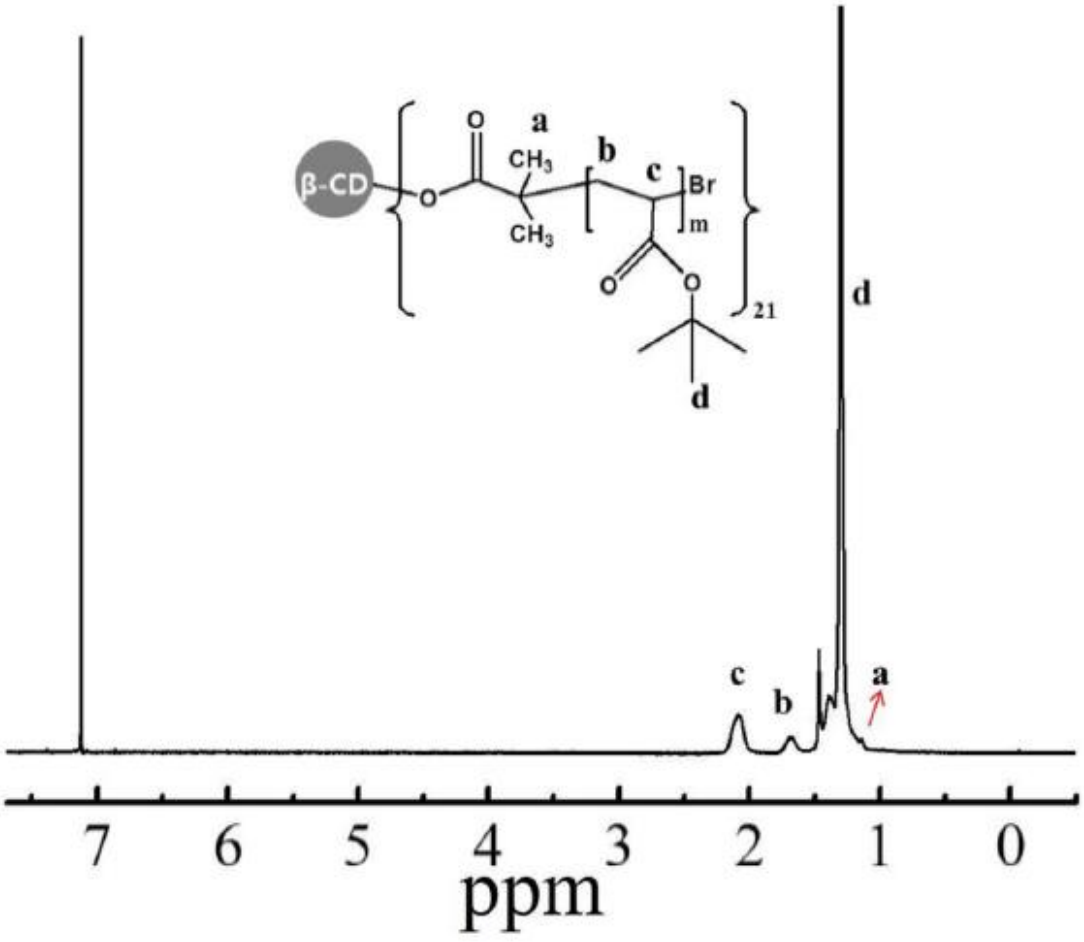

Figure 3.26 ^{1}H-NMR spectrum of star-like PtBA in $CDCl_3$

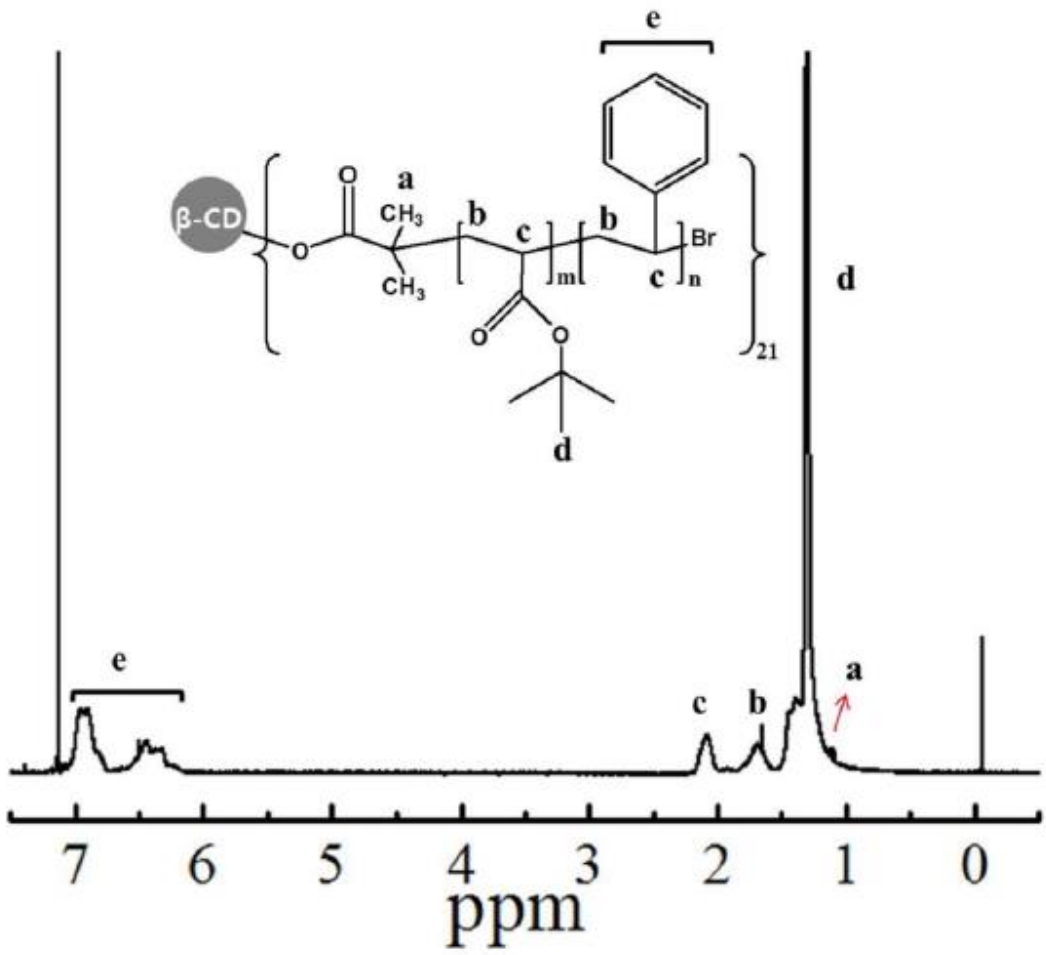

Figure 3.27 ^{1}H-NMR spectrum of star-like PtBA-*b*-PS in $CDCl_3$

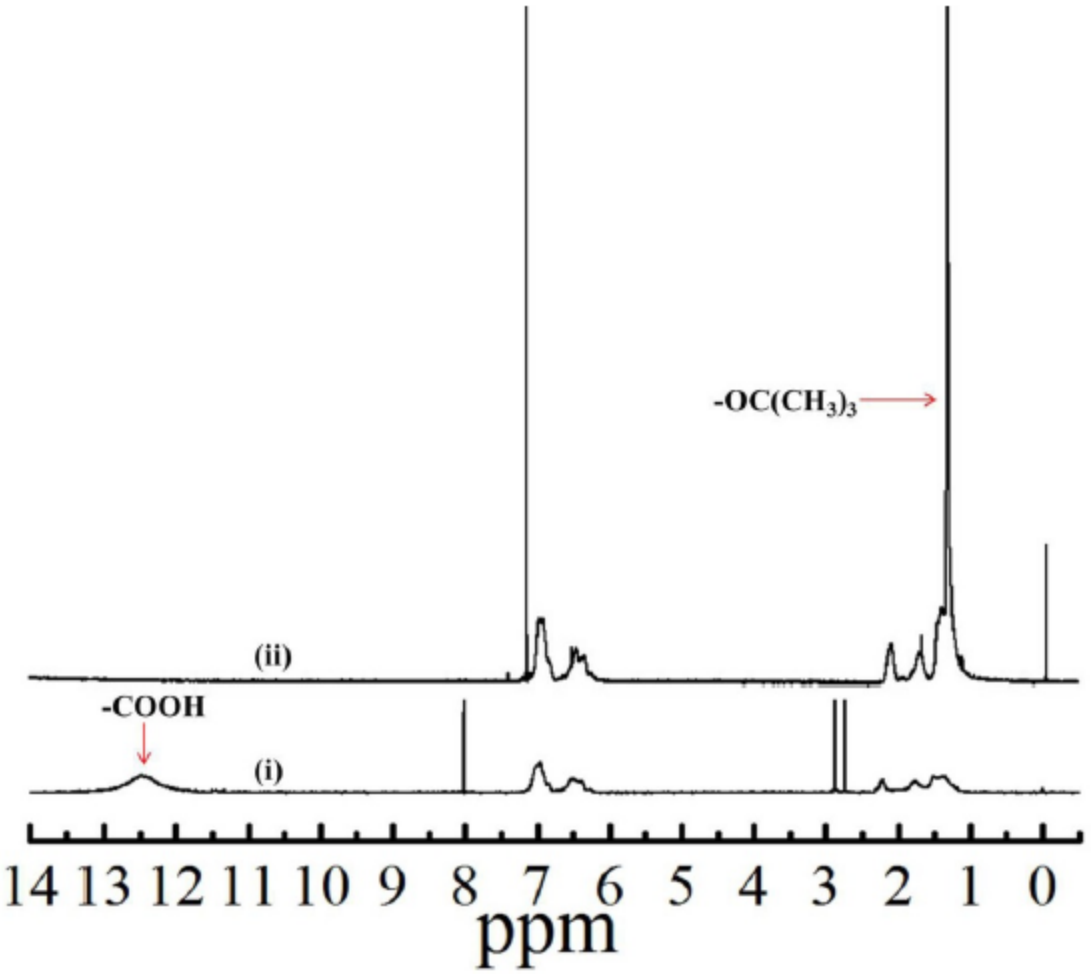

Figure 3.28 ^{1}H-NMR spectra of star-like diblock copolymers. (i) star-like PtBA-*b*-PS in $CDCl_3$, and (ii) the resulting amphiphilic star-like PAA-*b*-PS in d_7-DMF.

The resulting amphiphilic PAA-*b*-PS diblock copolymers were exploited as nanoreactors to template the nucleation and growth of monodisperse plasmonic Au and Ag nanoparticles capped with PS chains that are originally covalently connected to inner PAA chains (i.e., PS-capped plasmonic nanoparticles; lower left panel in **Scheme 3.2**). It is interesting to note that the reaction was conducted in the mixed solvents containing N,N-dimethylformamide (DMF) and benzyl alcohol (BA) at DMF/BA = 9/1 ratio by volume

(see the Experimental Section). In comparison to BA which is a non-solvent for PS blocks, DMF is a solvent for both PAA and PS blocks. As a result, structurally stable spherical macromolecules with well-defined shape comprising expanded inner PAA chains with collapsed outer PS chains were yielded. Subsequently, the metal-ion-containing precursors (i.e., $HAuCl_4 \bullet 3H_2O$ and $AgNO_3$, respectively) were added into the star-like PAA-*b*-PS DMF/BA solution and selectively populated in the compartment containing the expanded inner PAA chains rather than the collapsed outer PS chains. Within the PAA compartment, the metal moieties of precursors coordinated strongly with the carboxyl group of PAA blocks and grew into Au and Ag nanoparticles permanently anchored with the collapsed PS blocks in the DMF/BA mixed solvents (i.e., forming PS-capped Au and Ag nanoparticles; lower left panel in **Scheme 3.2**; see the Experimental Section). As ATRP is a living polymerization technique that produces polymer chains with well-defined molecular weight and low PDI,[114] the length of PAA blocks and in turn the shape of the resulting plasmonic nanoparticles can be strictly controlled. Moreover, by varying the ATRP time during the synthesis of each block in star-like diblock copolymer, the diameter of plasmonic nanoparticle templated within the PAA compartment and the length of PS blocks can be readily tailored. The molecular weights of PAA and PS in a series of synthesized star-like PAA-*b*-PS diblock copolymer and the corresponding diameters of PS-capped plasmonic nanoparticles are summarized in **Table 3.5**.

Table 3.5 Molecular weights of amphiphilic multi-arm, star-like PAA-*b*-PS diblock copolymers and the corresponding sizes of PS-capped noble metal nanoparticles.

Samples	$M_{n,\,PAA}$[a]	$M_{n,\,PS}$[b]	PDI[c]	Diameter of PS-capped Au nanoparticles[d] (nm)	Diameter of PS-capped Ag nanoparticles[d] (nm)
Sample A	3,300	8,200	1.12	3.2 ± 0.1	
Sample B	4,200	8,300	1.09	5.1 ± 0.2	
Sample C	11,600	8,600	1.13	12.2 ± 0.5	11.9 ± 0.3
Sample D	19,100	6,000	1.10	18.3 ± 0.4	18.1 ± 0.5

[a]Number average molecular weight, M_n of each PAA block calculated from the molecular weight difference between P*t*BA block (before hydrolysis) and PAA block (after hydrolysis).
[b]M_n of each PS block calculated from ^{1}H NMR data (**Figure 3.27**).
[c]PDI determined by GPC.
[d]Sizes obtained from TEM image analysis on nanoparticles. M_n of each P*t*BA block can be obtained from the calculation of ^{1}H-NMR spectrum (**Figure 3.26**) based on the ratio of the integral areas of methyl protons in *tert*-butyl group of P*t*BA chains (A_b) to that of methyl protons at the α-end of grafted P*t*BA (A_a):[12-13]

$$M_{n,PtBA} = \frac{\frac{A_b}{9}}{\frac{A_a}{6}} \times 128.17$$

where 128.17 is the molecular weight of the *t*BA monomer, and the integral areas (A_a and A_b) are obtained after deconvolution.

Figure 3.29 shows the representative transmission electron microscope (TEM) images of PS-capped Au and Ag nanoparticles. Uniform Au nanoparticles with the average diameters of 3.2 ± 0.1, 5.1 ± 0.2, 12.2 ± 0.5, and 18.3 ± 0.4 nm, respectively, crafted by capitalizing on four star-like PAA-*b*-PS diblock copolymers with different molecular weight of inner PAA blocks (Sample A to Sample D in **Table 3.5**) were clearly evident (**Figure 3.29a-d**). The hexagonal close-pack of PS-capped Au nanoparticles (**Figure 3.29b-d**) further substantiated the high quality of nanoparticles. Similarly, Ag nanoparticles with the average diameters of 11.9 ± 0.3 nm (**Figure 3.29e**) and 18.1 ± 0.5

nm (**Figure 3.29f**) were also created using the same templates in **Table 3.5** (i.e., Sample C for 11.9 ± 0.3 nm and Sample D for 18.1 ± 0.5 nm, respectively). It is noteworthy that the size distribution of these nanoparticles is less than 5% of their average size, suggesting that they are monodisperse. The size distribution histograms for PS-capped Au and Ag nanoparticles are shown in **Figure 3.30**. Compared with the size of the corresponding star-like PAA measured in DMF (**Table 3.7**), a slight decrease in diameter of the resulting nanoparticles is due likely to the use of 9/1 DMF/BA in the reaction and the minor volume shrinking of the PAA-containing compartment during the crystallization of nanoparticles.

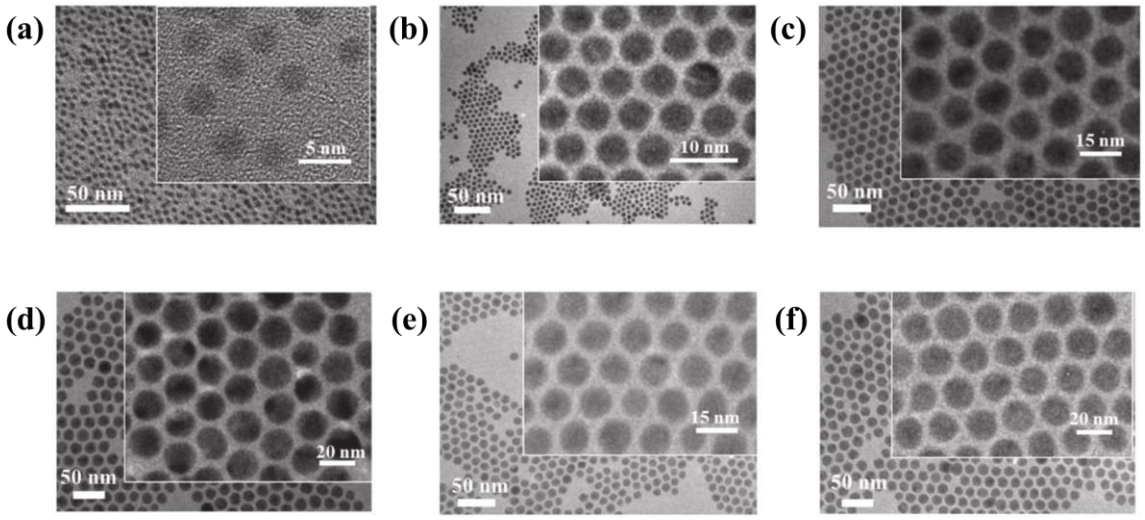

Figure 3.29 TEM images of monodisperse PS-capped noble metal nanoparticles crafted using amphiphilic star-like PAA-*b*-PS diblock copolymers as nanoreactors. PS-capped Au nanoparticles with diameters of a) 3.2 ± 0.1 nm, b) 5.1 ± 0.2 nm, c) 12.2 ± 0.5 nm, and d) 18.3 ± 0.4 nm. PS-capped Ag nanoparticles with diameters of e) 11.9 ± 0.3 nm and f) 18.1 ± 0.5 nm.

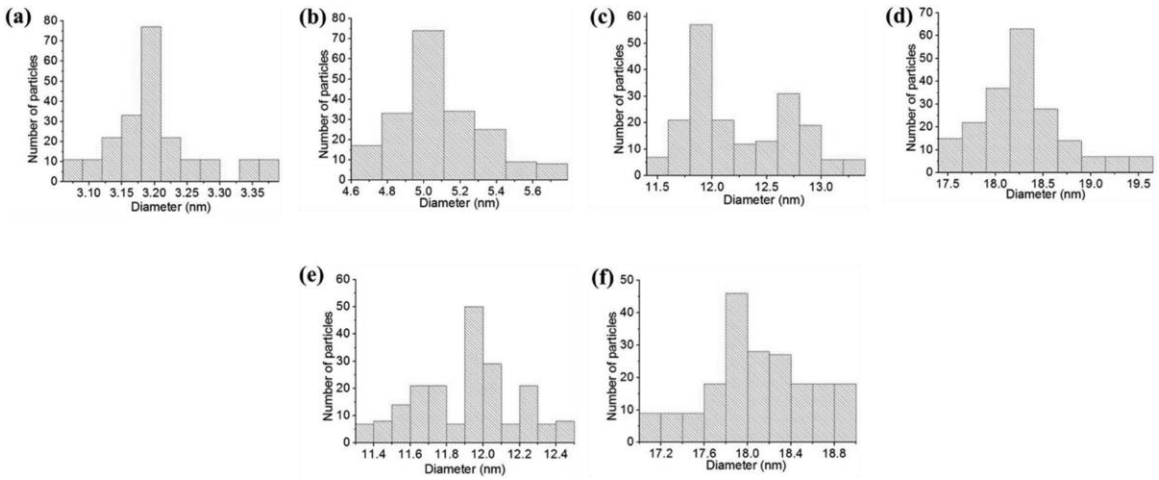

Figure 3.30 Histograms of the size distribution of randomly selected 200 nanoparticles for TEM images in **Figure 1.** PS-capped Au nanoparticles with diameters of a) 3.2 ± 0.1 nm, b) 5.1 ± 0.2 nm, c) 12.2 ± 0.5 nm, and d) 18.3 ± 0.4 nm. PS-capped Ag nanoparticles with diameters of e) 11.9 ± 0.3 nm and f) 18.1 ± 0.5 nm.

Prior to the second ATRP reaction of styrene, a small amount of star-like PAA (after hydrolyzed from P*t*BA) homopolymers (i.e., ~10 mg) were dissolved in anhydrous DMF (~10 mL) at c = 1 mg/mL at room temperature. The solutions were stirred for 3 days. The hydrodynamic diameters D_h of star-like PAA from DLS measurements agreed with their theoretical sizes (i.e., radius of gyration R_g) and summarized in **Table 3.6**.

Table 3.6 The hydrodynamic diameter from DLS measurements and the calculated radius of gyration of star-like PAA homopolymers.

Samples	D_h of Star-like PAA[a] (nm)	R_g of Star-like PAA[b] (nm)
Sample A	4.1 ± 0.2	3.25
Sample B	6.2 ± 0.5	3.66
Sample C	13.3 ± 0.7	6.09
Sample D	18.7 ± 1.0	7.82

[a]Hydrodynamic diameter, D_h of star-like PAA homopolymers in DMF obtained by DLS.
[b]Radius of gyration, R_g of star-like PAA calculated based on the following equation:[95]

$$< R_g^2 > = \frac{Nb^2}{6}\left(\frac{3-2f}{f}\right)$$

where N is the degree of polymerization of star-like PAA homopolymers calculated from M_n in **Table 3.5**, f is the number of arms, and b is the Kuhn length (~0.69 nm for PAA).[96]

We also note that due to the random arrangement of the lattice planes in each nanoparticle, the brightness of Au and Ag nanoparticles varied in TEM images (**Figure 3.29**).[115] Representative high-resolution TEM images of 3 nm (**Figure 3.29a**) and 18 nm (**Figure 3.29d**) Au nanoparticles showed that they are highly crystalline with a lattice spacing of ca. 2.4 Å, which is in good agreement with the (111) interplanar distance of the face-centered cubic (fcc) structure of Au (**Figure 3.31a-b**).

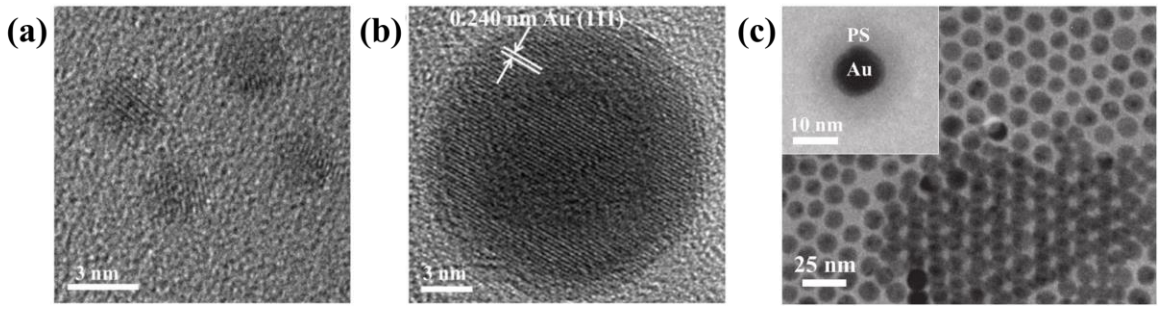

Figure 3.31 HRTEM images of Au nanoparticles permanently capped with PS chains on the surface. The diameters of Au core are a) 3 nm and b) 18 nm, respectively.

In contrast to rather weak physical adsorption or chemical coupling of ligands on the nanoparticle surface in previous works, the surface of plasmonic nanoparticles was reliably and permanently capped with soft PS chains enabled by the pre-existing strong covalent bonding between PAA and PS chains in star-like PAA-*b*-PS templates. Interestingly, single-layer and two-layer assemblies of PS-capped Au nanoparticles were observed (D = 12.2 ± 0.5 nm; top right and bottom right, respectively, in **Figure 3.31c**). Obviously, the formation of these assemblies was driven by the minimization of surface energy of mono- disperse PS-capped Au nanoparticles through reducing the exposed surface areas during the solvent (i.e., toluene; these PS-capped Au nanoparticles were re-dissolved in toluene after synthesis) evaporation. In order to examine the PS chains situated on the Au nanoparticle surface, the TEM grid can be exposed to RuO_4 vapor to preferentially stain the PS chains, yielding a dark appearance. The representative TEM image of PS-capped Au nanoparticles with the Au core diameter of 12 nm and PS shell thickness of 4 nm (Sample C in **Table 3.5**) stained by RuO_4 vapor is shown as an inset in **Figure 3.31c**. Quite intriguingly, a layer of PS chains covered on the surface of Au

nanoparticle was seen, and the interface between Au nanoparticle and PS shell is intimate (darker Au core and relatively light PS shell in inset). It is notable that despite the relatively close molecular weights of PAA and PS blocks (Sample C in **Table 3.5**, Supporting Information), the smaller thickness of PS shell compared to Au core suggested the collapsed chain conformation of PS blocks on the surface of Au nanoparticle. As a direct consequence, PS-capped Au nanoparticles can be readily dissolved in nonpolar solvents with a superior long- term stability (**Figure 3.32**). No precipitation was observed for months. Moreover, the superior stability of the PS-capped Au nanoparticles compared with oleylamine-capped Au nanoparticles was examined by employing UV irradiation as shown in **Figure 3.33**. The size and shape of PS-capped Au nanoparticles after irradiation (**Figure 3.33**a) were the same as those prior to irradiation (**Figure 3.29**) due to the presence of intimately linked PS chains. However, the spherical oleylamine-capped Au nanoparticles (**Figure 3.34**) aggregated heavily with irregular shapes after irradiation (**Figure 3.33b**) owing to the UV irradiation-induced desorption of ligands.[105] Clearly, the PS-capped Au nanoparticles were much more stable than those prepared by the conventional technique.

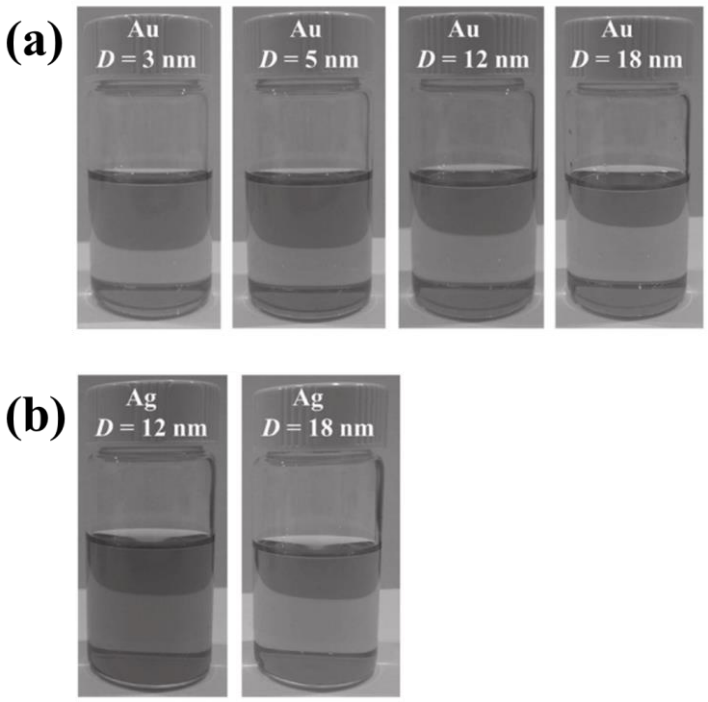

Figure 3.32 Digital images of PS-capped noble metal nanoparticles that are well dissolved in toluene. (a) PS-capped gold nanoparticles (b) PS-capped silver nanoparticles

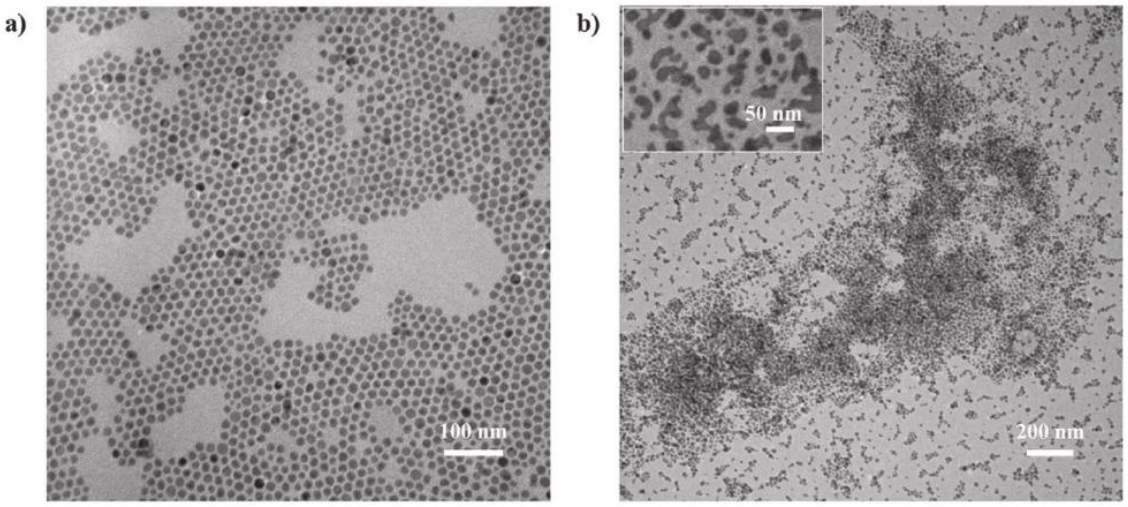

Figure 3.33 TEM images of a)18 nm PS-capped Au nanoparticles after irradiation of 254 nm UV light for 12 h and b) 18 nm oleylamine-capped Au nanoparticles after irradiation of 254 nm UV light for 1 h.

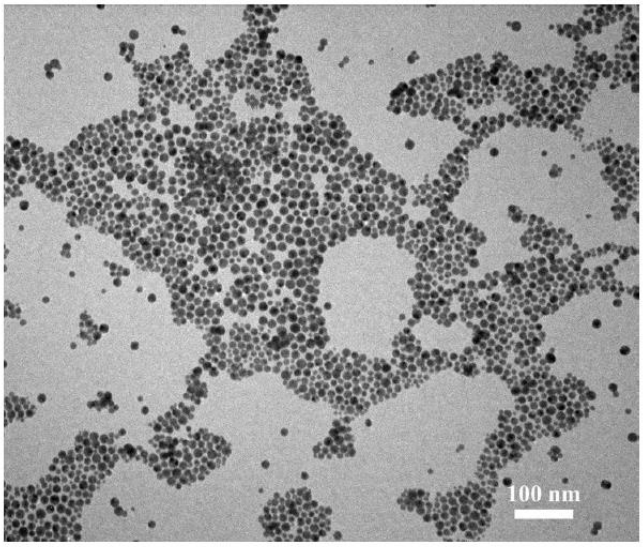

Figure 3.34 TEM image of oleylamine-capped Au nanoparticles with an average diameter of 18.1 ± 4.2 nm.

Typical X-ray diffraction (XRD) patterns of PS–capped plasmonic nanoparticles are shown in **Figure 3.35**. The peaks from PS-capped Au nanoparticles at scattering angle, 2θ of 37.81°, 43.96°, 64.23°, 77.19°, and 81.42° correspond to the diffraction from the (111), (200), (220), (311), and (222) crystal planes of fcc Au, respectively (**Figure 3.35a**). The PS-capped Ag nanoparticles showed the similar XRD pattern (**Figure 3.35b**). Clearly, the XRD measurements suggested that Au and Ag nanoparticles formed by the nanoreactor strategy were crystalline.

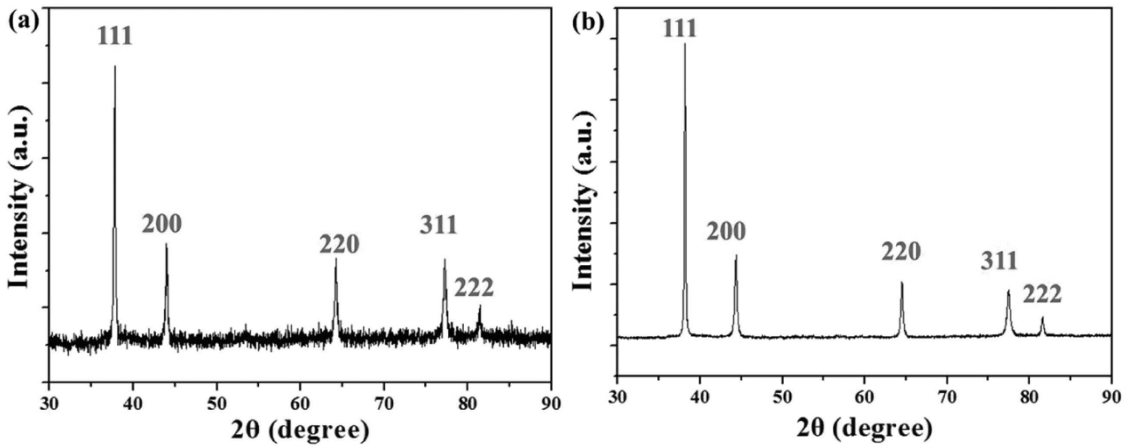

Figure 3.35 XRD patterns of a) PS-capped Au nanoparticles, and b) PS-capped Ag nanoparticles.

The SPR properties of PS-capped Au and Ag nanoparticles as a function of nanoparticle size were then systematically examined. The UV–vis absorption spectra of PS-capped Au nanoparticles and Ag nanoparticles in toluene are shown in **Figure 3.36**. Compared with oleylamine-capped Au nanoparticles, the red-shift of SPR peak position of PS-capped Au nanoparticles suggested the existence of PS shell due to the higher refractive index of PS than oleylamine (**Figure 3.37**, Supporting Information). As the diameter of Au nanoparticles increased, the intensity of the characteristic SPR peak increased associated with a marginal red-shift in the peak position and a decreased full- width-at-half-maximum (FWHM) (**Figure 3.36a**). These observations correlated well with the reports in literature and can be attributed to more electrons in larger Au nanoparticles and non-negligible electromagnetic retardation.[116] Similarly, for PS-capped Ag nanoparticles, as the size increased from 11.9 ± 0.3 nm to 18.1 ± 0.5 nm, the characteristic SPR peak at around 420 nm exhibited an increase in intensity and a narrowing in FWHM (**Figure 3.36b**), which

agreed well with the reports in literature.[117] It is worth noting that such good agreements between our work and previous studies on plasmonic absorption behaviors of Au and Ag nanoparticles corroborated that our nanoreactor strategy renders the crafting of high-quality noble metal nanoparticles that possess as good plasmonic properties as those prepared by other means.[116-117]

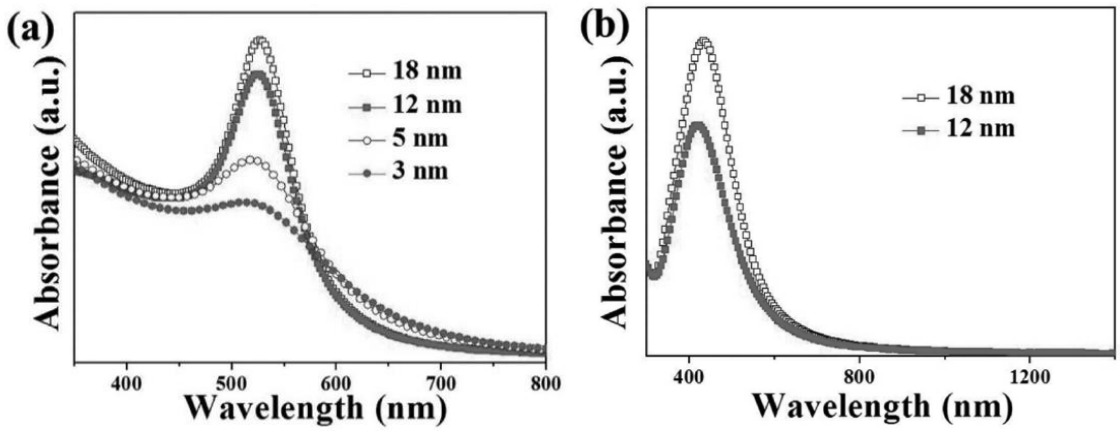

Figure 3.36 UV–vis spectra of a) PS-capped Au nanoparticles with diameters of 3.2 ± 0.1, 5.1 ± 0.2, 12.2 ± 0.5, and 18.3 ± 0.4 nm, respectively, and b) PS-capped Ag nanoparticles with diameters of 11.9 ± 0.3 and 18.1 ± 0.5 nm, respectively.

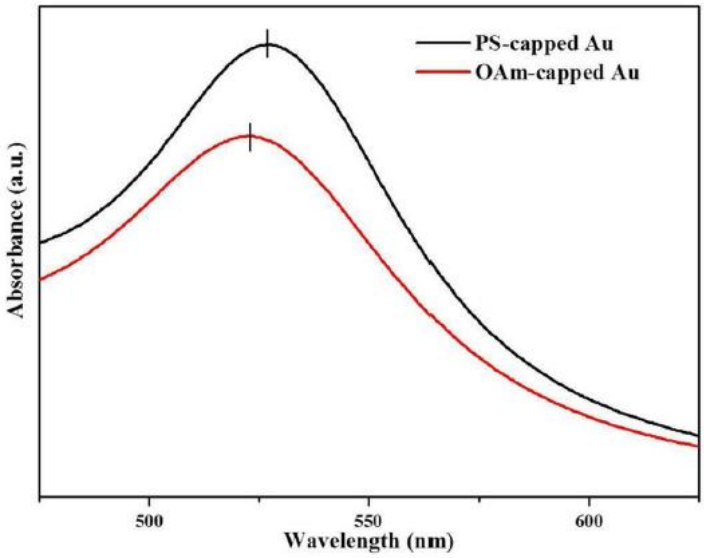

Figure 3.37 UV-vis spectra of 18-nm PS-capped Au nanoparticles and oleylamine-capped Au nanoparticles. The red-shift in SPR peak position (from 523 nm for oleylamine-capped Au to 527 nm for PS-capped Au nanoparticles) resulted from the higher refractive index of PS shell (n = 1.59) compared with toluene (n = 1.49). This agrees well with both theoretical prediction[118] and experimental result[119].

According to Mie theory, compared with the wavelength of light, nanoparticle with a finite diameter (typically below 50 nm) responds as an induced dipole resulting from the electric field of incident light when being irradiated with light (i.e., dipole approximation). Based on this dipole approximation, one most primitive theoretical model for the optical spectrum of noble metal nanoparticles is given as follows.[120]

$$E(\lambda) = \frac{24\pi^2 N R^3 \varepsilon_{out}^{3/2}}{\lambda \ln(10)} \left[\frac{\varepsilon_i(\lambda)}{\left(\varepsilon_r(\lambda) + \chi\varepsilon_{out}\right)^2 + \varepsilon_i(\lambda)^2} \right] \qquad (1)$$

E(λ) is the extinction (i.e., the sum of absorption and scattering cross-section), N is the areal density of nanoparticles, R is the radius of spherical noble metal nanoparticles, ε_{out} is the dielectric constant of the surrounding medium (assumed to be frequency-independent), λ is the wavelength of the absorbing radiation, ε_i and ε_r represent the imaginary and real portions of the dielectric function of nanoparticle, ε ($\varepsilon(\omega) = \varepsilon_i(\omega) + i\varepsilon_r(\omega)$, where ω is the angular frequency of light), and the value of χ describing the aspect ratio of nanoparticle is 2 for sphere.[121] From this model, it is clear that the experimental optical spectrum of noble metal nanoparticles depends on their radius R and the dielectric function ε.

When 2R is less than electronic mean-free path (=50 nm for Au and Ag), the scattering of free electrons on the surface affects their responses to optical excitation, thereby resulting in depolarization.[122] The spontaneous emission of radiation from the induced dipole, which increases rapidly with the nanoparticle size, causes a radiative damping.[123] Both depolarization and radiative damping lead to the red-shift of the SPR peak as the nanoparticle size increases.[123] Considering the intrinsic size effect that includes the effect of free electrons, surface damping, and interband transitions, dielectric function ε(ω) described above is thus modified based on Drude model to reflect the size-dependent effect and given in the following.[124]

$$\varepsilon(\omega, R) = \varepsilon_{\text{bulk}} + \frac{\omega_P^2}{\omega^2 + i\omega\gamma_D} - \frac{\omega_P^2}{\omega^2 + i\omega\left(\gamma_D + \frac{AV_F}{R}\right)} \qquad (2)$$

ε_{bulk}, ω_P, γ_D, V_F and R are the bulk dielectric constant, the plasma frequency, the bulk damping constant, the Fermi velocity of electron cloud, and the radius of spherical noble metal nanoparticles, respectively. After solving the dielectric function $\varepsilon(\omega, R)$, the optical spectrum of noble metal nanoparticles can be simulated by numerical methods such as discrete dipole approximation. The simulation results reported in literature have also shown the same plasmonic characteristics (i.e., an increase in intensity, a decrease in FWHM, and a slight red-shift as the nanoparticle size increases) as seen in our experiments.

3.2.3 Conclusion

In summary, we demonstrate in-situ precision synthesis of hairy plasmonic Au and Ag nanoparticles with tailored sizes and compositions by capitalizing on amphiphilic star-like PAA-*b*-PS diblock copolymers as nanoreactors. These nanoreactors were synthesized via sequential ATRP of tBA and St from the β-cyclodextrin-based macroinitiator, followed by subsequent hydrolysis of inner PtBA blocks. Intriguingly, these hairy plasmonic nanoparticles can be regarded as hard/ soft core/shell nanoparticles composed of monodisperse plasmonic nanoparticle core intimately and permanently capped with PS shell of uniform length. By simply varying the molecular weights of inner hydrophilic PAA blocks and outer hydrophobic PS blocks in star-like PAA-*b*-PS nanoreactors, the diameter of plasmonic nanoparticles and the thickness of PS shell, respectively, can be accurately controlled. It is interesting to note that the ability to tune the length of PS blocks permanently situated on the surface of plasmonic nanoparticles render the deliberate variation of distance between adjacent plasmonic nanoparticles for enhanced SERS.[125]

Furthermore, hairy nanoparticles of this kind can be homogeneously dispersed in PS matrix, PS-derived polymer matrix (for example, phenyltrinetoxysilane via forming a homogeneous hybrid due to the pi-pi interaction between phenyl groups), or PS blocks in PS-containing linear diblock or triblock copolymers[126] that virtually eliminating enthalpic interaction of nanoparticles with the host matrix.[127] Moreover, the PS shell (i.e., PS "hair") can be further carbonized under inert atmosphere to yield conductive carbon-coated plasmonic nanoparticles.[128-129] As the carbon coating promotes the charge transfer, such carbon-coated plasmonic nanoparticles may find promising applications in biosensors[130] and solar cells.[79] This will be the subject of future study. Finally, although noble metals were chosen as examples to demonstrate the effectiveness of our nanoreactor strategy in producing mono- disperse hairy nanoparticles, we envision that given a variety of precursors that are amenable to such nanoreactor-based reactions, this strategy offer great potential to create a myriad of other hairy nanoparticles with well-controlled dimensions and compositions for applications in energy conversion and storage, catalysis, nanotechnology, plasmonic devices, surface plasmon-based biosensing and bioimaging.

3.2.4 Experimental Section

Materials: 2-Bromoisobutyryl bromide (98%), N,N,N′,N″,N″- pentamethyldiethylene triamine (PMDETA, 99%), anhydrous 1-methyl-2-pyrrolidinone (NMP, 99.5%), trifluoroacetic acid (TFA, 99.9%), gold(III) chloride trihydrate ($HAuCl_4 \bullet 3H_2O$, ≥99.9%), silver nitrate ($AgNO_3$, ≥99.0%), oleylamine (technical grade, 70%), and tert-butylamine borane (TBAB, 97%) were purchased from Sigma-Aldrich, and used as received. β-

cyclodextrin (β-CD, SigmaAldrich) was dried at 80°C under vacuum overnight prior to use. CuBr (98%, Sigma-Aldrich) was stirred in acetic acid overnight, washed with ethanol and diethyl ether, respectively, and dried under vacuum. tBA (Sigma-Aldrich, 98%), anisole (TCI America, 99.0%), methyl ethyl ketone (MEK, Fisher Scientific, 99.9%) and DMF (Fisher Scientific, 99.9%) were dried over calcium hydride (CaH_2) and distilled under reduced pressure prior to use. Styrene (St, Sigma-Aldrich, ≥99%) was washed with 10% NaOH aqueous solution and water successively, dried over anhydrous $MgSO_4$ and CaH_2 sequentially, and distilled under reduced pressure. All other reagents were purified by common purification procedures.

Synthesis of Multiarm, Star-Like Poly(tert-Butyl Acrylate) (PtBA) Terminated with Bromine End Groups (Star-like PtBA-Br): Heptakis[2,3,6-tri-O-(2-bromo-2-methylpropionyl)]-β-cyclodextrin (denoted 21Br-β-CD) was prepared according to previous work.[12-13] Using 21Br-β-CD as the macroinitiator, star-like PtBA-Br was synthesized by ATRP of tBA monomers in MEK. Typically, CuBr (35.0 mg), PMDETA (85.0 mg), 21Br-β-CD (50 mg), tBA (21 mL), and MEK (21 mL) were mixed in an argon purged ampule and degassed by three freeze-pump-thaw cycles. The ampule was sealed and dipped in an oil bath at 60°C. After a certain desired time, the reaction was quenched by dipping the ampule in liquid N_2. The mixture was then diluted with THF and passed through a column of neutral alumina to remove the catalyst and subsequently purified by fractional precipitation with methanol/water (v/v = 1/1) as the precipitator. The product was dried at 40°C under vacuum for 2 d.

Synthesis of Multiarm, Star-Like Poly(tert-Butyl Acrylate)-block-Polystyrene (PtBA-*b*-PS) Diblock Copolymer: A typical ATRP reaction was performed as follows. The reaction mixture at styrene: star-like PtBA (i.e., Br in PtBA macroinitiator): copper bromide: PMDETA = 800: 1: 1: 2 (molar ratio) in anisole (1 g St in 1 mL solvent) was placed in a argon purged ampule and degassed by three freeze-pump-thaw cycles. The polymerization was performed at 90°C and quenched by dipping the ampule in liquid N_2 after a certain desired time. The crude product was diluted with THF and passed through a neutral alumina column to remove the catalyst and purified by fractional precipitation with methanol/water (v/v = 1/1) as the precipitator. The product, multiarm, star-like PtBA-*b*-PS was dried at 40°C under vacuum for 2 d.

Synthesis of Multiarm, Star-Like Poly(Acrylic Acid)-block-Polystyrene (PAA-*b*-PS) Diblock Copolymer by Hydrolysis: By hydrolyzing tert-butyl ester groups of PtBA blocks in PtBA-*b*-PS diblock copolymers, amphiphilic star-like PAA-*b*-PS diblock copolymers were created. Briefly, star-like PtBA-*b*-PS (0.4 g) was dissolved in $CHCl_3$ (40 mL), followed by the addition of TFA (3 mL). The reaction mixture was stirred at room temperature for 24 h. After the hydrolysis, the resulting amphiphilic star-like PAA-*b*-PS diblock copolymer was gradually precipitated in $CHCl_3$. The final product was washed with $CHCl_3$, and thoroughly dried under vacuum at 40°C.

Synthesis of PS-Capped Au Nanoparticles: By capitalizing on star-like PAA-*b*-PS diblock copolymers as nanoreactors, the strong coordination interaction between Au

precursors ($HAuCl_4 \cdot 3H_2O$) that are selectively partitioned in the space occupied by inner hydrophilic PAA blocks of star-like PAA-*b*-PS diblock copolymers and the carboxyl groups of PAA led to the nucleation and growth of PS-capped Au nanoparticles. In a typical procedure, star-like PAA-*b*-PS (10 mg) was dissolved in mixed solvents containing DMF (9 mL) and BA (1 mL) at room temperature, followed by the addition of $HAuCl_4 \cdot 3H_2O$ as precursor with TBAB as reducer. The molar ratio of acrylic acid (AA) units in PAA blocks to precursor was set at 1:10 in order to maximize the loading of precursors into the PAA compartment noted above. Compared to BA which is a poor solvent for the outer PS blocks, DMF is a good solvent for both inner PAA and outer PS blocks. Thus, the addition of BA resulted in the formation of structurally stable, sphere-shaped macromolecule composed of inner expanded PAA chain and outer collapsed PS chains. Meanwhile, the precursors $HAuCl_4 \cdot 3H_2O$ were preferentially incorporated in the compartment containing the inner PAA blocks in the mixed solvents of DMF/BA. As noted above, $HAuCl_4 \cdot 3H_2O$ coordinated with the carboxyl groups of PAA blocks within the compartment, leading to the nucleation and growth of Au nanoparticles and eventually forming Au nanoparticles fully occupied the PAA compartment with PS blocks capped on the surface. The solution was stirred under argon at room temperature to ensure that all the chemicals were completely dissolved and then immersed in an oil bath at 60°C under argon for 2 h. The solution was then purified by ultracentrifugation with toluene as solvent and ethanol as precipitant several times to remove remaining precursors and mixed solvents, yielding Au nanoparticles intimately and stably capped with PS.

Synthesis of PS-Capped Ag Nanoparticles: Similarly, PS-capped Ag nanoparticles were synthesized using star-like PAA-*b*-PS diblock copolymers as nanoreactors. The mixed solvent and their ratio as well as the formation mechanism were the same as the synthesis of PS-capped Au nanoparticles described above. The precursors and reducer used were $AgNO_3$ and ethanol, respectively. The molar ratio of AA units in PAA blocks to precursor was set at 1:10 in order to maximize the loading of precursors into the PAA compartment noted above. Likewise, after all the chemicals in the mixture solution stirred under argon at room temperature were completely dissolved, it was immersed in an oil bath at 100°C under argon for 10 h. The same purification procedure as PS-capped Au nanoparticles was taken to yield Ag nanoparticles intimately and stably capped with PS.

Synthesis of Oleylamine-Capped Au Nanoparticles: Oleylamine-capped Au nanoparticles with a diameter of 18.1 ± 4.2 nm were prepared by following the method previously reported.[131] Briefly, $HAuCl_4 \bullet 3H_2O$ (24 mg) and oleylamine (1.2 mL) were dissolved in toluene (1 mL). This mixture was added to a boiling solution of oleylamine (2.09 mL) and toluene (49 mL) to start the reaction. After 2 h, the solution was purified by ultracentrifugation several times with toluene as solvent and ethanol as precipitant to remove unreacted precursors and mixed solvents, yielding oleylamine capped Au nanoparticles.

Characterizations: The number average molecular weight, Mn, and polydispersity index, PDI, were measured by gel permeation chromatography (GPC) equipped with an LC-

20AD HPLC pump and a refractive index detector (RID-10A, 120V) at 35°C. A series of monodisperse polystyrene were used as the standard samples with THF as the eluent at a flow rate of 1.0 mL min^{-1} to calibrate the GPC. All proton nuclear magnetic resonance (1H NMR) spectra of star-like PtBA and star-like PtBA-*b*-PS in $CDCl_3$ and star-like PAA-*b*-PS in d_7-DMF were recorded using a Varian VXR-300 spectroscope. The size and morphology of PS-capped Au and Ag nanoparticles were examined by TEM (JEOL 100; operated at 100 kV) and high-resolution TEM (HRTEM, TECNAIG2 F30; operated at 300 kV). TEM samples were prepared by dropping nanoparticle solution onto a carbon-coated copper TEM grid (300 mesh) and evaporating toluene under ambient condition. In order to observe the PS shell on the surface of nanoparticles, TEM samples were subsequently stained with RuO_4 vapor. The plasmonic properties of nanoparticles were measured by UV–vis spectroscopy (Varian; UV–vis–NIR spectrophotometer, Cary 5000). Mercury low pressure UV lamp at 254 nm (4 W) was used for the irradiation of dilute solution containing PS-capped Au or oleylamine-capped Au nanoparticles. Dynamic light scattering data was acquired using laser light scattering spectrometer (Malvern Autosizer 4700) at 25°C. The crystalline structures of nanoparticles were evaluated by XRD (X'pert PRO, Netherlands).

3.3 Infrared-Emitting Gradient Quantum Dots by Cation Exchange

"Infrared-Emitting Gradient Quantum Dots by Cation Exchange", *In Preparation.*

Abstract

Quantum Dots (QD) for optoelectronic devices have received much attention over the past decade due to their large-area solution processability as well as size-dependent optical properties. Although there has already been remarkable breakthroughs in visible-light emitting QDs for LED applications that has led to commercialization, efficient and stable infrared (IR) emitting QDs that have high potential in optoelectronic applications such as photodetectors and lasers have yet to be fully realized. The major bottleneck for commercialization of these low band gap material are their low chemical stability in ambient environments as well as difficulties in precisely tuning and maintaining the target optical characteristics.

Herein, our strategy utilizes a well-controlled yet facile cation exchange process to create Core/Graded Shell-Shell QDs with precisely tuned spatial composition to accurately control the optical properties in the IR region while simultaneously enhancing stability by utilizing inorganic nanotemplates. We first synthesize CdSe/$Cd_{1-x}Zn_xSe_{1-y}S_y$/ZnS QDs with precisely-tuned spatial composition by utilizing the different chemical reactivity of the four component atoms. Subsequently, we successfully synthesize PbSe/$PbSe_{1-x}S_x$/PbS QDs and AgSe/$AgSe_{1-x}S_x$/AgS QDs with tailored dimensions via a simple yet robust cation exchange process that effectively replaces the Cd and Zn cations with the cations of interest (Pb or Ag) while not disturbing the anionic framework. It is worth noting that bulk of the cation exchange reaction takes place in less than five minutes and continued reaction time

leads to a gradual and controllable increase in either the PbS or AgS shell layer thickness resulting in precision control over optical properties via band gap alignment tuning of the core and shell materials.

Our results show that we can precisely control the absorption properties of our IR QDs from 1000 nm to 3000 nm either by controlling the cation exchange time or by tuning the optical wavelengths of the inorganic nanotemplate (i.e. CdSe/$Cd_{1-x}Zn_xSe_{1-y}S_y$/ZnS QDs). Colloidal stability of the IR QDs in solution are also excellent for several months. Moreover, absorption wavelengths are well-maintained for more than 30 days without any noticeable shifts.

3.3.1 Introduction

Medium wavelength infrared (MWIR) semiconductor nanocrystals (NCs), or so called quantum dots (QDs), are a key player in the design of next generation optoelectronic applications such as scintillators, lasing media, photodetectors, and photoimaging devices.[132-133] Colloidal QDs have interesting optical properties related to their band gaps called photoluminescence (PL) where there is light emission after the absorption of photons. In order to obtain PL and absorbance in the MWIR range (3–5 μm), materials with narrow band gap (< 0.4 eV) are required. Among all narrow band gap semiconductors, lead chalcogenide (PbS, PbSe, and PbTe) QDs have been widely studied. The band gap of these semiconductors can be further fine-tuned by changing their sizes to below their Bohr radii, a phenomenon called quantum confinement effect.[134-136] The exciton Bohr radius of PbS, PbSe, and PbTe is 18, 46, and 150 nm, respectively.[137] Usually the band gap will

decrease with increasing anion atomic number, so one would expect PbTe to have the smallest band gap among the three QDs. Experimental values of direct energy band gap for bulk PbS, PbSe, and PbTe at 300 K, however, are 0.41 eV, 0.27 eV, and 0.31 eV, respectively.[138] Interestingly, PbSe, instead of PbTe, has the narrowest band gap among the three lead chalcogenides, and there is still no satisfactory explanation of this anomaly at present.[138] In addition to the lowest band gap, PbSe is also known for its efficient multiple exciton generation (MEG) that may greatly improve efficiencies in solar cells as well as photodetectors (MEG is more efficient in PbSe than in PbS).[139-140] PbSe QDs, however, also has its own shortcomings which is low stability under ambient environments (e.g. susceptible to oxidation in air).[141-144] PbSe QDs dispersed in hexane and stored in air can undergo oxidation of up to 50% of its original volume in only a few hours.[144]

PbSe QDs have been coated with various materials to passivate the dangling Pb (e.g. $PbCl_2$[141], PbS[145]) or Se (e.g. CdSe layer) sites on the QD surface to improve their stability and have shown great advancements in stability in ambient environments. Among them, a novel synthesis method developed by Beard et al. demonstrating a facile synthesis method for stable PbSe QDs with a thin $PbCl_2$ outer coating via cation exchange (CE) of CdSe[141] or ZnSe[146] QDs utilizing $PbCl_2$ as the reactant caught our attention in particular. Not only was the CE reaction successful, but they noted that by increasing the CE time, the QD size will continue to increase due to the Ostwald ripening effect even after the CE process is complete.[147] Moreover, although the initial CE was instantaneous, the following growth phase was conducted over minutes or even hours, thus allowing more precise control over dimensions. Our group has adopted this CE process to core/shell QD systems

in order to fine tune the interaction between the core and shell material by precisely controlling the shell thickness over time scales that are highly reproducible.

We have focused, especially in controlling the PbS shell thickness of PbSe/PbS core/shell QDs as they have a type-II core/shell QD structure (i.e. $E_c(PbS) > E_c(PbSe) > E_v(PbS) > E_v(PbSe)$[148] which means the spread of the hole wavefunction across the PbSe and PbS material may occur resulting in a red shift in PL emission (relative to that of the PbSe core) as well as extended exciton lifetimes.[133, 149] Moreover, thick shell layers are known to cause suppressed absorption intensity of the first exciton peak and induce a larger stokes shift in QDs. Furthermore, the CdSe/$Cd_{1-x}Zn_xSe_{1-y}S_y$/ZnS core/shell QDs that has been utilized as the nanotemplate for CE, has a gradient interface layer between the CdSe and ZnS layer which has also been demonstrated to show suppressed absorption of the first-exciton peak. In addition, QY of PbSe/$PbSe_{1-y}S_y$ (y=0.5) core-alloyed shell QDs was reported to be higher at 65% compared to PbSe core only QDs (40%) or PbSe/PbS core-shell QDs (50%).[149] Suppressed first exciton peak absorption, PL red-shift, and high QY may be important to tackle, especially for PbSe based QDs which showed anti-stokes shift as the size of plain PbSe QD size increased. For instance, 4 nm PbSe QDs showed a stokes shift of 100meV while that of 6.1 nm PbSe QDs was -10 meV.[149]

Herein, we report on a facile method to synthesize PbSe/$PbSe_{1-y}S_y$/PbS QDs and AgSe/$AgSe_{1-x}S_x$/AgS QDs with precisely tunable dimensions by controlling both the (1) CE reaction time as well as (2) initial inorganic nanotemplate (i.e. CdSe/$Cd_{1-x}Zn_xSe_{1-y}S_y$/ZnS QD) dimensions. The CE reaction involves an instantaneous CE reaction followed by slow growth of the PbS shell layer which is simply performed by extending the CE time, which not only improves the QD stability, but also allows fine-tuning of the QD's emission

wavelength. Furthermore, by first synthesizing a CdSe/$Cd_{1-x}Zn_xSe_{1-y}S_y$/ZnS QD which is more readily characterizable (i.e. CdSe and ZnS have distinct lattice dimensions) and then performing CE to create PbSe/$PbSe_{1-y}S_y$/PbS QDs, we can have clearer understanding of the relationship between the crystal dimensions and optical properties. PbSe/$PbSe_{1-y}S_y$ QDs[149-150] synthesized directly is difficult to characterize as the crystal structure of PbSe and PbS is very similar. It is also worth mentioning that we can prevent the PbSe material from ever being exposed to air because it is directly surrounded by a thick PbS shell in-situ, thus ensuring improved stability. Our final goal is to simultaneously improve stability while also tuning emission properties. By focusing on the synthesis and characterizations of PbSe QDs which have the narrowest band gap among three lead chalcogenides we aim to create stable MWIR QDs.

3.3.2 Results/Discussion

Figure 3.38a (right column) depicts the schematic representation of CdSe/$Cd_{1-x}Zn_xSe_{1-y}S_y$/ZnS QDs with a composition gradient interface between the CdSe core and ZnS shell and also a thick passivating ZnS shell layer. The gradient interface between the core and shell material allows for the delocalization of electrons into the interfacial layer thus allowing a red-shift in the optical properties compared to the CdSe core size while also reducing the strain and instability caused by the lattice mismatch between the core and shell material. This composition gradient interface is achieved by capitalizing on the higher reactivity between Cd and Se compared to that between Zn and Se, thus allowing more Cd to occupy the inner core and more Zn to occupy the outer shell. The thick ZnS shell is achieved by adding an excess of Zn and S compared to Cd and Se. **Figure 3.38a (left**

column) & Figure 3.38b shows absorption and emission spectra as well as TEM images of the chemical composition gradient QDs prepared at 240^{o}C using 2.45 nm green-emitting CdSe QDs as seeds. The diameter of the QDs (**Figure 3.38b**) increased from 2.45 nm for the as-prepared CdSe QD core (**Figure 3.38b**; QD size was 2.45 nm when calculated from the first exciton peak wavelength[151]) to 5.25 nm for CdSe/$Cd_{1-x}Zn_xSe_{1-y}S_y$/ZnS QDs with a thin ZnS outer shell and 7.40 nm for CdSe/$Cd_{1-x}Zn_xSe_{1-y}S_y$/ZnS QDs with a thick ZnS outer shell. Due to the suppressed absorption peak, it is unclear where the absorption peak is exactly situated for the CdSe/$Cd_{1-x}Zn_xSe_{1-y}S_y$/ZnS QDs. However, from the PL peak position shift of 13 nm, we can estimate a 6.5% increase of the effective core diameter due to the gradient interface between the core and shell material. As one monolayer of ZnS is 3.1 angstroms, the 5.25 nm CdSe/$Cd_{1-x}Zn_xSe_{1-y}S_y$/ZnS QDs have 4.3 ZnS layers while the 7.40 nm CdSe/$Cd_{1-x}Zn_xSe_{1-y}S_y$/ZnS QDs have 7.7 ZnS layers (monolayer of ZnS is 3.1 angstrom between consecutive planes along the [002] axis in bulk wurtzite ZnS[152]). **Figure 3.39** summarizes the absorption and emission properties of three CdSe/$Cd_{1-x}Zn_xSe_{1-y}S_y$/ZnS QDs each emitting a red, green, and blue color (from here on denoted Red, Green, and Blue QDs). All three QDs have been synthesized by utilizing the chemical reactivity differences between the reactants to create a gradient interface but the specific synthesis procedures differ to achieve the three different emission colors (See Experimental Section for detailed synthesis procedure).

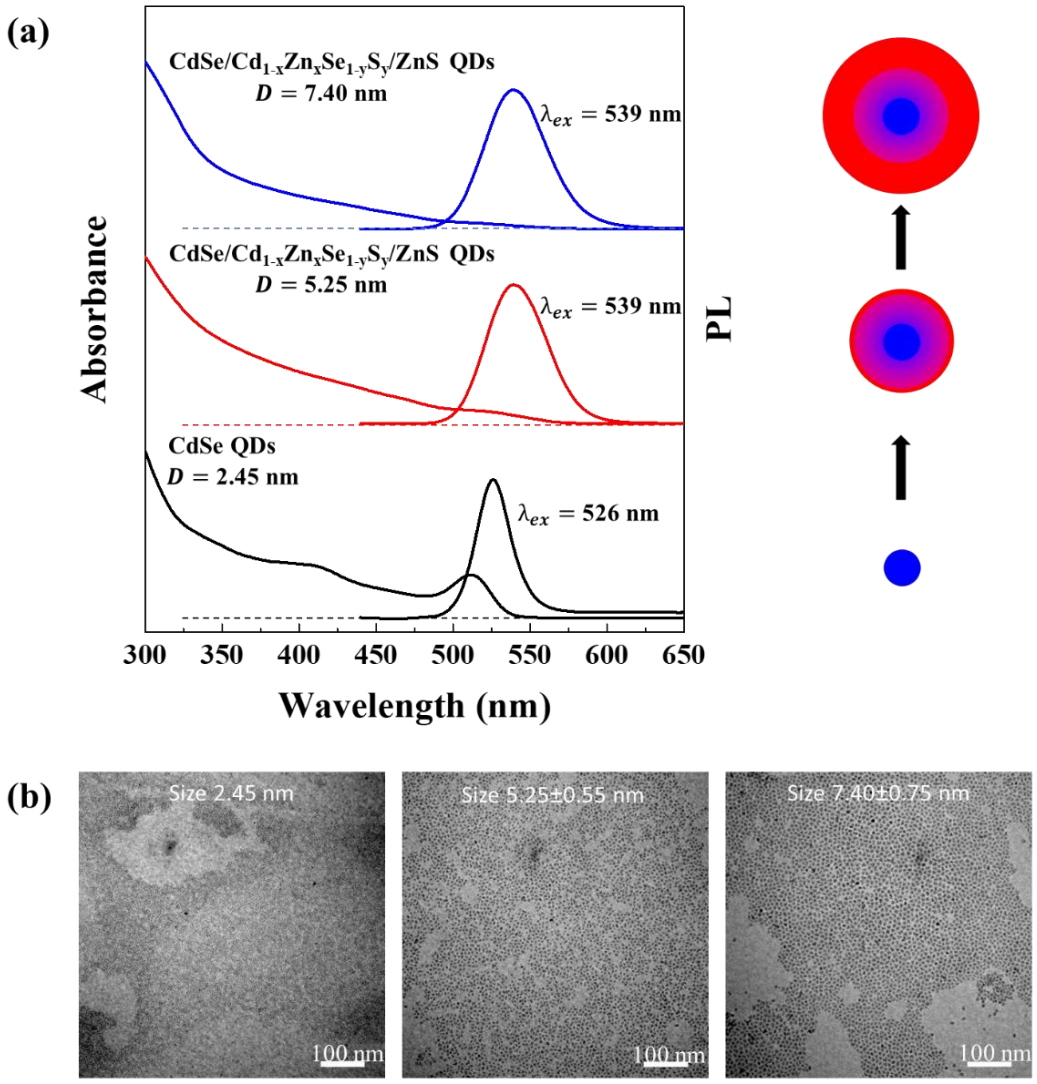

Figure 3.38 Tuning Absorption Wavelengths. (a) The absorption and emission spectra of $CdSe/Cd_{1-x}Zn_xSe_{1-y}S_y/ZnS$ QDs in which the diameter of originally green-emitting CdSe QD core is 2.45 nm. (b) TEM images of – left column: plain CdSe QDs as core (green-emitting; D = 2.45 nm), middle column: $CdSe/Cd_{1-x}Zn_xSe_{1-y}S_y/ZnS$ QDs with thin ZnS shell (D = 5.25 nm), right column: $CdSe/Cd_{1-x}Zn_xSe_{1-y}S_y/ZnS$ QDs with thick ZnS shell (D = 7.40 nm). All chemical composition gradient QDs were synthesized using 2.45 nm green-emitting CdSe QDs as seeds.

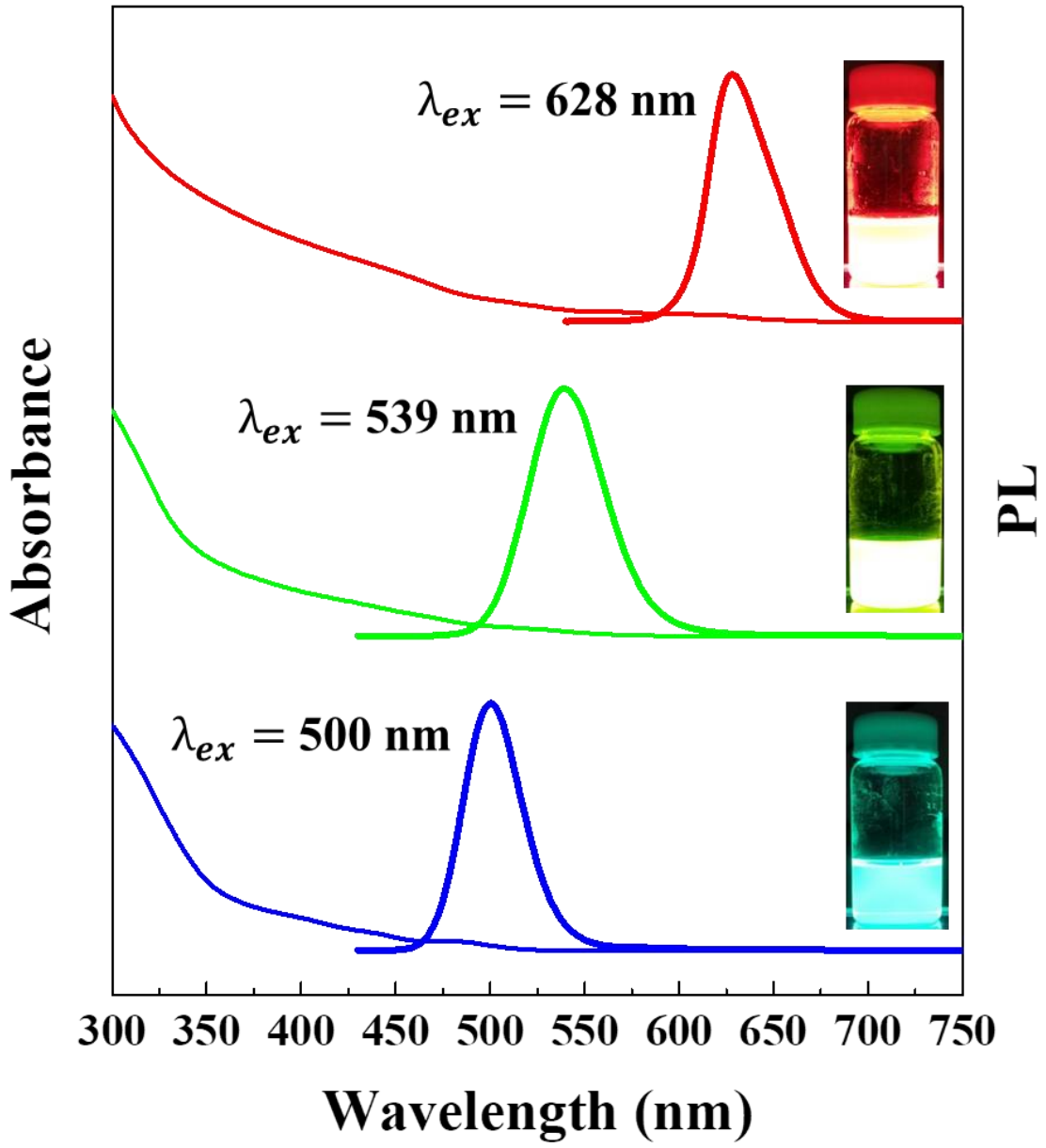

Figure 3.39 Absorption and emission properties of three CdSe/$Cd_{1-x}Zn_xSe_{1-y}S_y$/ZnS QDs each emitting in the red, green, and blue wavelength regime.

Figure 3.40a describes the synthetic scheme for converting the highly stable CdSe/$Cd_{1-x}Zn_xSe_{1-y}S_y$/ZnS QDs to PbSe/$PbSe_{1-y}S_y$/PbS QDs in a one-step CE reaction. The CE process is driven by the difference in solvation energy for the cations (i.e. the ligand's propensity for selective ion binding).[147, 153-154] It is worth emphasizing that after initial CE, the PbS shell thickness continues to grow and this process is finely tunable by simply changing the reaction time. We can understand this process in combination to the Ostwald ripening effect in which smaller particles dissolve and redeposit on larger particles. The ability to precisely control the PbS shell thickness over a PbSe core is quite important as PbSe/$PbSe_{1-y}S_y$/PbS QDs are Type-II core/shell QDs in which the alignment of the band gap may allow emission red-shift as a function of the shell thickness.

Figure 3.40b & Figure 3.40c shows TEM images of the chemical composition gradient PbSe/$PbSe_{1-y}S_y$/PbS QDs prepared at 190^{o}C using CdSe/$Cd_{1-x}Zn_xSe_{1-y}S_y$/ZnS QDs (**Figure 3.40b** – CE from 7.40 nm green-emitting CdSe/$Cd_{1-x}Zn_xSe_{1-y}S_y$/ZnS QDs; **Figure 3.40c** – CE from 7.57 nm red-emitting CdSe/$Cd_{1-x}Zn_xSe_{1-y}S_y$/ZnS QDs) as templates. From the TEM image we can see that both QDs before and after CE are both quite monodisperse. One direct and simple indication of CE can be observed from the inset, in which the normally green or red cadmium-based QDs have been fully converted to a dark-brown color which is representative of lead-based QDs. Also from the inset, we can note that the lead-based QD is colloidally stable in solution. Even after 6 months of storage in air at RT, we did not observe any precipitation. The diameter of the QDs increased from 7.40±0.75 nm for the as-prepared CdSe/$Cd_{1-x}Zn_xSe_{1-y}S_y$/ZnS QDs QDs (**Figure 3.38b**) to 7.76±0.41 nm for PbSe/$PbSe_{1-y}S_y$/PbS QDs (Green QD CE for 5 min) to 12.14±0.80 nm for PbSe/$PbSe_{1-y}S_y$/PbS QDs (Green QD CE for 25 min), and eventually to 15.03±0.61 nm

for PbSe/$PbSe_{1-y}S_y$/PbS QDs (Green QD CE for 125 min). A monolayer of PbS is 1.2 nm.[150] The 7.57±0.73 nm red-emitting CdSe/$Cd_{1-x}Zn_xSe_{1-y}S_y$/ZnS QDs also show a very similar trend where the size increase is precisely controllable by a function of CE time. The QD size increases via two distinct processes. First of all, the crystal density of the reactant QD is much lower than that of the product QD. Although the volumetric change in the core material from CdSe to PbSe is relatively small (4.5% increase from zinc-blende CdSe or 7.5% increase from wurtzite CdSe), the volumetric change in the shell material from ZnS to PbS is significant (32.1% increase from zinc-blende ZnS). Secondly, it has been proposed that the material to grow larger QDs are provided via the Ostwald ripening effect in which smaller QDs dissolve and redeposit on larger QDs. We observed very small QDs below 3 nm in the system after CE in which was removed in the purification steps. One limitation of the CE of core/shell QDs may be that it is not clear when the core material (Se) will dissolve and deposit on the PbSe/$PbSe_{1-y}S_y$/PbS QD shell. The reactant amount of Se compared to S, however, is very small (molar ratio 1:45) and most of the Se is situated near the core of the QD, that they may not have a significant effect on optical properties.

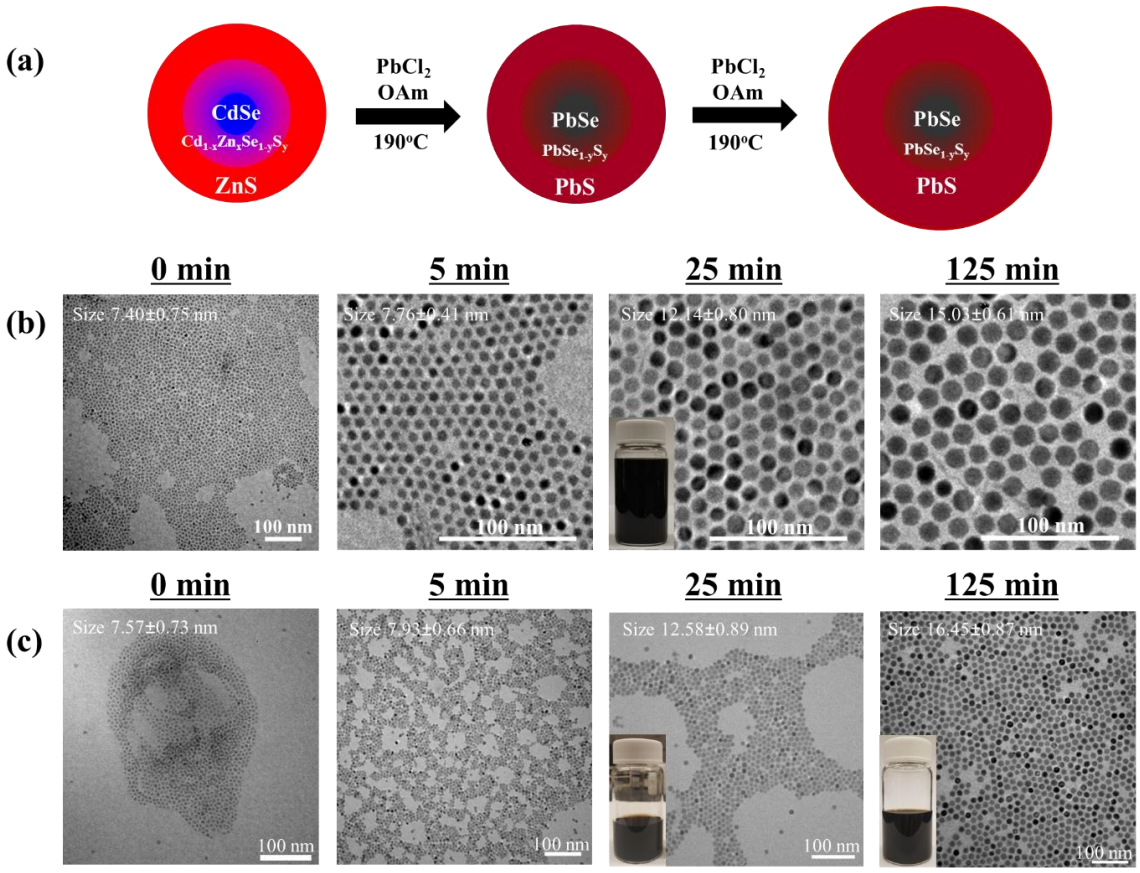

Figure 3.40 Cation Exchange of CdSe/$Cd_{1-x}Zn_xSe_{1-y}S_y$/ZnS QDs into PbSe/$PbSe_{1-y}S_y$/PbS QDs. (a) Schematic representation of crafting PbSe/$PbSe_{1-y}S_y$/PbS QDs via cation exchange. TEM images of (b) PbSe/$PbSe_{1-y}S_y$/PbS QDs synthesized by utilizing green-emitting CdSe/$Cd_{1-x}Zn_xSe_{1-y}S_y$/ZnS QDs as nanotemplates and (c) PbSe/$PbSe_{1-y}S_y$/PbS QDs synthesized by utilizing red-emitting CdSe/$Cd_{1-x}Zn_xSe_{1-y}S_y$/ZnS QDs as nanotemplates. The left column in (b) and (c) are TEM images of the corresponding green and red emitting CdSe/$Cd_{1-x}Zn_xSe_{1-y}S_y$/ZnS QDs that has been used as nanotemplates.

Table 3.7 Expected material property changes before and after cation exchange.

Cation Exchange	Density	Molar Weight	Molar Volume	Expected Volume Increase
CdSe (WZ) → PbSe (RS)	5.81 g/cm^3 (CdSe) 8.10 g/cm^3 (PbSe)	191.37 g/mol (CdSe) 286.16 g/mol (PbSe)	32.94 cm^3/mol (CdSe) 35.33 cm^3/mol (PbSe)	7.26%
CdSe (ZB) → PbSe (RS)	5.66 g/cm^3 (CdSe) 8.10 g/cm^3 (PbSe)	191.37 g/mol (CdSe) 286.16 g/mol (PbSe)	33.81 cm^3/mol (CdSe) 35.33 cm^3/mol (PbSe)	4.50%
CdS (ZB) → PbS (RS)	4.82 g/cm^3 (CdS) 7.60 g/cm^3 (PbS)	144.46 g/mol (CdS) 239.30 g/mol (PbS)	29.97 cm^3/mol (CdS) 31.49 cm^3/mol (PbS)	5.06%
ZnSe (ZB) → PbSe (RS)	5.27 g/cm^3 (CdSe) 8.10 g/cm^3 (PbSe)	144.35 g/mol (CdSe) 286.16 g/mol (PbSe)	27.39 cm^3/mol (CdSe) 35.33 cm^3/mol (PbSe)	29.0%
ZnS (ZB) → PbS (RS)	4.09 g/cm^3 (ZnS) 7.60 g/cm^3 (PbS)	97.47 g/mol (ZnS) 239.30 g/mol (PbS)	23.83 cm^3/mol (ZnS) 31.49 cm^3/mol (PbS)	32.1%

Figure 3.41 shows HRTEM images of PbSe/PbSe$_{1-y}$S$_y$/PbS QDs with excellent crystallinity. Due to the extremely small crystallographic mismatch between PbSe and PbS of only 3%[149] the QDs appear to be a single crystal. The lattice spacing, however, show values that are intermediate of the characteristic values for PbSe (#78-1903) and PbS (#78-1900). For instance, PbSe/PbSe$_{1-y}$S$_y$/PbS QDs (Green QD CE for 5 min; **Figure 3.41a**) have a lattice spacing of 0.350 nm (1 1 1) that is in between that of 0.353 nm for PbSe and

that of 0.342 nm for PbS. This observation also agrees well with the intermediate XRD peaks that will be discussed in the later sections.

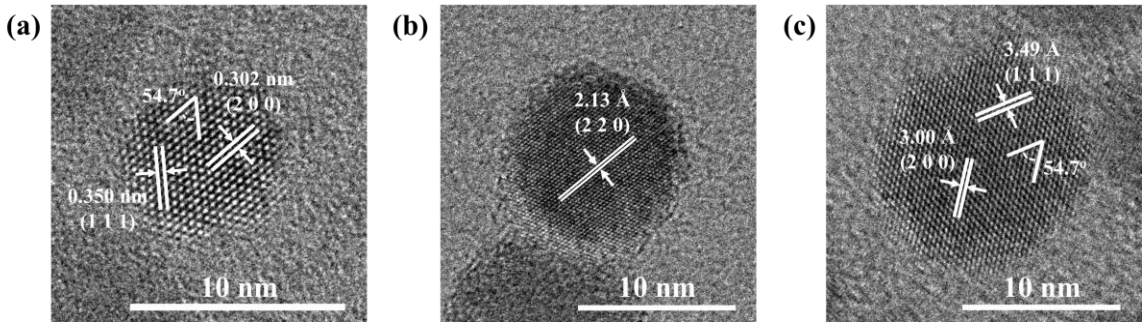

Figure 3.41 HRTEM images of PbSe/PbSe$_{1-y}$S$_y$/PbS QDs. (a) PbSe/PbSe$_{1-y}$S$_y$/PbS QDs cation exchanged for 5 min from 7.40 nm green-emitting CdSe/Cd$_{1-x}$Zn$_x$Se$_{1-y}$S$_y$/ZnS QDs (b) PbSe/PbSe$_{1-y}$S$_y$/PbS QDs cation exchanged for 25 min from 7.40 nm green-emitting CdSe/Cd$_{1-x}$Zn$_x$Se$_{1-y}$S$_y$/ZnS QDs (c) PbSe/PbSe$_{1-y}$S$_y$/PbS QDs cation exchanged for 25 min from 7.57 nm red-emitting CdSe/Cd$_{1-x}$Zn$_x$Se$_{1-y}$S$_y$/ZnS QDs

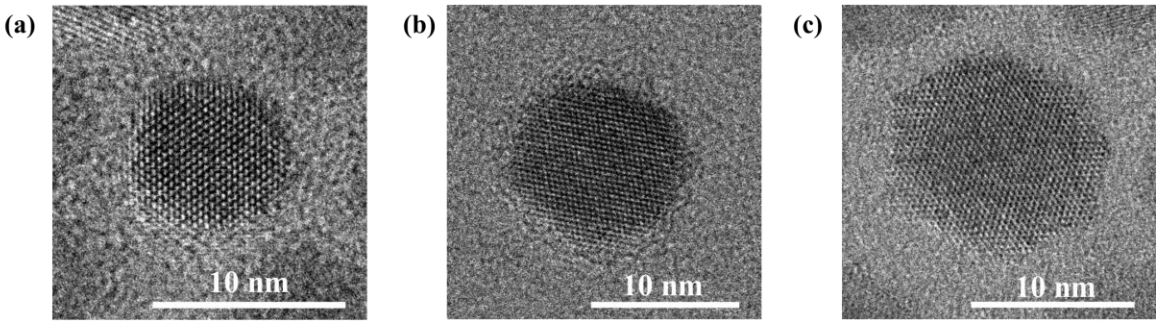

Figure 3.42 Additional HRTEM images of PbSe/PbSe$_{1-y}$S$_y$/PbS QDs. (a) PbSe/PbSe$_{1-y}$S$_y$/PbS QDs cation exchanged for 5 min from 7.40 nm green-emitting CdSe/Cd$_{1-x}$Zn$_x$Se$_{1-y}$S$_y$/ZnS QDs (b) PbSe/PbSe$_{1-y}$S$_y$/PbS QDs cation exchanged for 25 min from 7.40 nm

green-emitting CdSe/$Cd_{1-x}Zn_xSe_{1-y}S_y$/ZnS QDs (c) PbSe/$PbSe_{1-y}S_y$/PbS QDs cation exchanged for 25 min from 7.57 nm red-emitting CdSe/$Cd_{1-x}Zn_xSe_{1-y}S_y$/ZnS QDs

Figure 3.43a shows the suppressed absorption peak of PbSe/$PbSe_{1-y}S_y$/PbS QDs due to the thick outer PbS shell. The first exciton absorption peak is completely unobservable when viewed over the entire spectrum. If we zoom in as shown in **Figure 3.43b**, we can now observe the presence of a weak first exciton absorption peak at around 1800 nm. As the PbSe/$PbSe_{1-y}S_y$/PbS QD size increases from 7.76 nm (Green QDs CE for 5 min) to 12.14 nm (Green QDs CE for 25 min), however, even this absorption peak at 1800 nm is clearly suppressed due to the absorption primarily from the thick PbS shell. Suppression of the first exciton absorption peak was not observed for PbSe/$PbSe_{1-y}S_y$ QDs (synthesized via CE of CdSe/$Cd_{1-x}Zn_xSe_{1-y}S_y$ QDs without a ZnS shell; See Experimental Section) that did not have a PbS shell as shown in **Figure 3.44**.

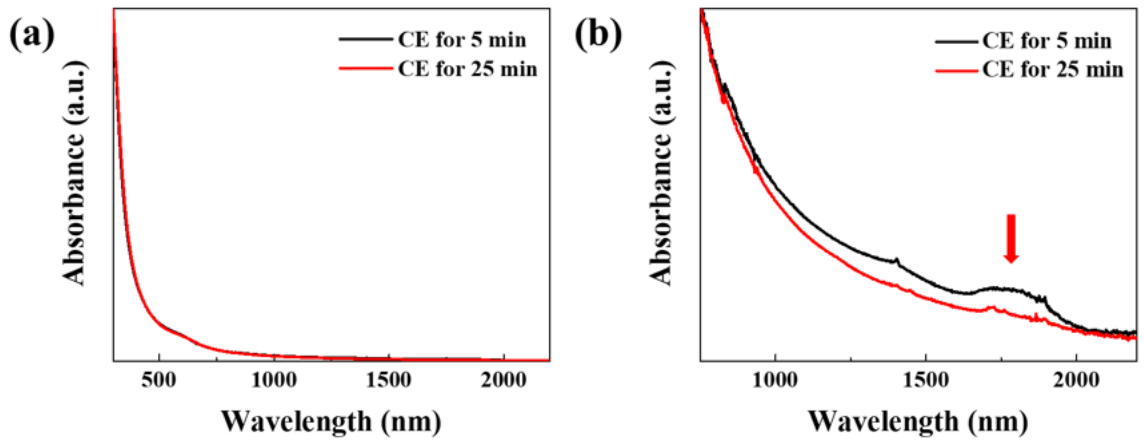

Figure 3.43 Suppressed Absorbance for PbSe/PbSe$_{1-y}$S$_y$/PbS QDs. Absorption spectra of PbSe/PbSe$_{1-y}$S$_y$/PbS QDs synthesized via cation exchange of green-emitting CdSe/Cd$_{1-x}$Zn$_x$Se$_{1-y}$S$_y$/ZnS QDs as nanotemplates for different reaction times. Legend indicates the time spent on cation exchange reactions. Left column shows the overall absorption spectra and the right column shows an enlarged absorption spectra to visualize the presence of first exciton absorption peak.

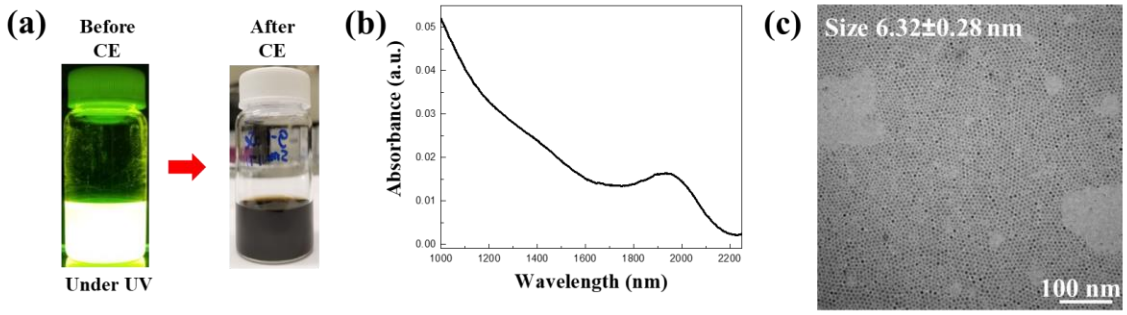

Figure 3.44 PbSe/PbSe$_{1-y}$S$_y$ QDs cation exchanged for 5 min from CdSe/Cd$_{1-x}$Zn$_x$Se$_{1-y}$S$_y$. (a) QD solution before and after cation exchange for 5 min (left - CdSe/Cd$_{1-x}$Zn$_x$Se$_{1-y}$S$_y$ QD solution under UV excitation; right - PbSe/PbSe$_{1-y}$S$_y$ QD solution under ambient light) (b) Absorption spectrum of PbSe/PbSe$_{1-y}$S$_y$ QDs (c) TEM image of PbSe/PbSe$_{1-y}$S$_y$ QDs.

Figure 3.45 shows the proposed CE mechanism of CdSe/$Cd_{1-x}Zn_xSe_{1-y}S_y$/ZnS QDs to PbSe/$PbSe_{1-y}S_y$/PbS QDs via XRD analysis. (The XRD graph to the left and schematic to the right are color coded to match each other) (**Figure 3.46** shows the relative position of the PbSe/$PbSe_{1-y}S_y$/PbS QD's XRD peaks in relation to those for PbSe, PbS, CdSe, and ZnS) After just 30 seconds of CE, the characteristic peaks for the CdSe/$Cd_{1-x}Zn_xSe_{1-y}S_y$/ZnS QDs completely disappear, and only those for either PbSe or PbS are observed under XRD analysis. The XRD peaks overlap more precisely with that of PbS (#78-1900) in the earlier stages of CE (i.e. CE for 30 s & 5 min). As shown in **Figure 3.45** (black & red box), it is likely that the CE process begins from the outer shell material, creating an overwhelming signal from the outer PbS shell material compared to that of the PbSe core material. As the CE process continues towards the inner core (i.e. CE for 25 min), the XRD peaks shift more towards that of the PbSe (#78-1903) material, thus positioning themselves intermediate between that of the PbSe and PbS. Similar observations have been previously made in literature where alloy structures of two compounds show intermediate XRD peaks.[155] As PbSe/$PbSe_{1-y}S_y$/PbS QDs also have an interfacial gradient layer, where there is a mixture of PbSe and PbS material, the intermediate XRD peak position supports the successful synthesis of PbSe/$PbSe_{1-y}S_y$/PbS QDs with an interfacial composition gradient. As the reaction continues to 125 min, the characteristic peaks shift back to higher angles which overlaps more with that of the PbS (#78-1900) peaks. This is because, as the CE process continues, a thicker PbS shell is formed on the outside of PbSe/$PbSe_{1-y}S_y$/PbS QDs, so that the overwhelming signal from the PbS material dominates. We've also repeated the same measurements for the PbSe/$PbSe_{1-y}S_y$/PbS QDs cation exchanged from green-emitting CdSe/$Cd_{1-x}Zn_xSe_{1-}$

$_{y}S_{y}$/ZnS QDs (**Figure 3.47** & **Figure 3.48**). The results show a similar trend to that observed in **Figure 3.45**, however, the shift to lower angles (XRD peaks for PbSe are situated at lower angles compared to PbS) after 25 minutes is less pronounced (**Figure 3.49**), which strongly corroborates our proposed CE mechanism. In other words, for the green-emitting CdSe/$Cd_{1-x}Zn_xSe_{1-y}S_y$/ZnS QDs there is less Se compared to that in the red-emitting CdSe/$Cd_{1-x}Zn_xSe_{1-y}S_y$/ZnS QDs, thus there will be less PbSe in the final cation exchanged QDs as well, resulting in a less pronounced shift towards lower angles where the characteristic peaks of PbSe is situated. To further verify complete CE from Cd and Zn into Pb, PL of the PbSe/$PbSe_{1-y}S_y$/PbS QD solution was measured along the visible wavelengths. **Figure 3.50**a shows a comparison between the PL of red-emitting CdSe/$Cd_{1-x}Zn_xSe_{1-y}S_y$/ZnS QDs and the PL from the corresponding PbSe/$PbSe_{1-y}S_y$/PbS QDs (Red QD CE for 30 s). After only 30 s of CE, PL across the visible spectrum completely disappeared. Even if we try to magnify the PbSe/$PbSe_{1-y}S_y$/PbS QD PL curve in **Figure 3.50a**, there is not even a small bump that may indicate PL emission. We continued on to test the device limits to measure even the smallest PL from the QDs while exciting the QDs with the strongest excitation possible from the spectrophotometer. (excitation slit width 15 nm; emission slit width 20 nm; sensitivity set to high) This setting would not be used in normal circumstances as even QDs with extremely QY (e.g. <1%) will show PL counts over the detection limit. Under these extreme settings, we were able to observe a small PL peak from the PbSe/$PbSe_{1-y}S_y$/PbS QDs cation exchanged for 30 s and 5 min. The small PL peak, however, completely disappeared for PbSe/$PbSe_{1-y}S_y$/PbS QDs cation exchanged for 25 min further corroborating our proposed schematic in **Figure 3.45** in which complete cation exchange takes place by 25 min.

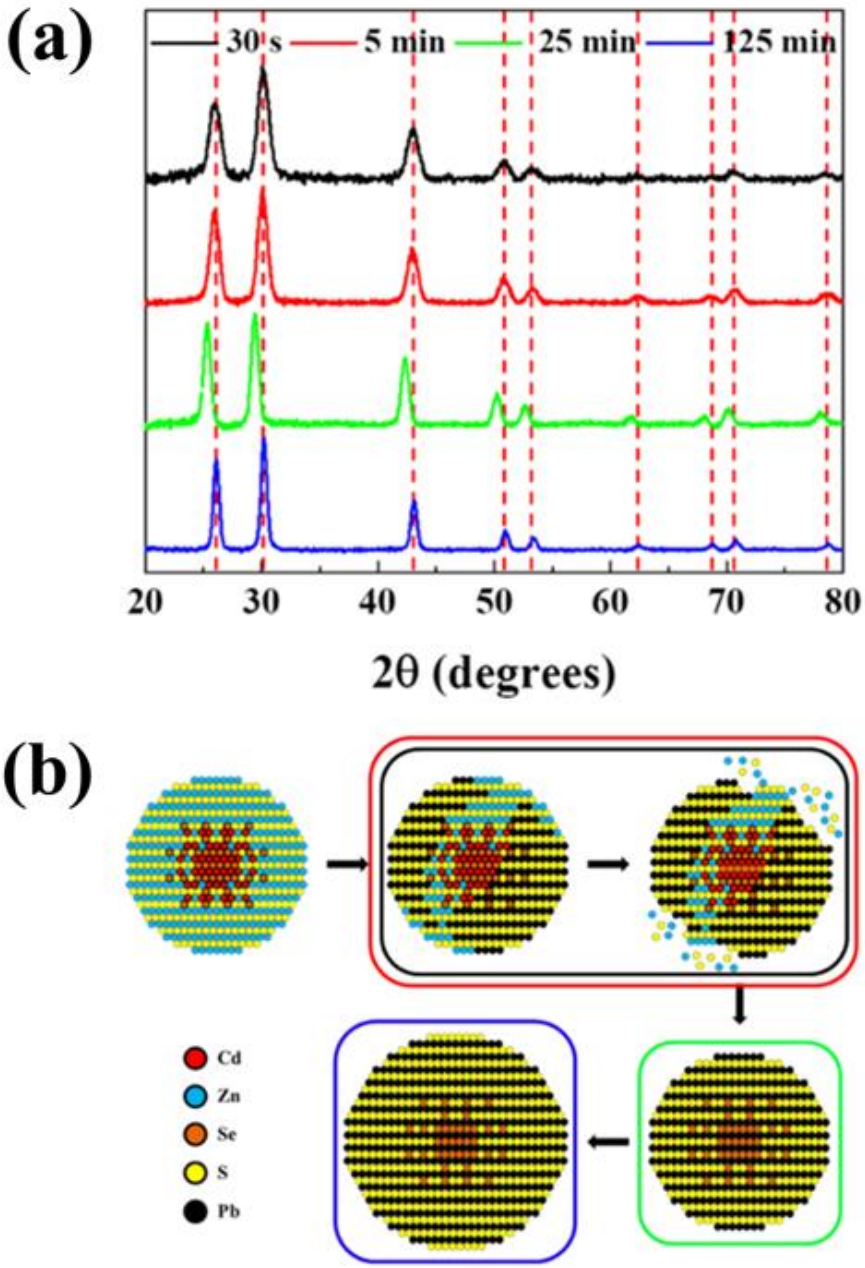

Figure 3.45 Cation exchange mechanism of $CdSe/Cd_{1-x}Zn_xSe_{1-y}S_y/ZnS$ QDs to $PbSe/PbSe_{1-y}S_y/PbS$ QDs verified by XRD. (a) XRD of $PbSe/PbSe_{1-y}S_y/PbS$ QDs after different cation exchange times (30 s, 5 min, 25 min, 125 min) from 7.57 nm red-emitting $CdSe/Cd_{1-x}Zn_xSe_{1-y}S_y/ZnS$ QDs (b) Schematic showing expected cation exchange mechanism based on XRD data. The XRD data and schematic is color coded.

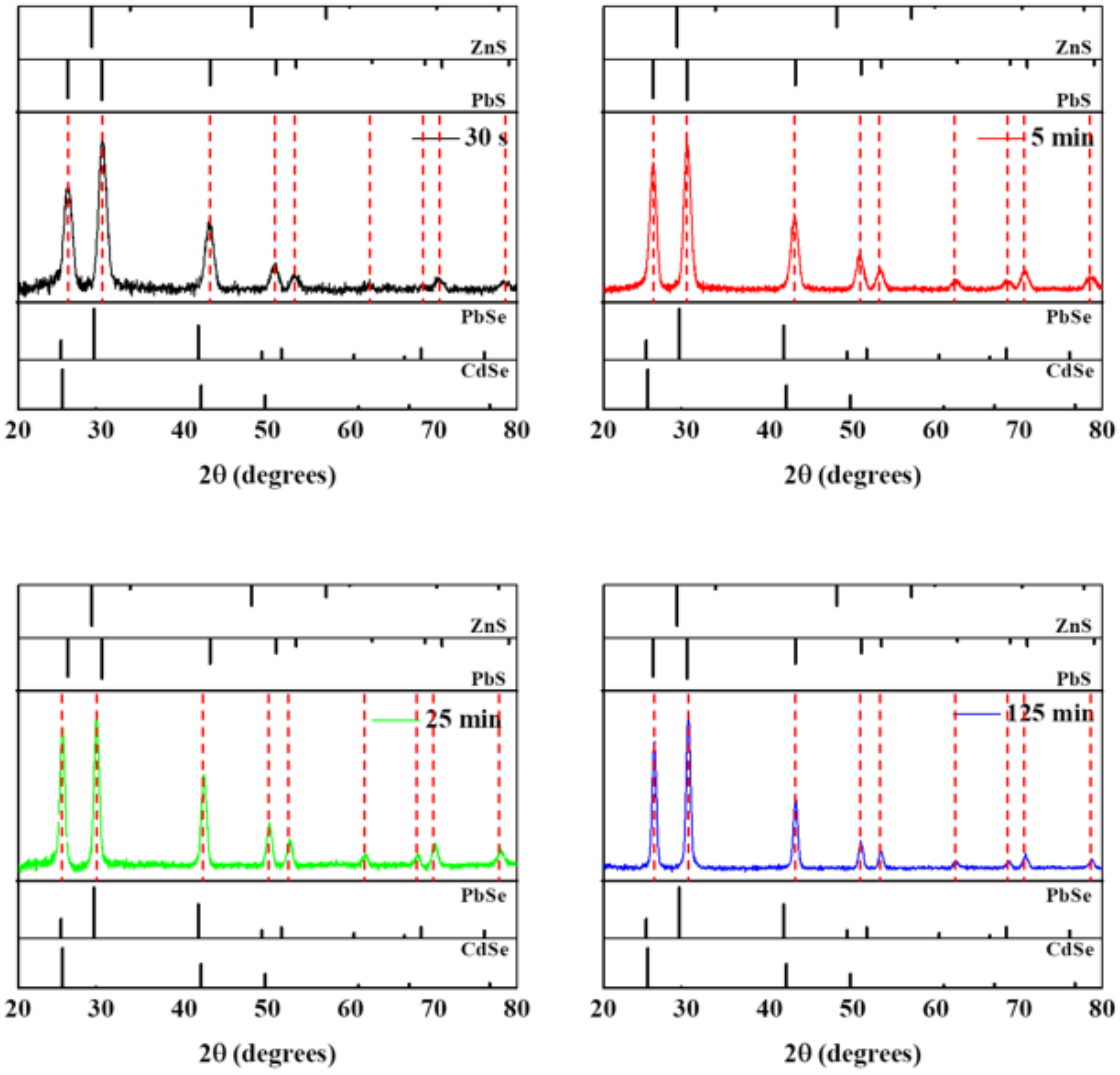

Figure 3.46 XRD of PbSe/$PbSe_{1-y}S_y$/PbS QDs after different cation exchange times (30 s, 5 min, 25 min, 125 min) from 7.57 nm red-emitting CdSe/$Cd_{1-x}Zn_xSe_{1-y}S_y$/ZnS QDs.

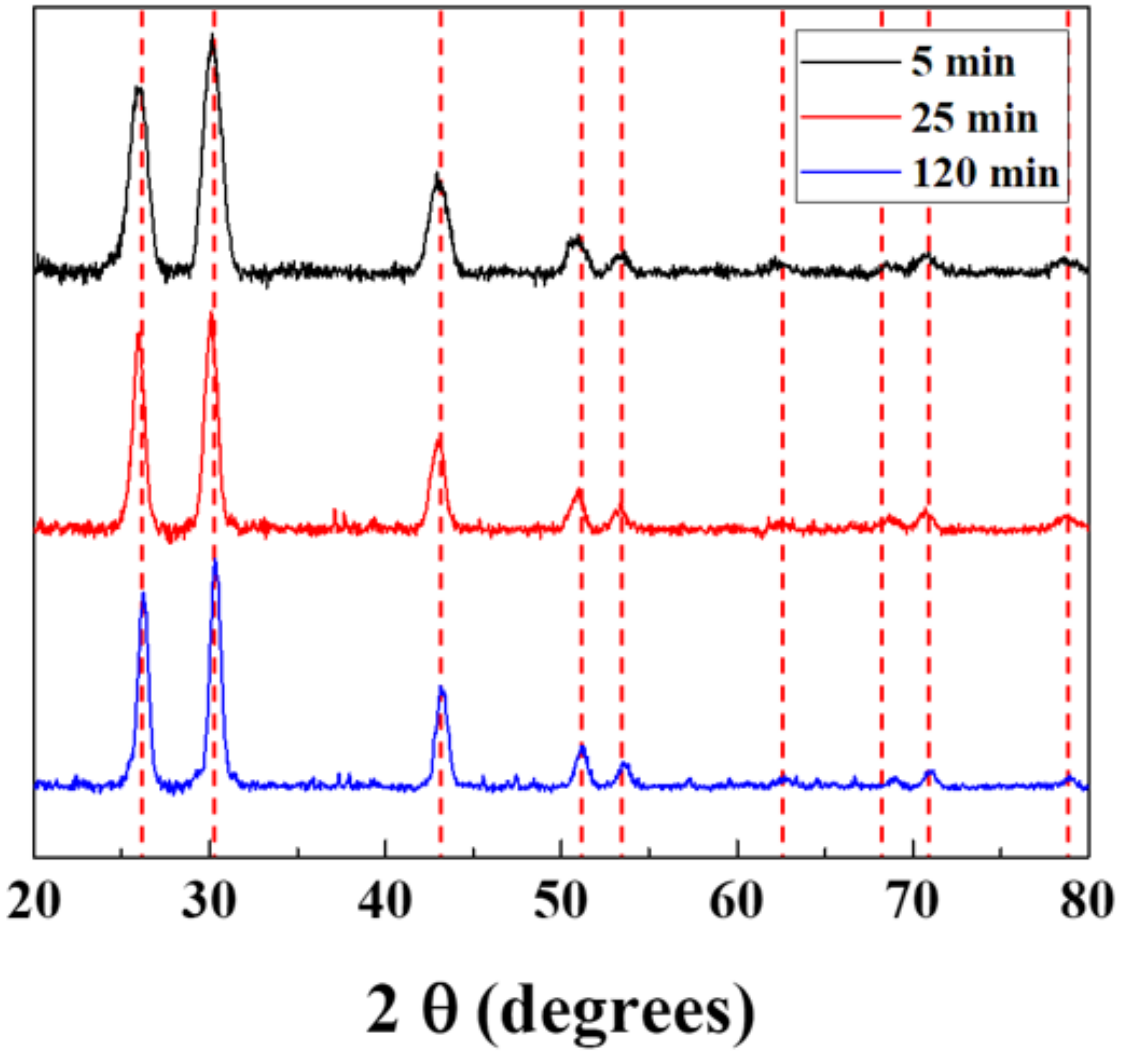

Figure 3.47 XRD of PbSe/$PbSe_{1-y}S_y$/PbS QDs after different cation exchange times (30 s, 5 min, 25 min, 125 min) from 7.40 nm green-emitting CdSe/$Cd_{1-x}Zn_xSe_{1-y}S_y$/ZnS QDs.

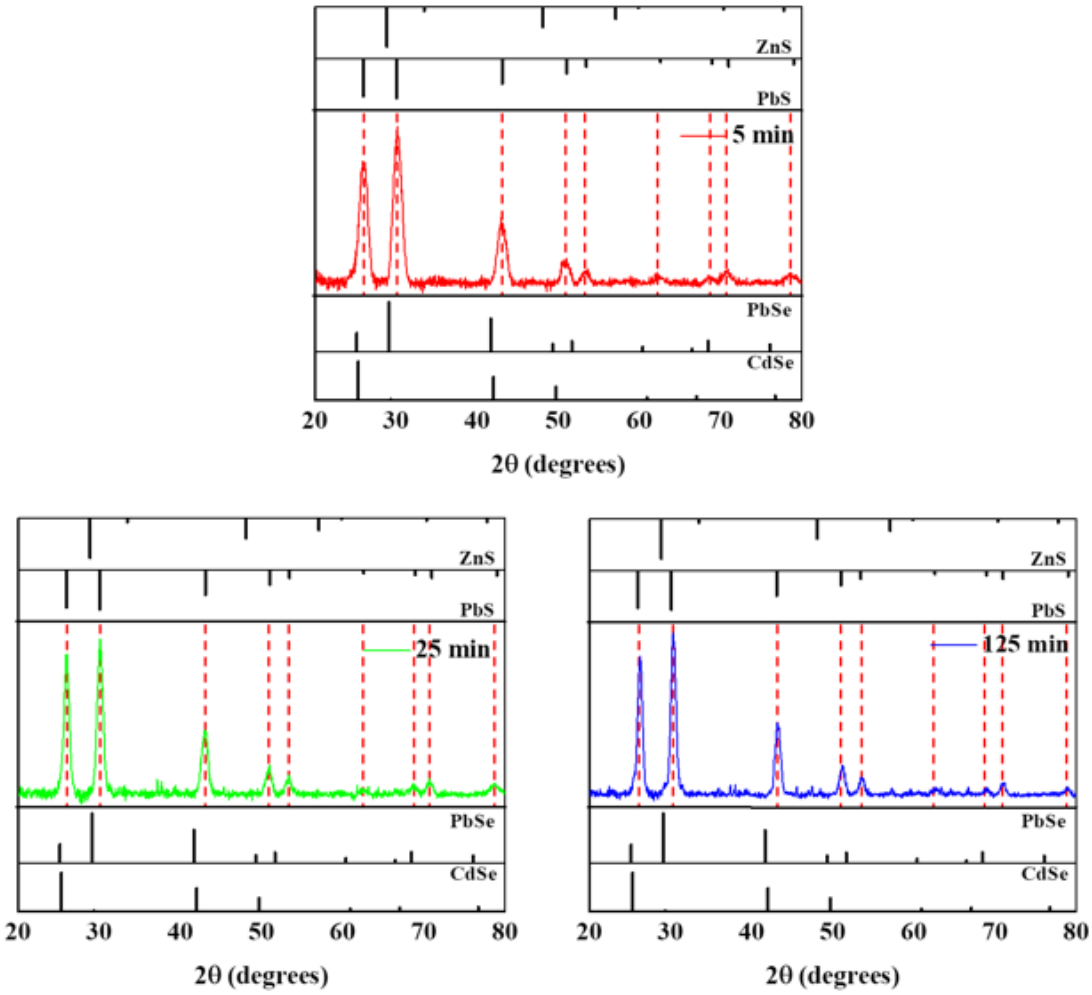

Figure 3.48 XRD of PbSe/$PbSe_{1-y}S_y$/PbS QDs after different cation exchange times (30 s, 5 min, 25 min, 125 min) from 7.40 nm green-emitting CdSe/$Cd_{1-x}Zn_xSe_{1-y}S_y$/ZnS QDs.

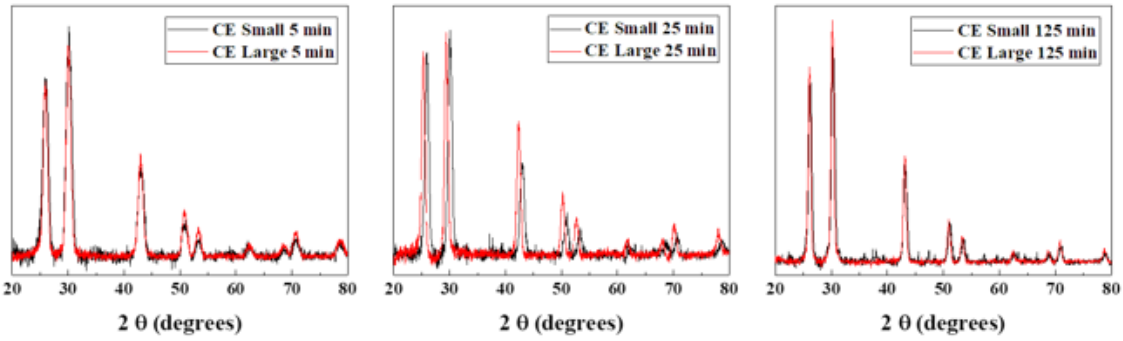

Figure 3.49 XRD comparison of PbSe/PbSe$_{1-y}$S$_y$/PbS QDs utilizing either 7.40 nm green-emitting CdSe/Cd$_{1-x}$Zn$_x$Se$_{1-y}$S$_y$/ZnS QDs or 7.57 nm red-emitting CdSe/Cd$_{1-x}$Zn$_x$Se$_{1-y}$S$_y$/ZnS QDs as nanotemplates at different cation exchange times (5 min, 25 min, 125 min).

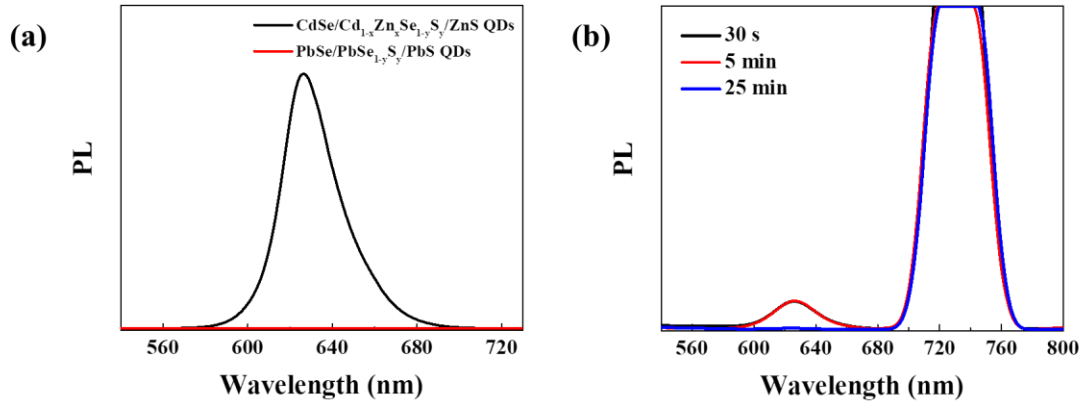

Figure 3.50 PL of PbSe/PbSe$_{1-y}$S$_y$/PbS QDs (CE from 7.57 nm red-emitting CdSe/Cd$_{1-x}$Zn$_x$Se$_{1-y}$S$_y$/ZnS QDs) at visible wavelengths. (a) PL of PbSe/PbSe$_{1-y}$S$_y$/PbS QDs after 30 s cation exchang reaction (excitation slit width: 4 nm; emission slit width: 4 nm; sensitivity set to low) (b) PL of PbSe/PbSe$_{1-y}$S$_y$/PbS QDs after cation exchange for different durations (30 s, 5 min, 25 min) (excitation slit width: 15 nm; emission slit width: 20 nm; sensitivity set to high)

As complete CE occurred between the CE reaction time of 5 min and 25 min, EDS (**Figure 3.51** & **Figure 3.52**) was performed to further verify the elemental composition of the PbSe/$PbSe_{1-y}S_y$/PbS QDs cation exchanged for 5 min and 25 min. **Figure 3.51** shows point scan EDS measurements performed via HRTEM and **Figure 3.52** shows area scan EDS measurements performed via SEM. Although overlap of the peaks for several atom types prevent us from clearly determining the quantitative presence of each element, it is evident that the Pb signals overwhelm that of either Cd or Zn atoms. The peak assigned to Cu and Zn in **Figure 3.51**, is likely coming from only Cu as the signal at that position disappeared in **Figure 3.52** where the sample holder doesn't contain a copper grid while that for the HRTEM does include the copper grid. Moreover, fluorescence lines assigned to the K transition of Zn (Ka1 8637 eV; Ka2 8614 eV; Ka3 8463 eV) is completely absent in **Figure 3.51** as well, further corroborating the complete removal of Zn. As for Cd (La1 3133 eV; Lb1 3315 eV) there is also no clear signal observed in **Figure 3.51** nor **Figure 3.52**. It seems EDS measurements are not sensitive enough to tell the difference between the PbSe/$PbSe_{1-y}S_y$/PbS QDs cation exchanged for 5 min and 25 min, however, they do further support the successful CE reaction and also the negligible to non-existent presence of Cd and Zn atoms in the QDs

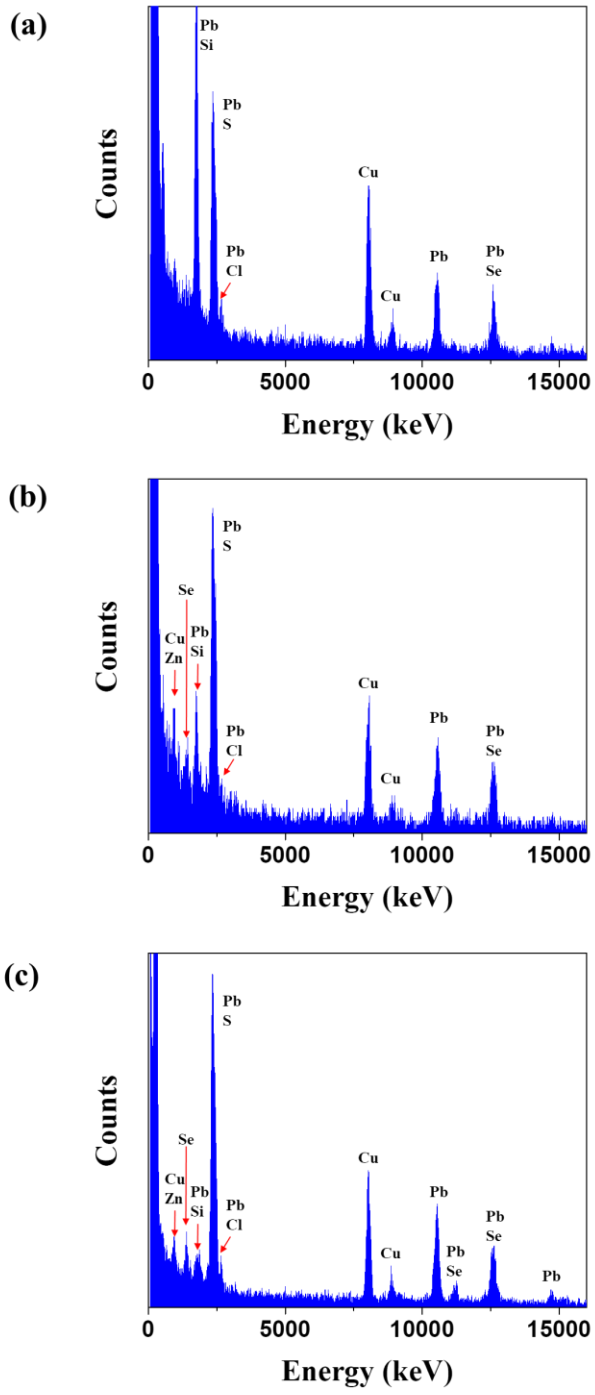

Figure 3.51 EDS (Point Scan) of individual QDs under HRTEM. (a) PbSe/$PbSe_{1-y}S_y$/PbS QDs (Green QD CE for 5 min) (b) PbSe/$PbSe_{1-y}S_y$/PbS QDs (Green QD CE for 25 min) (c) PbSe/$PbSe_{1-y}S_y$/PbS QDs (Red QD CE for 25 min)

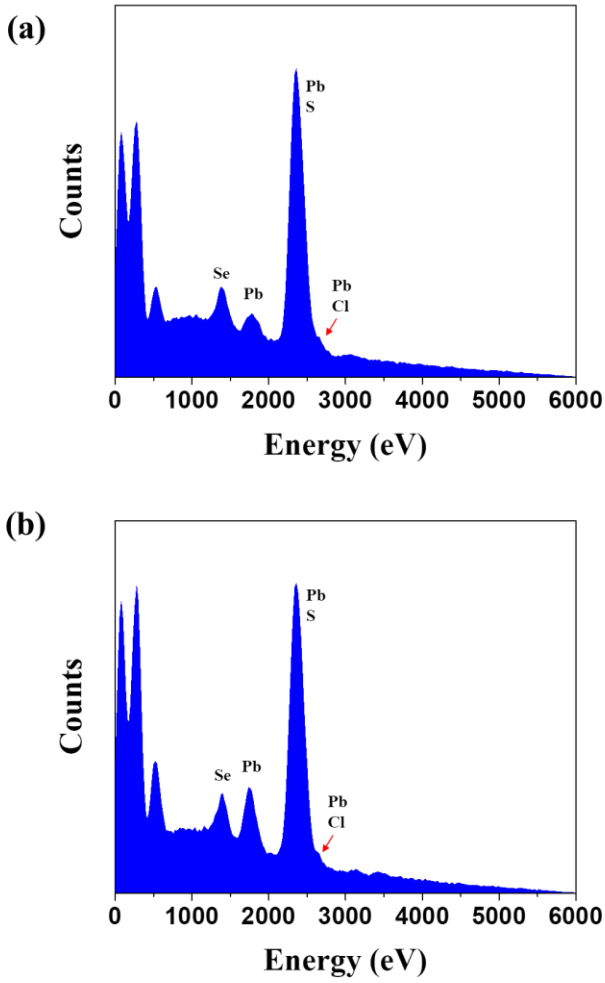

Figure 3.52 EDS (Area Scan) via SEM. (a) PbSe/$PbSe_{1-y}S_y$/PbS QDs (Red QD CE for 5 min) (b) PbSe/$PbSe_{1-y}S_y$/PbS QDs (Red QD CE for 25 min)

Figure 3.53 shows the stability of PbSe/$PbSe_{1-y}S_y$/PbS QDs by measuring the absorption peak position after storage under ambient environment (exposed to light; exposed to air; at room temperature; dispersed in tetrachloroethylene) for 50 days. It has been reported that PbSe QDs which is easily oxidized when exposed to air will show a blue shift in the absorption peak in less than a week.[144] In stark contrast, PbSe/$PbSe_{1-y}S_y$/PbS

QDs show no noticeable shift in the absorption peak position after 50 days. All PbSe/PbSe$_{1-y}$S$_y$/PbS QD batches synthesized show no shift in the peak position, however, it is relatively difficult to tell for QDs with a thicker PbS shell due to suppressed absorption as shown in **Figure 3.43**.

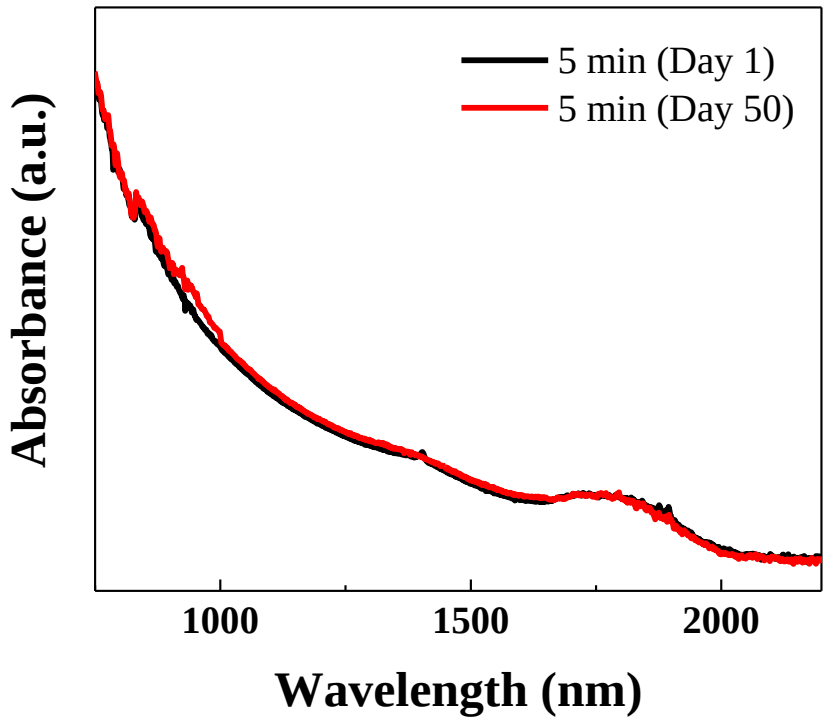

Figure 3.53 Stability of PbSe/PbSe$_{1-y}$S$_y$/PbS QDs characterized via absorption peak shift. The PbSe/PbSe$_{1-y}$S$_y$/PbS QDs were dispersed in TCE and exposed to ambient air and light. PbSe/PbSe$_{1-y}$S$_y$/PbS QDs (Green QD CE for 5 min) was used as QDs with thicker shells had stronger absorption suppression that it was difficult to decipher the first exciton peak position.

Figure 3.54 shows the PL of PbSe/$PbSe_{1-y}S_y$/PbS QDs after different CE times. PbSe/$PbSe_{1-y}S_y$/PbS QDs with clear emission in the IR has been successfully synthesized. It is interesting to note that there is a constant red-shift in the PL emission as the CE reaction continues. After a 125 min CE reaction, the PL is at approximately 2300 nm which is a distinct shift from ~1700 nm (CE for 30 s) or ~2050 nm (CE for 5 min). This is in stark contrast to many reports on PbSe/PbS QDs in which a change in the PbS layer thickness eventually resulted in an emission blue-shift. For a PbSe core only QD, a 2300 nm PL peak would correspond to approximately 9 nm.[135] From the absorption data of red-emitting CdSe/$Cd_{1-x}Zn_xSe_{1-y}S_y$/ZnS QDs in **Figure 3.39**, the effective core size (i.e. size of the CdSe/$Cd_{1-x}Zn_xSe_{1-y}S_y$) is calculated to be approximately 5.3 nm. Even considering the size increase of the effective core size after CE due to the increase in the molar volume, the effective core size cannot increase to 9 nm which would be a near 70% increase. Thus we can clearly see that the PL extension to 2300 nm is influenced by the PbS shell layer. As for the broad shoulder at low wavelengths (1400-1800 nm) observed for the PbSe/$PbSe_{1-y}S_y$/PbS QDs (CE for 5 min), is likely due to QDs that have not been fully cation exchanged. This is corroborated by the PL emission peak for the PbSe/$PbSe_{1-y}S_y$/PbS QDs (CE for 125 min) that has no shoulder peak as the QD has been fully cation exchanged. The ondulation (1680-1860 nm) in the PL curve for PbSe/$PbSe_{1-y}S_y$/PbS QDs (CE for 30 s) is due to the absorption from the hexane solvent.

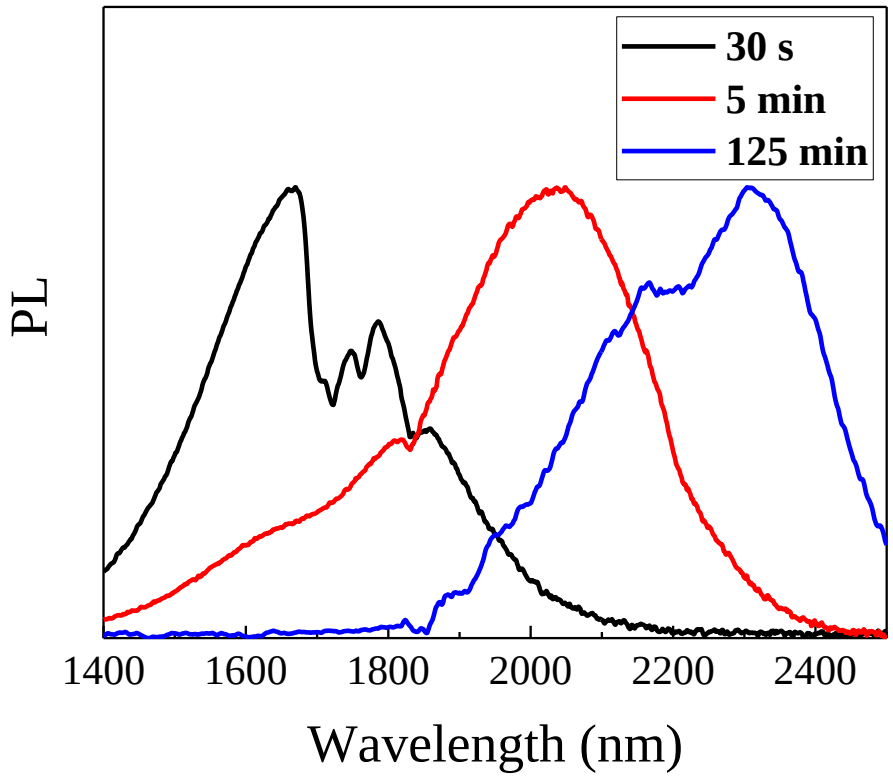

Figure 3.54 PL of PbSe/PbSe$_{1-y}$S$_y$/PbS QDs after different cation exchange times. PbSe/PbSe$_{1-y}$S$_y$/PbS QDs were all synthesized via cation exchange of red-emitting CdSe/Cd$_{1-x}$Zn$_x$Se$_{1-y}$S$_y$/ZnS QDs as nanotemplates. PbSe/PbSe$_{1-y}$S$_y$/PbS QDs (CE for 5 min) and PbSe/PbSe$_{1-y}$S$_y$/PbS QDs (CE for 5 min) were dispersed in TCE, while PbSe/PbSe$_{1-y}$S$_y$/PbS QDs (CE for 30 s) was dispersed in hexane for PL measurement.

In **Figure 3.43** and **Figure 3.54**, we showed that the CE reaction time can control the optical properties (i.e. absorption & PL) of PbSe/PbSe$_{1-y}$S$_y$/PbS QDs. Now in **Figure 3.55** we demonstrate that the starting CdSe/Cd$_{1-x}$Zn$_x$Se$_{1-y}$S$_y$/ZnS QD emission wavelength (or size) can also influence the optical properties of PbSe/PbSe$_{1-y}$S$_y$/PbS QDs after identical CE times. **Figure 3.55** shows the absorbance of PbSe/PbSe$_{1-y}$S$_y$/PbS QDs that were each

synthesized by utilizing red, green, and blue CdSe/$Cd_{1-x}Zn_xSe_{1-y}S_y$/ZnS QDs as nanotemplates. All three CE reactions were performed for 5 min. It is clearly observed that the change in optical properties of CdSe/$Cd_{1-x}Zn_xSe_{1-y}S_y$/ZnS QDs via precise control of QD dimensions is directly translated into optical property changes of the PbSe/$PbSe_{1-y}S_y$/PbS QDs as well. The PbSe/$PbSe_{1-y}S_y$/PbS QD synthesized from the red-emitting CdSe/$Cd_{1-x}Zn_xSe_{1-y}S_y$/ZnS QD (red emission wavelength = 628 nm) absorbs at approximately 2100 nm while those synthesized from CdSe/$Cd_{1-x}Zn_xSe_{1-y}S_y$/ZnS QDs with a smaller core (green emission wavelength = 539 nm; blue emission wavelength = 500 nm) absorb at 1800 nm and 1700 nm, respectively. This is because the CE process simply replaces the Cd and Zn cations with Pb cations from the more sturdy Se and S anionic framework. The extent to which the Se and S atoms are situated in the original QD is relatively fixed that the size of the original CdSe core decides the size of the final PbSe core dimensions as well.

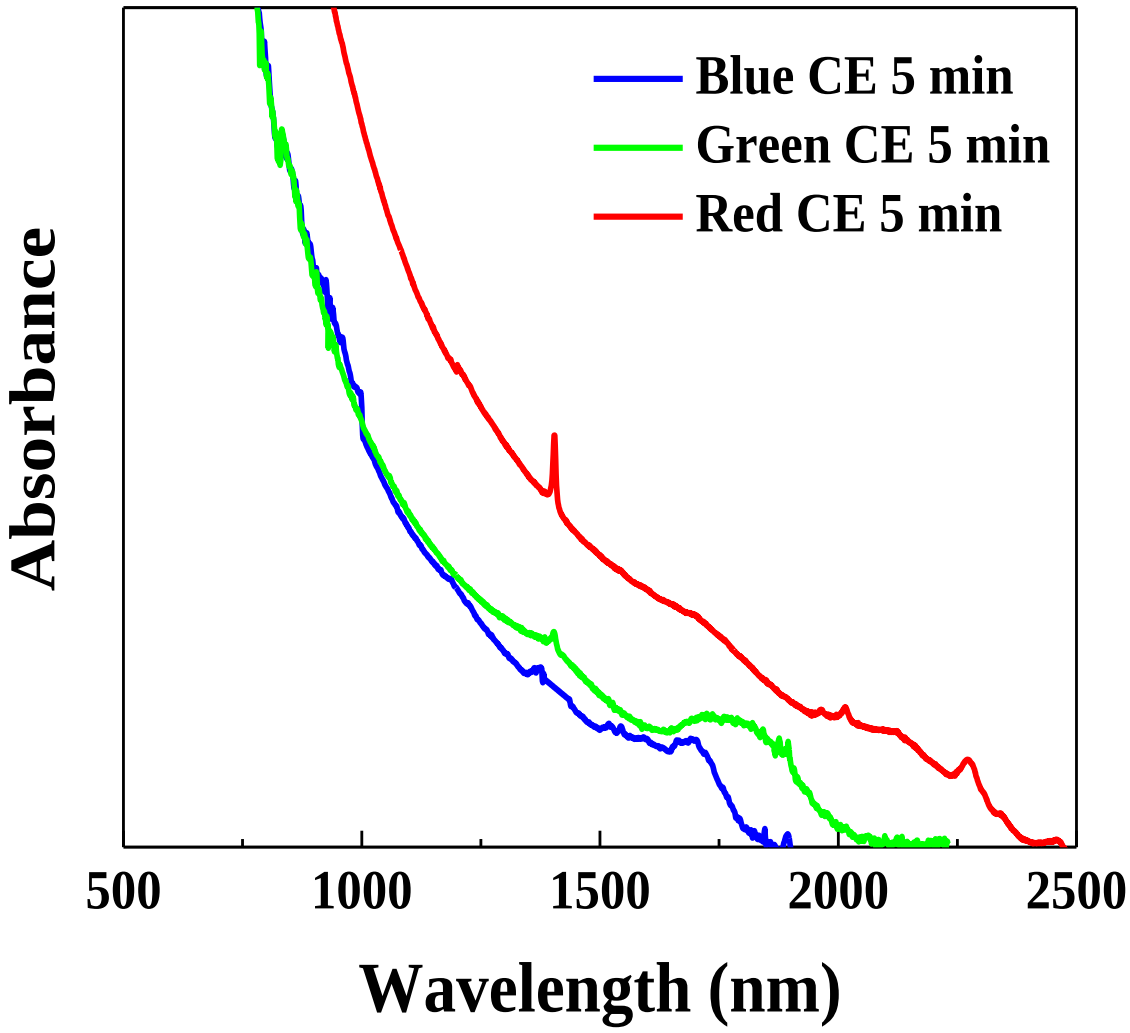

Figure 3.55 Controlled absorbance wavelength of PbSe/$PbSe_{1-y}S_y$/PbS QDs by tuning absorbance wavelength of CdSe/$Cd_{1-x}Zn_xSe_{1-y}S_y$/ZnS QDs. The cation exchange reaction time was 5 miin for all experiments.

3.3.3 Conclusion

In summary, we demonstrated the precision synthesis of composition gradient PbSe/$PbSe_{1-y}S_y$/PbS QDs via capitalizing on cation exchange of well-defined pre-synthesized CdSe/$Cd_{1-x}Zn_xSe_{1-y}S_y$/ZnS QDs as nanotemplates. The chemical composition gradient CdSe/$Cd_{1-x}Zn_xSe_{1-y}S_y$/ZnS QD nanotemplates were synthesized by utilizing well-known chemical reactivity differences between the reactants. Cation exchange reaction in which the sturdy anion framework is maintained while selectively replacing the cations was successfully conducted. The selective replacement Cd and Zn atoms with Pb atoms was successfully performed by creating a solution environment in which the selected ligand binding with Cd and Zn atoms was more favorable compared to that with Pb atoms. Due to the difference in crystal density between the reactant CdSe/$Cd_{1-x}Zn_xSe_{1-y}S_y$/ZnS QD and product PbSe/$PbSe_{1-y}S_y$/PbS QD, the size of the QD increased after the cation exchange reaction. Moreover, by utilizing Ostwald ripening effects the PbS shell layer on the PbSe/$PbSe_{1-y}S_y$/PbS QDs was precisely tunable along time scales that were precisely reproducible (i.e. PbS shell growth takes place over minutes and not seconds thus making experiments reproducible). The obtained PbSe/$PbSe_{1-y}S_y$/PbS QDs have PL that range between 1700 nm to 2300 nm (SWIR region) as a function of cation exchange time. It is important to note that not only the cation exchange time, but also the initial CdSe/$Cd_{1-x}Zn_xSe_{1-y}S_y$/ZnS QD size has an effect on the absorbance wavelength of PbSe/$PbSe_{1-y}S_y$/PbS QDs in the IR region. In future experiments we will continue to increase the cation exchange reaction time as well as increase the starting CdSe/$Cd_{1-x}Zn_xSe_{1-y}S_y$/ZnS QD size in order to push PL and absorbance to MWIR ranges (above 3000 nm). Moreover, to craft

environmentally benign MWIR QDs, cation exchange reactions utilizing Ag atoms will be conducted as well.[156]

3.3.4 Experimental Section

Materials: Lead(II) chloride ($PbCl_2$) (ultra-dry, 99.999%), selenium powder (200 mesh, 99.999%), sulfur powder (precipitated, 99.5%) cadmium oxide (98.9%), zinc acetate dihydrate ($ZnAc_2$) (ACS reagent grade, 98.0~101.0%), trioctylphosphine oxide (TOPO) (>98%), 1-octadecene (ODE) (tech. grade, 90%), oleic acid (OA) (tech. grade, 90%), and tetrachloroethylene (TCE) (ultrapure, spectrophotometric grade, 99+%) were obtained from Alfa Aesar. Trioctylphosphine (TOP) (97%), octadecylphosphonic acid (ODPA) (97%), and zinc acetylacetonate hydrate was obtained from Sigma-Aldrich. 1-dodecanethiol (>98%) was obtained from Sigma-Aldrich. Oleylamine (OAm) (50.0%) was obtained from TCI Chemicals. Toluene, hexane and methanol (ACS reagent grade) were obtained from BDH Chemicals. All chemicals were used as received without any further purification.

Preparation of green-emitting CdSe QDs: ODPA-capped CdSe QDs were synthesized by following a reported method.(cite) A mixture of CdO (50 mg), ODPA (400 mg), and TOPO (4 g) was placed in a three neck flask and degassed at 140^{o}C for 1 h. The temperature was then raised to 290^{o}C. After complete solubilization of the reactants that the solution became transparent and colorless, 1 ml of 1M Se/TOP solution was quickly injected into

the reaction flask to initiate nucleation and growth. The heating mantle was removed after 1 sec and the reaction flask was quickly placed in a water bath. 5 ml of toluene was added as the reaction solution reached 60^{o}C. The resulting ODPA-capped CdSe QDs were precipitated with methanol twice and dispersed in toluene.

Preparation of Cd-oleate and Zn-oleate precursor solution: 154 mg CdO, 1581 mg zinc acetyl acetonate, 90 ml ODE, and 30 ml OA were placed in 250 ml three-neck flask. The mixture was degassed at 120^{o}C for 1 h. In an argon environment, the temperature was raised to 300^{o}C until the solution became transparent. Then the heating mantle was removed and the solution was allowed to cool to RT.

Synthesis of green-emitting CdSe/Cd$_{1-x}$Zn$_x$Se$_{1-y}$S$_y$/ZnS QDs: 20 ml of the Cd-oleate and Zn-oleate precursor solution (described above) was added to a 100 ml three-neck flask. The solution was degassed at 120^{o}C for 1 h. In an argon environment, the temperature was increased to 240^{o}C. At 240^{o}C, 0.4 umol of CdSe QDs in toluene was quickly injected followed by dropwise addition of a shell precursor solution (15.8 mg Se + 256 mg S in 4 ml TOP) forming CdSe/Cd$_{1-x}$Zn$_x$Se$_{1-y}$S$_y$ QDs. In order to further passivate CdSe/Cd$_{1-x}$Zn$_x$Se$_{1-y}$S$_y$ QDs with a ZnS shell, 2 ml of 0.5M S/TOP was added. After 90 min, the heating mantle was removed and the solution was allowed to cool to RT. At around 60^{o}C, 10 ml of hexane was added. The final CdSe/Cd$_{1-x}$Zn$_x$Se$_{1-y}$S$_y$/ZnS QDs were precipitated acetone twice and then re-dispersed in the desired solvent.

Synthesis of red-emitting CdSe/$Cd_{1-x}Zn_xSe_{1-y}S_y$/ZnS QDs: For synthesis of cadmium-based QDs with graded architecture, we've adopted and modified a previously reported method.[157-158] 1 mmol CdO, 2 mmol $Zn(Ac)_2$, 5 ml Oleic Acid, and 15 ml Octadecene were placed in a three neck flask. The mixture was then degassed for 1h at 150^{o}C followed by a temperature increase to 300^{o}C. After the solution became transparent, 0.4 mL 1M Se/TOP was quickly injected. To passivate the QD surface, 0.3 mL of dodecanethiol was added dropwise. Then in order to fully passivate the QD with a thick shell, 1 mL 2M S/TOP was added and allowed to react for several minutes. After cooling the solution, 10 ml Hexane was added.

Synthesis of PbSe/$PbSe_{1-x}S_x$/PbS QDs: For cation exchange of cadmium-based QDs into lead-based QDs, we've adopted and modified a previously reported method.[141] 5 ml oleyl amine and 1 mmol 278 mg $PbCl_2$ was added to a three-neck flask. The solution was degassed at RT for 1 h. The temperature was raised to 190^{o}C in an argon environment. 1 ml of 0.05M CdSe/$Cd_{1-x}Zn_xSe_{1-y}S_y$/ZnS QDs in ODE was quickly injected and allowed to undergo cation exchange for desired reaction times. The heating mantle was then removed and allowed to cool to RT. At around 70^{o}C, 4 ml of OA and 5 ml of hexane was added to the solution. The PbSe/$PbSe_{1-x}S_x$/PbS QDs were precipitated with methanol twice and dispersed in hexane. The final hexane solution was centrifuged at 1000 rpm (unreacted $PbCl_2$ precipitates) and the supernatant was collected for further characterization.

Characterization: The morphology of as-prepared CdSe QDs, CdSe/$Cd_{1-x}Zn_xSe_{1-y}S_y$/ZnS QDs, and PbSe/$PbSe_{1-x}S_x$/PbS QDs was examined using high resolution transmission electron microscope (Tecnai F30). Aabsorption and emission spectra upto NIR wavelenghts were recorded using a UV-vis spectrometer (UV-2600, Shimadzu) and a spectrofluorophotometer (RF-5301PC, Shimadzu), respectively. For IR absorption spectra, Cary 5000 UV-Vis-NIR spectrophotometer which is capable to measure absorbance up to 3300 nm was utilized. For IR PL spectra, FieldSpec 3 Spectroradiometer was utilized. The transmission electron microscope (TEM) images were obtained by a JEOL 100CX II TEM. High resolution TEM images as well as EDS (point scan) measurements were obtained by FEI Tecnai G2 F30 TEM. EDS (area scan) was performed by LEO 1530 SEM. The X-ray diffraction (XRD) patterns were obtained using a PANalytical Empyrean Alpha-1 X-ray diffractometer.

CHAPTER 4. CONCLUSIONS AND FUTURE WORK

4.1 Conclusions

This thesis presents the development of new strategies to synthesize metallic nanoparticles (NPs), metal chalcogenide nanocrystals (NCs), and perovskite quantum dots (QDs). The strategies rely on the use of well-defined polymer nanoreactors (i.e. nanotemplates) or inorganic nanotemplates to guide the growth of new nanomaterials.

This dissertation first presented the background of relevant polymerization techniques and the current state-of-the-art in unimolecular nanoreactors in nanocomposite synthesis. It then presented the relevant background as well as the state-of-the-art regarding the specific nanomaterials that was the focus of this dissertation. The thesis then moved onto the three main research topics that utilized nanotemplates to create three different types of nanomaterials. They were all-inorganic perovskite quantum dots such as $CsPbBr_3$ QDs, metallic nanoparticles which included Au and Ag NPs, and metal chalcogenide nanocrystals such as PbSe/$PbSe_{1-x}S_x$/PbS NCs.

The polymer nanoreactor (e.g. Star-like PAA-*b*-PS) approach was utilized to craft the PS-capped Au NPs, PS-capped Ag NPs, and PS-capped perovskite $CsPbBr_3$ QDs. The polymer nanoreactor approach allowed the formation of monodisperse and well-defined organic-inorganic nanocomposites by utilizing unimolecular star-like block copolymer nanoreactors. It should be emphasized that the formation of nanomaterials with permanently tethered polymers of various kinds while simultaneously controlling nanomaterial dimension is not achievable via any other method. The unimolecular star-like

block copolymer nanoreactors were synthesized via sequential ATRP reactions from a cyclic-structured brominated β-cyclodextrin macroinitiator. The intrinsic precision of the ATRP reaction led to the precise control over the nanomaterial dimensions. For instance, by controlling the inner block copolymer length (i.e. PAA block of star-like PAA-*b*-PS) of the polymer nanoreactors, the size of the NPs was precisely regulated. Precise control over nanomaterial dimensions has been successfully demonstrated for PS-capped Au NPs and PS-capped Ag NPs by crafting these nanomaterials in polymer nanoreactors with various inner PAA block copolymer lengths. Also by controlling the outer block copolymer length (i.e. PS block of star-like PAA-*b*-PS), the colloidal stability of the NPs greatly improved. It should be emphasized that due to the permanently tethered PS, the PS-capped Au NPs not only demonstrated improved colloidal stability but also striking improvements in UV-resistance compared to Au NPs with non-permanent linear organic ligands bound on the surface. For instance, PS-capped Au NPs displayed no change in morphology after UV irradiation for 12 h while oleyl amine-capped Au NPs were completely deformed after 1 h of UV irradiation. The polymer nanoreactors were also successfully utilized in crafting PS-capped cesium-based all-inorganic perovskite nanocrystals (PS-capped $CsPbBr_3$ QDs) with markedly enhanced stability as well as precisely tuned dimensions. We specifically demonstrated that the change in the PS molecular weight covalently bound to the QD surface has a direct influence on improving the QD's stability when exposed to water. For instance, PS-capped $CsPbBr_3$ QDs displayed up to twenty times increase in water stability compared to conventional oleic acid/oleyl amine-capped $CsPbBr_3$ QDs. It is worth emphasizing that the polymer nanoreactor approach allowed perovskite QDs to have individual protective shell coatings that could be tailored to any desired thickness for the

first time. As the current bottleneck for perovskite material commercialization is in its low stability, perovskite QDs with improved water stability as well as colloidal stability while maintaining excellent quantum yield clearly showed the advantage of using unimolecular polymer nanoreactors.

The inorganic nanotemplate approach was undertaken to craft well-defined and stable PbSe/$PbSe_{1-x}S_x$/PbS QDs with precisely tunable optical properties in the IR. The inorganic nanotemplate approach utilized cation exchange reaction of well-defined inorganic QDs to create new QDs that maintain the same anionic framework of the original inorganic nanotemplate. Herein, we demonstrated the precision synthesis of composition gradient PbSe/$PbSe_{1-y}S_y$/PbS QDs via capitalizing on cation exchange of pre-synthesized CdSe/$Cd_{1-x}Zn_xSe_{1-y}S_y$/ZnS QDs as nanotemplates. The CdSe/$Cd_{1-x}Zn_xSe_{1-y}S_y$/ZnS QD nanotemplates with an interfacial chemical composition gradient between the core and shell material were synthesized by utilizing well-known chemical reactivity differences between the four reactants (i.e. Cd, Zn, Se, and S). Cation exchange reaction in which the cations are replaced while maintaining the anionic framework was successfully performed. The driving force for the selective replacement Cd and Zn atoms by Pb atoms was in creating a solution environment in which the ligand binding with Cd and Zn atoms was more favorable compared to that with Pb atoms. Due to the crystal density differences between the reactant CdSe/$Cd_{1-x}Zn_xSe_{1-y}S_y$/ZnS QD and product PbSe/$PbSe_{1-y}S_y$/PbS QD, the size of the QD increased after the cation exchange reaction. Moreover, by capitalizing on the Ostwald ripening effect, the PbS shell layer on the PbSe/$PbSe_{1-y}S_y$/PbS QDs was precisely tunable. The obtained PbSe/$PbSe_{1-y}S_y$/PbS QDs had PL that range between 1700 nm to 2300 nm (SWIR region) as a function of cation exchange time. In addition to the

cation exchange time, we also demonstrated that the initial CdSe/$Cd_{1-x}Zn_xSe_{1-y}S_y$/ZnS QD size influences the absorbance wavelength of PbSe/$PbSe_{1-y}S_y$/PbS QDs in the IR region as well. It is worth mentioning that in addition to accurate structure control, this strategy allows PbSe, which easily oxidizes in air to be immediately protected by a shell layer resulting in improved stability. It should be emphasized that the PbSe/$PbSe_{1-y}S_y$/PbS QDs have excellent colloidal stability (> 6 months) as well as outstanding oxidative stability (> 50 days).

4.2 Future Work

The first goal of this dissertation was to explore various types of nanocomposites that has yet to be realized via the polymer nanoreactor approach. This dissertation has demonstrated its use in metallic NPs as well as in all-inorganic perovskite QDs. The work presented in this dissertation, however, is only the beginning and there still lies tremendous amount of work to be done in creating novel materials via this versatile approach as well as applying these novel nanocomposites into actual devices.

For instance, the PS-capped perovskite QDs is likely to facilitate uniform dispersion in PS or PS-containing polymer matrices by reducing enthalpic interactions of the PS-capped perovskite QDs with PS-containing host matrix for uniform perovskite QDs/polymer nanocomposites. Moreover, via optimal control of the PS chain length, homogenous films of stand-alone PS-capped perovskite QD films may be achievable without a host polymer matrix. These PS-capped perovskite QD films with readily tunable perovskite QD to polymer ratio may exhibit amplified stimulated emission in lasing

applications where the QD loading is of key importance. Moreover, large-sized PS-capped perovskite QD-containing nanocomposites can also be exploited in creating nanocomposite scintillators for spectroscopic gamma-ray detection and/or X-ray imaging where high QD loading is favorable. Moreover, to further improve performance for lighting applications, the outer PS-capping on the perovskite QDs can be replaced by polymers superior optical stability such as polydimentylsiloxane (PDMS) to improve optical and thermal stability.

As mentioned previously, the polymer nanoreactor approach is amenable for the synthesis of a large array of polymer-capped nanomaterials with controlled dimensions, desired functionality, design complexity, and high stability. For instance, future plans include crafting environmentally benign lead-free $CsSbBr_3$ QDs via using star-like PAA-*b*-PE polymer nanoreactors and also core/shell perovskite QDs using star-like triblock copolymer nanoreactors. Moreover, the polymer nanoreactor approach which focused on zero-dimensional structures for this disseration can branch off into one-dimensional structures. By replacing the cyclic structured β-cyclodextrin with linear cellulose to act as the starting macroinitiator for synthesizing the nanoreactors, the polymer nanoreactors can achieve one-dimensional structures such as nanorods, nanotubes, and core/shell nanorods.

The second goal of this dissertation was to craft nanomaterials by capitalizing on the inorganic nanotemplate approach. The dissertation has demonstrated its use in crafting $PbSe/PbSe_{1-x}S_x/PbS$ QDs with a composition gradient interfacial layer. The work presented in this dissertation, however, still leaves many areas yet to be explored. For instance, we have yet to fully demonstrate the effect of $PbSe/PbSe_{1-x}S_x/PbS$ QD's shell layer thickness on PL red-shift as well as its effect in affecting photodetector performance. Also we will

continue to increase the cation exchange reaction time as well as increase the starting CdSe/$Cd_{1-x}Zn_xSe_{1-y}S_y$/ZnS QD size in order to push the band gap towards MWIR ranges (above 3000 nm). Moreover, to demonstrate the versatility of this approach branching off into other environmentally benign elements (e.g. Ag) while maintaining similar characteristics in the IR may be desirable.

CHAPTER 5. PUBLICATIONS

1. **Y.J. Yoon**, Z. Kang, Z. Lin*, "Infrared-Emitting Gradient Quantum Dots by Cation Exchange", (In Preparation).

2. **S. Zhang†, Y.J. Yoon†**, Z. Lin*, "Improved photovoltaic performance of perovskite solar cells by interfacial engineering using precisely controlled $CsPbBr_xI_{3-x}$ perovskite QDs via amphiphilic star-like block copolymers as nanoreactors", (In Preparation). **†Co-First Author**

3. **Y.J. Yoon**, Y. Chang, S. Zhang, S. Pan, Y. He, C.H. Lin, S. Yu, Y. Chen, Z. Wang, J. Jung, N. Thadhani, V.V. Tsukruk, Z. Kang, Z. Lin*, "Enabling tailorable optical properties and markedly enhanced stability of perovskite quantum dots by permanently ligating with polymer hairs via amphiphilic star-like block copolymer nanoreactors", (Under Review).

4. E. Lafalce, Q. Zeng, C.H. Lin, M.J. Smith, S.T. Malak, J. Jung, **Y.J. Yoon**, Z. Lin, V.V. Tsukruk, Z.V. Vardeny, "Robust lasing modes in colloidal quantum dot microdisks using a non-hermitian exceptional point", (Under Review).

5. Y. Chang, **Y.J. Yoon**, G. Li, E. Xu, S. Yu, C. Lu, Z. Wang, Y. He, C.H. Lin, B.K. Wagner, V.V. Tsukruk, Z. Kang, N. Thadhani, Y. Jiang*, Z. Lin*, "All-inorganic perovskite nanocrystals with a stellar set of stabilities and their use in white light-emitting diodes", *ACS Appl. Mater. Interfaces* (Accepted).

6. **Y.J. Yoon**, Z. Lin, Z. Kang, "Infrared-Emitting Gradient Quantum Dots by Cation Exchange", *US Patent Application* (2018) 62/720,200.

7. Q. Zeng, E. Lafalce*, C.H. Lin, M.J. Smith, S.T. Malak, J. Jung, **Y.J. Yoon**, Z. Lin, V.V. Tsukruk, Z.V. Vardeny, "Spectral and directional properties of elliptical quantum-dot microlasers", *J. of Photonics for Energy* 8(3) (2018) 032218.

8. C.H. Lin, Q. Zeng, E. Lafalce, S. Yu, M.J. Smith, **Y.J. Yoon**, Y. Chang, Y. Jiang, Z. Lin, Z.V. Vardeny, V.V. Tsukruk*, "Large-area lasing and multicolor perovskite quantum dot patterns", *Adv. Optical Mater.* 6 (2018) 1800474.

9. J. Geldmeier, L. Rile, **Y.J. Yoon**, J. Jung, Z. Lin, V.V. Tsukruk*, "Dewetting-induced photoluminescent enhancement of poly (laurylmethacrylate)/quantum dot thin films", *Langmuir* 33 (2017) 14325-14331.

10. Y. Chen, D. Yang, **Y.J. Yoon**, X. Pang, Z. Wang, J. Jung, Y. He, Y.W. Harn, M. He, S. Zhang, G. Zhang*, Z. Lin*, "Hairy uniform permanently ligated hollow nanoparticles with precise dimension control and tunable optical properties", *J. Am. Chem. Soc.* 139 (2017) 12956-12967.

11. Y. He, X. Pang, B. Jiang, C. Feng, Y.W. Harn, Y. Chen, **Y.J. Yoon**, S. Pan, C. Lu, Y. Chang, M. Zebarjadi, Z. Kang, N. Thadhani, J. Peng, Z. Lin*, "Unconventional route to uniform hollow semiconducting nanoparticles with tailorable dimensions, compositions, surface chemistry and near-infrared absorption", *Angew. Chem.* 129 (2017) 13126-13131.

12. S.T. Malak, **Y.J. Yoon**, M.J. Smith, C.H. Lin, J. Jung, Z. Lin, V.V. Tsukruk*, "Decay-to-recovery behavior and on-off recovery of photoluminescence intensity from core-shell quantum dots", *ACS Photonics* 4 (2017) 1691-1704.

13. S.T. Malak, G. Liang, R. Thevamaran, **Y.J. Yoon**, M.J. Smith, J. Jung, C.H. Lin, Z. Lin, E.L. Thomas, V.V. Tsukruk*, "High-resolution quantum dot photopatterning via interference lithography assisted microstamping", *J. Phys. Chem. C* 121 (2017) 13370-13380.

14. M.J. Smith, S.T. Malak, J. Jung, **Y.J. Yoon**, C.H. Lin, S. Kim, K.M. Lee, R. Ma, T.J. White, T.J. Bunning, Z. Lin, V.V. Tsukruk*, "Robust, uniform, and highly emissive quantum dot-polymer films and patterns using thiol-ene chemistry", *ACS Appl. Mater. Interfaces* 9 (2017) 17435-17448.

15. C.H. Lin, Q. Zeng, E. Lafalce, M.J. Smith, S.T. Malak, J. Jung, **Y.J. Yoon**, Z. Lin, Z.V. Vardeny, V.V. Tsukruk*, "Large-scale robust quantum dot microdisk lasers with controlled high quality cavity modes", *Adv. Optical Mater.* 5 (2017) 1700011.

16. S.T. Malak, M.J. Smith, **Y.J. Yoon**, C.H. Lin, J. Jung, Z. Lin, V.V. Tsukruk*, "Programmed emission transformations: negative-to-positive patterning using the decay-to-recovery behavior of quantum dots", *Adv. Optical Mater.* 5 (2017) 1600509.

17. **Y. Chen†, Y.J. Yoon†**, X. Pang, Y. He, J. Jung, C. Feng, G. Zhang*, Z. Lin*, "Precisely size-tunable monodisperse hairy plasmonic nanoparticles via amphiphilic star-like block copolymers", *Small* 12 (2016) 6714-6723. **†Co-First Author (Featured on Cover)**

18. J. Jung, C.H. Lin, **Y.J. Yoon**, S.T. Malak, Y. Zhai, E.L. Thomas, Z.V. Vardeny, V.V. Tsukruk, Z. Lin*, "Crafting core/graded shell-shell quantum dots with suppressed reabsorption and tunable stokes shift as high optical gain materials", *Angew. Chem.* 128 (2016) 5155-5159. **(Selected as VIP Paper)**

19. C.H. Lin, E. Lafalce, J. Jung, M.J. Smith, S.T. Malak, S. Aryal, **Y.J. Yoon**, Y. Zhai, Z. Lin, Z.V. Vardeny, V.V. Tsukruk*, "Core/alloyed-shell quantum dot robust solid films with high optical gains", *ACS Photonics* 3 (2016) 647-658.

20. S.T. Malak, E. Lafalce, J. Jung, C.H. Lin, M.J. Smith, **Y.J. Yoon**, Z. Lin, Z.V. Vardeny, V.V. Tsukruk*, "Enhancement of optical gain characteristics of quantum dot films by optimization of organic ligands", *J. Mater. Chem. C* 4 (2016) 10069-10081.

21. J. Jung, **Y.J. Yoon**, Z. Lin*, "Intimate organic-inorganic nanocomposites via rationally designed conjugated polymer-grafted precursors", *Nanoscale* 8 (2016) 16520-16527.

22. J. Jung, **Y.J. Yoon**, Z. Lin*, "Semiconducting organic-inorganic nanocomposites by intimately tethering conjugated polymers to inorganic tetrapods", *Nanoscale* 8 (2016) 8887-8898.

23. S.T. Malak, J. Jung, **Y.J. Yoon**, M.J. Smith, C.H. Lin, Z. Lin, V.V. Tsukruk*, "Large-area multicolor emissive patterns of Quantum Dot-Polymer Films via Targeted Recovery of Emission Signature", *Adv. Optical Mater.* 4 (2016) 608-619.

24. X. Xin, B. Li, J. Jung, **Y.J. Yoon**, R. Biswas*, Z. Lin*, "Ab initio simulation of charge transfer at the semiconductor quantum dot/TiO_2 interface in quantum dot-sensitized solar cells", *Part. Part. Syst. Charact.* 32 (2015) 80-90. **(Featured on Cover)**

25. J. Jung, **Y.J. Yoon**, M. He, Z. Lin*, "Organic-inorganic nanocomposites composed of conjugated polymers and semiconductor nanocrystals for photovoltaics", *J. Polym. Sci., Part B: Polym. Phys.* 52 (2014) 1641-1660.

REFERENCES

1. Kongkanand, A.; Tvrdy, K.; Takechi, K.; Kuno, M.; Kamat, P. V., Quantum Dot Solar Cells. Tuning Photoresponse through Size and Shape Control of CdSe−TiO2 Architecture. *J. Am. Chem. Soc.* **2008,** *130* (12), 4007-4015.

2. Wang, J.-S.; Matyjaszewski, K., Controlled/"living" radical polymerization. atom transfer radical polymerization in the presence of transition-metal complexes. *J. Am. Chem. Soc.* **1995,** *117* (20), 5614-5615.

3. Kato, M.; Kamigaito, M.; Sawamoto, M.; Higashimura, T., Polymerization of Methyl Methacrylate with the Carbon Tetrachloride/Dichlorotris-(triphenylphosphine)ruthenium(II)/Methylaluminum Bis(2,6-di-tert-butylphenoxide) Initiating System: Possibility of Living Radical Polymerization. *Macromolecules* **1995,** *28* (5), 1721-1723.

4. Matyjaszewski, K., Atom Transfer Radical Polymerization (ATRP): Current Status and Future Perspectives. *Macromolecules* **2012,** *45* (10), 4015-4039.

5. Huisgen, R., 1,3-Dipolar Cycloadditions. Past and Future. *Angew. Chem. Int. Ed.* **1963,** *2* (10), 565-598.

6. Liang, L.; Astruc, D., The copper(I)-catalyzed alkyne-azide cycloaddition (CuAAC) “click” reaction and its applications. An overview. *Coordin. Chem. Rev.* **2011,** *255* (23–24), 2933-2945.

7. Rostovtsev, V.; Green, G.; Fokin, V.; Sharpless, K., A stepwise huisgen cycloaddition process: copper(I)-catalyzed regioselective "ligation" of azides and terminal alkynes. *Angew. Chem. Int. Ed.* **2002,** *41*, 2596-2599.

8. Tornøe, C. W.; Christensen, C.; Meldal, M., Peptidotriazoles on Solid Phase: [1,2,3]-Triazoles by Regiospecific Copper(I)-Catalyzed 1,3-Dipolar Cycloadditions of Terminal Alkynes to Azides. *J. Org. Chem.* **2002,** *67* (9), 3057-3064.

9. Hein, J. E.; Fokin, V. V., Copper-catalyzed azide-alkyne cycloaddition (CuAAC) and beyond: new reactivity of copper(i) acetylides. *Chem. Soc. Rev.* **2010,** *39* (4), 1302-1315.

10. Himo, F.; Lovell, T.; Hilgraf, R.; Rostovtsev, V. V.; Noodleman, L.; Sharpless, K. B.; Fokin, V. V., Copper(I)-Catalyzed Synthesis of Azoles. DFT Study Predicts Unprecedented Reactivity and Intermediates. *J. Am. Chem. Soc.* **2005,** *127* (1), 210-216.

11. Worrell, B. T.; Malik, J. A.; Fokin, V. V., Direct Evidence of a Dinuclear Copper Intermediate in Cu(I)-Catalyzed Azide-Alkyne Cycloadditions. *Science* **2013,** *340* (6131), 457-460.

12. Pang, X.; Zhao, L.; Akinc, M.; Kim, J. K.; Lin, Z., Novel Amphiphilic Multi-Arm, Star-Like Block Copolymers as Unimolecular Micelles. *Macromolecules* **2011,** *44* (10), 3746-3752.

13. Pang, X.; Zhao, L.; Feng, C.; Lin, Z., Novel Amphiphilic Multiarm, Starlike Coil–Rod Diblock Copolymers via a Combination of Click Chemistry with Living Polymerization. *Macromolecules* **2011,** *44* (18), 7176-7183.

14. Pang, X.; Zhao, L.; Han, W.; Xin, X.; Lin, Z., A general and robust strategy for the synthesis of nearly monodisperse colloidal nanocrystals. *Nat. Nanotechnol.* **2013,** *8*, 426-431.

15. Pang, X.; He, Y.; Jung, J.; Lin, Z., 1D nanocrystals with precisely controlled dimensions, compositions, and architectures. *Science* **2016,** *353* (6305), 1268-1272.

16. Gao, C.; Yan, D., Hyperbranched polymers: from synthesis to applications. *Prog. Polym. Sci.* **2004,** *29* (3), 183-275.

17. Gao, H.; Matyjaszewski, K., Synthesis of functional polymers with controlled architecture by CRP of monomers in the presence of cross-linkers: From stars to gels. *Prog. Polym. Sci.* **2009,** *34* (4), 317-350.

18. Gao, H.; Matyjaszewski, K., Synthesis of Star Polymers by a Combination of ATRP and the "Click" Coupling Method. *Macromolecules* **2006,** *39* (15), 4960-4965.

19. Gao, H.; Matyjaszewski, K., Synthesis of Miktoarm Star Polymers via ATRP Using the "In−Out" Method: Determination of Initiation Efficiency of Star Macroinitiators. *Macromolecules* **2006,** *39* (21), 7216-7223.

20. Gao, H.; Ohno, S.; Matyjaszewski, K., Low Polydispersity Star Polymers via Cross-Linking Macromonomers by ATRP. *J. Am. Chem. Soc.* **2006,** *128* (47), 15111-15113.

21. Kagan, C.; Mitzi, D.; Dimitrakopoulos, C., *Science* **1999,** *286*, 945-947.

22. Lee, M.; Teuscher, J.; Miyasaka, T.; Murakami, T.; Snaith, H., *Science* **2012,** *338*, 643-647.

23. Jeon, N.; Noh, J.; Kim, Y.; Yang, W.; Ryu, S.; Seok, S., Solvent engineering for high-performance inorganic-organic hybrid perovskite solar cells. *Nat. Mater.* **2014,** *13*, 897-903.

24. Green, M.; Ho-Baillie, A.; Snaith, H., The emergence of perovskite solar cells. *Nature Photonics* **2014,** *8*, 506-514.

25. McMeekin, D.; Sadoughi, G.; Rehman, W.; Eperon, G.; Saliba, M.; Horantner, M.; Haghighirad, A.; Sakai, N.; Korte, L.; Rech, B.; Johnston, M.; Herz, L.; Snaith, H., A mixed-cation lead mixed-halide perovskite absorber for tandem solar cells. *Science* **2016,** *351*, 151-155.

26. Zhou, H.; Chen, Q.; Li, G.; Luo, S.; Song, T.; Duan, H.; Hong, Z.; You, J.; Liu, Y.; Yang, Y., Interface engineering of highly efficient perovskite solar cells. *Science* **2014,** *345* (6196), 542-546.

27. Yang, W.; Noh, J.; Jeon, N.; Kim, Y.; Ryu, S.; Seo, J.; Seok, S., High-performance photovoltaic perovskite layers fabricated through intramolecular exchange. *Science* **2015,** *348* (6240), 1234-1237.

28. Kim, H.; Ohkita, H.; Benten, H.; Ito, S., Photovoltaic Performance of Perovskite Solar Cells with Different Grain Sizes. *Adv. Mater.* **2016,** *28*, 917-922.

29. Zhang, Y.; Tan, L.; Fu, Q.; Chen, L.; Ji, T.; Hu, X.; Chen, Y., Enhancing the grain size of organic halide perovskites by sulfonate-carbon nanotube incorporation in high performance perovskite solar cells. *Chem. Commun.* **2016,** *52*, 5674-5677.

30. Chen, J.; Shi, T.; Li, X.; Zhou, B.; Cao, H.; Wang, Y., Origin of the high performance of perovskite solar cells with large grains. *Appl. Phys. Lett.* **2016,** *108*, 053302.

31. Mali, S.; Shim, C.; Hong, C., Highly stable and efficient solid-state solar cells based on methlammonium lead bromide (CH3NH3PbBr3) perovskite quantum dots. *NPG Asia Materials* **2015,** *7*, e208.

32. Cha, M.; Da, P.; Wang, J.; Wang, W.; Chen, Z.; Xiu, F.; Zheng, G.; Wang, Z., Enhancing Perovskite Solar Cell Performance by Interface Engineering Using CH3NH3PbBr0.9I2.1 Quantum Dots. *J. Am. Chem. Soc.* **2016,** *138*, 8581-8587.

33. Protesescu, L.; Yakunin, S.; Bodnarchuk, M.; Krieg, F.; Caputo, R.; Hendon, C.; Yang, R.; Walsh, A.; Kovalenko, M., Nanocrystals of Cesium Lead Halide Perovskites (CsPbX3, X=Cl, Br, and I): Novel Optoelectronic Materials Showing Bright Emission with Wide Color Gamut. *Nano Lett.* **2015,** *15*, 3692-3696.

34. Eaton, S.; Lai, M.; Gibson, N.; Wong, A.; Dou, L.; Ma, J.; Wang, L.; Leone, S.; Yang, P., Lasing in robust cesium lead halide perovskite nanowires. *PNAS* **2016,** *113*, 1993-1998.

35. Fu, Y.; Zhu, H.; Schrader, A.; Liang, D.; Ding, Q.; Joshi, P.; Hwang, L.; Zhu, X.; Jin, S., Nanowire Lasers of Formamidinium Lead Halide Perovskites and Their Stabilized Alloys with Improved Stability. *Nano Lett.* **2016,** *16*, 1000-1008.

36. Zhu, H.; Fu, Y.; Meng, F.; Wu, X.; Gong, Z.; Ding, Q.; Gustafsson, M.; Trinh, M.; Jin, S.; Zhu, X., Lead halide perovskite nanowire lasers with low lasing thresholds and high quality factors. *Nat. Mater.* **2015,** *14*, 636-642.

37. Zhang, X.; Lin, H.; Huang, H.; Reckmeier, C.; Zhang, Y.; Choy, W.; Rogach, A., Enhancing the Brightness of Cesium Lead Halide Perovskite Nanocrystal Based Green Light-Emitting Devices through the Interface Engineering with Perfluorinated Ionomer. *Nano Lett.* **2016,** *16*, 1415-1420.

38. Wang, Y.; Zhu, Y.; Huang, J.; Cai, J.; Zhu, J.; Yang, X.; Shen, J.; Jiang, H.; Li, C., CsPbBr3 Perovskite Quantum Dots-Based Monolithic Electrospun Fiber Membrane as an Ultrastable and Ultrasensitive Fluorescent Sensor in Aqueous Medium. *J. Phys. Chem. Lett.* **2016,** *7* (21), 4253-4258.

39. Zhang, F.; Zhong, H.; Chen, C.; Wu, X.; Hu, X.; Huang, H.; Han, J.; Zou, B.; Dong, Y., Brightly Luminescent and Color-Tunable Colloidal CH3NH3PbX3 (X=Br,I,Cl) Quantum Dots: Potential Alternatives for Display Technology. *ACS Nano* **2016,** *9*, 4533-4542.

40. Tian, Y.; Merdasa, A.; Peter, M.; Abdellah, M.; Zheng, K.; Ponseca, C.; Pullerits, T.; Yartsev, A.; Sundstrom, V.; Scheblykin, I., Giant Photoluminescence Blinking of Perovskite Nanocrystals Reveals Single-Trap Control of Luminescence. *Nano Lett.* **2015,** *15*, 1603-1608.

41. Nedelcu, G.; Protesescu, L.; Yakunin, S.; Bodnarchuk, M.; Grotevent, M.; Kovalenko, M., Fast Anion-Exchange in Highly Luminescent Nanocrystals of Cesium Lead Halide Perovskites (CsPbX3, X= Cl, Br, I). *Nano Lett.* **2015,** *15*, 5635-5640.

42. Roo, J.; Ibanez, M.; Geiregat, P.; Nedelcu, G.; Walravens, W.; Maes, J.; Martins, J.; Driessche, I.; Kovalenko, M.; Hens, Z., Highly Dynamic Ligand Binding and Light Absorption Coefficient of Cesium Lead Bromide Perovskite Nanocrystals. *ACS Nano* **2016,** *10*, 2071-2081.

43. Jaiswal, J. K.; Mattoussi, H.; Mauro, J. M.; Simon, S. M., Long-term multiple color imaging of live cells using quantum dot bioconjugates. *Nat. Biotechnol.* **2003,** *21* (1), 47-51.

44. Frasco, M.; Chaniotakis, N., Semiconductor Quantum Dots in Chemical Sensors and Biosensors. *Sensors* **2009,** *9*, 7266-7286.

45. Wang, C.; Zhang, Y.; Wang, A.; Wang, Q.; Tang, H.; Shen, W.; Li, Z.; Deng, Z., Controlled Synthesis of Composition Tunable Formamidinium Cesium Double Cation Lead Halide Perovskite Nanowires and Nanosheets with Improved Stability. *Chem. Mater.* **2017,** *29* (5), 2157-2166.

46. Wang, H.-C.; Lin, S.-Y.; Tang, A.-C.; Singh, B. P.; Tong, H.-C.; Chen, C.-Y.; Lee, Y.-C.; Tsai, T.-L.; Liu, R.-S., Mesoporous Silica Particles Integrated with All-Inorganic CsPbBr3 Perovskite Quantum-Dot Nanocomposites (MP-PQDs) with High Stability and Wide Color Gamut Used for Backlight Display. *Angew. Chem. Int. Ed.* **2016,** *55* (28), 7924-7929.

47. Kim, Y.; Yassitepe, E.; Voznyy, O.; Comin, R.; Walters, G.; Gong, X.; Kanjanaboos, P.; Nogueira, A. F.; Sargent, E. H., Efficient Luminescence from Perovskite Quantum Dot Solids. *ACS Appl. Mater. Interfaces* **2015,** *7* (45), 25007-25013.

48. Yassitepe, E.; Yang, Z.; Voznyy, O.; Kim, Y.; Walters, G.; Castañeda, J. A.; Kanjanaboos, P.; Yuan, M.; Gong, X.; Fan, F.; Pan, J.; Hoogland, S.; Comin, R.; Bakr, O. M.; Padilha, L. A.; Nogueira, A. F.; Sargent, E. H., Amine-Free Synthesis of Cesium Lead Halide Perovskite Quantum Dots for Efficient Light-Emitting Diodes. *Adv. Funct. Mater.* **2016,** *26* (47), 8757-8763.

49. Meyns, M.; Perálvarez, M.; Heuer-Jungemann, A.; Hertog, W.; Ibáñez, M.; Nafria, R.; Genç, A.; Arbiol, J.; Kovalenko, M. V.; Carreras, J.; Cabot, A.; Kanaras, A. G., Polymer-Enhanced Stability of Inorganic Perovskite Nanocrystals and Their Application in Color Conversion LEDs. *ACS Appl. Mater. Interfaces* **2016,** *8* (30), 19579-19586.

50. Huang, H.; Chen, B.; Wang, Z.; Hung, T. F.; Susha, A. S.; Zhong, H.; Rogach, A. L., Water resistant CsPbX3 nanocrystals coated with polyhedral oligomeric silsesquioxane and their use as solid state luminophores in all-perovskite white light-emitting devices. *Chem. Sci.* **2016,** *7* (9), 5699-5703.

51. Gomez, L.; de Weerd, C.; Hueso, J. L.; Gregorkiewicz, T., Color-stable water-dispersed cesium lead halide perovskite nanocrystals. *Nanoscale* **2017,** *9* (2), 631-636.

52. Hoke, E.; Slotcavage, D.; Dohner, E.; Bowring, A.; Karunadasa, H.; McGehee, M., Reversible photo-induced trap formation in mixed-halide hybrid perovskites for photovoltaics. *Chem. Sci.* **2015,** *6*, 613-617.

53. Saliba, M.; Matsui, T.; Seo, J.; Domanski, K.; Correa-Baena, J.; Nazeeruddin, M.; Zakeeruddin, S.; Tress, W.; Abate, A.; Hagfeldt, A.; Gratzel, M., Cesium-containing triple cation perovskite solar cells: improved stability, reproducibility and high efficiency. *Energy Environ. Sci.* **2016,** *9*, 1989-1997.

54. Choi, H.; Jeong, J.; Kim, H.; Kim, S.; Walker, B.; Kim, G.; Kim, J., Cesium-doped methylammonium lead iodide perovskite light absorber for hybrid solar cells. *Nano Energy* **2014,** *7*, 80-85.

55. Lee, J.; Kim, D.; Kim, H.; Seo, S.; Cho, S.; N., P., Formamidinium and Cesium Hybridization for Photo- and Moisture-Stable Perovskite Solar Cell. *Adv. Energy Mater.* **2015,** *5*, 1501310.

56. Chen, Y.; Yoon, Y.; Pang, X.; He, Y.; Jung, J.; Feng, C.; Zhang, G.; Lin, Z., Precisely Size-Tunable Monodisperse Hairy Plasmonic Nanoparticles via Amphiphilic Star-Like Block Copolymers. *Small* **2016,** *12* (48), 6714-6723.

57. Notarianni, M.; Vernon, K.; Chou, A.; Aljada, M.; Liu, J.; Motta, N., Plasmonic effect of gold nanoparticles in organic solar cells. *Sol. Energy* **2014,** *106*, 23-37.

58. Yeh, Y.-C.; Creran, B.; Rotello, V. M., Gold nanoparticles: preparation, properties, and applications in bionanotechnology. *Nanoscale* **2012,** *4* (6), 1871-1880.

59. Jana, N.; Gearheart, L.; Murphy, C., Seed-Mediated Growth Approach for Shape-Controlled Synthesis of Spheroidal and Rod-like Gold Nanoparticles Using a Surfactant Template. *Adv. Mater.* **2001,** *13* (18), 1389-1393.

60. Nikoobakht, B.; El-Sayed, M., Preparation and Growth Mechanism of Gold Nanorods (NRs) Using See-Mediated Growth Method. *Chem. Mater.* **2003,** *15*, 1957-1962.

61. Chen, H.; Shao, L.; Li, Q.; Wang, J., Gold Nanorods and their plasmonic properties. *Chem. Soc. Rev.* **2013,** *42*, 2679-2724.

62. Perez-Juste, J.; Pastoriza-Santos, I.; Liz-Marzan, L.; Mulvaney, P., Gold nanorods: Synthesis, characterization and applications. *Coordin. Chem. Rev.* **2005,** *249*, 1870-1901.

63. Huang, X.; El-Sayed, M., Gold nanoparticles: Optical properties and implementations in cancer diagnosis and photothermal therapy. *Journal of Advanced Research* **2010,** *1*, 13-28.

64. Lohse, S.; Murphy, C., The Quest for Shape Control: A History of Gold Nanorod Synthesis. *Chem. Mater.* **2013,** *25*, 1250-1261.

65. Dreaden, E.; Alkilany, A.; Huang, X.; Murphy, C.; El-Sayed, M., The golden age: gold nanoparticles for biomedicine. *Chem. Soc. Rev.* **2012,** *41*, 2740-2779.

66. Eustis, S.; El-Sayed, M., Why gold nanoparticles are more precious than pretty gold: Noble metal surface plasmon resonance and its enhancement of the radiative and nonradiative properties of nanocrystals of different shapes. *Chem. Soc. Rev.* **2005,** *35*, 209-217.

67. Vigderman, L.; Khanal, B.; Zubarev, E., Functional Gold Nanorods: Synthesis, Self-Assembly, and Sensing Applications. *Adv. Mater.* **2012,** *24* (36), 4811-4841.

68. Huang, X.; Neretina, S.; El-Sayed, M., Gold Nanorods: From Synthesis and Properties to Biological and Biomedical Applications. *Adv. Mater.* **2009,** *21* (48), 4880-4910.

69. Li, J.; Guo, H.; Li, Z.-Y., Microscopic and macroscopic manipulation of gold nanorod and its hybrid nanostructures [Invited]. *Photon. Res.* **2013,** *1* (1), 28-41.

70. Li, Q.-L.; Lu, W.-X.; Wan, N.; Ding, S.-N., Tuning optical properties of perovskite nanocrystals by supermolecular mercapto-β-cyclodextrin. *Chem. Commun.* **2016,** *52* (83), 12342-12345.

71. Akkerman, Q. A.; D'Innocenzo, V.; Accornero, S.; Scarpellini, A.; Petrozza, A.; Prato, M.; Manna, L., Tuning the Optical Properties of Cesium Lead Halide Perovskite

Nanocrystals by Anion Exchange Reactions. *J. Am. Chem. Soc.* **2015,** *137* (32), 10276-10281.

72. Loiudice, A.; Saris, S.; Oveisi, E.; Alexander, D. T. L.; Buonsanti, R., CsPbBr3 QD/AlOx Inorganic Nanocomposites with Exceptional Stability in Water, Light, and Heat. *Angew. Chem. Int. Ed.* **2017,** *56* (36), 10696-10701.

73. Hu, H.; Wu, L.; Tan, Y.; Zhong, Q.; Chen, M.; Qiu, Y.; Yang, D.; Sun, B.; Zhang, Q.; Yin, Y., Interfacial Synthesis of Highly Stable CsPbX3/Oxide Janus Nanoparticles. *J. Am. Chem. Soc.* **2018,** *140* (1), 406-412.

74. Xin, Y.; Zhao, H.; Zhang, J., Highly Stable and Luminescent Perovskite–Polymer Composites from a Convenient and Universal Strategy. *ACS Appl. Mater. Interfaces* **2018,** *10* (5), 4971-4980.

75. Zhang, H.; Wang, X.; Liao, Q.; Xu, Z.; Li, H.; Zheng, L.; Fu, H., Embedding Perovskite Nanocrystals into a Polymer Matrix for Tunable Luminescence Probes in Cell Imaging. *Adv. Funct. Mater.* **2017,** *27* (7), 1604382-n/a.

76. Raja, S. N.; Bekenstein, Y.; Koc, M. A.; Fischer, S.; Zhang, D.; Lin, L.; Ritchie, R. O.; Yang, P.; Alivisatos, A. P., Encapsulation of Perovskite Nanocrystals into Macroscale Polymer Matrices: Enhanced Stability and Polarization. *ACS Appl. Mater. Interfaces* **2016,** *8* (51), 35523-35533.

77. Wei, Y.; Deng, X.; Xie, Z.; Cai, X.; Liang, S.; Ma, P. a.; Hou, Z.; Cheng, Z.; Lin, J., Enhancing the Stability of Perovskite Quantum Dots by Encapsulation in Crosslinked Polystyrene Beads via a Swelling–Shrinking Strategy toward Superior Water Resistance. *Adv. Funct. Mater.* **2017,** *27* (39), 1703535-n/a.

78. Massignani, M.; LoPresti, C.; Blanazs, A.; Madsen, J.; Armes, S. P.; Lewis, A. L.; Battaglia, G., Controlling Cellular Uptake by Surface Chemistry, Size, and Surface Topology at the Nanoscale. *Small* **2009,** *5* (21), 2424-2432.

79. Zheng, D.; Pang, X.; Wang, M.; He, Y.; Lin, C.; Lin, Z., Unconventional Route to Hairy Plasmonic/Semiconductor Core/Shell Nanoparticles with Precisely Controlled Dimensions and Their Use in Solar Energy Conversion. *Chem. Mater.* **2015,** *27* (15), 5271-5278.

80. Xu, H.; Xu, Y.; Pang, X.; He, Y.; Jung, J.; Xia, H.; Lin, Z., A general route to nanocrystal kebabs periodically assembled on stretched flexible polymer shish. *Sci. Adv.* **2015,** *1*, e1500025.

81. Xu, H.; Pang, X.; He, Y.; He, M.; Jung, J.; Xia, H.; Lin, Z., An Unconventional Route to Monodisperse and Intimate Semiconducting Organic-Inorganic Nanocomposites. *Angew. Chem. Int. Ed.* **2015,** *54*, 4636-4640.

82. Yang, D.; Pang, X.; He, Y.; Wang, Y.; Chen, G.; Wang, W.; Lin, Z., Precisely Size-Tunable Magnetic/Plasmonic Core/Shell Nanoparticles with Controlled Optical Properties. *Angew. Chem. Int. Ed.* **2015,** *54* (41), 12091-12096.

83. He, M.; Pang, X.; Liu, X.; Jiang, B.; He, Y.; Snaith, H.; Lin, Z., Monodisperse Dual-functional Upconversion Nanoparticles Enabled Near-Infrared Organolead Halide Perovskite Solar Cells. *Angew. Chem. Int. Ed.* **2016,** *55*, 4280-4284.

84. Wang, M.; Pang, X.; Zheng, D.; He, Y.; Sun, L.; Lin, C.; Lin, Z., Nonepitaxial growth of uniform and precisely size-tunable core/shell nanoparticles and their enhanced plasmon-driven photocatalysis. *J. Mater. Chem. A* **2016,** *4* (19), 7190-7199.

85. Jiang, B.; Pang, X.; Li, B.; Lin, Z., Organic-inorganic nanocomposites via placing monodisperse ferroelectric nanocrystals in direct and permanent connect with ferroelectric polymers. *J. Am. Chem. Soc.* **2015,** *137*, 11760-11767.

86. Hou, S.; Guo, Y.; Tang, Y.; Quan, Q., Synthesis and Stabilization of Colloidal Perovskite Nanocrystals by Multidentate Polymer Micelles. *ACS Appl. Mater. Interfaces* **2017,** *9* (22), 18417-18422.

87. Chen, Y.; Yang, D.; Yoon, Y. J.; Pang, X.; Wang, Z.; Jung, J.; He, Y.; Harn, Y. W.; He, M.; Zhang, S.; Zhang, G.; Lin, Z., Hairy Uniform Permanently Ligated Hollow Nanoparticles with Precise Dimension Control and Tunable Optical Properties. *J. Am. Chem. Soc.* **2017,** *139* (37), 12956-12967.

88. Chen, Y.; Wang, Z.; He, Y.; Yoon, Y. J.; Jung, J.; Zhang, G.; Lin, Z., Light-enabled reversible self-assembly and tunable optical properties of stable hairy nanoparticles. *PNAS* **2018**.

89. Li, X.; Wu, Y.; Zhang, S.; Cai, B.; Gu, Y.; Song, J.; Zeng, H., CsPbX3 Quantum Dots for Lighting and Displays: Room-Temperature Synthesis, Photoluminescence Superiorities, Underlying Origins and White Light-Emitting Diodes. *Adv. Funct. Mater.* **2016,** *26* (15), 2435-2445.

90. Krieg, F.; Ochsenbein, S. T.; Yakunin, S.; ten Brinck, S.; Aellen, P.; Süess, A.; Clerc, B.; Guggisberg, D.; Nazarenko, O.; Shynkarenko, Y.; Kumar, S.; Shih, C.-J.; Infante, I.; Kovalenko, M. V., Colloidal CsPbX3 (X = Cl, Br, I) Nanocrystals 2.0: Zwitterionic Capping Ligands for Improved Durability and Stability. *ACS Energy Lett.* **2018,** *3* (3), 641-646.

91. Zhang, T.; Li, G.; Chang, Y.; Wang, X.; Zhang, B.; Mou, H.; Jiang, Y., Full-spectra hyperfluorescence cesium lead halide perovskite nanocrystals obtained by efficient halogen anion exchange using zinc halogenide salts. *CrystEngComm* **2017,** *19* (8), 1165-1171.

92. Pan, J.; Sarmah, S. P.; Murali, B.; Dursun, I.; Peng, W.; Parida, M. R.; Liu, J.; Sinatra, L.; Alyami, N.; Zhao, C.; Alarousu, E.; Ng, T. K.; Ooi, B. S.; Bakr, O. M.; Mohammed, O. F., Air-Stable Surface-Passivated Perovskite Quantum Dots for Ultra-

Robust, Single- and Two-Photon-Induced Amplified Spontaneous Emission. *J. Phys. Chem. Lett.* **2015,** *6* (24), 5027-5033.

93. Kang, J.; Wang, L.-W., High Defect Tolerance in Lead Halide Perovskite CsPbBr3. *J. Phys. Chem. Lett.* **2017,** *8* (2), 489-493.

94. Swarnkar, A.; Ravi, V. K.; Nag, A., Band Edge Energies and Excitonic Transition Probabilities of Colloidal CsPbX3 (X = Cl, Br, I) Perovskite Nanocrystals. *ACS Energy Lett.* **2017,** *2*, 1089.

95. Xu, Y.; Li, W.; Qiu, F.; Lin, Z., Self-assembly of 21-arm star-like diblock copolymer in bulk and under cylindrical confinement. *Nanoscale* **2014,** *6* (12), 6844-6852.

96. Li, H.; Liu, B.; Zhang, X.; Gao, C.; Shen, J.; Zou, G., Single-Molecule Force Spectroscopy on Poly(acrylic acid) by AFM. *Langmuir* **1999,** *15* (6), 2120-2124.

97. Liu, C.; Li, Z.; Hajagos, T. J.; Kishpaugh, D.; Chen, D. Y.; Pei, Q., Transparent Ultra-High-Loading Quantum Dot/Polymer Nanocomposite Monolith for Gamma Scintillation. *ACS Nano* **2017,** *11* (6), 6422-6430.

98. Shinde, A.; Gahlaut, R.; Mahamuni, S., Low-Temperature Photoluminescence Studies of CsPbBr3 Quantum Dots. *J. Phys. Chem. C* **2017,** *121* (27), 14872-14878.

99. Chiba, T.; Hoshi, K.; Pu, Y.-J.; Takeda, Y.; Hayashi, Y.; Ohisa, S.; Kawata, S.; Kido, J., High-Efficiency Perovskite Quantum-Dot Light-Emitting Devices by Effective Washing Process and Interfacial Energy Level Alignment. *ACS Appl. Mater. Interfaces* **2017,** *9* (21), 18054-18060.

100. Jung, J.; Lin, C. H.; Yoon, Y. J.; Malak, S. T.; Zhai, Y.; Thomas, E. L.; Vardeny, V.; Tsukruk, V. V.; Lin, Z., Crafting Core/Graded Shell–Shell Quantum Dots with Suppressed Re-absorption and Tunable Stokes Shift as High Optical Gain Materials. *Angew. Chem. Int. Ed.* **2016,** *55* (16), 5071-5075.

101. Jain, P. K.; Huang, X.; El-Sayed, I. H.; El-Sayed, M. A., Noble Metals on the Nanoscale: Optical and Photothermal Properties and Some Applications in Imaging, Sensing, Biology, and Medicine. *Accounts Chem. Res.* **2008,** *41* (12), 1578-1586.

102. Ishida, T.; Haruta, M., Gold Catalysts: Towards Sustainable Chemistry. *Angew. Chem. Int. Ed.* **2007,** *46* (38), 7154-7156.

103. Brus, L., Noble Metal Nanocrystals: Plasmon Electron Transfer Photochemistry and Single-Molecule Raman Spectroscopy. *Accounts Chem. Res.* **2008,** *41* (12), 1742-1749.

104. Park, J.; Joo, J.; Kwon, S. G.; Jang, Y.; Hyeon, T., Synthesis of Monodisperse Spherical Nanocrystals. *Angew. Chem. Int. Ed.* **2007,** *46* (25), 4630-4660.

105. Ling, D.; Hackett, M. J.; Hyeon, T., Surface ligands in synthesis, modification, assembly and biomedical applications of nanoparticles. *Nano Today* **2014,** *9* (4), 457-477.

106. Álvarez-Puebla, R. A.; Contreras-Cáceres, R.; Pastoriza-Santos, I.; Pérez-Juste, J.; Liz-Marzán, L. M., Au@pNIPAM Colloids as Molecular Traps for Surface-Enhanced, Spectroscopic, Ultra-Sensitive Analysis. *Angew. Chem. Int. Ed.* **2009,** *48* (1), 138-143.

107. Wang, B.; Li, B.; Zhao, B.; Li, C. Y., Amphiphilic Janus Gold Nanoparticles via Combining "Solid-State Grafting-to" and "Grafting-from" Methods. *J. Am. Chem. Soc.* **2008,** *130* (35), 11594-11595.

108. Chai, J.; Wang, D.; Fan, X.; Buriak, J. M., Assembly of aligned linear metallic patterns on silicon. *Nat. Nanotechnol.* **2007,** *2* (8), 500-506.

109. Zhao, B.; Brittain, W. J., Polymer brushes: surface-immobilized macromolecules. *Prog. Polym. Sci.* **2000,** *25* (5), 677-710.

110. Riess, G., Micellization of block copolymers. *Prog. Polym. Sci.* **2003,** *28* (7), 1107-1170.

111. Rodríguez-Hernández, J.; Chécot, F.; Gnanou, Y.; Lecommandoux, S., Toward 'smart' nano-objects by self-assembly of block copolymers in solution. *Prog. Polym. Sci.* **2005,** *30* (7), 691-724.

112. Darling, S. B., Directing the self-assembly of block copolymers. *Prog. Polym. Sci.* **2007,** *32* (10), 1152-1204.

113. Crooks, R. M.; Zhao, M.; Sun, L.; Chechik, V.; Yeung, L. K., Dendrimer-Encapsulated Metal Nanoparticles: Synthesis, Characterization, and Applications to Catalysis. *Accounts Chem. Res.* **2001,** *34* (3), 181-190.

114. Matyjaszewski, K.; Tsarevsky, N. V., Nanostructured functional materials prepared by atom transfer radical polymerization. *Nat. Chem.* **2009,** *1* (4), 276-288.

115. Shimizu, T.; Teranishi, T.; Hasegawa, S.; Miyake, M., Size Evolution of Alkanethiol-Protected Gold Nanoparticles by Heat Treatment in the Solid State. *J. Phys. Chem. B* **2003,** *107* (12), 2719-2724.

116. Willets, K. A.; Duyne, R. P. V., Localized Surface Plasmon Resonance Spectroscopy and Sensing. *Annu. Rev. Phys. Chem.* **2007,** *58* (1), 267-297.

117. Wang, X.; Zhuang, J.; Peng, Q.; Li, Y., A general strategy for nanocrystal synthesis. *Nature* **2005,** *437* (7055), 121-124.

118. Templeton, A. C.; Pietron, J. J.; Murray, R. W.; Mulvaney, P., Solvent Refractive Index and Core Charge Influences on the Surface Plasmon Absorbance of Alkanethiolate Monolayer-Protected Gold Clusters. *The Journal of Physical Chemistry B* **2000,** *104* (3), 564-570.

119. Kang, Y.; Taton, T. A., Core/Shell Gold Nanoparticles by Self-Assembly and Crosslinking of Micellar, Block-Copolymer Shells. *Angewandte Chemie International Edition* **2005,** *44* (3), 409-412.

120. Kreibig, U.; Vollmer, M., *Optical Properties of Metal Clusters*. Springer-Verlag Berlin Heidelberg: 1995.

121. Link, S.; El-Sayed, M. A., Spectral Properties and Relaxation Dynamics of Surface Plasmon Electronic Oscillations in Gold and Silver Nanodots and Nanorods. *J. Phys. Chem. B* **1999,** *103* (40), 8410-8426.

122. Sqalli, O.; Bernal, M.-P.; Hoffmann, P.; Marquis-Weible, F., Improved tip performance for scanning near-field optical microscopy by the attachment of a single gold nanoparticle. *Appl. Phys. Lett.* **2000,** *76* (15), 2134-2136.

123. Kelly, K. L.; Coronado, E.; Zhao, L. L.; Schatz, G. C., The Optical Properties of Metal Nanoparticles: The Influence of Size, Shape, and Dielectric Environment. *J. Phys. Chem. B* **2003,** *107* (3), 668-677.

124. Noguez, C., Surface Plasmons on Metal Nanoparticles: The Influence of Shape and Physical Environment. *J. Phys. Chem. C* **2007,** *111* (10), 3806-3819.

125. Cao, Y. C.; Jin, R.; Mirkin, C. A., Nanoparticles with Raman Spectroscopic Fingerprints for DNA and RNA Detection. *Science* **2002,** *297* (5586), 1536-1540.

126. Pang, X.; He, Y.; Jiang, B.; Iocozzia, J.; Zhao, L.; Guo, H.; Liu, J.; Akinc, M.; Bowler, N.; Tan, X.; Lin, Z., Block copolymer/ferroelectric nanoparticle nanocomposites. *Nanoscale* **2013,** *5* (18), 8695-8702.

127. Ziolo, R. F.; Giannelis, E. P.; Weinstein, B. A.; O'Horo, M. P.; Ganguly, B. N.; Mehrotra, V.; Russell, M. W.; Huffman, D. R., Matrix-Mediated Synthesis of Nanocrystalline γ-Fe₂O₃: A New Optically Transparent Magnetic Material. *Science* **1992,** *257* (5067), 219-223.

128. Mai, W.; Sun, B.; Chen, L.; Xu, F.; Liu, H.; Liang, Y.; Fu, R.; Wu, D.; Matyjaszewski, K., Water-Dispersible, Responsive, and Carbonizable Hairy Microporous Polymeric Nanospheres. *J. Am. Chem. Soc.* **2015,** *137* (41), 13256-13259.

129. Wu, D.; Li, Z.; Zhong, M.; Kowalewski, T.; Matyjaszewski, K., Templated Synthesis of Nitrogen-Enriched Nanoporous Carbon Materials from Porogenic Organic Precursors Prepared by ATRP. *Angew. Chem. Int. Ed.* **2014,** *53* (15), 3957-3960.

130. Wang, L.; Bai, J.; Bo, X.; Zhang, X.; Guo, L., A novel glucose sensor based on ordered mesoporous carbon–Au nanoparticles nanocomposites. *Talanta* **2011,** *83* (5), 1386-1391.

131. Compton, O. C.; Osterloh, F. E., Evolution of Size and Shape in the Colloidal Crystallization of Gold Nanoparticles. *J. Am. Chem. Soc.* **2007,** *129* (25), 7793-7798.

132. Kershaw, S. V.; Susha, A. S.; Rogach, A. L., Narrow bandgap colloidal metal chalcogenide quantum dots: synthetic methods, heterostructures, assemblies, electronic and infrared optical properties. *Chem. Soc. Rev.* **2013,** *42* (7), 3033-3087.

133. Mishra, N.; Mukherjee, B.; Xing, G.; Chakrabortty, S.; Guchhait, A.; Lim, J. Y., Cation exchange synthesis of uniform PbSe/PbS core/shell tetra-pods and their use as near-infrared photodetectors. *Nanoscale* **2016,** *8* (29), 14203-14212.

134. Wise, F. W., Lead Salt Quantum Dots: the Limit of Strong Quantum Confinement. *Accounts Chem. Res.* **2000,** *33* (11), 773-780.

135. Pietryga, J. M.; Schaller, R. D.; Werder, D.; Stewart, M. H.; Klimov, V. I.; Hollingsworth, J. A., Pushing the Band Gap Envelope: Mid-Infrared Emitting Colloidal PbSe Quantum Dots. *J. Am. Chem. Soc.* **2004,** *126* (38), 11752-11753.

136. Pietryga, J. M.; Werder, D. J.; Williams, D. J.; Casson, J. L.; Schaller, R. D.; Klimov, V. I.; Hollingsworth, J. A., Utilizing the Lability of Lead Selenide to Produce Heterostructured Nanocrystals with Bright, Stable Infrared Emission. *J. Am. Chem. Soc.* **2008,** *130* (14), 4879-4885.

137. Liu, T. C. Y., *Semiconductor Nanocrystals and Metal Nanoparticles: Physical Properties and Device Applications*. CRC Press: 2016.

138. Dalven, R., A review of the semiconductor properties of PbTe, PbSe, PbS and PbO. *Infrared Phys.* **1969,** *9* (4), 141-184.

139. McGuire, J. A.; Sykora, M.; Joo, J.; Pietryga, J. M.; Klimov, V. I., Apparent Versus True Carrier Multiplication Yields in Semiconductor Nanocrystals. *Nano Lett.* **2010,** *10* (6), 2049-2057.

140. Beard, M. C.; Midgett, A. G.; Hanna, M. C.; Luther, J. M.; Hughes, B. K.; Nozik, A. J., Comparing Multiple Exciton Generation in Quantum Dots To Impact Ionization in Bulk Semiconductors: Implications for Enhancement of Solar Energy Conversion. *Nano Lett.* **2010,** *10* (8), 3019-3027.

141. Zhang, J.; Gao, J.; Church, C. P.; Miller, E. M.; Luther, J. M.; Klimov, V. I.; Beard, M. C., PbSe Quantum Dot Solar Cells with More than 6% Efficiency Fabricated in Ambient Atmosphere. *Nano Lett.* **2014,** *14* (10), 6010-6015.

142. Talapin, D. V.; Murray, C. B., PbSe Nanocrystal Solids for n- and p-Channel Thin Film Field-Effect Transistors. *Science* **2005,** *310* (5745), 86-89.

143. Luther, J. M.; Law, M.; Song, Q.; Perkins, C. L.; Beard, M. C.; Nozik, A. J., Structural, Optical, and Electrical Properties of Self-Assembled Films of PbSe Nanocrystals Treated with 1,2-Ethanedithiol. *ACS Nano* **2008,** *2* (2), 271-280.

144. Sykora, M.; Koposov, A. Y.; McGuire, J. A.; Schulze, R. K.; Tretiak, O.; Pietryga, J. M.; Klimov, V. I., Effect of Air Exposure on Surface Properties, Electronic Structure, and Carrier Relaxation in PbSe Nanocrystals. *ACS Nano* **2010,** *4* (4), 2021-2034.

145. Yanover, D.; Vaxenburg, R.; Tilchin, J.; Rubin-Brusilovski, A.; Zaiats, G.; Čapek, R. K.; Sashchiuk, A.; Lifshitz, E., Significance of Small-Sized PbSe/PbS Core/Shell Colloidal Quantum Dots for Optoelectronic Applications. *J. Phys. Chem. C* **2014,** *118* (30), 17001-17009.

146. Kim, S.; Marshall, A. R.; Kroupa, D. M.; Miller, E. M.; Luther, J. M.; Jeong, S.; Beard, M. C., Air-Stable and Efficient PbSe Quantum-Dot Solar Cells Based upon ZnSe to PbSe Cation-Exchanged Quantum Dots. *ACS Nano* **2015,** *9* (8), 8157-8164.

147. Zhang, J.; Chernomordik, B. D.; Crisp, R. W.; Kroupa, D. M.; Luther, J. M.; Miller, E. M.; Gao, J.; Beard, M. C., Preparation of Cd/Pb Chalcogenide Heterostructured Janus Particles via Controllable Cation Exchange. *ACS Nano* **2015,** *9* (7), 7151-7163.

148. Wei, S.-H.; Zunger, A., Electronic and structural anomalies in lead chalcogenides. *Physical Review B* **1997,** *55* (20), 13605-13610.

149. Lifshitz, E.; Brumer, M.; Kigel, A.; Sashchiuk, A.; Bashouti, M.; Sirota, M.; Galun, E.; Burshtein, Z.; Le Quang, A. Q.; Ledoux-Rak, I.; Zyss, J., Air-Stable PbSe/PbS and PbSe/PbSexS1-x Core−Shell Nanocrystal Quantum Dots and Their Applications. *J. Phys. Chem. B* **2006,** *110* (50), 25356-25365.

150. Brumer, M.; Kigel, A.; Amirav, L.; Sashchiuk, A.; Solomesch, O.; Tessler, N.; Lifshitz, E., PbSe/PbS and PbSe/PbSexS1–x Core/Shell Nanocrystals. *Adv. Funct. Mater.* **2005,** *15* (7), 1111-1116.

151. Yu, W. W.; Qu, L.; Guo, W.; Peng, X., Experimental Determination of the Extinction Coefficient of CdTe, CdSe, and CdS Nanocrystals. *Chem. Mater.* **2003,** *15* (14), 2854-2860.

152. Dabbousi, B. O.; Rodriguez-Viejo, J.; Mikulec, F. V.; Heine, J. R.; Mattoussi, H.; Ober, R.; Jensen, K. F.; Bawendi, M. G., (CdSe)ZnS Core−Shell Quantum Dots: Synthesis and Characterization of a Size Series of Highly Luminescent Nanocrystallites. *J. Phys. Chem. B* **1997,** *101* (46), 9463-9475.

153. Beberwyck, B. J.; Surendranath, Y.; Alivisatos, A. P., Cation Exchange: A Versatile Tool for Nanomaterials Synthesis. *J. Phys. Chem. C* **2013,** *117* (39), 19759-19770.

154. Luther, J. M.; Zheng, H.; Sadtler, B.; Alivisatos, A. P., Synthesis of PbS Nanorods and Other Ionic Nanocrystals of Complex Morphology by Sequential Cation Exchange Reactions. *J. Am. Chem. Soc.* **2009,** *131* (46), 16851-16857.

155. Mokari, T.; Habas, S. E.; Zhang, M.; Yang, P., Synthesis of Lead Chalcogenide Alloy and Core–Shell Nanowires. *Angew. Chem. Int. Ed.* **2008,** *47* (30), 5605-5608.

156. Son, D. H.; Hughes, S. M.; Yin, Y.; Paul Alivisatos, A., Cation Exchange Reactions in Ionic Nanocrystals. *Science* **2004,** *306* (5698), 1009-1012.

157. Bae, W. K.; Char, K.; Hur, H.; Lee, S., Single-Step Synthesis of Quantum Dots with Chemical Composition Gradients. *Chem. Mater.* **2008,** *20* (2), 531-539.

158. Jung, J.; Lin, C. H.; Yoon, Y. J.; Malak, S. T.; Zhai, Y.; Thomas, E. L.; Vardeny, V.; Tsukruk, V. V.; Lin, Z., Crafting Core/Graded Shell–Shell Quantum Dots with Suppressed Re-absorption and Tunable Stokes Shift as High Optical Gain Materials. *Angew. Chem. Int. Ed.* **2016,** *55* (16), 5071-5075.